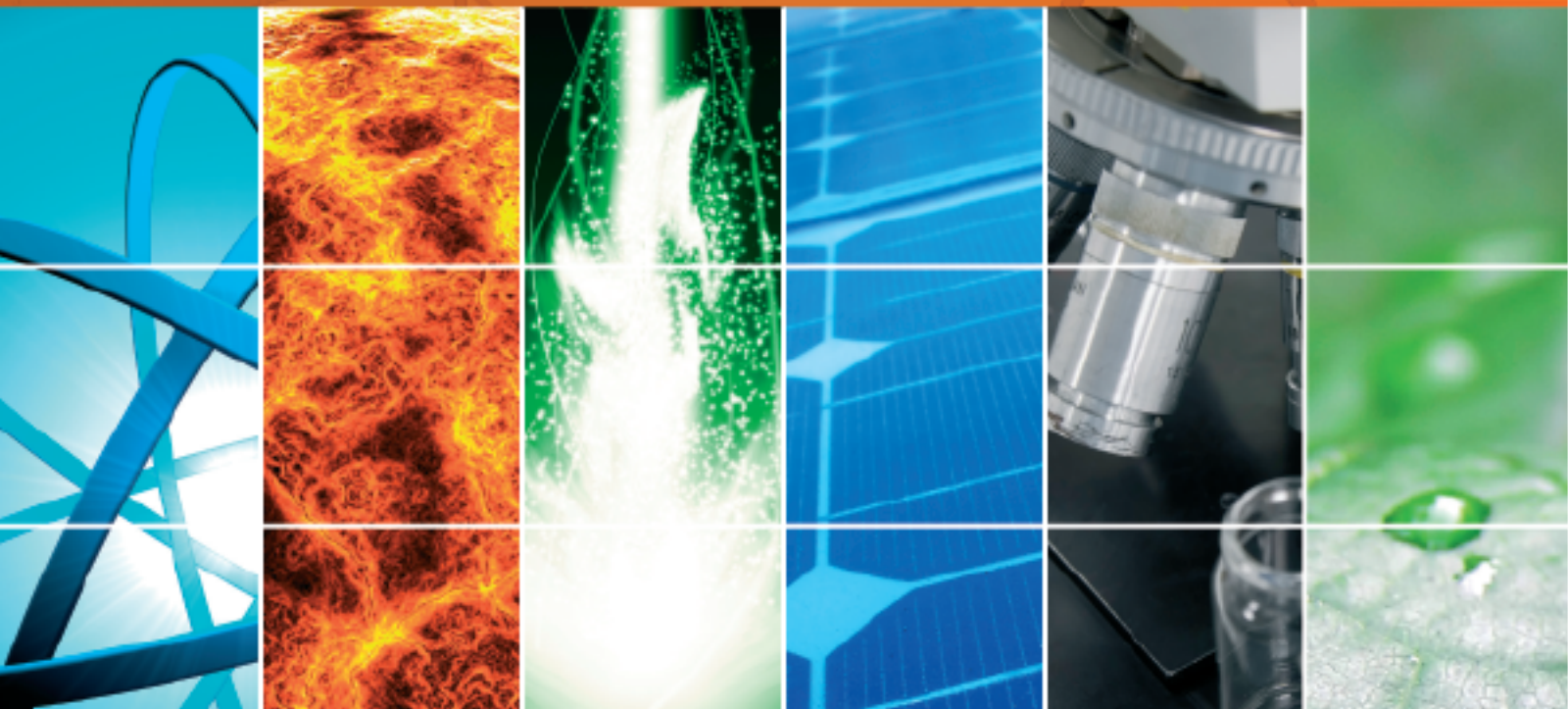


Progress in Photovoltaic Devices and Systems

Guest Editors: Hongxing Yang, Hui Shen, Tao Xu,
and Dimitrios Karamanis





Progress in Photovoltaic Devices and Systems

International Journal of Photoenergy

Progress in Photovoltaic Devices and Systems

Guest Editors: Hongxing Yang, Hui Shen, Tao Xu,
and Dimitrios Karamanis



Copyright © 2015 Hindawi Publishing Corporation. All rights reserved.

This is a special issue published in "International Journal of Photoenergy." All articles are open access articles distributed under the Creative Commons Attribution License, which permits unrestricted use, distribution, and reproduction in any medium, provided the original work is properly cited.

Editorial Board

M. S. A. Abdel-Mottaleb, Egypt
Xavier Allonas, France
Nicolas Alonso-Vante, France
Wayne A. Anderson, USA
Yanhui Ao, China
Raja S. Ashraf, UK
Vincenzo Augugliaro, Italy
Detlef W. Bahnemann, Germany
Ignazio Renato Bellobono, Italy
Raghu N. Bhattacharya, USA
Thomas M. Brown, Italy
Stephan Buecheler, Switzerland
Gion Calzaferri, Switzerland
Chungheng Chen, China
Sung Oh Cho, Republic of Korea
Věra Cimrová, Czech Republic
Juan M. Coronado, Spain
Ying Dai, China
Dionysios D. Dionysiou, USA
Abderrazek Douhal, Spain
Mahmoud M. El-Nahass, Egypt
Polycarpos Falaras, Greece
Chris Ferekides, USA
Paolo Fornasiero, Italy
Hermenegildo García, Spain
Germà Garcia-Belmonte, Spain
Elisa Isabel Garcia-Lopez, Italy
Beverley Glass, Australia
M. A. Gondal, Saudi Arabia
Anthony M. Harriman, UK
Jr-Hau He, Taiwan
Shinya Higashimoto, Japan
Wing-Kei Ho, Hong Kong
Cheuk-Lam Ho, Hong Kong
Fuqiang Huang, China
Jürgen Hüpkes, Germany
Adel A. Ismail, Egypt
Chun-Sheng Jiang, USA
Misook Kang, Republic of Korea
Shahed Khan, USA
Sun-Jae Kim, Korea

Sungjee Kim, Korea
Jong Hak Kim, Korea
Fernando Langa, Spain
Cooper H. Langford, Canada
Tae-Woo Lee, Korea
Lecheng Lei, China
Zhaosheng Li, China
Xinjun Li, China
Stefan Lis, Poland
Vittorio Loddo, Italy
Gongxuan Lu, China
Dongge Ma, China
Nai Ki Mak, Hong Kong
Rajaram S. Mane, India
Dionissios Mantzavinos, Greece
Ugo Mazzucato, Italy
Sheng Meng, China
Jacek Miller, Poland
Claudio Minero, Italy
Thomas Moehl, Switzerland
Antoni Morawski, Poland
Franca Morazzoni, Italy
Fabrice Morlet-Savary, France
Mohammad Muneer, India
Kun Na, Korea
Ebinazar B. Namdas, Australia
Maria da Graça P. Neves, Portugal
Tebello Nyokong, South Africa
Tsuyoshi Ochiai, Japan
Kei Ohkubo, Japan
Haridas Pal, India
Leonidas Palilis, Greece
Leonardo Palmisano, Italy
Ravindra K. Pandey, USA
Hyunwoong Park, Korea
Thierry Pauporté, France
Pierre Pichat, France
Gianluca Li Puma, UK
Tijana Rajh, USA
Peter Robertson, UK
Avigdor Scherz, Israel

Elena Selli, Italy
Ganesh D. Sharma, India
Jinn Kong Sheu, Taiwan
Panagiotis Smirniotis, USA
Bhushan Sopori, USA
Zofia Stasicka, Poland
Elias Stathatos, Greece
Jegadesan Subbiah, Australia
M. Swaminathan, India
Kazuhiro Takanabe, Saudi Arabia
Mohamad-Ali Tehfe, Canada
K. R. Justin Thomas, India
Yang Tian, China
Nikolai V. Tkachenko, Finland
Ahmad Umar, Saudi Arabia
Thomas Unold, Germany
Veronica Vaida, USA
Roel van De Krol, Germany
Mark van Der Auweraer, Belgium
Rienk Van Grondelle, The Netherlands
W. G.J.H.M. Van Sark, The Netherlands
Sergey Varlamov, Australia
Xuxu Wang, China
Sheng Wang, China
Mingkui Wang, China
David Worrall, UK
Jeffrey C. S. Wu, Taiwan
Yanfa Yan, USA
Jiannian Yao, China
Minjoong Yoon, Korea
Hongtao Yu, USA
Ying Yu, China
Jiangbo Yu, USA
Klaas Zachariasse, Germany
Juan Antonio Zapien, Hong Kong
Tianyou Zhai, China
Guijiang Zhou, China
Yong Zhou, China
Rui Zhu, China

Contents

Progress in Photovoltaic Devices and Systems, Hongxing Yang, Hui Shen, Tao Xu, and Dimitrios Karamanis
Volume 2015, Article ID 926063, 3 pages

Morphological Effect of CNT/TiO₂ Nanocomposite Photoelectrodes Dye-Sensitized Solar Cell on Photovoltaic Performance with Various Annealing Temperatures, Mohd Zikri Razali, Huda Abdullah, and Izamarlina Asaahari
Volume 2015, Article ID 501978, 12 pages

Experiment Investigation on Electrical and Thermal Performances of a Semitransparent Photovoltaic/Thermal System with Water Cooling, Guiqiang Li, Gang Pei, Ming Yang, and Jie Ji
Volume 2014, Article ID 360235, 7 pages

Experiment and Simulation Study on the Amorphous Silicon Photovoltaic Walls, Wenjie Zhang, Bin Hao, and Nianping Li
Volume 2014, Article ID 643637, 14 pages

Integrating Photovoltaic Systems in Power System: Power Quality Impacts and Optimal Planning Challenges, Aida Fazliana Abdul Kadir, Tamer Khatib, and Wilfried Elmenreich
Volume 2014, Article ID 321826, 7 pages

SiO₂ Antireflection Coatings Fabricated by Electron-Beam Evaporation for Black Monocrystalline Silicon Solar Cells, Minghua Li, Hui Shen, Lin Zhuang, Daming Chen, and Xinghua Liang
Volume 2014, Article ID 670438, 5 pages

An Improved Method for Sizing Standalone Photovoltaic Systems Using Generalized Regression Neural Network, Tamer Khatib and Wilfried Elmenreich
Volume 2014, Article ID 748142, 8 pages

Seismic and Power Generation Performance of U-Shaped Steel Connected PV-Shear Wall under Lateral Cyclic Loading, Hongmei Zhang, Jinzhi Dong, Yuanfeng Duan, Xilin Lu, and Jinqing Peng
Volume 2014, Article ID 362638, 15 pages

A Newton-Based Extremum Seeking MPPT Method for Photovoltaic Systems with Stochastic Perturbations, Heng Li, Jun Peng, Weirong Liu, Zhiwu Huang, and Kuo-Chi Lin
Volume 2014, Article ID 938526, 13 pages

A Review of Solar Photovoltaic Concentrators, Mehrdad Khamooshi, Hana Salati, Fuat Egelioglu, Ali Hooshyar Faghiri, Judy Tarabishi, and Saeed Babadi
Volume 2014, Article ID 958521, 17 pages

A Simple Approach in Estimating the Effectiveness of Adapting Mirror Concentrator and Tracking Mechanism for PV Arrays in the Tropics, M. E. Ya'acob, H. Hizam, H. Abdul Rahman, W. Z. Wan Omar, Myo Than Htay, and A. H. M. A. Rahim
Volume 2014, Article ID 341863, 7 pages

Optimum Availability of Standalone Photovoltaic Power Systems for Remote Housing Electrification, Tamer Khatib and Wilfried Elmenreich
Volume 2014, Article ID 475080, 5 pages

Superior Antireflection Coating for a Silicon Cell with a Micronanohybrid Structure, Hsi-Chien Liu and Gou-Jen Wang
Volume 2014, Article ID 807812, 8 pages

Design and Optimization of Fresnel Lens for High Concentration Photovoltaic System, Lei Jing,
Hua Liu, Yao Wang, Wenbin Xu, Hongxin Zhang, and Zhenwu Lu
Volume 2014, Article ID 539891, 7 pages

Effective Passivation of Large Area Black Silicon Solar Cells by SiO₂/SiN_x:H Stacks, Zengchao Zhao,
Bingye Zhang, Ping Li, Wan Guo, and Aimin Liu
Volume 2014, Article ID 683654, 6 pages

Investigating the Impact of Shading Effect on the Characteristics of a Large-Scale Grid-Connected PV Power Plant in Northwest China, Yunlin Sun, Siming Chen, Liying Xie, Ruijiang Hong, and Hui Shen
Volume 2014, Article ID 763106, 9 pages

Manipulation of MoSe₂ Films on CuIn(Ga)Se₂ Solar Cells during Rapid Thermal Process, Wei-Ting Lin,
Shih-Hao Chan, Shao-Ze Tseng, Jih-Jian He, Sheng-Hui Chen, Ruei-Fu Shih, Chien-Wei Tseng, Tomi T. Li,
Sung-Cheng Hu, Wan-Xuan Peng, and Yung-Tien Lu
Volume 2014, Article ID 253285, 5 pages

Chaos Synchronization Based Novel Real-Time Intelligent Fault Diagnosis for Photovoltaic Systems,
Chin-Tsung Hsieh, Her-Terng Yau, and Jen Shiu
Volume 2014, Article ID 759819, 9 pages

Editorial

Progress in Photovoltaic Devices and Systems

Hongxing Yang,¹ Hui Shen,² Tao Xu,³ and Dimitrios Karamanis⁴

¹Renewable Energy Research Group, Department of Building Services Engineering, The Hong Kong Polytechnic University, Kowloon, Hong Kong

²Institute for Solar Energy Systems, Sun Yat-Sen University, Guangzhou, China

³Department of Chemistry and Biochemistry, Northern Illinois University, 1425 W Lincoln Hwy, DeKalb, IL, USA

⁴Department of Environmental and Natural Resources Management, University of Patras, Agrinio, Greece

Correspondence should be addressed to Hongxing Yang; hong-xing.yang@polyu.edu.hk

Received 15 January 2015; Accepted 15 January 2015

Copyright © 2015 Hongxing Yang et al. This is an open access article distributed under the Creative Commons Attribution License, which permits unrestricted use, distribution, and reproduction in any medium, provided the original work is properly cited.

Photovoltaic technology is becoming one of the main solutions to the energy issues for the substitution of fossil fuels in the near future. A global cumulative solar photovoltaic capacity of nearly 139 GW was installed in 2013, which became another historic year for solar PV technology. Looking ahead, if distributed PV systems and large scale PV plants do in fact provide the end users with self-sufficiency, it is essential for scientists and engineers all over the world to further exploit solar cells with high efficiency and optimize the PV systems. Thus, related research is needed within current technologies and innovative ideas, including design, modeling, fabrication, and characterization of and modules as well as implementation of PV systems.

Scientific papers in this special issue have covered recent advances in photovoltaic. This issue contains seventeen papers on various aspects of photovoltaic technologies, which fall into following topics:

- (1) development, modeling, and reliability improvements of high efficiency solar cells;
- (2) building integrated PV systems;
- (3) developments in power electronics converters used in PV applications;
- (4) distributed generation systems consisting of PV systems and integration with smart grid and smart building;
- (5) power converters for photoenergy conversion.

We here would like to express our sincere gratefulness to all authors and referees who contributed a lot to this issue. A brief overview of the papers is presented as follows.

In “Experiment Investigation on Electrical and Thermal Performances of a Semitransparent Photovoltaic/Thermal System with Water Cooling,” the authors establish a semi-transparent photovoltaic/thermal (SPV/T) system with water cooling for building integrated applications, which yields electrical power and hot water, as well as a natural illumination for the building. The performance of SPV/T system is investigated by adopting the PV efficiency, thermal efficiency, and exergy analysis.

In “Experiment and Simulation Study on the Amorphous Silicon Photovoltaic Walls,” the authors test the temperature distribution and the instant power of two amorphous silicon PV walls with and without ventilation and simulate the annual power output at different conditions. They provide some valuable suggestions for the design and construction of PV walls located at low latitudes in China.

In “Integrating Photovoltaic Systems in Power System: Power Quality Impacts and Optimal Planning Challenges,” the authors overview the major challenges in photovoltaic based distributed generation (PVDG). The paper evolves the background of PVDG and its impacts on power quality and the maximum allowable penetration level of PVDG connected to a distribution system.

In “SiO₂ Antireflection Coatings Fabricated by Electron-Beam Evaporation for Black Monocrystalline Silicon Solar Cells,” a double-layer antireflection coatings with the heterostructure of SiO₂/SiN_x:H is developed enhancing the EQE in short wavelengths. An absolute conversion efficiency increase of 0.32% is achieved in solar cell applying this double antireflection coating compared to the conventional single SiN_x:H coated solar cells.

In “An Improved Method for Sizing Standalone Photovoltaic Systems Using Generalized Regression Neural Network,” an improved approach for sizing standalone PV system (SAPV) is presented, which is based on a combination of an analytical method and a machine learning approach for a generalized artificial neural network (GRNN). The GRNN assists to predict the optimal size of a PV system using the geographical coordinates of the targeted site instead of using mathematical formulas. According to the results, the proposed method can be efficiently used for SAPV sizing whereas the proposed GRNN based model predicts the sizing curves of the PV system accurately with a prediction error of 0.6%. Moreover, hourly meteorological and load demand data are used in this research in order to consider the uncertainty of the solar energy and the load demand.

In “Seismic and Power Generation Performance of U-Shaped Steel Connected PV-Shear Wall under Lateral Cyclic Loading,” a new form of reinforced concrete shear wall integrated with photovoltaic module is proposed in this paper, aiming to apply PV module to the facades of high-rise buildings. The seismic behavior, including failure pattern, lateral force-top displacement relationship, and deformation capacity, was investigated. Two main results are demonstrated through the experiment: (1) the U-shaped steel connectors provide enough deformation capacity for the compatibility of the PV module to the shear wall during the whole cyclic test; (2) the electricity generation capacity is effective and stable during this seismic simulation test.

In “A Newton-Based Extremum Seeking MPPT Method for Photovoltaic Systems with Stochastic Perturbations,” a novel Newton-based stochastic extremum seeking MPPT method is proposed. Different from conventional gradient-based extremum seeking MPPT algorithm, the convergence rate of the proposed controller can be totally user-assignable rather than determined by unknown power map. The stability and convergence of the proposed controller are rigorously proved. The author further discusses the effects of partial shading and PV module ageing on the proposed controller. Numerical simulations and experiments are conducted to show the effectiveness of the proposed MPPT algorithm.

In “A Review of Solar Photovoltaic Concentrators,” the author reviews the different types of PV concentrators, their performance with advantages and disadvantages, concentration ratio, acceptance angle, brief comparison between their efficiencies, and appropriate cooling system.

In “A Simple Approach in Estimating the Effectiveness of Adapting Mirror Concentrator and Tracking Mechanism for PV Arrays in the Tropics,” a practical in-field method is conducted in Serdang, Selangor, Malaysia, for the two technologies in comparison to the common fixed flat PV arrays. The data sampling process is measured under stochastic weather characteristics with the main target of calculating the effectiveness of PV power output. The data are monitored, recorded, and analysed in real time via GPRS online monitoring system for 10 consecutive months. Based on the analysis, it is shown that tracking mechanism generates approximately 88 Watts (9.4%) compared to the mirror concentrator which generates 144 Watts (23.4%) of the cumulative dc power for different array configurations at

standard testing condition (STC) references. The significant increase in power generation shows feasibilities of implying both mechanisms for PV generators and thus contributes to additional reference in PV array design.

In “Optimum Availability of Standalone Photovoltaic Power Systems for Remote Housing Electrification,” the author discussed the availability of PV systems to determine the optimum availability at which standalone PV systems must be designed. Optimization methods and PV systems software, such as HOMER and PV.MY, were used for this purpose. Six PV systems with six availability levels were analyzed, in terms of wasted energy, cost of energy, battery usage, and power shortages, using real meteorological data. Results show that PV systems with 99% availability are recommended, because of their high reliability and favorably wasted energy.

In “Superior Antireflection Coating for a Silicon Cell with a Micronanohybrid Structure,” a high antireflection silicon solar cell is developed. A novel two-stage metal-assisted etching (MAE) method is proposed for the fabrication of an antireflective layer of a micronanohybrid structure array. The processing time for the etching on an N-type high-resistance (NH) silicon wafer can be controlled to around 5 min. The resulting micronanohybrid structure array can achieve an average reflectivity of 1.21% for a light spectrum of 200–1000 nm. A P-N junction on the fabricated micronanohybrid structure array is formed using a low-cost liquid diffusion source. A high antireflection silicon solar cell with an average efficiency of 13.1% can be achieved. Compared with a conventional pyramid structure solar cell, the shorted circuit current of the proposed solar cell is increased by 73%. The major advantage of the two-stage MAE process is that a high antireflective silicon substrate can be fabricated cost-effectively in a relatively short time. The proposed method is feasible for the mass production of low-cost solar cells.

In “Design and Optimization of Fresnel Lens for High Concentration Photovoltaic System,” the author proposed a practical optimization design in which the solar direct light spectrum and multijunction cell response range are taken into account in combination, particularly for the Fresnel concentrators with a high concentration and a small aspect ratio. In addition, the change of refractive index due to temperature variation in outdoor operation conditions is also considered in the design stage. The calculation results show that this novel Fresnel lens achieves an enhancement of energy efficiency of about 10% compared with conventional Fresnel lens for a given solar spectrum, solar cell response, and corrected sunshine hours of different ambient temperature intervals.

In “Effective Passivation of Large Area Black Silicon Solar Cells by $\text{SiO}_2/\text{SiN}_x:\text{H}$ Stacks,” the performance of black silicon solar cells with various passivation films was characterized. Large area (mm^2) black silicon was prepared by silver-nanoparticle-assisted etching on pyramidal silicon wafer. The conversion efficiency of black silicon solar cell without passivation is 13.8%. For the SiO_2 and $\text{SiN}_x:\text{H}$ passivation, the conversion efficiency of black silicon solar cells increases to 16.1% and 16.5%, respectively. Compared to

the single film of surface passivation of black silicon solar cells, the $\text{SiO}_2/\text{SiN}_x\text{:H}$ stacks exhibit the highest efficiency of 17.1%. The investigation of internal quantum efficiency (IQE) suggests that the $\text{SiO}_2/\text{SiN}_x\text{:H}$ stacks films decrease the Auger recombination through reducing the surface doping concentration and surface state density of the Si/SiO₂ interface, and SiN_x:H layer suppresses the Shockley-Read-Hall (SRH) recombination in the black silicon solar cell, which yields the best electrical performance of b-Si solar cells.

In “Investigating the Impact of Shading Effect on the Characteristics of a Large-Scale Grid-Connected PV Power Plant in Northwest China,” a shading simulation model for PV modules is established by the author and its reliability is verified under the standard testing condition (STC) in laboratory. Based on the investigation result of a 20 MWp grid-connected PV plant in northwest China, the typical shading phenomena are classified and analyzed individually, such as power distribution buildings shading and wire poles shading, plants and birds droppings shading, and front-row PV arrays shading. A series of experiments is also conducted on-site to evaluate and compare the impacts of different typical shading forms. Finally, some feasible solutions are proposed to avoid or reduce the shading effect of PV system during operation in such region.

In “Manipulation of MoSe₂ Films on CuIn(Ga)Se₂ Solar Cells during Rapid Thermal Process,” the CuIn(Ga)Se₂ (CIGS) crystalline quality and MoSe₂ thickness of films produced by the rapid thermal selenization process under various selenization pressures were investigated. When the selenization pressure increased from 48 Pa to 1.45×10^4 Pa, the CIGS films were smooth and uniform with large crystals of varying sizes. However, the MoSe₂ thicknesses increased from 50 nm to 2,109 nm, which created increased contact resistivity for the CIGS/MoSe₂/Mo structures. The efficiency of CIGS solar cells could be increased from 1.43% to 4.62% due to improvement in the CIGS crystalline quality with increasing selenization pressure from 48 Pa to 1.02×10^3 Pa. In addition, the CIGS crystalline quality and MoSe₂ thickness were modified by the pressure released valve (PRV) selenization process method. The crystalline qualities of the CIGS films were similarly affected by the selenization pressure at 1.02×10^3 Pa in the PRV selenization method and the MoSe₂ thicknesses were reduced from 1,219 nm to 703 nm. A higher efficiency of 5.2% was achieved with the thinner MoSe₂ obtained by using the PRV selenization method.

In “Chaos Synchronization Based Novel Real-Time Intelligent Fault Diagnosis for Photovoltaic Systems,” the author used Matlab to simulate the faults in the solar photovoltaic system. The maximum power point tracker (MPPT) is used to keep a stable power supply to the system when the system has faults. The characteristic signal of system fault voltage is captured and recorded, and the dynamic error of the fault voltage signal is extracted by chaos synchronization. Then, the extension engineering is used to implement the fault diagnosis. Finally, the overall fault diagnosis system only needs to capture the voltage signal of the solar photovoltaic system, and the fault type can be diagnosed instantly.

Acknowledgments

We wish to take this opportunity to thank all contributors and peer reviewers. We would like to thank Dr. Yuanhao Wang from the Renewable Energy Research Group of The Hong Kong Polytechnic University for his coordination of the whole review process.

*Hongxing Yang
Hui Shen
Tao Xu
Dimitrios Karamanis*

Research Article

Morphological Effect of CNT/TiO₂ Nanocomposite Photoelectrodes Dye-Sensitized Solar Cell on Photovoltaic Performance with Various Annealing Temperatures

Mohd Zikri Razali,¹ Huda Abdullah,¹ and Izamarlina Asaahari²

¹ Department of Electrical, Electronic & System Engineering, Faculty of Engineering and Built Environment, Universiti Kebangsaan Malaysia, 43600 Bangi, Selangor, Malaysia

² Fundamental Studies of Engineering Unit (UPAK), Faculty of Engineering and Built Environment, Universiti Kebangsaan Malaysia, 43600 Bangi, Selangor, Malaysia

Correspondence should be addressed to Huda Abdullah; huda@eng.ukm.my

Received 13 May 2014; Accepted 23 July 2014

Academic Editor: Tao Xu

Copyright © 2015 Mohd Zikri Razali et al. This is an open access article distributed under the Creative Commons Attribution License, which permits unrestricted use, distribution, and reproduction in any medium, provided the original work is properly cited.

This research focused on the fabrication of dye-sensitized solar cell based on a photoanode of carbon nanotube/titanium dioxide (CNT/TiO₂) nanocomposite photoanode synthesized through acid-catalyzed sol-gel method. The results show the improvement of the chemical and electrical properties of the solar cells annealed at different temperatures. The CNT/TiO₂ colloidal solution was synthesized using titanium tetraisopropoxide and CNT/2-propanol solution. The thin films were doctor-bladed on a fluorine tin oxide glass before being annealed at 550, 650, and 750°C. The field emission scanning electron microscopy morphological images show that the thin films were homogeneously distributed and maintained their spherical structures. The X-ray diffraction patterns show that the films consisted of anatase and rutile phases with large crystallite sizes due to temperature increment. The atomic force microscopy analysis presents the thin film roughness in terms of root mean square roughness. The photovoltaic performance was analyzed using *IV* curve and electrochemical impedance spectroscopy (EIS). The thin films annealed at 750°C had the highest energy conversion efficiency at 5.23%. The EIS analysis estimated the values of the effective electron lifetime (τ_{eff}), effective electron diffusion coefficient, effective electron diffusion (L_n), and effective recombination rate constant (k_{eff}). A large τ_{eff} , small k_{eff} , and longer L_n can improve photovoltaic performance efficiency.

1. Introduction

Dye-sensitized solar cell (DSSC) is considered a relatively new type of solar cell as it was first discovered by O'Regan and Grätzel in 1991 [1, 2]. DSSCs show better potential compared with Si solar cells because they are cheap [3, 4], more environmentally friendly, and simpler to manufacture [5]. DSSCs have attracted substantial attention worldwide. Grätzel's cell has a solar conversion efficiency of ~13%, which is significantly lower than that of Si solar cells. To improve the performance of DSSC devices, a number of factors need to be considered. Electron transport across a TiO₂ electrode is one of the most important factors affecting the conversion efficiency of DSSC. As the electron mobility increases, the DSSC efficiency also increases. However, charge recombination generally inhibits the transport of the injected electrons from TiO₂

to the conducting glass substrate, thus decreasing the performance of DSSCs. Therefore, a rapid photoinduced electron transport in the TiO₂ working electrode and the suppression of charge recombination ensure a higher DSSC conversion efficiency.

A similar literature suggests that carbon nanotubes (CNTs) are suitable semiconductor supports because of their combination of electronic, adsorption, mechanical, and thermal properties [6, 7]. CNTs provide interpenetrating electrodes with high surface areas for DSSCs. The introduction of CNTs into the electrodes of organic solar cells [8, 9] and dye-sensitized solar cells [10] has been performed, and researchers have concluded that CNTs efficiently enhance the electronic conductivity of the electrode, thus increasing the photoconversion efficiency of the photovoltaic device. Furthermore, previous studies have shown that the

introduction of CNTs decreases TiO₂ crystalline grain and particle sizes [11]. Previous studies also suggest that a TiO₂ semiconductor with large particle or crystalline sizes has a large surface area and has numerous contact points among the particles, carbon nanotubes, and underlying substrates. These results are beneficial for the improvement of the cell performance. Therefore, CNTs are regarded as promising materials for use in DSSCs, and the utilization of CNTs to improve the photoconversion efficiency of DSSCs is expected and should be conducted. In the past decade, several studies have reported that the incorporation of CNTs in a nanocrystalline TiO₂ working electrode prepared using blended fabrication with commercial TiO₂ (P25) increases the solar energy conversion efficiency of DSSCs [12]. However, further increasing the CNT loading may inhibit the improvement of DSSC cell performance because of serious CNT aggregations.

In this study, we prepared CNT/TiO₂ nanocomposite thin films annealed at various temperatures from 550°C to 750°C. We investigated the morphological and photocatalytic activity properties of the CNT/TiO₂ solar cell. This morphological structure was examined using field emission scanning electron microscopy (FESEM), X-ray diffraction (XRD), and atomic force microscopy (AFM). The photovoltaic properties of the solar cell were determined using *IV* curve analysis and electrochemical impedance spectroscopy (EIS). The results show that the annealing temperatures significantly affect the combination of TiO₂ nanoparticles with CNT and hence influence the performance of the CNT/TiO₂ dye-sensitized solar cell.

2. Methodology

2.1. Preparation of the CNT/TiO₂ Nanocomposite Solution.

The CNT/TiO₂ nanocomposite photoanode was synthesized using modified acid-catalyzed sol-gel method. CNT powder was acid-treated first before being used. The synthesis was conducted by boiling raw CNT in a concentrated nitric acid solution for 5 h. The CNT solution was then filtered and washed with distilled water several times to remove the excess acid. Afterward, the mixture was dried in oven for 24 h. Then, 2-propanol (Solaronix, SA) anhydrate solution (40 mL) was used as the starting material. Precisely 0.06 g of CNT nanopowder (Sigma-Aldrich, USA) was sonicated in the 2-propanol solution for 1 h to adequately disperse the particles. Titanium tetraisopropoxide (TTIP) (10 mL) (Sigma-Aldrich, Belgium), which was the titanium precursor, was poured into the CNT/2-propanol solution. The mixture was continuously sonicated for an additional 1 h to improve the interactions between the two materials. Diluted ethanol (100 mL) was slowly dropped into the solution, and the solution was heated at 100°C for 12 h in a wet furnace to remove the excess water. Last, the CNT/TiO₂ gel-look solution was produced. Figure 1 shows the flowchart of this preparation.

2.2. Preparation of CNT/TiO₂ Nanocomposite Thin Film. Fluorine tin oxide (FTO) glass (Solaronix, SA) was used as the conductive substrate. The FTO glass was ultrasonically

cleaned with acetone, methanol, and deionized distilled water. The CNT/TiO₂ thin films were prepared by applying the nanocomposite on the FTO conducting glass. The gel-look product from the above preparation was then added with carbowax 400 (R&M Chemical, UK) that acted as binder. The gel solution was vigorously stirred for 1 h to produce a viscous gel paste. The CNT/TiO₂ nanocomposite mixture was doctor-bladed onto the conductive substrate to form a 0.25 cm² active area. The thin films were dried on a hot plate at 60°C for 15 min. Subsequently, the CNT/TiO₂ thin films were annealed in air using a dry furnace at different annealing temperatures of 550, 650, and 750°C for 30 min. Figure 2 shows the flowchart of this preparation.

2.3. Preparation of CNT/TiO₂ Dye-Sensitized Solar Cell.

The fabricated dye-sensitized solar cell has two parts, namely, CNT/TiO₂ thin film electrode and platinum thin film counter electrode. The electrodes were immersed in ruthenium dye (N719-Solaronix, SA) for 24 h. The counter electrodes were coated with platinum thin film using screen printing technique and annealed in a furnace at 350°C for 30 min. A parafilm spacer was sandwiched between the annealed CNT/TiO₂ and counter electrodes, and both sides of the substrate were clipped. Iodolyte MPN-100 (Solaronix SA) was used as the electrolyte in this solar cell. The dye-sensitized solar cell frame was sealed using silicon glue to prevent electrolyte leakage during the experiments. Figure 3 shows the flowchart of this preparation.

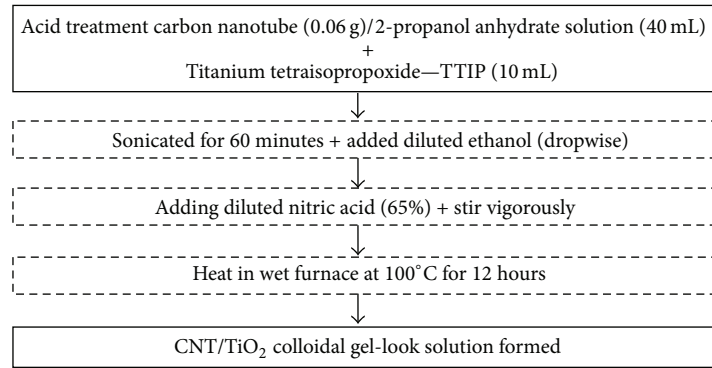
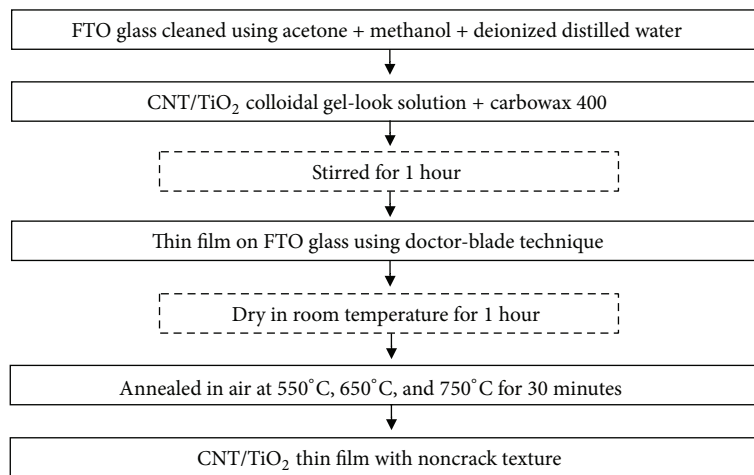
2.4. Characterization.

The morphological structures and energy-dispersive X-ray (EDX) analysis of the CNT/TiO₂ thin films were analyzed and conducted using a FESEM instrument (Zeisz Supra: 15 kV). XRD analysis was conducted using an X-ray diffractometer (Siemens D-5000) with CuK α irradiation ($\lambda = 1.5406 \text{ \AA}$) to determine the crystalline orientations of the CNT/TiO₂ thin film. AFM analysis was conducted to determine the average roughness of the thin film using 3D images. A G300 instrument (GAMRY Instruments) with simulated AM 1.5 xenon illumination having a 100 mW/cm² light output was used to analyze the photovoltaic efficiency and electrochemical impedance of the solar cell.

3. Result and Discussion

3.1. Field Emission Scanning Electron Microscopy (FESEM).

Figure 4 shows the FESEM images of the surface morphologies of the CNT/TiO₂ nanocomposite thin films sintered at different temperatures. From these FESEM images, we can see the arrangement of CNT particles within the nanoporous CNT/TiO₂ films [13]. The diluted ethanol solution acted as the solvent and as a soft template for the films. This preparation technique generates good interactions between the CNT and TiO₂ nanoparticles. The diluted ethanol also improves the pore formation within the nanocomposite thin films. In addition, acid-catalyzed modification method assists in the formation and interactions between the CNT and TiO₂ nanoparticles because of the strong chemical absorption [14].

FIGURE 1: Flowchart for CNT/TiO₂ nanocomposite solution.FIGURE 2: Flowchart for CNT/TiO₂ nanocomposite thin films.

Although this preparation technique limits the crystalline growth of the nanocomposite, it still improves the dye absorption for dye-sensitized solar cell application.

Figure 4 also presents the images of the CNT/TiO₂ thin films annealed at 550, 650, and 750°C. These images were observed at 100 nm with 20 Kx magnifications. All the annealed samples consisted of irregularly arranged and shaped TiO₂ and CNT nanoparticles. The thin film nanoparticles were randomly connected to a noncrack surface. We found that CNT nanoparticles had large sizes in the pore structures of almost all samples, especially for the thin film annealed at 750°C [15]. We also noticed that the varying temperatures affected the morphological structures of the films. The addition of diluted ethanol assisted in the dispersion of the CNT/TiO₂ nanoparticles. Highly dispersed films, in turn, assisted the electron transport inside the films. The films annealed at high temperatures generated large particles size of around 10 nm to 20 nm and produce large surface areas with high porosities inside the films for dye absorption. Another researcher [16] confirmed that samples annealed at high temperatures show more sintered nanoparticles that merged to form the neck between adjacent nanoparticles with better contacts for efficient electron transfer.

Figure 5 shows the average thickness of all samples. Table 1 shows that the average thicknesses for samples annealed at 550, 650, and 750°C were approximately 21.68, 21.27, and 16.07 μm, respectively. High annealing temperatures decrease the average thickness because of the resulting large surface areas and high porosities inside the films. Table 1 presents the data for EDX analysis conducted from the FESEM analysis. The EDX analysis was used to identify the elements or materials contained in the thin films. Figure 6 shows the EDX data to simplify it using a graphical diagram. From this analysis, we discovered the presence of carbon (C), titanium (Ti), and oxygen (O) in all samples. The carbon and titanium elements almost linearly increased with increasing annealing temperature as mentioned in another study [17]. Besides EDX measurement, all these elements (C, Ti, and O) can be proven and supported by using the X-ray diffraction (XRD) measurement analysis.

3.2. X-Ray Diffraction (XRD). The phase transition of the CNT/TiO₂ thin films was studied based on the annealing temperatures. Figure 7 shows the XRD patterns of the CNT/TiO₂ thin films annealed at 550, 650, and 750°C,

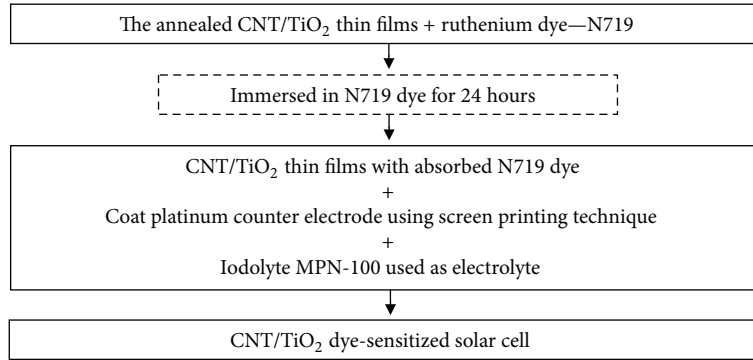


FIGURE 3: Flowchart for CNT/TiO₂ dye-sensitized solar cell fabrication.

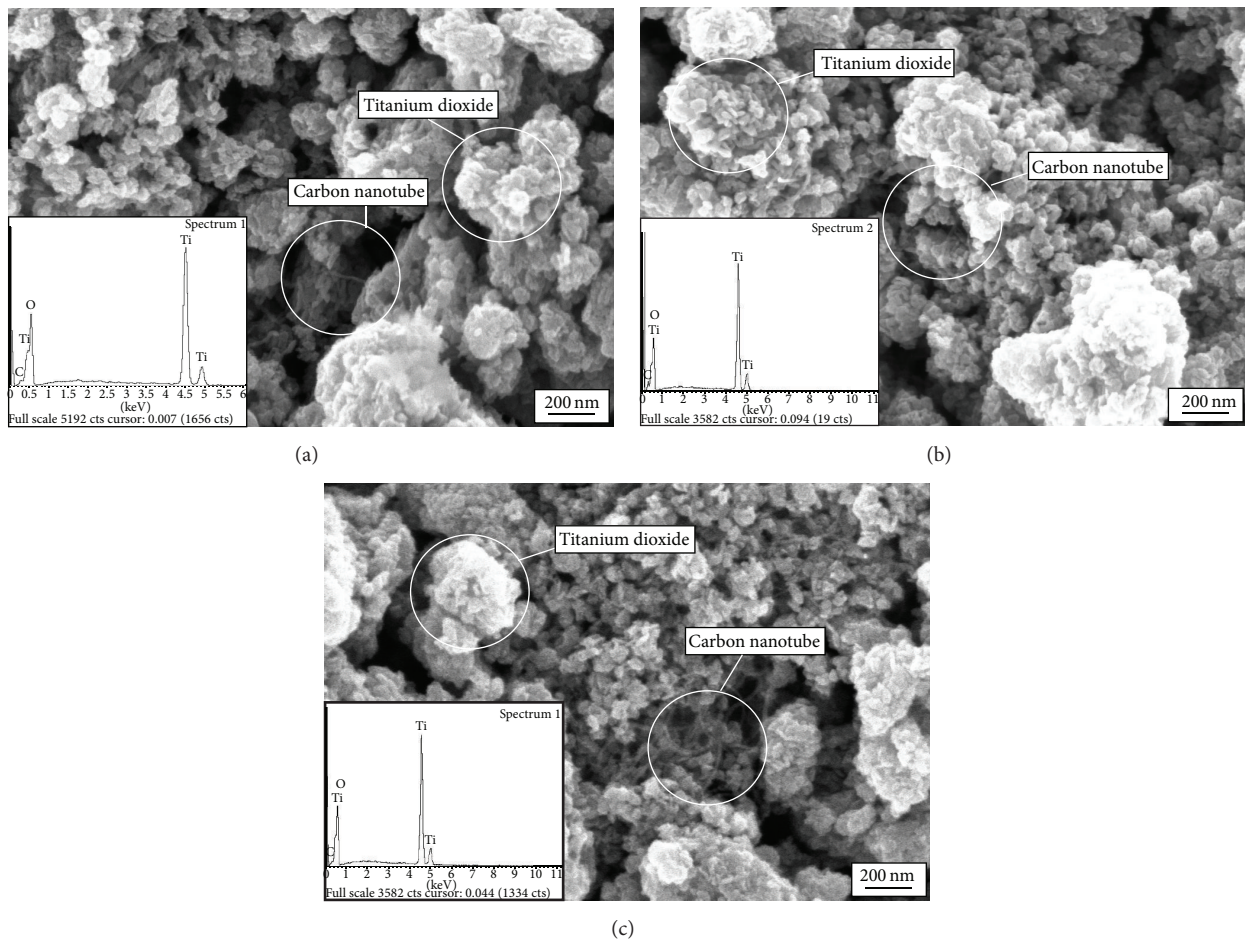


FIGURE 4: FESEM images of CNT/TiO₂ thin films annealed at different temperatures: (a) 550°C, (b) 650°C, and (c) 750°C.

respectively. As the annealing temperature increases, the TiO₂ nanoparticles go through phase transitions to achieve anatase and rutile structures. The patterns were analyzed and compared using the database file of PDF number 01-078-2486 (TiO₂-anatase) and PDF number 01-086-0147 (TiO₂-rutile). The XRD patterns were calculated at an angle of 2θ between 20° and 60°. The peaks that appeared from these

patterns were (101), (004), (200), and (211) at 25.2°, 37.96°, 47.84°, and 55.40°, respectively, for the anatase phase, and the peak was (211) at 54.04° for the rutile phase. The major peaks corresponded to the anatase phase with a crystallographic plane of (101) at 25.2° for all the films. The rutile phase was hardly observed and only occurred in the thin film annealed at 750°C. Brookite phase was not observed in these patterns.

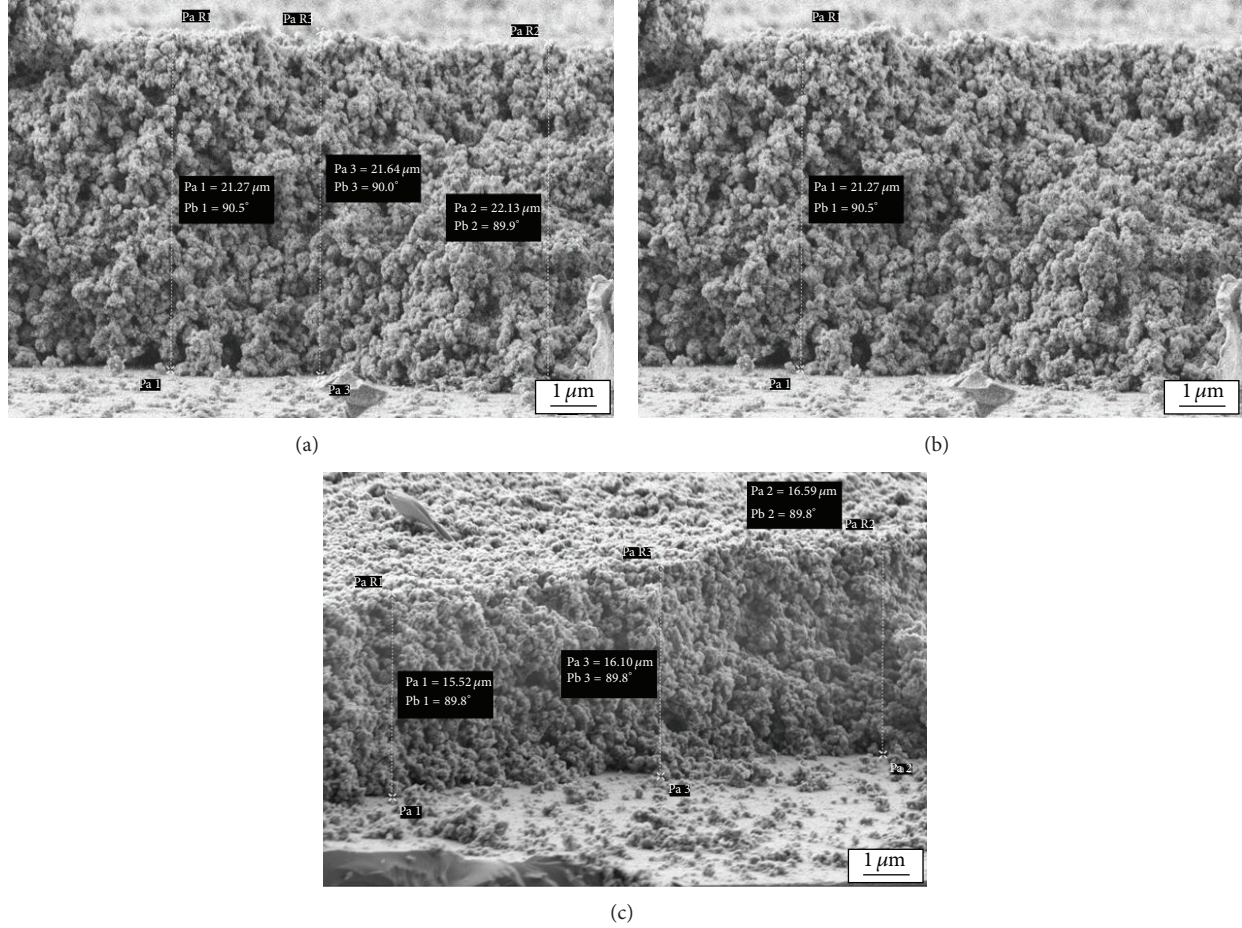


FIGURE 5: CNT/TiO₂ thin film's average thickness of (a) 550°C, (b) 650°C, and (c) 750°C annealing temperature.

TABLE 1: EDX analysis data for all CNT/TiO₂ thin films.

Sample	Temperature, °C	Element weight, %		
		Carbon	Titanium	Oxygen
(a)	550	1.31	52.78	45.91
(b)	650	1.42	54.91	43.67
(c)	750	1.46	53.58	44.96

TABLE 2: XRD analysis parameters for all CNT/TiO₂ thin films.

Sample	Temperature, °C	Major peak	Crystalline size, nm	Lattice parameter		
				<i>a</i>	<i>b</i>	<i>c</i>
(a)	550	Anatase	15.62	3.7845	Null	9.5143
(b)	650	Anatase	17.10	3.7845	Null	9.5143
(c)	750	Anatase	17.96	3.7845	Null	9.5143

Based on other studies [18, 19], the CNT peaks are usually located at 26.0° and 43.4°, although CNT elements were not detected in this present study. This phenomenon could occur because of the peaks of the crystalline TiO₂ anatase phase at 25.2°, which partly covers the CNT main peak at 26.0°. Moreover, overlapping peaks may occur because the

crystalline structure of TiO₂ is larger than that of CNT. A quantitative evaluation of the crystallite size using Scherrer's equation was conducted and the results are shown in Table 2 with a graphical diagram in Figure 8:

$$D = \frac{k\lambda}{B \cos \theta}, \quad (1)$$

where λ is the wavelength of 1.492 nm, B is the full width at half-maximum of the main peak, and θ is the main peak position divided by 2 [20, 21]. Scherrer's equation proves that the film crystallite size slightly increased with increasing of annealing temperatures. The data in Table 2 show that the crystallite sizes for the thin films annealed at 550, 650, and 750°C are 15.62, 17.10, and 17.96 nm, respectively.

The crystallite size increased, and the crystal size in the nanoparticles grew with increasing temperature. The comparison with the XRD peaks of P25, which contains both anatase and rutile phases, confirmed that the annealed TiO₂ nanoparticles at 750°C formed rutile peaks. In high-temperature annealing, the average crystal size increases, reducing the grain boundaries and crystal defects because of the present anatase and rutile phases. The decreased number of trap sites on the nanoparticles reduced the number of

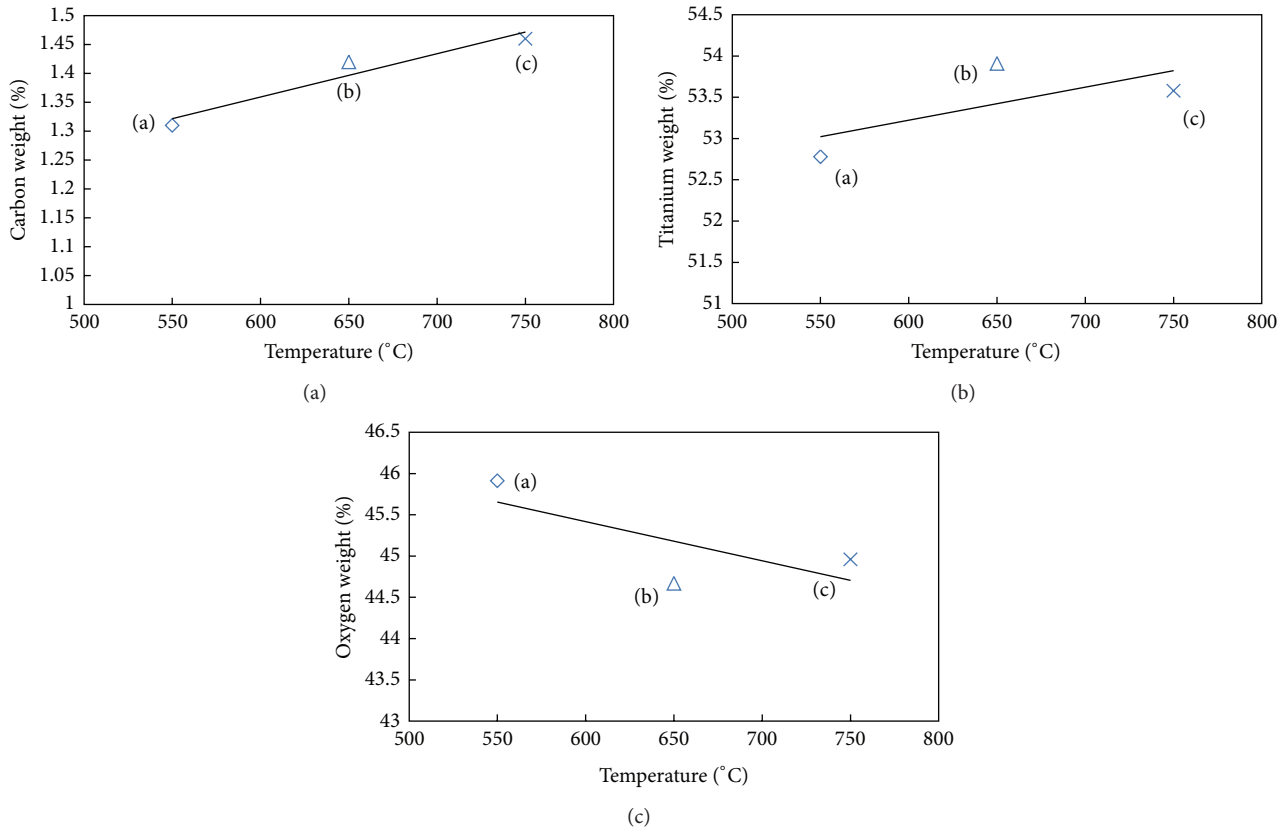


FIGURE 6: EDX graphical data for (a) carbon, (b) titanium, and (c) oxygen versus annealing temperature.

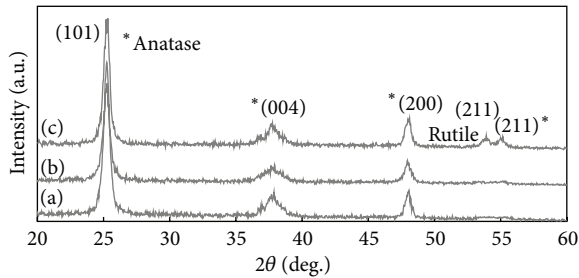


FIGURE 7: XRD patterns of CNT/TiO₂ films annealed at (a) 550°C, (b) 650°C, and (c) 750°C.

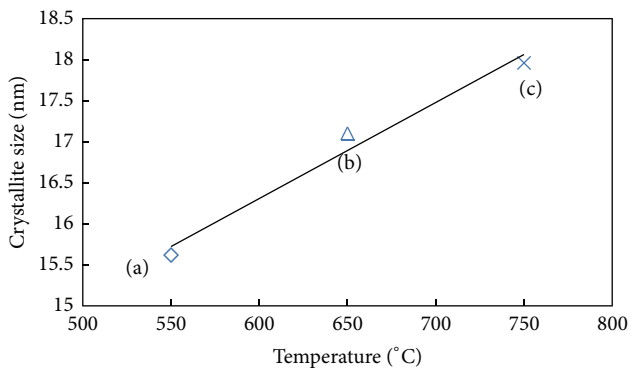


FIGURE 8: XRD graphical data for crystallite size versus temperature.

obstacles for the fast-moving electron. These effects influenced the charge-trap conditions and consequently increased the electron diffusion speed [22]. Although the combination of the anatase and rutile phases has been proven to enhance the photocurrent density, excessive rutile TiO₂ nanoparticles could form a barrier for the electrons because of high-energy level of the rutile phase [23]. Therefore, the best and optimum temperature determined in this present study is 750°C because the sample annealed at this temperature provided a combination of small amounts of the rutile and anatase phases.

The increase in crystallite size of the TiO₂ nanoparticles provides a better contact point between the nanoparticles. Hence, this advantage provides a more efficient charge transport and faster photo induction for the electron transfer [24]. The lattice parameter data in Table 2 from the database PDF number 01-078-2486 (TiO₂-anatase) show the same value for all the samples with $a = 3.7845$, $b = \text{null}$, and $c = 9.5143$. These results suggest that the incorporation of CNTs into TiO₂ thin films does not affect the TiO₂ lattice structure [25].

3.3. Atomic Force Microscopy (AFM). The CNT/TiO₂ thin film topography and upper surface were observed using AFM. The images in Figure 9 show the samples from all annealing temperatures. These images show that, with increasing annealing temperature, the texture of the thin films becomes rougher and the nanoparticle arrangement becomes

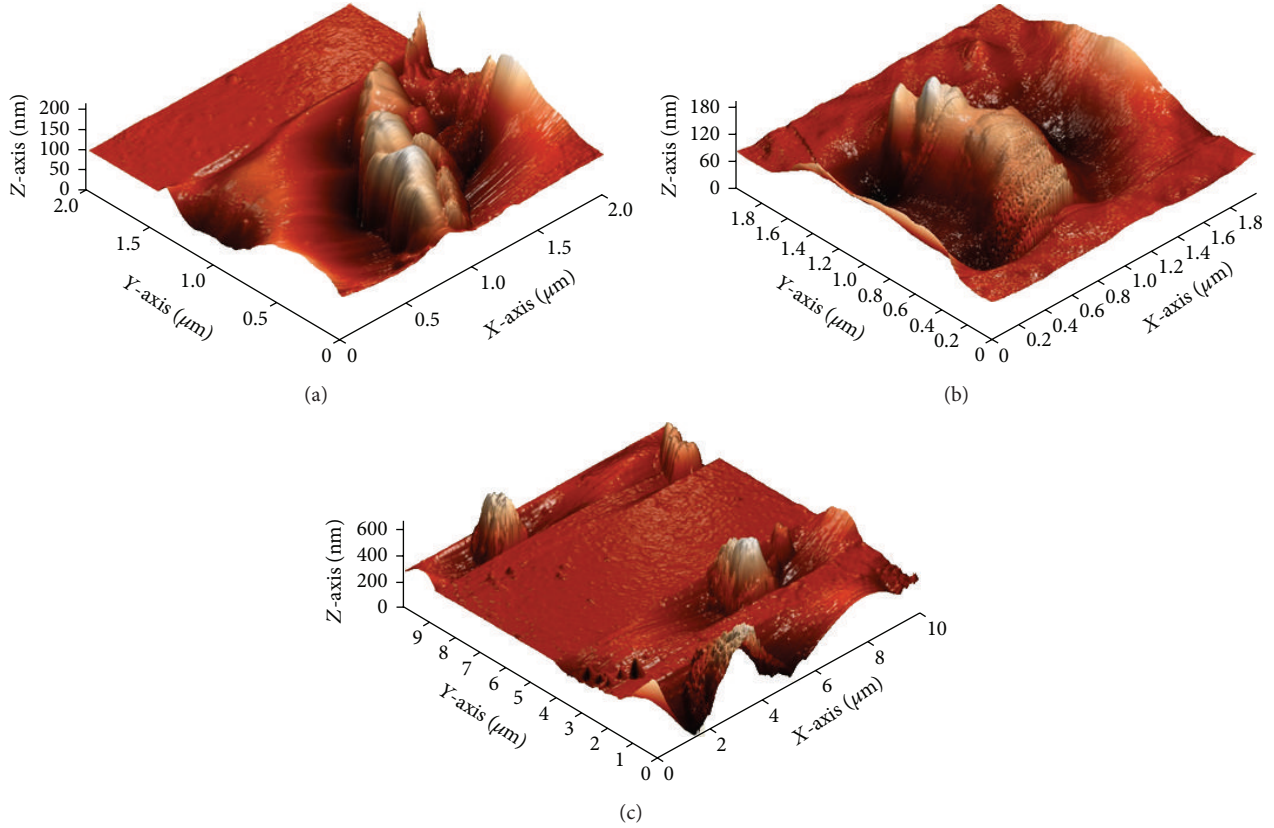


FIGURE 9: AFM images for CNT/TiO₂ films annealed at (a) 550°C, (b) 650°C, and (c) 750°C.

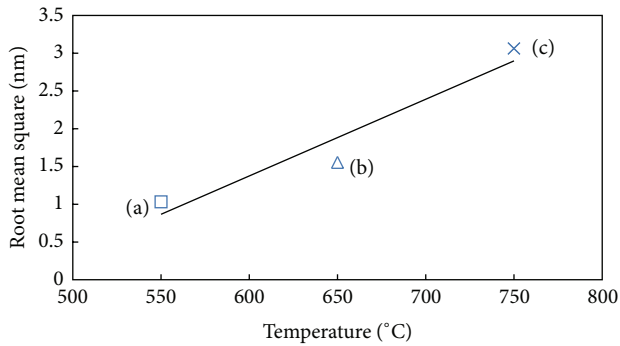


FIGURE 10: Graph for roughness average versus annealing temperature.

structured. The root mean square roughness (R_q) values demonstrate the morphologies of the films with a uniform and dense granular surface structure. The AFM results confirm that the lowest annealing temperature (550°C) has R_q value of only around 1.032 nm. The roughness average gradually increases with increasing annealing temperature. Average roughness values for thin films annealed at 650°C and 750°C are 1.554 nm and 3.063 nm, respectively. The R_q values for all films are listed in Table 3 and are graphically shown in Figure 10.

TABLE 3: Root mean square roughness (R_q) data for all samples.

Sample	Temperature, °C	Root mean square roughness (R_q), nm
(a)	550	1.032
(b)	650	1.554
(c)	750	3.063

The AFM measurements analyzed the surface morphologies of the thin films. This characterization is significant to the photoelectrode of the solar cell as the reflection angle of photoelectrode surface can be investigated from R_q values. With the increase in roughness, the increase in the surface texture angle in the thin films will bounce the light on the surface films, indirectly reflecting it back to the film surface. This phenomenon shows that the thin film thickness and crystallite size decrease as the average roughness increases with increasing annealing temperature. This phenomenon can increase the light absorption of the photovoltaic metal oxide and improve the light-to-electricity conversion energy because the light or photon reflectance angle decreased [26].

3.4. *Dye-Sensitized Solar Cell Efficiency Performance.* Figure 11 shows the IV curves of the CNT/TiO₂ dye-sensitized solar cell. The efficiency of the photoelectric conversion

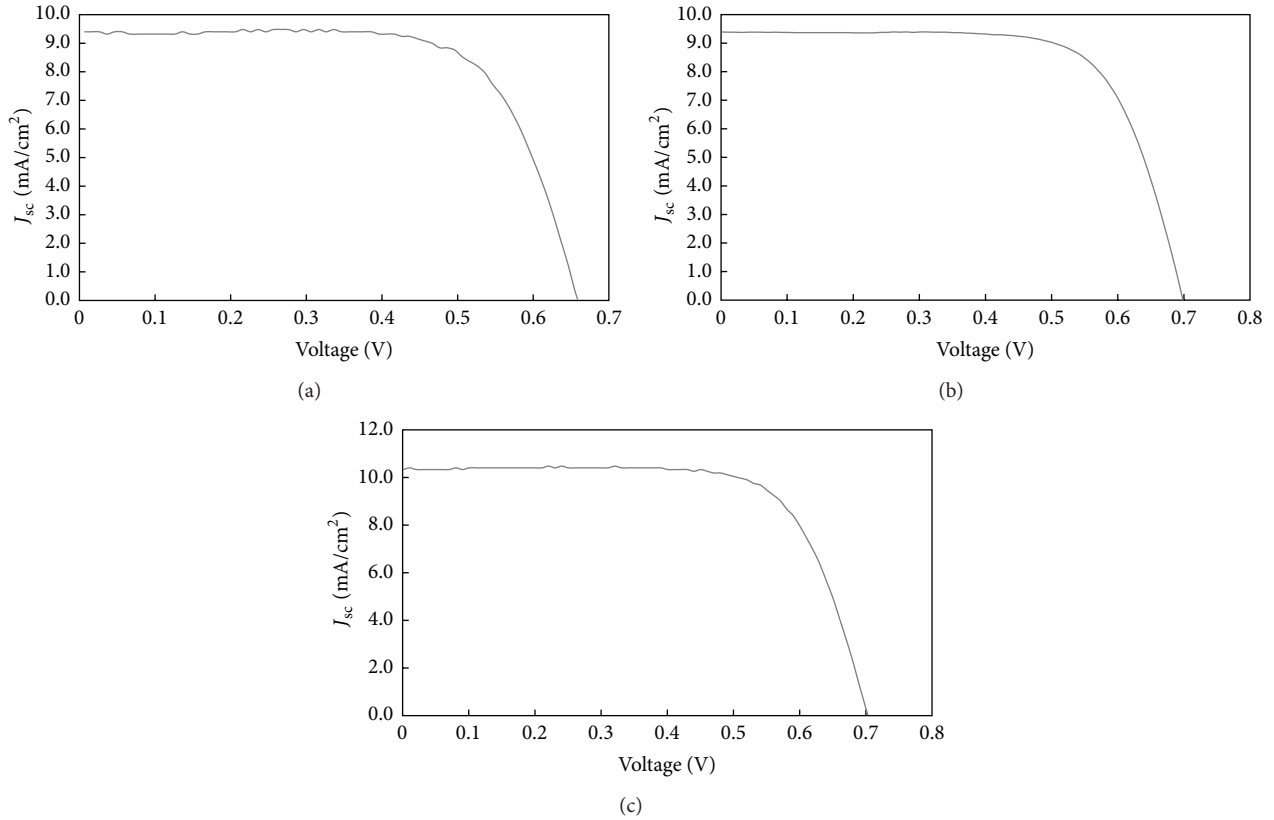


FIGURE 11: I - V curve efficiency for dye-sensitized solar cell annealed at (a) 550°C, (b) 650°C, and (c) 750°C.

of the photoelectrode solar cell is strongly dependent on the annealing temperature and concentration of added CNT. The active areas of solar cell photoelectrode were around 0.25 cm² [27]. The maximum current or short-circuit current density (J_{sc}) (mA/cm²) was obtained when the solar cell was short-circuited. The open-circuit voltage (V_{oc}) (V) was determined from the potential difference between the CNT/TiO₂ conduction band edge and electrochemical potential of the redox couple of the electrolyte. The fill factor (FF) and solar energy conversion efficiency (η) can be determined using equations [28, 29]

$$\begin{aligned}
 FF &= \frac{I_{max} \times V_{max}}{I_{sc} \times V_{oc}}, \\
 \eta &= \frac{P_{out}}{P_{in}} \times 100 = \frac{I_{max} \times V_{max}}{P_{in}} \times 100 \quad (2) \\
 &= \frac{I_{sc} \times V_{oc} \times FF}{P_{in}} \times 100.
 \end{aligned}$$

Table 4 shows the evaluated and summarized data from the solar cell efficiency analysis. Both V_{oc} and J_{sc} increased from 0.68 V to 0.71 V for (V_{oc}) and from 9.40 mA/cm² to 10.33 mA/cm² for (J_{sc}). The FF and η also increased with increasing the annealing temperature. The FF increased from 69% to 71% for the annealed thin films at 550°C to 750°C. η expectedly increased gradually from 4.53%, 4.67%, and

5.23% for the thin films annealed at 550, 650, and 750°C, respectively.

Figure 12 represents the graphical diagram of the efficiency versus temperature. The increasing annealing temperature and insertion of CNT decrease the internal resistance at the TiO₂/dye/electrolyte interface, thus reducing the charge recombination rate of the excited electrons and holes in the dye-sensitized solar cell [30]. These factors cause the increase in the V_{oc} and J_{sc} values of these solar cells. The improvement in the short-circuit current densities shows the improvement in the collection and transport of electrons between the conductive substrate and thin films in the dye-sensitized solar cell [31]. The highest efficiency was achieved through the morphological structures of the thin films. From FESEM images, we can see that the thin film annealed at 750°C is significantly compact and has high porosity. The thin film also has a compact structure with unagglomerated dispersed nanoparticles that enhances the dye absorption on the TiO₂ surface. Moreover, the thin films consisting of anatase and rutile phases reduce the internal obstacle and assist in the electron transport in the cell. The thin film annealed at 750°C and formed with a high average roughness captures more electrons and reflection of photons from the sun into the photoelectrode area.

However, the CNT concentration should be maintained at ~0.06 g to avoid agglomeration within the films, which causes light-harvesting competition between the dye and

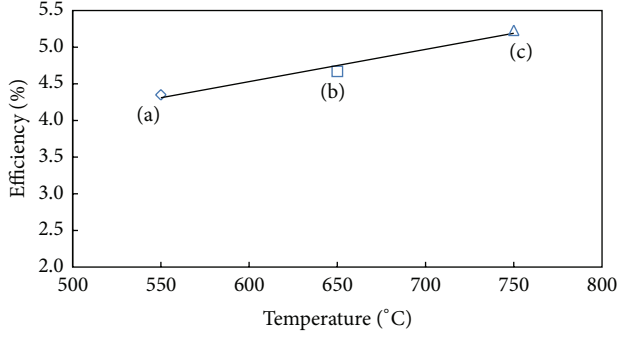


FIGURE 12: The DSSC percentage efficiency versus temperature for all samples.

TABLE 4: Dye-sensitized solar cell parameter data for all samples.

Sample	Temperature/°C	V_{oc}/V	$J_{sc}/\text{mA}/\text{cm}^{-2}$	Fill factor/%	$\eta/\%$
(a)	550	0.68	9.40	69	4.35
(b)	650	0.70	9.39	71	4.67
(c)	750	0.71	10.33	71	5.23

CNT that consequently increases the charge transport resistance and reduces the solar cell efficiency [32]. In addition, excess CNT may cause aggregation of the TiO_2 grains (as observed in the FESEM result), resulting in a decrease in amount of adsorbed dye on the working electrode. Moreover, excessive amounts of CNT may cause the working electrode to be less transparent, leading to a reduced DSSC efficiency.

3.5. Electrochemical Impedance Spectroscopy. EIS analysis was used to investigate the electron transport and charge recombination that occurs in these CNT/ TiO_2 dye-sensitized solar cells. The solar cell impedance spectrum from EIS analysis is generally composed of three semicircles, which are usually recognized as Z_1 : Pt/Electrolyte, Z_2 : TiO_2 /Dye/Electrolyte, and Z_3 : diffusion of I_3^- in the electrolyte. The transmission line for DSSC generally consists of several resistances and capacitances, which are situated in different boundaries. The R_{Pt} and C_{Pt} are the charge-transfer resistance and capacitance in the counter electrode/electrolyte boundary, respectively. The sheet resistance of the conducting substrates, R_s , and charge-transfer resistance, R_{ct} , are attributable to the electron recombination in the electrolyte/CNT/ TiO_2 /dye boundary. R_t is the electron transport resistance at the metal oxide photoanode, and C_μ is the chemical capacitance within the metal oxide conductive electrode. Z_D is the limited Warburg impedance and redox diffusion in the electrolyte. R_{FTO} and C_{FTO} are the charge-transfer resistance and internal capacitance for the electron recombination in the FTO/electrolyte boundary, respectively. By using the fitted line from the transmission equivalent circuit model, we can plot and analyze the impedance spectra [33].

Figures 13(a) to 13(c) illustrate the DSSC impedance spectrum in the Nyquist plot diagram for the thin films annealed

at 550, 650, and 750°C. In Figure 13, the high frequency semicircle Z_1 corresponds to the counter electrode R_{Pt} and Helmholtz C_{Pt} . The middle semicircle indicates the R_{ct} and C_μ between the metal oxide and electrolyte layers of the CNT/ TiO_2 . The last semicircle at low frequency is attributed to the diffusion impedance in the electrolyte boundary [34]. Although the Nyquist plot diagram in Figures 13(a) to 13(c) does not show three perfect semicircles, the parameters for the solar cell performance still can be extracted from the impedance spectra. The parameters are as follows:

- (i) k_{eff} is the reaction rate constant of the electron recombination in the metal oxide interface and is estimated from the peak frequency ω_{max} at the center of the semicircle;
- (ii) τ_{eff} is the effective electron lifetime within the solar cell and is calculated from

$$\tau_{eff} = \frac{1}{2\pi f_{max}}; \quad (3)$$

- (iii) τ_{eff} is the inverse of k_{eff} , which determines the peak frequency of the CNT/ TiO_2 semicircles and is defined as

$$\omega_{max} = f_{max} = k_{eff} = \frac{1}{\tau_{eff}}; \quad (4)$$

- (iv) D_{eff} is the effective electron diffusion coefficient and calculated as

$$D_{eff} = \left(\frac{R_{ct}}{R_t} \right) \left(\frac{L^2}{\tau_{eff}} \right), \quad (5)$$

where L is the photoanode thin film thickness and R_{ct} and R_t are estimated from the EIS measurement;

- (v) L_n is the effective electron diffusion length of the CNT/ TiO_2 photoelectrode and is determined as

$$L_n = D_{eff} \times \tau_{eff}. \quad (6)$$

Figure 13 and Table 5 demonstrate all the three CNT/ TiO_2 photoelectrode solar cell diagrams and the data from the different film thicknesses and annealing temperatures. Several differences are observed and these can assist us to determine the solar cell internal performance (e.g., D_{eff} and τ_{eff} data). Even though the thin film annealed at 550°C has significantly higher D_{eff} ($8.37 \times 10^7 \text{ cm}^2\text{s}^{-1}$) compared with the other samples, it has the lowest τ_{eff} (14.33 ms). The thin films annealed at 650°C and 750°C have significantly higher τ_{eff} values (27.01 ms and 100.35 ms, resp.). The k_{eff} for the thin film annealed at 750°C is the lowest. These circumstances decrease the electron transport rate within the cell and consequently affect the overall solar cell performance. From the photovoltaic measurements, we determined the solar cell efficiency to be around 5.23% for the thin film annealed at 750°C, and this result is supported and proven by the EIS analysis. EIS analysis results show that the thin film has $\tau_{eff} = 100.35 \text{ ms}$, $k_{eff} = 9.96 \times 10^{-3}$, $D_{eff} = 1.76 \times 10^7$,

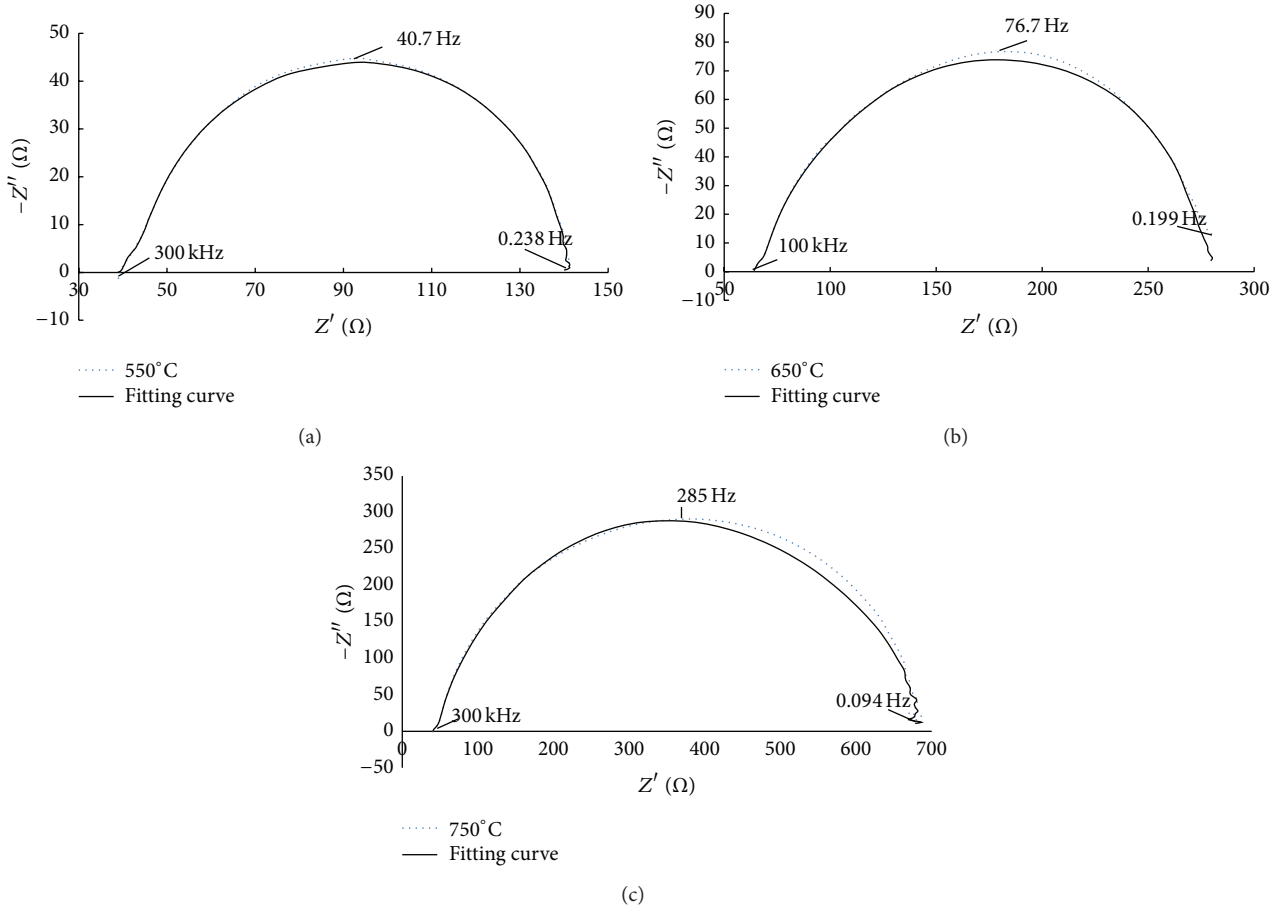


FIGURE 13: Electrochemical impedance spectroscopy (EIS) measurements for (a) 550°C, (b) 650°C, and (c) 750°C.

TABLE 5: Parameters determined by electrochemical impedance spectroscopy analysis.

Sample	L (μm)	ω_{max} (Hz)	R_s (Ω)	R_{ct} (Ω)	R_t (Ω)	R_{pt} (Ω)	C_μ (μF)	Z_D	τ_{eff} (ms)	K_{eff} (s^{-1})	D_{eff} ($\text{cm}^2 \cdot \text{s}^{-1}$)	L_n (μm)
(a)	21.68	40.7	31.12	7.35	2.88×10^{-6}	9.68	2.79×10^{-5}	0.052	14.33	6.98×10^{-2}	8.37×10^7	1.20×10^9
(b)	21.27	76.7	34.56	8.43	2.82×10^{-6}	10.64	2.81×10^{-5}	0.054	27.01	3.70×10^{-2}	5.01×10^7	1.35×10^9
(c)	16.07	285	37.83	20.66	3.02×10^{-6}	12.86	3.34×10^{-5}	0.060	100.35	9.96×10^{-3}	1.76×10^7	1.77×10^9

and $L_n = 1.77 \times 10^9$. These improvements are caused by the increasing annealing temperature that improves and enhances the surface morphology and thin film thickness of the solar cell. Moreover, the L_n of the thin film is larger compared with its film thickness (16.07 μm), which is important for a high efficiency [35, 36]. A high annealing temperature also has a positive effect as the thin film annealed at 750°C has a large surface area for dye adsorption and high porosity that assist in the electron transport inside the films. Based on a previous study [37], the recombination effects in a photoelectrode from the back reaction, low catalytic activity in counter electrode (redox couple decrease), and slow electron/ion transport between the photoelectrode and counter electrode are the main limitations of a dye-sensitized solar cell.

4. Conclusion

In conclusion, dye-sensitized solar cells based on CNT/TiO₂ photoelectrode were successfully fabricated. The solar cell preparation with different annealing temperatures (550, 650, and 750°C) has a high power conversion efficiency. Precisely 0.06 g of CNT was used in this research. We confirmed that the CNT/TiO₂ solar cell annealed at 750°C provides the highest photoconversion efficiency (5.23%) compared with those annealed at 550°C and 650°C (4.35% and 4.67%, resp.). The FESEM and XRD analysis results show that the thin films are compact and noncrack and have high porosities. The best annealing temperature is 750°C as the anatase and rutile phases occur within the film formed at this temperature. The combination improves the electron mobility within the cell.

AFM analysis shows that the roughness average of the film is 31.063 nm. In EIS analysis, thin film annealed at 750°C has better τ_{eff} (100.35 ms), which improves the electron transport within the cell and reduces the recombination reaction rate by almost 75% compared with other solar cells. The excellent electron transport was also determined from $D_{\text{eff}} = 1.76 \times 10^{-7}$, effective $k_{\text{eff}} = 9.96 \times 10^{-3}$, and $L_n = 1.77 \times 10^9$. All these measurements and analyses proved that the dye-sensitized solar cell annealed at 750°C has the best morphological and internal structure to achieve high photovoltaic efficiency.

Conflict of Interests

The authors declare that there is no conflict of interests regarding the publication of this paper.

Acknowledgments

The authors are grateful to the Laboratory of Photonics Institute of Microengineering and Nanoelectronics (IMEN) and Centre for Research and Instrumentation Management (CRIM), Universiti Kebangsaan Malaysia, for providing the facilities. The work was partially supported by a Grant from the Ministry of Higher Education (ERG-S/1/2013/TK07/UKM/03/2).

References

- [1] B. O'Regan and M. Grätzel, "A low-cost, high-efficiency solar cell based on dye-sensitized colloidal TiO₂ films," *Nature*, vol. 353, no. 6346, article 737, 1991.
- [2] M. Grätzel, "Photoelectrochemical cells," *Nature*, vol. 414, no. 6861, pp. 338–344, 2001.
- [3] Q. Zhang, C. S. Dandeneau, X. Zhou, and C. Cao, "ZnO nanostructures for dye-sensitized solar cells," *Advanced Materials*, vol. 21, no. 41, pp. 4087–4108, 2009.
- [4] M. Grätzel, "Perspectives for dye-sensitized nanocrystalline solar cells," *Progress in Photovoltaics: Research and Applications*, vol. 8, no. 1, pp. 171–185, 2000.
- [5] J. van de Lagemaat, N.-G. Park, and A. J. Frank, "Influence of electrical potential distribution, charge transport, and recombination on the photopotential and photocurrent conversion efficiency of dye-sensitized nanocrystalline TiO₂ solar cells: a study by electrical impedance and optical modulation techniques," *Journal of Physical Chemistry B*, vol. 104, no. 9, pp. 2044–2052, 2000.
- [6] A. Kongkanand, R. M. Domínguez, and P. V. Kamat, "Single wall carbon nanotube scaffolds for photoelectrochemical solar cells. Capture and transport of photogenerated electrons," *Nano Letters*, vol. 7, no. 3, pp. 676–680, 2007.
- [7] W. Wang, P. Serp, P. Kalck, and J. L. Faria, "Photocatalytic degradation of phenol on MWNT and titania composite catalysts prepared by a modified sol-gel method," *Applied Catalysis B: Environmental*, vol. 56, no. 4, pp. 305–312, 2005.
- [8] A. J. Miller, R. A. Hatton, and S. R. P. Silva, "Interpenetrating multiwall carbon nanotube electrodes for organic solar cells," *Applied Physics Letters*, vol. 89, no. 13, Article ID 133117, 2006.
- [9] A. J. Miller, R. A. Hatton, G. Y. Chen, and S. R. P. Silva, "Carbon nanotubes grown on In₂O₃: Sn glass as large area electrodes for organic photovoltaics," *Applied Physics Letters*, vol. 90, no. 2, Article ID 023105, 2007.
- [10] S.-R. Jang, R. Vittal, and K.-J. Kim, "Incorporation of functionalized single-wall carbon nanotubes in dye-sensitized TiO₂ solar cells," *Langmuir*, vol. 20, no. 22, pp. 9807–9810, 2004.
- [11] T. Y. Lee, P. S. Alegaonkar, and J.-B. Yoo, "Fabrication of dye sensitized solar cell using TiO₂ coated carbon nanotubes," *Thin Solid Films*, vol. 515, no. 12, pp. 5131–5135, 2007.
- [12] W. Wang, P. Serp, P. Kalck, and J. L. Faria, "Visible light photodegradation of phenol on MWNT-TiO₂ composite catalysts prepared by a modified sol-gel method," *Journal of Molecular Catalysis A: Chemical*, vol. 235, no. 1-2, pp. 194–199, 2005.
- [13] J. Bisquert, "Chemical capacitance of nanostructured semiconductors: its origin and significance for nanocomposite solar cells," *Physical Chemistry Chemical Physics*, vol. 5, no. 24, pp. 5360–5364, 2003.
- [14] R. Kern, R. Sastrawan, J. Ferber, R. Stangl, and J. Luther, "Modeling and interpretation of electrical impedance spectra of dye solar cells operated under open-circuit conditions," *Electrochimica Acta*, vol. 47, no. 26, pp. 4213–4225, 2002.
- [15] J. C. Yu and L. Zhang, "Direct sonochemical preparation and characterization of highly active mesoporous TiO₂ with a bicrystalline framework," *Chemistry of Materials*, vol. 14, no. 11, pp. 4647–4653, 2002.
- [16] J. Xi, N. A. Dahoudi, Q. Zhang, Y. Sun, and G. Cao, "Effect of annealing temperature on the performances and electrochemical properties of TiO₂ dye-sensitized solar cells," *Science of Advanced Materials*, vol. 4, no. 7, pp. 727–733, 2012.
- [17] M. C. Kao, "Effect of annealing temperature of TiO₂ thin films for application in dye-sensitized solar cell," *Hsiuping Journal*, vol. 125, p. 134, 2011.
- [18] S.-W. Lee and W. M. Sigmund, "Formation of anatase TiO₂ nanoparticles on carbon nanotubes," *Chemical Communications*, vol. 9, no. 6, pp. 780–781, 2003.
- [19] Y. Yu, J. C. Yu, J. G. Yu et al., "Enhancement of photocatalytic activity of mesoporous TiO₂ by using carbon nanotubes," *Applied Catalysis A: General*, vol. 289, p. 186, 2005.
- [20] H. Abdullah, N. P. Ariyanto, S. Shaari, B. Yulianto, and S. Junaidi, "Study of porous nanoflake ZnO for dye-sensitized solar cell application," *The American Journal of Engineering and Applied Sciences*, vol. 21, p. 236, 2009.
- [21] B. D. Cullity and S. R. Stock, *Elements of X-Ray Diffraction*, Prentice Hall, 3rd edition, 2001.
- [22] S. Nakade, Y. Saito, W. Kubo et al., "Enhancement of electron transport in nano-porous TiO₂ electrodes by dye adsorption," *Electrochemistry Communications*, vol. 5, no. 9, pp. 804–808, 2003.
- [23] Y. H. Jung, K.-H. Park, J. S. Oh, D.-H. Kim, and C. K. Hong, "Effect of TiO₂ rutile nanorods on the photoelectrodes of dye-sensitized solar cells," *Nanoscale Research Letters*, vol. 8, no. 1, pp. 1–6, 2013.
- [24] Y. Yu, L.-L. Ma, W.-Y. Huang et al., "Sonication assisted deposition of Cu₂O nanoparticles on multiwall carbon nanotubes with polyol process," *Carbon*, vol. 43, no. 3, pp. 670–673, 2005.
- [25] E. R. Morales, N. R. Mathews, D. Reyes-Coronado et al., "Physical properties of the CNT: TiO₂ thin films prepared by sol-gel dip coating," *Solar Energy*, vol. 86, no. 4, pp. 1037–1044, 2012.
- [26] N. P. Ariyanto, H. Abdullah, and N. S. A. Ghani, "Surface morphology characterisation of Sn-doped ZnO films for antireflective coating," *Materials Research Innovations*, vol. 13, no. 3, pp. 157–160, 2009.

- [27] N. P. Ariyanto, H. Abdullah, J. Syarif, B. Yulianto, and S. Shaari, "Fabrication of zinc oxide-based dye-sensitized solar cell by chemical bath deposition," *Functional Materials Letters*, vol. 3, no. 4, pp. 303–307, 2010.
- [28] Y. Lee and M. Kang, "The optical properties of nanoporous structured titanium dioxide and the photovoltaic efficiency on DSSC," *Materials Chemistry and Physics*, vol. 122, no. 1, pp. 284–289, 2010.
- [29] H. Abdullah, M. Z. Razali, and M. A. Yarmo, "Preparation of titanium dioxide paste for dye sensitized solar cells (DSSCs)," *Advanced Materials Research*, vol. 139–141, pp. 153–156, 2010.
- [30] J. Yu, T. Ma, and S. Liu, "Enhanced photocatalytic activity of mesoporous TiO₂ aggregates by embedding carbon nanotubes as electron-transfer channel," *Physical Chemistry Chemical Physics*, vol. 13, no. 8, pp. 3491–3501, 2011.
- [31] K. M. Lee, C. W. Hu, H. W. Chen, and K. C. Ho, "Incorporating carbon nanotube in a low-temperature fabrication process for dye-sensitized TiO₂ solar cells," *Solar Energy Materials and Solar Cells*, vol. 92, no. 12, pp. 1628–1633, 2008.
- [32] J. Yu, J. Fan, and B. Cheng, "Dye-sensitized solar cells based on anatase TiO₂ hollow spheres/carbon nanotube composite films," *Journal of Power Sources*, vol. 196, no. 18, pp. 7891–7898, 2011.
- [33] V. Dhas, S. Muduli, S. Agarkar et al., "Enhanced DSSC performance with high surface area thin anatase TiO₂ nanoleaves," *Solar Energy*, vol. 85, no. 6, pp. 1213–1219, 2011.
- [34] M. Adachi, M. Sakamoto, J. Jiu, Y. Ogata, and S. Isoda, "Determination of parameters of electron transport in dye-sensitized solar cells using electrochemical impedance spectroscopy," *The Journal of Physical Chemistry B*, vol. 110, no. 28, pp. 13872–13880, 2006.
- [35] Y. Zhang, J. Zhang, P. Wang et al., "Anatase TiO₂ hollow spheres embedded TiO₂ nanocrystalline photoanode for dye-sensitized solar cells," *Materials Chemistry and Physics*, vol. 123, no. 2-3, pp. 595–600, 2010.
- [36] A. Mathew, G. M. Rao, and N. Munichandraiah, "Effect of TiO₂ electrode thickness on photovoltaic properties of dye sensitized solar cell based on randomly oriented Titania nanotubes," *Materials Chemistry and Physics*, vol. 127, no. 1-2, pp. 95–101, 2011.
- [37] M. Liberatore, F. Decker, L. Burtone et al., "Using EIS for diagnosis of dye-sensitized solar cells performance," *Journal of Applied Electrochemistry*, vol. 39, no. 11, pp. 2291–2295, 2009.

Research Article

Experiment Investigation on Electrical and Thermal Performances of a Semitransparent Photovoltaic/Thermal System with Water Cooling

Guiqiang Li, Gang Pei, Ming Yang, and Jie Ji

Department of Thermal Science and Energy Engineering, University of Science and Technology of China, 96 Jinzhai Road, Hefei City 230026, China

Correspondence should be addressed to Gang Pei; peigang@ustc.edu.cn

Received 25 March 2014; Accepted 2 July 2014; Published 1 September 2014

Academic Editor: Hongxing Yang

Copyright © 2014 Guiqiang Li et al. This is an open access article distributed under the Creative Commons Attribution License, which permits unrestricted use, distribution, and reproduction in any medium, provided the original work is properly cited.

Different from the semitransparent building integrated photovoltaic/thermal (BIPV/T) system with air cooling, the semitransparent BIPV/T system with water cooling is rare, especially based on the silicon solar cells. In this paper, a semitransparent photovoltaic/thermal system (SPV/T) with water cooling was set up, which not only would provide the electrical power and hot water, but also could attain the natural illumination for the building. The PV efficiency, thermal efficiency, and exergy analysis were all adopted to illustrate the performance of SPV/T system. The results showed that the PV efficiency and the thermal efficiency were about 11.5% and 39.5%, respectively, on the typical sunny day. Furthermore, the PV and thermal efficiencies fit curves were made to demonstrate the SPV/T performance more comprehensively. The performance analysis indicated that the SPV/T system has a good application prospect for building.

1. Introduction

Building integrated photovoltaic/thermal (BIPV/T) is one of the most applicable solutions for solar PV. For BIPV/T, it can take away the heat from PV cells to keep a high electrical efficiency and then supply the electrical power and heat source for the building. Chow et al. indicated that the limited building space for accommodating solar devices has driven a demand on the use of PV/T technology [1]. Ooshaksaraei et al. illustrated the characterization of air-based photovoltaic/thermal panels with bifacial solar cells [2]. J. H. Kim and J. T. Kim took the experiment on the performance of an unglazed PV/T collector with two different absorber types [3]. Matuska investigated the influence of building integration of polycrystalline PV modules on their performance and potential for use of active liquid cooling by use of BIPV-T collectors through simulation analysis [4]. Nonetheless considering the comfort and the architectural lighting, as the facade or roof in building, the BIPV/T still needed to maintain the natural lighting of the building spaces.

It is known for BIPV that the transparency of the PV system is realised by either thin PV cells becoming transparent or leaving spaces between the PV cells to allow the natural illumination partially into the building [5]. Kang et al. used the dye-sensitized solar cells (DSCs) to replace building windows which allowed light transmission and application of various colors but had a lower efficiency in terms of electricity generation than silicon solar cells [6].

However, due to the cooling structure, it is more difficult for BIPV/T to maintain the natural lighting of the building spaces than BIPV. Many researchers improved BIPV/T to achieve this purpose. For BIPV/T with air cooling, Vats et al. designed a building integrated semitransparent photovoltaic/thermal (BISPVT) system for roof and facade which could provide electricity, space heating, and day lighting [7–9]. Kamthania et al. presented the performance evaluation of a hybrid photovoltaic/thermal (Semitransparent PV/T) double pass facade for space heating [10]. But for BIPV/T with water cooling, less work has been focused on the semitransparent photovoltaic/thermal system, which is due

TABLE I: Area size of the SPV/T.

Component	Area size (m ²)
PV	0.112
Total area (excluding gap)	0.27

to the common whole flat plate PV/T process technology with water cooling. Suppose that a semitransparent photovoltaic/thermal system (SPV/T) with water cooling was built, it not only would provide the electrical power, space heating, and hot water for the building, but also could attain the natural illumination, which would further expand the application scope of the BIPV/T.

Therefore, this paper presented a semitransparent photovoltaic/thermal system with water cooling for building application through improving the PV/T structure. The system adopted a technology that the PV was directly laminated on the surface of the square tube, and the space was left between square tubes. The schematic diagram of the semitransparent photovoltaic/thermal system with water cooling on a roof was shown in Figure 1 and the sunlight can be allowed through the gap into the building space. Considering that the crystalline silicon PV has a higher electrical efficiency than other solar PVs, thus the semitransparent photovoltaic/thermal system adopted the crystalline silicon PV to obtain a higher PV power. The experiment focused on the electrical and thermal performances of the SPV/T system, which indicated that the SPV/T system has a good PV/T performance.

2. Experimental Rig Setup

2.1. SPV/T Solar Collector Structure. The SPV/T consisted of PV, the cooling square tube, the storage tank, the connecting pipe, and other major components. The constituent layers of PV/T were shown in Figure 2(a). The PV was inserted within the encapsulated materials, which included the transparent TPT (tedlar polyester-tedlar) and the EVA (ethylene-vinyl acetate) layers on the top, and the EVA and opaque TPT layers underneath. TPT is known for its good electrical insulation and EVA is the adhesive material. Further down the square pipe is a layer of thermal insulation, which covered the two side surfaces and bottom surfaces of the square pipe. There is an insulated air layer between the front glazing and the PV encapsulation, the same as that between the back glazing and the thermal insulation layer.

Four PV cells were connected in series and laminated together on one square tube. The size of each PV cell is 15.6 cm * 1.0 cm and that of the square pipe is 80.0 cm * 1.5 cm. The SPV/T system has 18 square pipes (Figure 2(b)). The real photo of SPV/T was shown in Figure 3(c), and the sunlight can pass through the spaces between the square pipes to reach the ground.

Other size parameters of this SPV/T system were shown in Table 1.

2.2. Experimental Test Device. The SPV/T system cooperated with a maximum power point tracker (MPPT); thus the output value of PV could maintain at its maximum value.



FIGURE 1: Schematic diagram of the SPV/T with water cooling on a roof.

During operation, the cooling water was circulated from the bottom port of the storage tank, then entered into the lower inlet of the SPV/T collector and took away the heat from the PV, at last outflowed from the upper outlet of the SPV/T collector, and returned to the top port of the storage tank. A 1.5 W mini water pump was installed as an auxiliary loop tool, and the flow rate was approximately 0.031 m³/h. The volume of water tank was 20 L. Three thermocouples were vertically and symmetrically arranged in the tank to test the water temperature in the storage tank. The ambient temperature and wind speed were measured by ambient monitor. The components of the test equipment are listed in Table 2.

3. Testing and Evaluation of the Semitransparent Photovoltaic/Thermal System

3.1. Experimental Test Profile. The prototype of the SPV/T system was designed and installed on a rooftop at University of Science and Technology of China in Hefei (31°53'N, 117°15'E). The orientation of the system was facing south at a 32° tilt angle.

3.2. Evaluation Performance of SPV/T System. The electrical efficiency of PV from the experiment was given:

$$\eta_{\text{sys,pv}} = \frac{I_m \cdot V_m}{G \cdot A_{\text{pv}}} \quad (1)$$

where I_m and V_m are the current and the voltage of the PV operating at the maximum power; G is the total solar radiation, Wm^{-2} ; A_{pv} is PV area, m^2 .

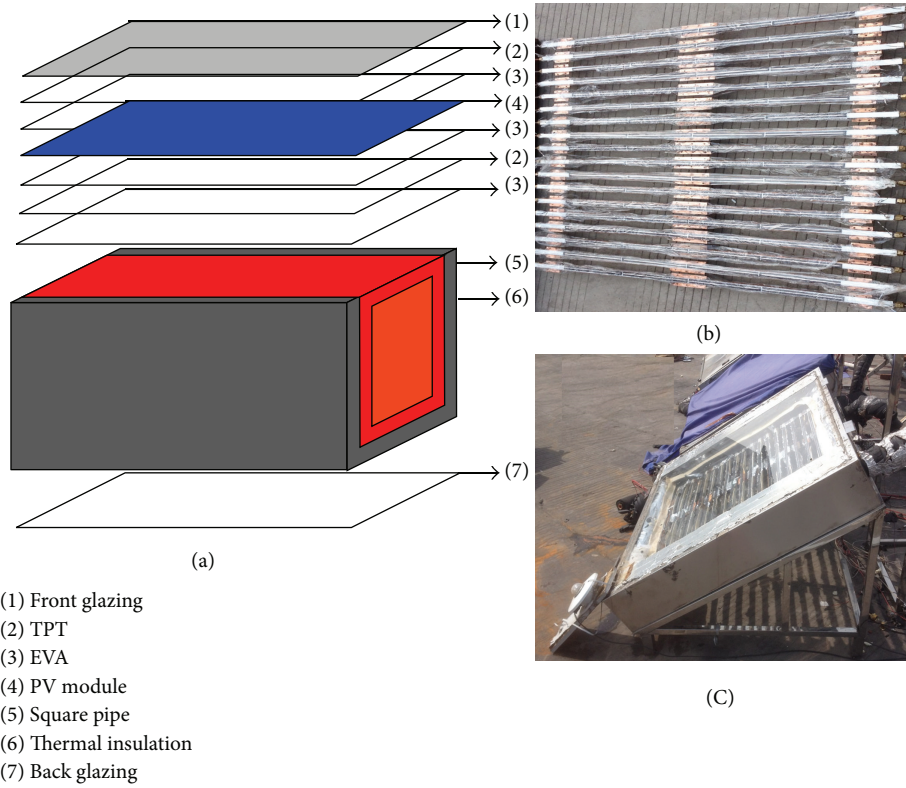


FIGURE 2: SPV/T structure: (a) constituent layers of PV/T, (b) PV/T, and (c) photo of SPV/T solar collector.

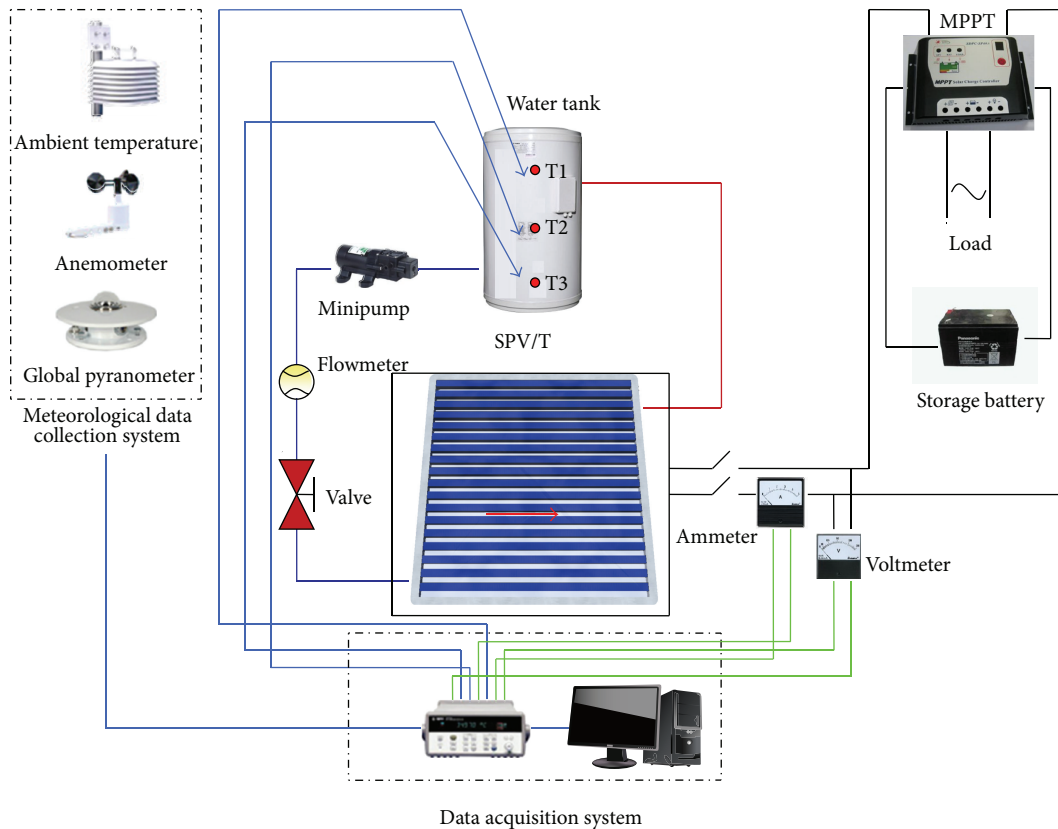


FIGURE 3: Testing schematic diagram of SPV/T system.

TABLE 2: Specification of the test components.

Test equipment	Specification	Suppliers names	Quantity	Position
Ultrasonic flowmeter	TUF-2000P	Shanghai Juguan Industry Automation Device Ltd.	1	Main pipe line
Thermocouple	0.2 mm copper-constantan	Homemade	3	Water tank
Pyranometer	TBQ-2	Jinzhou, China (Sun Co.)	1	Near experimental rig with the same tilted angle
Minipump	~1.5 KW	Homemade	1	Main pipe line
Ambient monitor	JZH-1	Jinzhou, China (Sun Co.)	1	Near experimental rig
Others: data acquisition instrument: Agilent 34970A (USA), test computer, electrical wires, etc.				

For the SPV/T system, the heating capacity obtained by the water in the tank can be expressed as follows:

$$\dot{Q}_{\text{sys,th}} = m_{w,\text{tank}} c \frac{d\bar{T}}{dt}, \quad (2)$$

where \bar{T} is the average water temperature in the tank, °C.

The system thermal efficiency $\eta_{\text{sys,th}}$ is calculated by

$$\eta_{\text{sys,th}} = \frac{\int_{t_1}^{t_2} \dot{Q}_{\text{sys,th}} dt}{A_c \int_{t_1}^{t_2} G dt}; \quad (3)$$

$\eta_{\text{sys,th}}$ can also be obtained by

$$\begin{aligned} \eta_{\text{sys,th}} &= \alpha_0 - U_s T_i^* \\ &= \alpha_0 - U_s \frac{T_i - \bar{T}_a}{\bar{G}}, \end{aligned} \quad (4)$$

where \bar{G} is the average solar radiation, Wm^{-2} , and A_c is the total area of the collector.

The exergy efficiency can be defined to describe the quality difference between electricity and heat. The exergy analysis method was based on the second law of thermodynamics, which revealed a system with a reasonable degree of energy and could evaluate the system performance better.

The exergy efficiency of PV unit conversion is defined as

$$\varepsilon_{\text{sys,pv}} = \frac{I_m \cdot V_m}{G \cdot A_{\text{pv}} \cdot \varphi_{\text{srad,max}}}, \quad (5)$$

where $\varphi_{\text{srad,max}}$ is the maximum efficiency ratio for determining the exergy of thermal emission at temperature T [11, 12] and the expression is

$$\varphi_{\text{srad,max}} = 1 + \frac{1}{3} \left(\frac{T_a}{T} \right)^4 - \frac{4}{3} \frac{T_a}{T}, \quad (6)$$

where T is equal to the 6000 K solar radiation temperature in the exergetic evaluation.

The exergy efficiency of thermal conversion is defined as

$$\varepsilon_{\text{sys}} = \frac{\int_{t_1}^{t_2} (\dot{E}_{X,\text{output}} - W_{\text{pump}}) dt}{\int_{t_1}^{t_2} \dot{E}_{X,\text{sun}} dt}, \quad (7)$$

where the exergy obtained in the storage tank could be written as follows [13], and assuming that the temperature value in the tank is the arithmetic average of three thermocouple temperature values:

$$\dot{E}_{X,\text{output}} = \dot{Q}_{\text{sys,th}} \left(1 - \frac{T_a}{T} \right), \quad (8)$$

$\dot{E}_{X,\text{sun}}$ is the exergy from the sun and could be written as

$$\dot{E}_{X,\text{sun}} = A_c G \varphi_{\text{srad,max}}. \quad (9)$$

4. Experimental Results and Discussion

4.1. Performance Analysis on a Typical Sunny Day. A typical day as an example, the test time was from 8:00 to 15:30. The environmental parameters during the test were shown in Figure 4. The average solar radiation and the average ambient temperature were 729.0 Wm^{-2} and 16.9°C , respectively. The average wind speed was approximately 1.5 ms^{-1} .

According to (1) and (2), the instantaneous PV efficiency and thermal efficiency can be obtained, as shown in Figure 5. The value of PV efficiency was between 0.095 and 0.13. The tendency of the PV efficiency curve was gradually declined during the test which was because the water temperature became higher. For thermal efficiency, the instantaneous values increased at first and then gradually declined. The maximum value of the thermal efficiency was 53.0%. The overall PV efficiency and the thermal efficiency on whole day were about 11.5% and 39.5%, respectively.

It is clear that for the SPV/T system, the exergy efficiency of the PV was much higher than that of the hot water (Figure 6). That is because in the SPV/T system applications the production of electricity is the main priority, and it is necessary to operate the PV modules at a low temperature. The water was heated from 19.4°C to 44.5°C during the test. Before 8:30, the water temperature increased slowly, and the exergy efficiency of the thermal output was below 1% and the highest exergy efficiency of the thermal output was between 12:30 and 13:00, and the maximum value was about 2.85%.

4.2. SPV/T Performance Curve Fitting. Referring to [14], in order to apprehend the electrical and thermal performance of the SPV/T system under the forced flow situation, Case I–Case II on the experiment with different initial temperatures

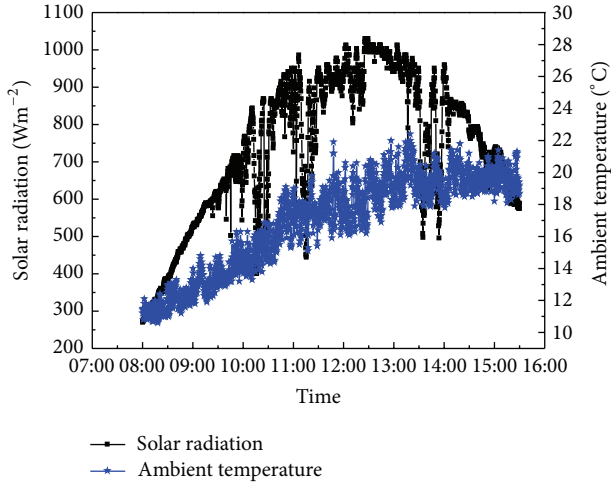


FIGURE 4: Environmental parameters during the test.

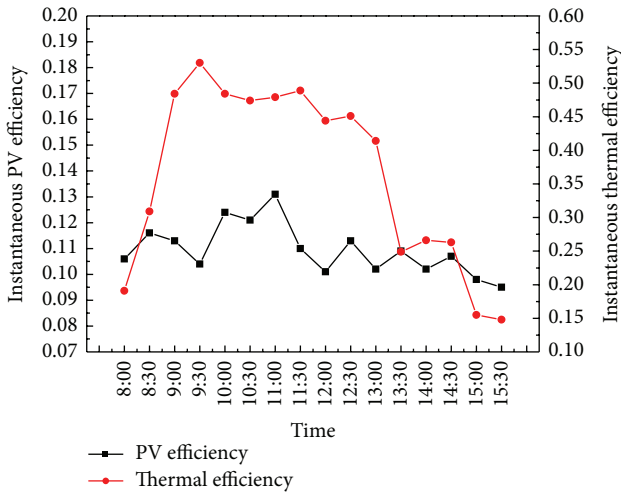


FIGURE 5: PV and thermal efficiency during the test.

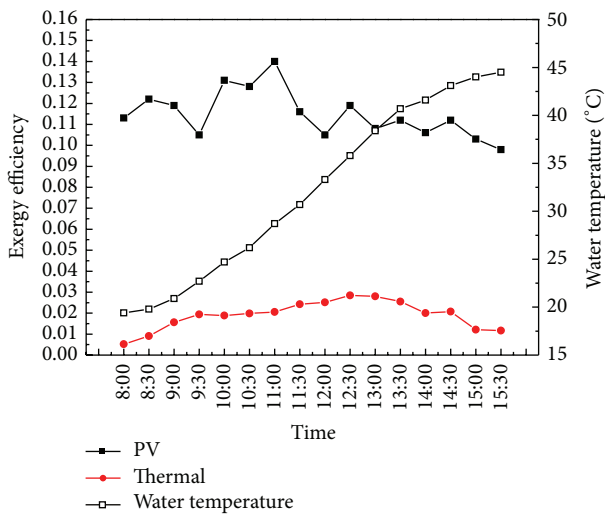


FIGURE 6: Exergy efficiency with water temperature variation during the test.

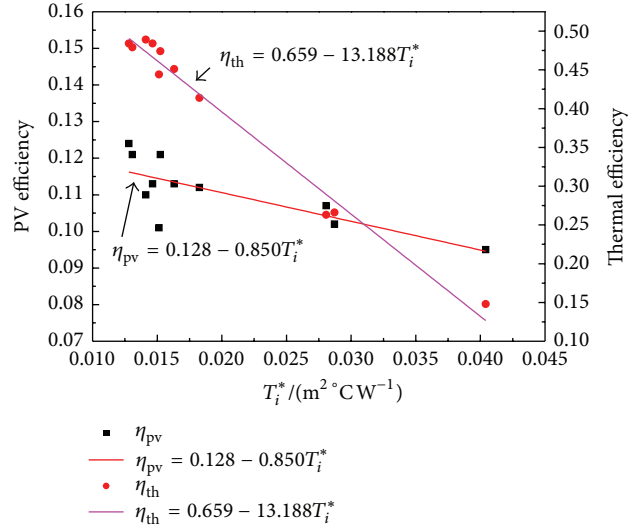


FIGURE 7: PV efficiency and thermal efficiency fit curves of the experimental results on SPV/T system.

were chosen to illustrate the overall performance, as shown in Table 3.

The PV efficiencies and thermal efficiencies of the SPV/T system in Case 1–Case 11 were fitted to a linear function to correspond to mutual relationships among the variables, as shown in Figure 7.

For the SPV/T system, the PV efficiency under the zero reduced temperature condition was 12.8%, which was reasonable and could be further improved by using the front glazing material with a higher transmissivity. The thermal efficiency intercept was 65.9%, which could also be improved by using selective absorber surface with low emissivity.

4.3. Experiment Error Analysis. The relative error (RE) of the dependent variable y can be calculated as follows:

$$RE = \frac{dy}{y} = \frac{\partial f}{\partial x_1} \frac{dx_1}{y} + \frac{\partial f}{\partial x_2} \frac{dx_2}{y} + \dots + \frac{\partial f}{\partial x_n} \frac{dx_n}{y}, \quad (10)$$

$$y = f(x_1, x_2, \dots, x_n),$$

where x_i , ($i = 1, \dots, n$), is the variable of the dependent variable y and $\partial f/\partial x$ is the error transferring coefficient of the variables.

The experimental relative mean error (RME) during the test period can be expressed as

$$RME = \frac{\sum_1^N |RE|}{N}. \quad (11)$$

According to (10)–(11), the RMEs of all variables were calculated and the results were given in Table 4.

5. Conclusion

This paper presented a semitransparent photovoltaic/thermal system (SPV/T) with water cooling, which not only could

TABLE 3: List of experimental results.

Parameters	Initial water temperature in the tank (°C)	Average environmental temperature (°C)	Average solar radiation ($W \cdot m^{-2}$)	Average water flow ($m^3 \cdot h^{-1}$)	PV efficiency (%)	System thermal efficiency (%)
Case 1	20.9	12.7	520.9	0.031	0.113	0.484
Case 2	24.7	14.5	710.6	0.031	0.124	0.484
Case 3	26.2	15.6	665.2	0.031	0.121	0.474
Case 4	28.7	17.4	778.0	0.031	0.121	0.479
Case 5	30.7	17.7	845.0	0.031	0.11	0.489
Case 6	33.3	17.9	930.8	0.031	0.101	0.444
Case 7	35.8	18.5	979.0	0.031	0.113	0.451
Case 8	38.4	19.4	969.2	0.031	0.112	0.414
Case 9	41.6	19.5	753.5	0.031	0.102	0.266
Case 10	43.1	19.7	806.1	0.031	0.107	0.263
Case 11	44.5	19.5	611.0	0.031	0.095	0.148

TABLE 4: The experimental RME of the variables.

Variable	T	G	$\eta_{sys,pv}$	$\eta_{sys,th}$
RME	0.066%	2.0%	4.2%	22.79%

provide the electrical power and hot water, but also would attain the natural illumination for the building, and in comparison with the common nontransparent BIPV/T system, it has more advantages.

Based on the experiment results, the PV efficiency and thermal efficiency of the SPV/T system on the sunny day were approximately 11.5% and 39.5%, respectively. Furthermore, the exergy analysis of the SPV/T system was made to indicate that the PV exergy efficiency was the main portion in the system exergy efficiency, which was because in PV/T system applications the production of electricity is the main priority, and it is necessary to operate the PV modules at low temperature. At the same time, the PV and thermal efficiencies fit curves were made to illustrate the SPV/T system performance comprehensively.

The experiment presented the overall electrical and thermal performances of the SPV/T system and verified the feasibility of it, which indicated a good application prospect.

Conflict of Interests

The authors declare that there is no conflict of interests regarding the publication of this paper.

Acknowledgments

The study was sponsored by the National Science Foundation of China (Grant nos. 51178442, 51408578), and “the Fundamental Research Funds for the Central Universities”, and China Postdoctoral Science Foundation (2014M550350).

References

- [1] T. T. Chow, G. N. Tiwari, and C. Menezo, “Hybrid solar: a review on photovoltaic and thermal power integration,” *International Journal of Photoenergy*, vol. 2012, Article ID 307287, 17 pages, 2012.
- [2] P. Ooshaksaraei, K. Sopian, R. Zulkifli, M. A. Alghoul, and S. H. Zaidi, “Characterization of a bifacial photovoltaic panel integrated with external diffuse and semimirror type reflectors,” *International Journal of Photoenergy*, vol. 2013, Article ID 465837, 7 pages, 2013.
- [3] J. H. Kim and J. T. Kim, “The experimental performance of an unglazed PVT collector with two different absorber types,” *International Journal of Photoenergy*, vol. 2012, Article ID 312168, 6 pages, 2012.
- [4] T. Matuska, “Simulation study of building integrated solar liquid PV-T collectors,” *International Journal of Photoenergy*, vol. 2012, Article ID 686393, 8 pages, 2012.
- [5] N. Sellami, T. K. Mallick, and D. A. McNeil, “Optical characterisation of 3-D static solar concentrator,” *Energy Conversion and Management*, vol. 64, pp. 579–586, 2012.
- [6] J.-G. Kang, J.-H. Kim, and J.-T. Kim, “Performance evaluation of DSC windows for buildings,” *International Journal of Photoenergy*, vol. 2013, Article ID 472086, 6 pages, 2013.
- [7] K. Vats and G. N. Tiwari, “Performance evaluation of a building integrated semitransparent photovoltaic thermal system for roof and faade,” *Energy and Buildings*, vol. 45, pp. 211–218, 2012.
- [8] K. Vats and G. N. Tiwari, “Energy and exergy analysis of a building integrated semitransparent photovoltaic thermal (BISPVT) system,” *Applied Energy*, vol. 96, pp. 409–416, 2012.
- [9] K. Vats, V. Tomar, and G. N. Tiwari, “Effect of packing factor on the performance of a building integrated semitransparent photovoltaic thermal (BISPVT) system with air duct,” *Energy and Buildings*, vol. 53, pp. 159–165, 2012.
- [10] D. Kamthania, S. Nayak, and G. N. Tiwari, “Performance evaluation of a hybrid photovoltaic thermal double pass facade for space heating,” *Energy and Buildings*, vol. 43, no. 9, pp. 2274–2281, 2011.
- [11] R. Petela, “Exergy of undiluted thermal radiation,” *Solar Energy*, vol. 74, no. 6, pp. 469–488, 2003.
- [12] R. Petela, “Exergy analysis of the solar cylindrical-parabolic cooker,” *Solar Energy*, vol. 79, no. 3, pp. 221–233, 2005.

- [13] T. T. Chow, G. Pei, K. F. Fong, Z. Lin, A. L. S. Chan, and J. Ji, "Energy and exergy analysis of photovoltaic-thermal collector with and without glass cover," *Applied Energy*, vol. 86, no. 3, pp. 310–316, 2009.
- [14] T. T. Chow, W. He, and J. Ji, "Hybrid photovoltaic-thermosyphon water heating system for residential application," *Solar Energy*, vol. 80, no. 3, pp. 298–306, 2006.

Research Article

Experiment and Simulation Study on the Amorphous Silicon Photovoltaic Walls

Wenjie Zhang,¹ Bin Hao,² and Nianping Li¹

¹ College of Civil Engineering, Hunan University, Changsha, Hunan 410082, China

² Center for Science and Technology of Construction, Ministry of Housing and Urban-Rural Development, Beijing 100835, China

Correspondence should be addressed to Nianping Li; linianping@126.com

Received 2 May 2014; Revised 7 July 2014; Accepted 21 July 2014; Published 27 August 2014

Academic Editor: Hongxing Yang

Copyright © 2014 Wenjie Zhang et al. This is an open access article distributed under the Creative Commons Attribution License, which permits unrestricted use, distribution, and reproduction in any medium, provided the original work is properly cited.

Based on comparative study on two amorphous silicon photovoltaic walls (a-Si PV walls), the temperature distribution and the instant power were tested; and with EnergyPlus software, similar models of the walls were built to simulate annual power generation and air conditioning load. On typical sunshine day, the corresponding position temperature of nonventilated PV wall was generally 0.5~1.5°C higher than that of ventilated one, while the power generation was 0.2%~0.4% lower, which was consistent with the simulation results with a difference of 0.41% in annual energy output. As simulation results, in summer, comparing the PV walls with normal wall, the heat per unit area of these two photovoltaic walls was 5.25 kWh/m² (nonventilated) and 0.67 kWh/m² (ventilated) higher, respectively. But in winter the heat loss of nonventilated one was smaller, while ventilated PV wall was similar to normal wall. To annual energy consumption of heating and cooling, the building with ventilated PV wall and normal wall was also similar but slightly better than nonventilated one. Therefore, it is inferred that, at low latitudes, such as Zhuhai, China, air gap ventilation is suitable, while the length to thickness ratio of the air gap needs to be taken into account.

1. Introduction

Solar energy is regarded as the world's richest renewable resource with the broadest distribution. In the circumstances where energy security and climate change remain critically important, the solar power generation technology drew increasing attention from various countries with the enhancing strategic importance. In addition to the development of large-scale ground photovoltaic (PV) power stations in the suburbs, the application of PV in buildings is also considered to be prospects in crowded urban area [1, 2].

Based on the differences of PV modules serving as building components, there are two forms divided roughly, the building-integrated photovoltaics (BIPV) and the building-attached photovoltaics (BAPV) [3]. Despite whatever form is taken, the reconstituted building envelope contributed by the integration of PV modules, compared to the normal building envelope, is varied in terms of structures, thermal performance [4–6], and so on, which will further influence

the indoor cooling and heating load of the buildings [7, 8] as well as the performances of PV modules [9–11], such as the decline of photoelectric conversion efficiency due to the increase of the panel temperature rise.

Photovoltaic wall (PV wall), as a common form of PV applied in buildings, the optimum design scheme and operation strategies were extensively studied. Yang et al. [12] established the heat transfer model of the PV wall. One-dimensional unsteady heat conduction equation was emphasized to simulate the heat gain of the PV wall and to compare it with that of the normal wall without PV modules. This research took concrete cases into account in order to investigate the summer heat gain of the PV wall. The result turned out to be that the PV modules will increase the temperature of the air gap in PV wall while it is producing electricity. However, the PV modules shelter from solar radiation functioned to lower down substantially the outdoor comprehensive temperature while reducing the heat gain of walls in summer. The final result would be the reduction of

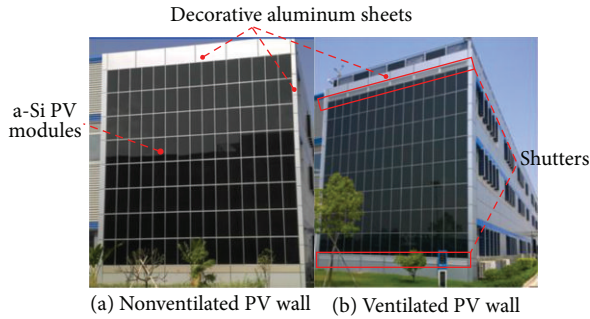


FIGURE 1: The two amorphous silicon PV walls under experiment.

the indoor cooling load of air conditioning. While, there is no description about the direction and location (latitude) of the PV wall.

Ji et al. [13–15] launched the comparison between the PV walls with air gap and the one with no air gap in terms of the electricity generation efficiency and indoor heat gain. The comparison experimental platform was constructed for the convenience of comparing the above-mentioned PV walls which were facing the west with different cooling methods. Respective mathematical models also were constructed. Based on the comparison of the experiments and calculation regarding the two types of PV walls, the result suggested that in Hong Kong these two cooling methods demonstrated nearly no differences in terms of electricity generation efficiency. However, with respect to the indoor heat gain, both methods substantially are different compared with each other. The problem is that the literature has not revealed the exact PV module types that were used in the experiments while the mathematical models did not take the relationship between the temperature rise of the PV panel and the electricity generation efficiency into account.

Zhu et al. [16] adopted the foamed plastic sheets as the simulated walls to make a box as the building and several bulbs displayed evenly as the simulated sunshine. Meanwhile, they came up with a model that was based on the temperature integral which can be used to investigate and simulate the multiheat exchange inside the PV walls. The result was congruent with the expected value. Concurrently, through comparison, it was found that the cooling down efficiency of the ventilated PV walls was 7% to 10% higher than that of the nonventilated ones. Certainly, this conclusion was drawn in the indoor experimental conditions, which meant that there may be certain limits in the real situation.

There is a plenty of comparative research over the thermal performance of the PV walls with different structures, analyzing the influence on the PV system efficiency and the indoor cooling and heating load; however, those were based on the constructed experiment equipment or real-scale experimental models. This research also conducted the comparison among the temperatures, immediate power under the positive sunshine condition, and generating capacity of each part of two PV walls based on the measurements on parameters of these two PV walls (one of them has the closed air gap between the PV modules and the walls while

the other has the open air gap with shutters to have air flows) like temperature, electricity generating power, and generating capacity. In addition, this research also resorted to the emulated software in order to build the models of the two PV walls and the conventional walls and compared the possible influence of the generating capacity of the two PV walls and the three walls on the indoor air conditioning load.

2. The PV Walls

The study is carried out on two PV walls in two buildings, respectively, which are the same at construction and functions in Zhuhai, China (coordinates: N22.378, E113.547), as Figure 1 shows. These two PV walls are identical in terms of the configuration, numbers, connecting ways of the electric system, wall materials, and size. They only slightly differ from each other with regard to the structure.

2.1. Structure. Similarities between two PV walls are as follows:

- (1) They are vertical to the ground, 5° south by east.
- (2) They are identical in terms of the building design structure size and functions. The inner sides of the PV walls are office areas which can be divided into three floors; there is a meeting room in each floor.
- (3) The overall size of the wall is 12.25 m (H) × 10.2 m (L), among which the size of the PV modules is 10.2 m (H) × 9.8 m (L). Other parts are constituted by the decorative aluminum sheets. The lower edge of the PV modules is 1.2 m away from the ground.
- (4) There are 10 mm gaps between the PV walls. In order to make sure that the air gap in the back of the PV wall will not be influenced, the silicone weatherproofing sealant is used to fill the gap between modules.
- (5) There are no buildings in the front side. There is a 4 m distance between the PV walls and the surrounding plants. No shadow is cast on the PV modules.
- (6) They are both in PV wall structure with air gap between the modules and the walls. The air gap is at thickness of 155 mm. Due to the horizontal steel sheet used to hang the PV modules, part of the air gap is only thick at 90 mm. For details refer to Figure 2.

What makes them different is the processing in the higher and lower edges of the two PV walls. The airless one (Figure 1(a)) closed the higher and lower edges by the aluminum sheets. The air gap of the back did not open to the outside. The ventilated one (Figure 1(b)) adopted the shutters in the higher and lower edges so that the air gap of the back of the PV modules can communicate with the outside. There are six groups of shutters, respectively, in the higher and lower positions, each of which has a size at 1600 (L) × 405 (H).

2.2. PV System. The electric systems of two PV walls are independent of each other. Each wall is constituted by 120 a-Si PV modules with 40 Wp (refer to Table 1 for details of

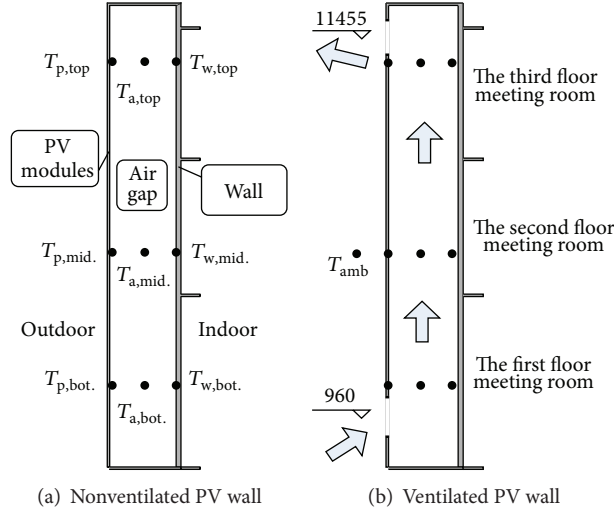


FIGURE 2: Diagram of the two PV walls' structure and the temperature sensor points.

parameters). The installed power of the system is 4.8 kW. Vertically, each row has 8 PV modules, which composed a group string. There are 15 group strings in total, which go through the combiner box and get connected to the grid by an inverter. The maximum input direct-current power of the inverter is 3200 Wp while the maximum input direct-current voltage is 550 V. The MPPT voltage ranges from 125 V to 550 V.

3. Experiment Study

3.1. Testing Parameters and Measure Points. The sensors that were used to measure the outdoor environmental parameters were deployed in the roof of the ventilated PV wall. No obstructions were found. The measured parameters included the temperature and the humidity of the outdoor weather, the wind direction and speed, and the solar radiation in the vertical and horizontal directions. The irradiating apparatus used to test the vertical direction was deployed on the surface where the PV modules were installed.

The panel temperature, temperature of the air gap, and the surface temperature of the wall were measured on the central axis of the vertical direction of the PV wall at different positions (the higher, middle, and lower positions). In addition, the temperatures of the exit and entrance for the air flow of the shutters in the higher and lower edges of the ventilated PV wall would also be tested. The measure points' positions were shown in Figure 2.

The instant current values and the instant voltage values of two PV systems would be measured and recorded in the inverter. Meanwhile, the cumulative generating capacity was also measured.

3.2. Measure System and Sensors. In order to continuously measure and record the above-mentioned parameters, the multichannel sensor would be connected to the itinerant detector. See Figure 3. Each parameter would be inspected through the itinerant detector which would send the data to

TABLE 1: The parameters of the a-Si PV modules used in the project.

Parameters	Information or value
Manufacturer	CG solar
Model number	CGS-40H/G1245 × 635
Maximum power at STC (P_{max})	40 W
Tolerance	±5%
Open circuit voltage (V_{oc})	60.5 V
Short circuit current (I_{sc})	1.16 A
Maximum power voltage (V_{mp})	43.8 V
Maximum power current (I_{mp})	0.92 A
Maximum system voltage	≤600 V DC
Maximum fuse rating	2 A
Length (mm)	1245
Width (mm)	635
Thickness (mm)	7

TABLE 2: Parameters of the major sensors used in testing.

Sensors	Parameters
Pyranometer	Directional response: less than $\pm 10 \text{ W}\cdot\text{m}^{-2}$ (for $1000 \text{ W}\cdot\text{m}^{-2}$ beam radiation)
	Temperature response: 1% (within an interval of 50°C)
	Nonlinearity: $\pm 0.2\%$ (from 100 to $1000 \text{ W}\cdot\text{m}^{-2}$)
	Spectral range: 300 to 2800 nm
Thermal resistance Pt100	Division value: 0.1°C
	Accuracy: $\leq \pm 0.5\%$
	Response time: $\leq 10 \text{ S}$
Direct-current electricity energy sensor	Range: $0\sim 200 \text{ V}/0\sim 10 \text{ A}$
	Division value: $1 \text{ mV}/1 \text{ mA}$ Accuracy: $\leq \pm 0.5\%$

the computer for loading and storage. The time interval for the recording is 1 minute. Due to the far distance between two

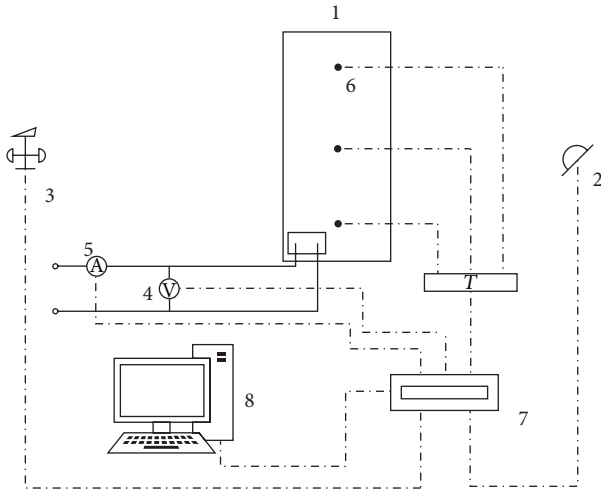


FIGURE 3: The thermal performance measure system with the ventilated PV wall. 1: PV wall; 2: pyranometer; 3: sensors for wind direction, speed, temperature, and humidity; 4: volumeter; 5: ampere meter; 6: temperature probe; 7: itinerant detector; 8: computer.

PV walls, two measure systems like this have been deployed in two PV walls in order to reduce the length of the Pt100 thermal resistance wire. Figure 3 showed the measure system in ventilated PV wall with the sensors to measure the outdoor environmental parameters.

Table 2 showed the sensor parameters which could influence the measure accuracy in the test.

4. Experiment Result Analysis

4.1. The Comparison of the Temperatures between the Panel, Wall Surfaces, and Air Gap of the PV Walls. Launch the analysis over the temperature fields of each measure point in the PV panel, outer wall surfaces, and air gap with typical sunshine condition day (Jan. 20, 2014). See Figures 4, 5, and 6. Due to the differences between the order of heat transmission and the heat storage capacity, the following features would be displayed.

- (1) The change of the temperature curves procrastinated to respond to the change of the sunshine in 0.5–2 hours, among which the wall surface temperature was most obvious. The possible reason came down to the order of heat transmission and the specific heat.
- (2) In the daytime with normal sunshine condition, put the temperature from high to low: panel, air gap, and wall surface. The temperature of the panel is 5–7°C higher than that of the wall surface and 3–5°C higher than that of the air gaps. In the sunset or night, the order was as follows: wall surface, air gap, and panel. They all had the 1–2°C disparity among each other due to the differences of their heat storage capacity and heat dissipation.
- (3) The temperatures for closed air gap, due to the thermal inertia, displayed the temperature from 6:30

to 8:30 which was 2–3°C lower than the environmental temperature. From 8:30 to 14:00, the temperature was almost identical to the environmental one while, from 14:00 to 6:00, the temperature was 1–2°C higher than the environmental one.

- (4) There would be the quick temperature rise in the panel after the sun rose while the temperature of the panel quickly went consistent with the environment after the sunset. Afterwards, till the sun rose again, the temperature kept identical with the environment.
- (5) The peak of the temperature of the panel and air gaps was at 15:30. The one of the wall surface was at 17:00.
- (6) The temperature curves in ventilated PV wall had a similar relationship and features with those of the nonventilated PV wall. However, the temperature disparities of the measure points were smaller than those of nonventilated PV wall.

4.2. The Comparison of the Temperature Field in Vertical Direction. Figure 6 shows the temperature of the panel of the nonventilated PV wall in the vertical direction. Take three points with the same distance in the bottom, middle, and top of the wall. Conspicuously, in the sunshine condition, the temperature disparity between the bottom and the middle parts was about 2–3°C while the one between the middle and top parts was only 0.5–1.5°C, which demonstrated that the temperature rise in the vertical direction gradually declined. The analysis revealed that the observed decline shared certain correlation with the closed flow field. The heat was accumulated in the top, leading to the reduction of the temperature rise.

Figure 7 showed that the wall surface of nonventilated PV wall also had the same tendency of the decline of the temperature rise. The temperature disparity between the bottom and middle parts was at 2.5°C while the temperatures of the middle and the top parts were nearly the same with disparity only at 0.5–1°C, which indicated that the temperature would be lower than the environment in sunshine condition while being higher than the environment without sunshine due to the thermal inertia and its position in the end of the heat transmission.

Figure 8 indicated that the wall in nonventilated PV wall also had the same tendency of the decline of the temperature rise in the vertical direction of the air gaps. The temperature disparity between the middle and bottom parts was at 2–4°C while that between the top and the middle parts was only 1–2°C. The temperature in the bottom with no sunshine was almost identical with the environment. When the environment temperature got rise due to the sunshine and the bottom temperature was lower than it. The situation of the temperature of the middle part was as stated above: the closed air gaps, due to the thermal inertia, had the lower temperature than the environment, probably at 2–3°C, from 6:30 to 8:30. The temperature kept identical with the environment from 8:30 to 14:00 while being higher than the environment at 1–2°C from 14:00 to 6:00. The temperature at top was always higher than the environment.

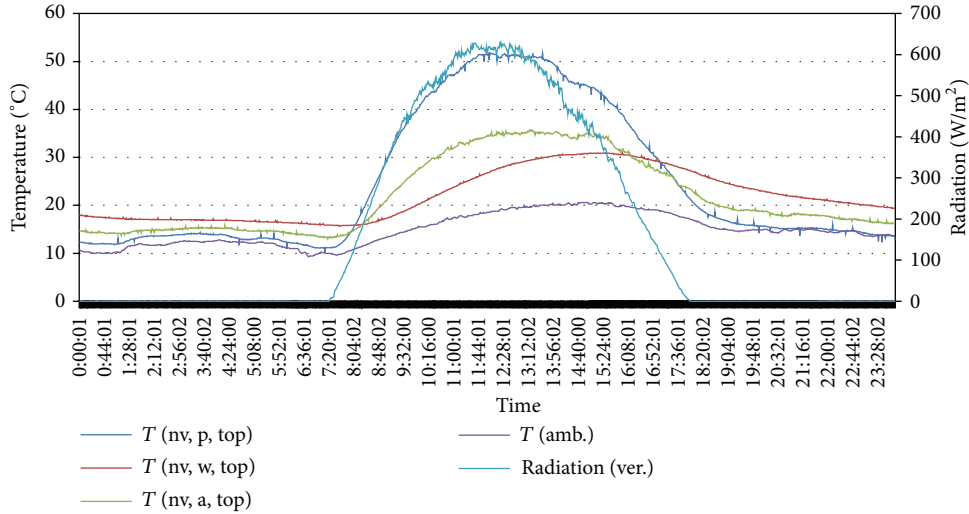


FIGURE 4: The temperature of different points (the top of panel, outer wall, and air gap) of the nonventilated PV wall under the typical sunshine condition.

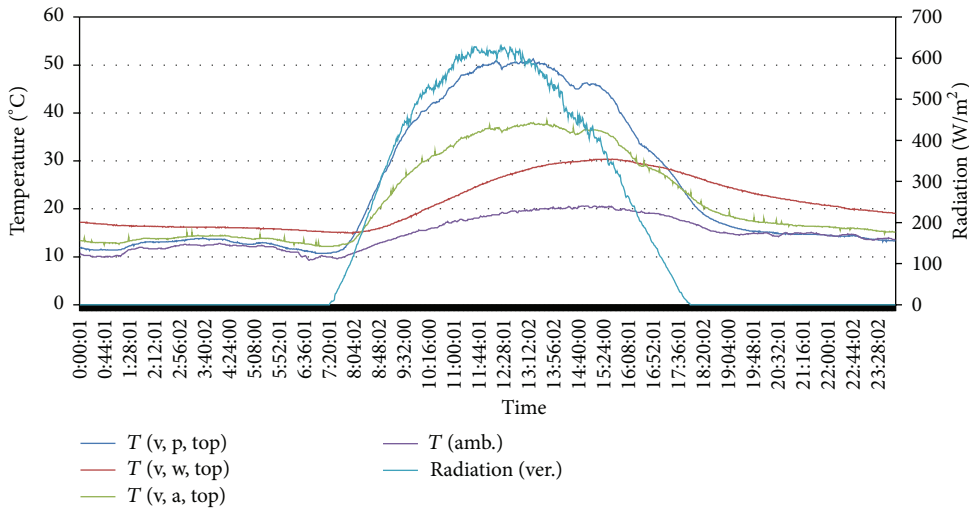


FIGURE 5: The temperature of different points (the top of panel, outer wall, and air gap) of the ventilated PV wall under the typical sunshine condition.

4.3. *The Comparison of the Temperature between Nonventilated PV Wall and Ventilated PV Wall.* The different approaches were taken to process the top and bottom edge of the nonventilated PV wall and ventilated PV wall. The difference of air gap led to the different influence of their temperature fields.

As shown by Figure 9, with sunshine condition, the temperature disparity of the panel at top in nonventilated PV wall and ventilated PV wall was only 0.5–1.5°C. Nonventilated PV wall was the higher one. The largest disparity appeared before 14:00, after which the disparity got closed. After the sunset, nearly no disparity was observed.

Figure 10 showed that there would be certain temperature disparity between the wall surface of the top of nonventilated PV wall and ventilated PV wall. In the daytime with sunshine, the temperature of nonventilated PV wall was generally higher at 2°C but dropped to 1°C after the sunset.

Figure 11 showed that the temperature of the air gap at top of the nonventilated PV wall was always higher than that of ventilated PV wall at 2°C, which declined early in the morning.

4.4. *The Comparison of the Electricity Generation between Nonventilated PV Wall and Ventilated PV Wall Systems.* In Figure 12 the comparison of the relations between output power and panel temperature of the two kinds of PV walls in the typical sunshine is shown. From it, we can see that, from 9:20 to 14:30, the panel temperature of ventilated PV wall is 0.5 to 1.5°C lower than that of nonventilated PV wall, while the output power is 0.2% to 0.4% higher than that of nonventilated PV wall; more obviously, from around 15:00 to 16:00, the panel temperature of ventilated PV wall fluctuates and turns out to be about 2°C higher than that

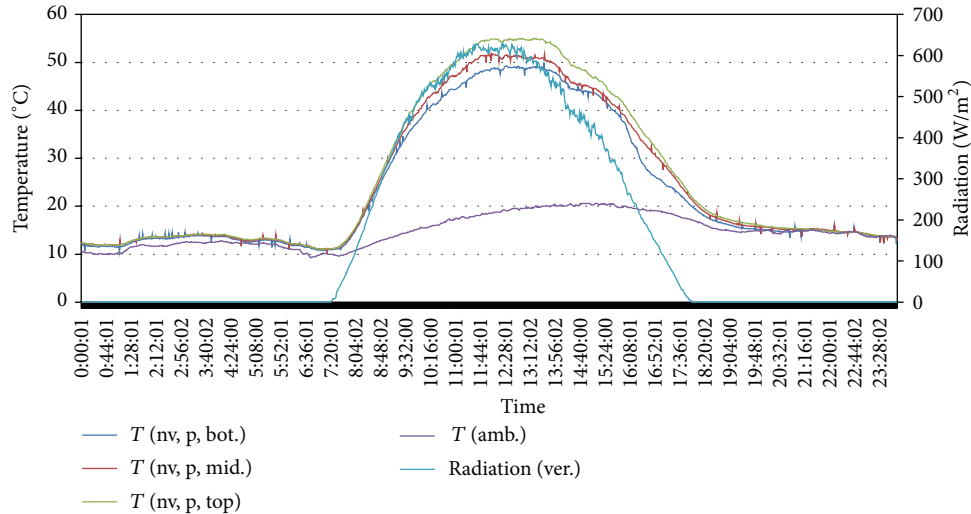


FIGURE 6: The temperature of different points (panel in vertical direction) of the nonventilated PV wall under the typical sunshine condition.

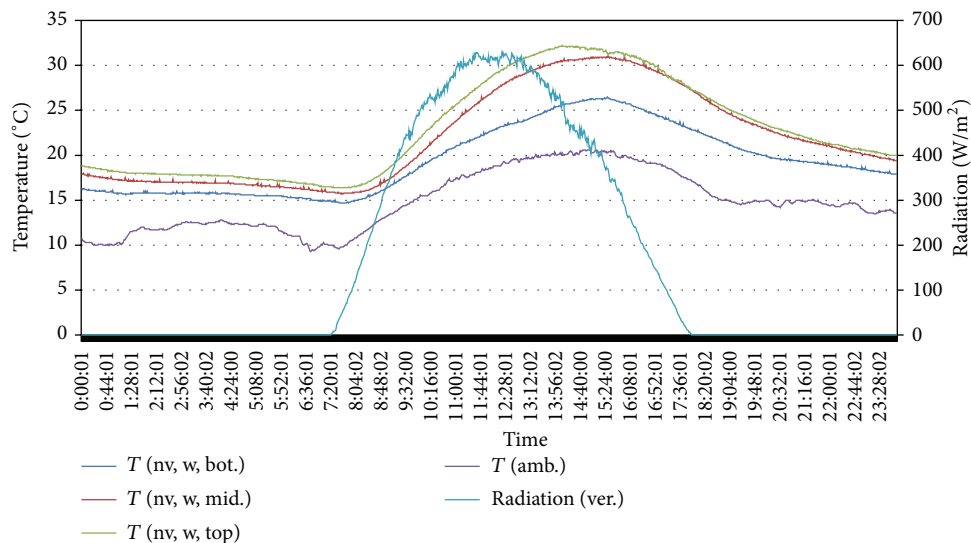


FIGURE 7: The temperature of different points (outer wall in vertical direction) of the nonventilated PV wall under the typical sunshine condition.

of nonventilated PV wall, along with which its generating efficiency significantly drops and is about 0.5% lower than that of nonventilated PV wall. For both of the systems, the peak output power occurs at 12:30 when the solar irradiance reaches a higher value of the day and is 3.351 kW and 3.337 kW, respectively. The generated energy throughout the day of the nonventilated is 18.71 kWh and of the ventilated is 18.78 kWh; there is a difference of 0.07 kWh (0.37%) between the two. The panel temperatures of both PV walls do not seem to be much different from each other and thus the difference of their power is smaller.

5. Simulation Study

5.1. Model Establishment. EnergyPlus Model cannot simulate only the energy cost of buildings, but also the electricity

generation of the PV system. In order to overall investigate the electricity generation of the PV walls and their influence on the indoor air conditioning energy cost, this research adopted the EnergyPlus software to simulate the data of the electricity generation and heat transmission performance in the domestic meteorological year.

First, model the system is based on the PV walls and the exact size of buildings. Figure 13 showed the pictures of the airless PV walls, the ventilated PV walls, and the ordinary walls. The air vents at top and bottom of the ventilated PV walls were in form of four windows that could be opened. Within these windows, there were venetian blinds which shared the same size with the exact shutters in order to simulate the ventilation effect of the shutters. The EnergyPlus software had three models that simulated the solar energy electricity generation system, which are Simple

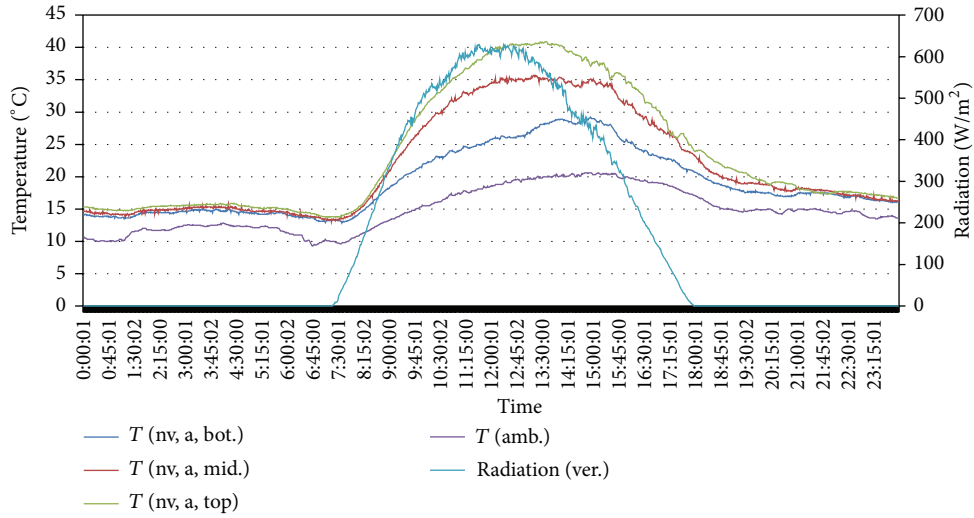


FIGURE 8: The temperature of different points (air gap in vertical direction) of the nonventilated PV wall under the typical sunshine condition.

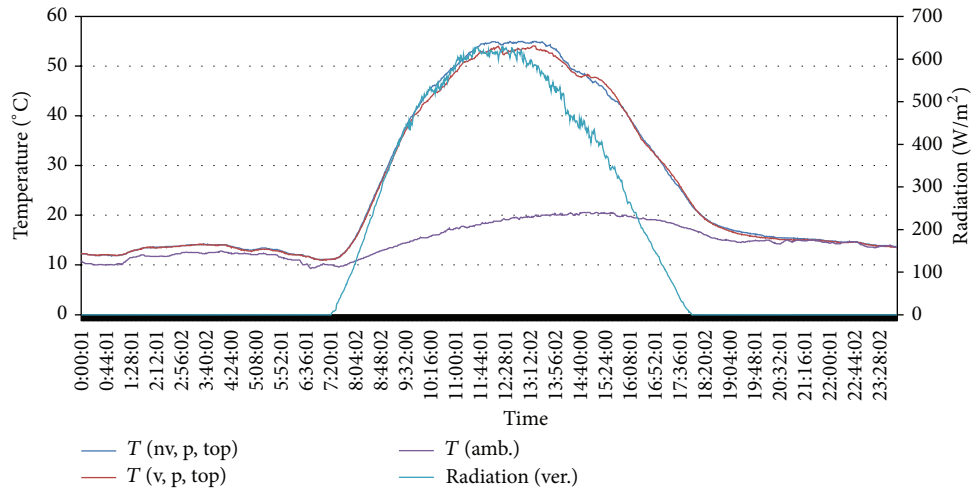


FIGURE 9: The panel temperature comparison at the top of nonventilated PV wall and ventilated PV wall.

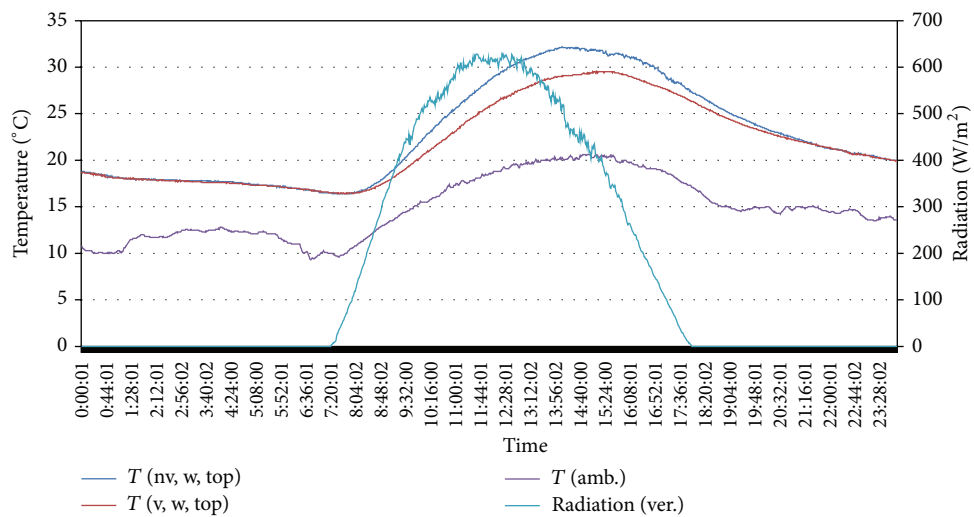


FIGURE 10: The outer wall temperature comparison at the top of nonventilated PV wall and ventilated PV wall.

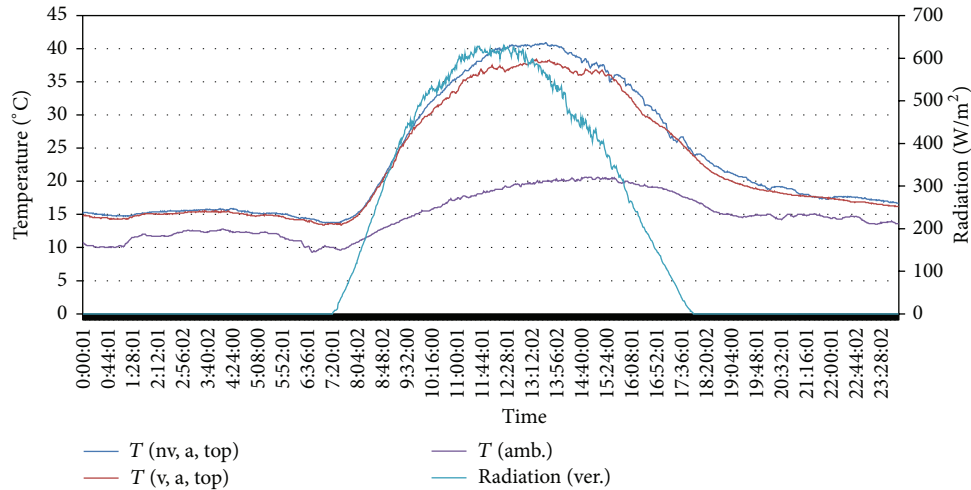


FIGURE 11: The air gap temperature comparison at the top of nonventilated PV wall and ventilated PV wall.

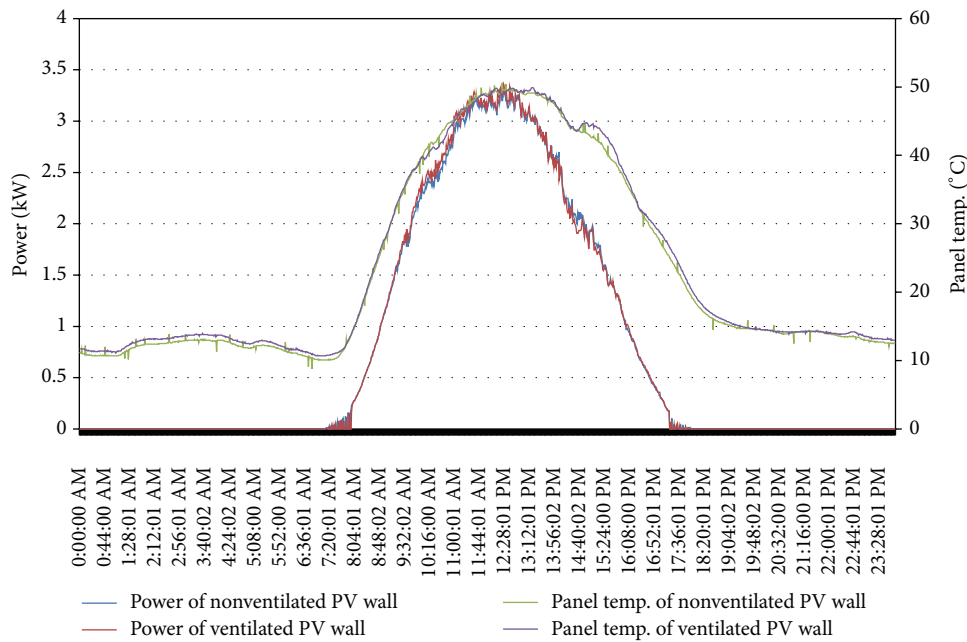


FIGURE 12: The comparison of the relations between output power and panel temperature of nonventilated PV wall and ventilated PV wall.

Model, Equivalent Diode Circuit Model, and Sandia Model. The Comparison among these three revealed that Sandia PV Model had the best effect of simulating the a-Si PV walls. Therefore, this research adopted the Sandia PV Model to simulate the dynamic electricity generation capacity of the PV walls. A plenty of the parameters used in the model were from the special indoor and outdoor tests over the same a-Si PV modules in order to guarantee the accuracy of the simulation. In an attempt to investigate the influence of the air gaps on the PV module temperature and the indoor heat transmission volumes, the Airflow Network Model in the EnergyPlus was adopted to simulate the air flow and the heat transfer features between the PV walls and normal walls.

5.2. Model Verification. In order to verify the accuracy of the model, some key parameters like the solar radiation, operating temperature of the components, wall surface temperature, and system direct-current output power would be verified through experiment. The experiment was conducted from 18th to 25th of January of 2014 (8 days in total). To simulate the solar radiation at each time point was the first step as well as the most important step for the entire simulation, as it may determine the electricity generation capacity simulation of the PV walls and their influence on the indoor air conditioning load.

Figure 14 showed the comparison between simulated solar radiation from the south and the measured value.

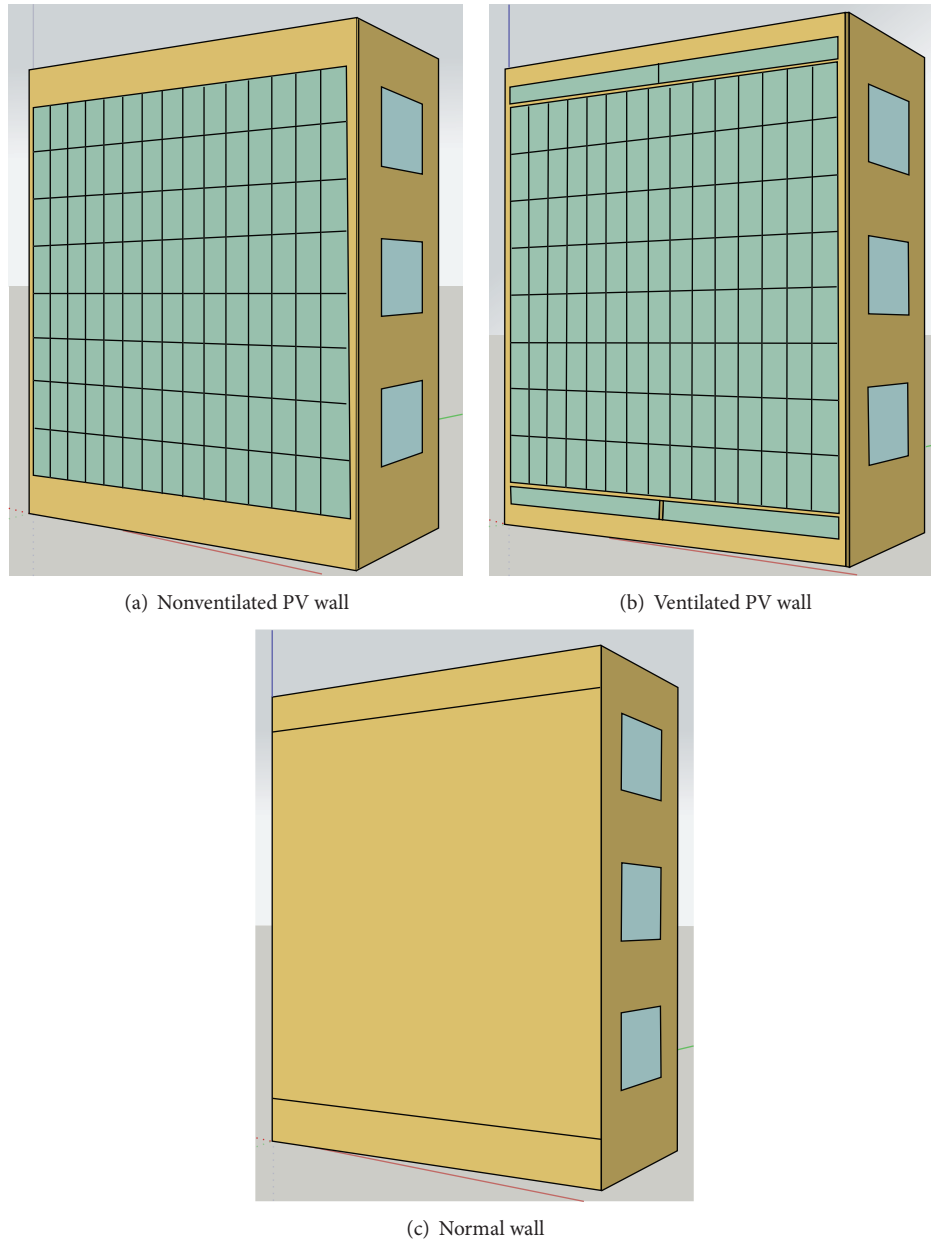


FIGURE 13: Schematic of simulation models with three different wall structures.

It is easy to discover that the simulated values were higher than the exact measure value in the noon of the fine day. However, the errors fell into the acceptable range. In overcast days, the simulated values were perfectly identical with the exact number.

Figure 15 showed the comparison between the simulated direct-current electricity generation capacity and the measured value, which revealed that the simulated values were comparatively identical with the measurements with errors less than 4.4%. It indicated that the Sandia PV Model used in this research could be the accurate simulation system for dynamic electricity generation power.

The temperature of the internal walls of the PV walls directly determined the indoor heat transmission volumes.

Therefore, this research also conducted the experiment to verify the simulated results.

Figure 16 showed the verification result of the outer wall simulated surface temperature of the ventilated PV wall, which suggested that, in most of time, the simulated surface temperature was consistent with the exact number. However, in some specific fine days, the temperature disparities were a little bit large. But even the largest temperature disparity was less than 3°C , which was acceptable.

The operating temperature of the PV modules could directly determine the energy output of the PV walls. Figure 17 shows the comparison between the simulated panel temperatures of the PV modules and the exact numbers. Through this experiment, it is easy to discover that

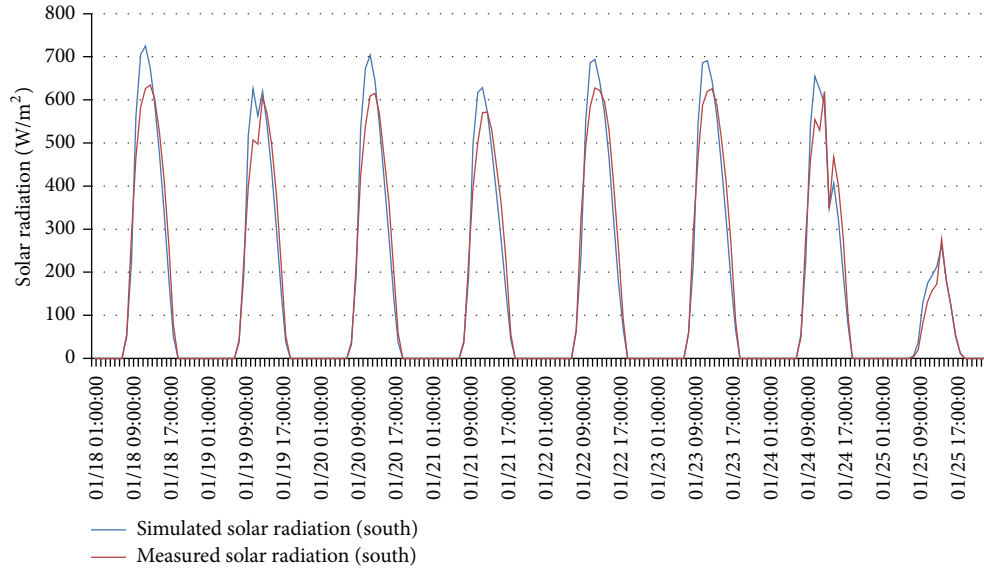


FIGURE 14: Comparison between the simulated solar radiation from the south and the measured value within the experiment days.

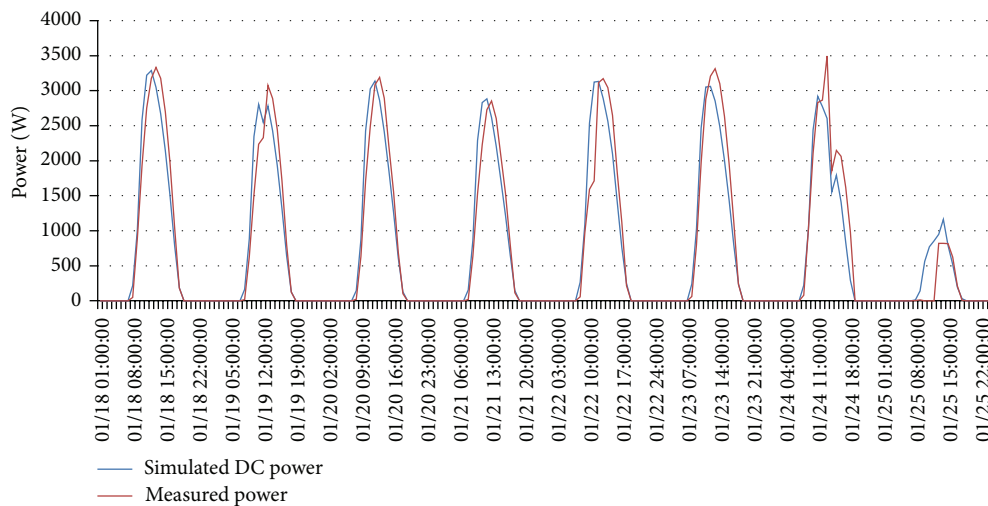


FIGURE 15: Comparison between the simulated electricity generation power and the measured value within the experiment days.

the simulated temperatures were generally lower than the exact ones. The largest temperature disparity was 5°C . However, due to the small power temperature coefficient of the a-Si PV modules which was generally $-0.25\%/^{\circ}\text{C}$, the influence over the electricity generation capacity of the PV system was controlled to be about -1% despite of the large temperature disparity at some times. This simulated temperature was also acceptable.

6. Simulation Result Analysis

6.1. The Comparison of Annual Electricity Generation Capacities. Figure 18 showed the annual electricity generation capacities of the simulated nonventilated PV wall model and the ventilated PV wall. According to Figure 18, the verified nonventilated PV wall model and the ventilated PV wall

model simulated the electricity generation capacities of the two PV systems. From Figure 18, it is easy to find that the electricity generation capacity of the ventilated PV wall model was slightly higher than that of the nonventilated PV wall model. The disparity between the capacities of these two models was expanded from January to October in every year, probably by 0.5% to 0.7%. The disparity was increased by 0.1%-0.2% in other months. The simulated results were as follows: the annual electricity generation capacity of the nonventilated PV wall model was about 2512.23 kWh while that of the ventilated PV wall model was 2522.64 kWh. The observed disparity was 10.41 kWh, which was about 0.41%.

6.2. The Comparison of Heat Gain and Building Energy Consumption with Different Structure Walls. In Zhuhai, May 1 to October 31 is the cooling season. Figure 19 displayed

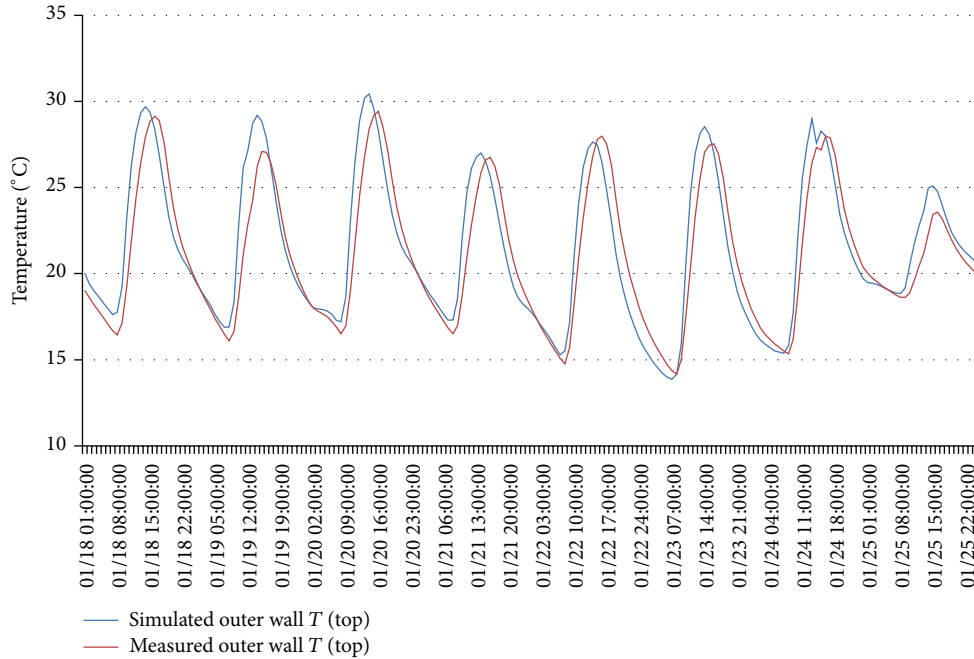


FIGURE 16: The comparison between the simulated outer wall surface temperature of the ventilated PV wall and the measured value within the experiment days.

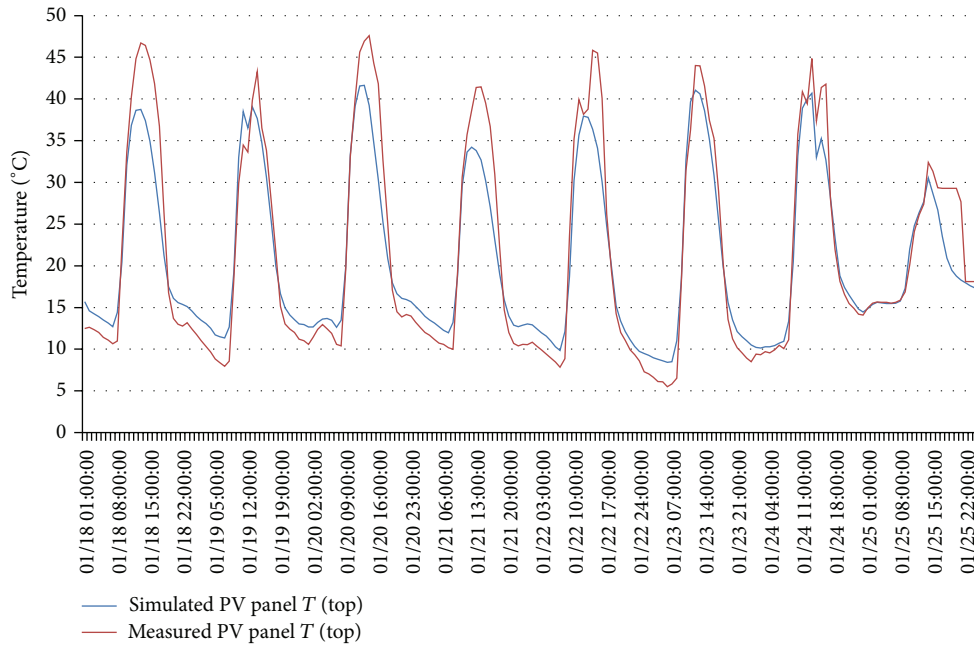


FIGURE 17: The comparison between the simulated panel temperature of the ventilated PV walls and measured value within the experiment days.

the conduction heat gain rate simulated of the nonventilated PV wall, ventilated PV wall, and normal wall during this period. Obviously, the heat gain of the nonventilated PV wall was larger than the ventilated one, especially from the end of September to the end of October. As Table 3 shows, Energy

consumption for cooling of ventilated PV wall model is lower than that of nonventilated PV wall model by 6.03 kWh/m^2 in summer.

Compared with the other two PV walls, the heat gain of the normal wall (7.56 kWh/m^2) was actually 3.71 kWh/m^2 less

TABLE 3: Comparison of the annual building heating and cooling energy consumption between different models.

Energy	Nonventilated PV wall model		Ventilated PV wall model		Normal wall model	
	Heating	Cooling	Heating	Cooling	Heating	Cooling
Electricity (kWh/m ²)	0	333.57	0	327.54	0	326.09
Natural gas (MJ/m ²)	35.65	0	43.04	0	51.30	0
Total (MJ/m ²)	1236.52		1222.17		1225.21	

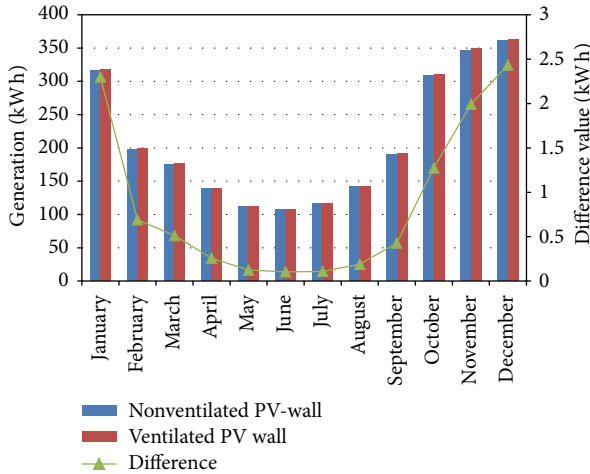


FIGURE 18: The comparison of annual electricity generation capacities month by month between nonventilated PV wall and ventilated PV wall with simulation.

than the nonventilated PV wall and 0.68 kWh/m² less than the ventilated one within 6 months; that means the two PV walls increased building cooling load instead.

Similarly, as shown in Table 3, according to the simulation result, the energy consumption of normal wall model for cooling is lower than the two PV wall models by 7.49 kWh/m² and 1.45 kWh/m², respectively.

There are two possible reasons for this result: on the one hand direct sun cannot shine on the south-facing wall for a long time in summer because of the local low latitude in Zhuhai; meanwhile due to the convective heat transfer effects between the normal wall and ambient air, the surface temperature is lower than PV wall for most of the daytime; another reason is probably that the absorption rate of normal wall is relatively lower, while that of the PV module is higher and regardless of whether the air gap is open to outer atmosphere, the heat in the air gap generated by PV panel cannot be effectively taken away but transmitted into the room through the wall. Specifically for the two PV curtain walls studied in this paper, the ratio of the height of PV wall (i.e., the length of the flow channel) to the thickness of air space (i.e., the distance between PV modules and walls) is much larger than such length to thickness ratio in the experimental apparatus used in laboratory experiments; meanwhile, in the practical engineering, there lay the structural support and electric power circuit in the air space, which will obstruct the air flow of the air layer and thus cannot achieve good ventilation and heat dissipation.

As shown in Figure 20, in winter (from November 1 to April 30 next year), the conduction heat loss rate of the normal wall (17.69 kWh/m²) is obviously larger than that of the ventilated PV wall by 1.75 kWh/m² and nonventilated PV wall by 7.09 kWh/m², respectively, which means that ranking of the building heat load in winter conditions for the three models was nonventilated PV wall, ventilated PV wall, and normal wall in descending order. The energy consumption in winter of the three models is shown in Table 3, which follows the same order as above.

According to Table 3 and comparison of these three models, ventilated PV wall model with normal wall model are similar at the annual total energy consumption of heating and cooling but slightly better than that of nonventilated PV wall model.

6.3. The Optimum Design Scheme and Operation Strategies with Different Structure Walls. Based on the above simulation results, some optimum design scheme and operation strategies for PV walls are proposed as follows.

- (1) During the scheme design phase, deciding whether to adopt south-facing PV wall, it is necessary to estimate the impact on indoor cooling and heating load considering the latitude with different solar elevation angle.
- (2) If we decide to adopt the south-facing PV wall, during the summer, the air gap between PV modules and walls may be ventilated, and the length to thickness ratio should be optimum designed to facilitate the air gap heat dissipation, to enable reduction indoor cooling load.
- (3) And during the winter, the air gap may be nonventilated to reduce building heat loss.
- (4) If there is only one status of the openings, the air gap ventilated or nonventilated can be decided by the annual cooling load and heating load.

7. Conclusions

Based on the above analysis of experimental and simulation results, the following conclusions can be drawn.

- (1) In the typical sunshine condition, compared to the air gap of nonventilated PV wall, the air gap of the ventilated PV wall will be easier compared to cooling the PV panel and make the temperature lower than that of the nonventilated PV wall. As a result, the influence of the temperature rise of the

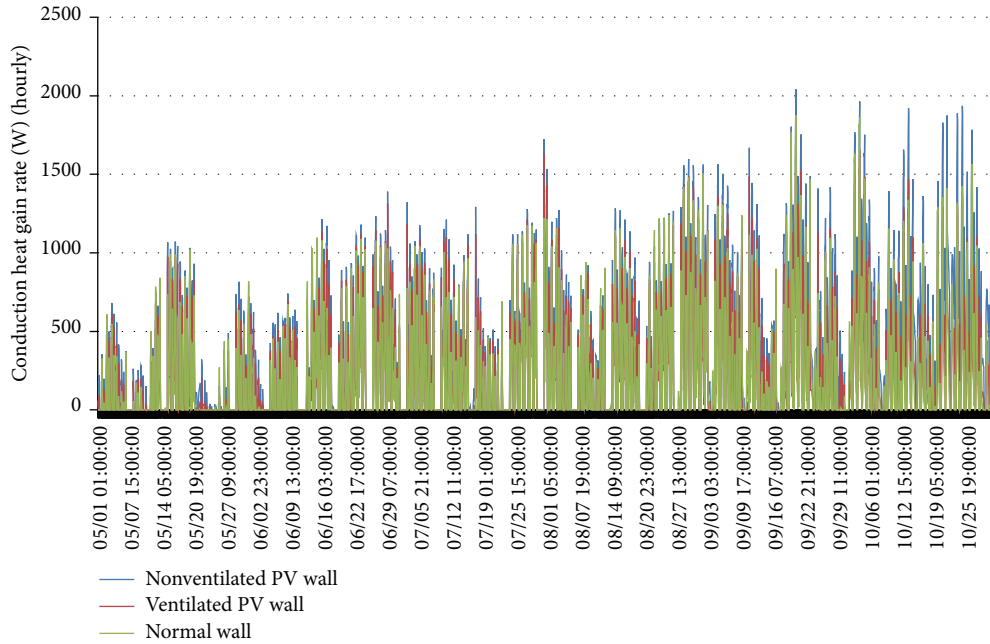


FIGURE 19: The comparison of the conduction heat gain rate between the nonventilated PV wall and the ventilated PV wall by simulation in summer.

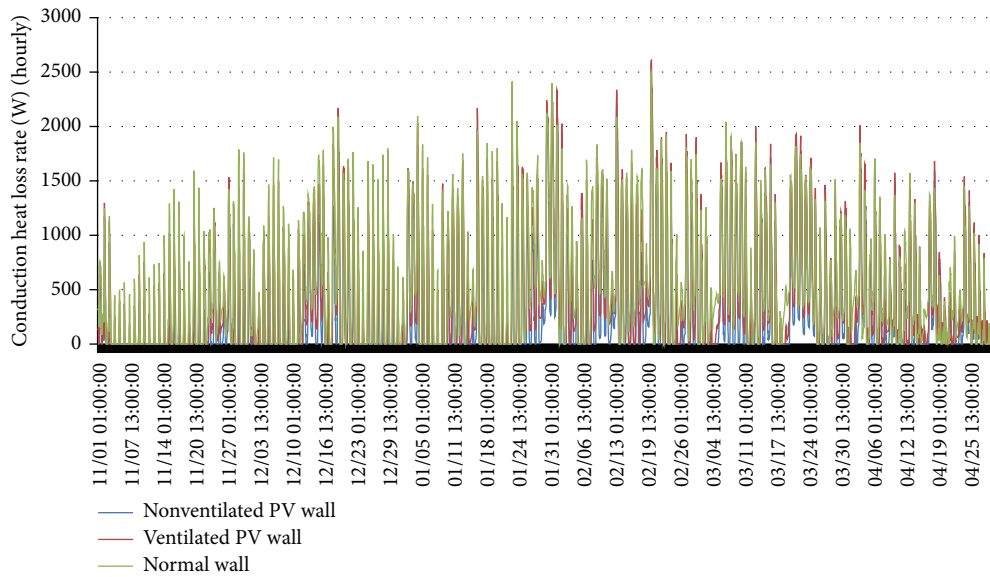


FIGURE 20: Comparison of the conduction heat loss rate between nonventilated PV wall and ventilated PV wall by simulation in winter.

PV panel on the electricity generation efficiency of the PV module would be dropped off while the PV conversion efficiency can be improved. However, in this study because the panel temperature difference of the two PV walls is small, the phenomenon is not obvious.

(2) At low latitudes similar to Zhuhai, China, in the building with south-facing PV wall compared to the one with normal wall, there is no obvious energy efficiency from the annual energy consumption of

air conditioning, and if the air gap ventilation is ineffective, the cooling load of the building with PV wall will be higher than that of building with normal wall.

(3) At low latitudes similar to Zhuhai, China, in the design and construction of PV walls, we need to consider the length to thickness ratio of the air gap, which may influence the cooling effect of the PV panel.

Nomenclature

Abbreviations

a-Si:	Amorphous silicon
BAPV:	Building-attached photovoltaics
BIPV:	Building-integrated photovoltaics
DC:	Direct current
PV module:	Photovoltaic module
PV wall:	Photovoltaic wall.

Symbols

T: Temperature ($^{\circ}\text{C}$).

Subscripts

a:	Air gap
amb.:	Ambient
p:	Photovoltaic panel
bot.:	At the bottom of the photovoltaic wall
mid.:	At the middle of the photovoltaic wall
nv:	Nonventilated PV wall
top:	At the top of the photovoltaic wall
v:	Ventilated PV wall.

Conflict of Interests

The authors declare that they have no financial and personal relationships with other people or organizations that can inappropriately influence their work. There are no professional or other personal interests of any nature or kind in any product, service, and/or company that could be construed as influencing the position presented in, or the review of, the paper.

Acknowledgment

This research was financially supported by the 12th Five-Year National Science & Technology Support Program—Novel Technology of Comprehensive Utilization of Solar Energy (no. 2012BAA10B02).

References

- [1] J. Q. Peng and L. Lu, "Investigation on the development potential of rooftop PV system in Hong Kong and its environmental benefits," *Renewable & Sustainable Energy Reviews*, vol. 27, pp. 149–162, 2013.
- [2] T. T. Chow, K. F. Fong, W. He, Z. Lin, and A. L. S. Chan, "Performance evaluation of a PV ventilated window applying to office building of Hong Kong," *Energy and Buildings*, vol. 39, no. 6, pp. 643–650, 2007.
- [3] C. H. Peng, Y. Huang, and Z. S. Wu, "Building-integrated photovoltaics (BIPV) in architectural design in China," *Energy and Buildings*, vol. 43, no. 12, pp. 3592–3598, 2011.
- [4] D. Infield, L. Mei, and U. Eicker, "Thermal performance estimation for ventilated PV façades," *Solar Energy*, vol. 76, no. 1–3, pp. 93–98, 2004.
- [5] J. Q. Peng, L. Lu, H. X. Yang, and J. Han, "Investigation on the annual thermal performance of a photovoltaic wall mounted on a multi-layer façade," *Applied Energy*, vol. 112, pp. 646–656, 2013.
- [6] J. Peng, L. Lu, and H. Yang, "An experimental study of the thermal performance of a novel photovoltaic double-skin facade in Hong Kong," *Solar Energy*, vol. 97, pp. 293–304, 2013.
- [7] W. He, Y. X. Zhang, W. Sun, J. X. Hou, Q. Y. Jiang, and J. Ji, "Experimental and numerical investigation on the performance of amorphous silicon photovoltaics window in East China," *Building and Environment*, vol. 46, no. 2, pp. 363–369, 2011.
- [8] Y. Wang, W. Tian, J. Ren, L. Zhu, and Q. Wang, "Influence of a building's integrated-photovoltaics on heating and cooling loads," *Applied Energy*, vol. 83, no. 9, pp. 989–1003, 2006.
- [9] K. E. Park, G. H. Kang, H. I. Kim, G. J. Yu, and J. T. Kim, "Analysis of thermal and electrical performance of semi-transparent photovoltaic (PV) module," *Energy*, vol. 35, no. 6, pp. 2681–2687, 2010.
- [10] H. Radhi, "Energy analysis of façade-integrated photovoltaic systems applied to UAE commercial buildings," *Solar Energy*, vol. 84, no. 12, pp. 2009–2021, 2010.
- [11] G. Y. Yun, M. McEvoy, and K. Steemers, "Design and overall energy performance of a ventilated photovoltaic façade," *Solar Energy*, vol. 81, no. 3, pp. 383–394, 2007.
- [12] H. X. Yang, R. H. Marshall, and B. J. Brinkworth, "Validated simulation for thermal regulation of photovoltaic wall structures," in *Proceedings of the 25th IEEE Photovoltaic Specialists Conference*, May 1996.
- [13] J. Jie, H. Wei, and H. N. Lam, "The annual analysis of the power output and heat gain of a PV-wall with different integration mode in Hong Kong," *Solar Energy Materials and Solar Cells*, vol. 71, no. 4, pp. 435–448, 2002.
- [14] J. Jie, Y. Hua, H. Wei, P. Gang, L. Jianping, and J. Bin, "Modeling of a novel Trombe wall with PV cells," *Building and Environment*, vol. 42, no. 3, pp. 1544–1552, 2007.
- [15] J. Jie, Y. Hua, P. Gang, and L. Jianping, "Study of PV-Trombe wall installed in a fenestrated room with heat storage," *Applied Thermal Engineering*, vol. 27, no. 8–9, pp. 1507–1515, 2007.
- [16] Z. Zhu, H. Yang, R. Jiang, and Q. Wu, "Study on conjugate heat transfer in a photovoltaic wall," *Acta Energetica Solaris Sinica*, vol. 23, no. 1, pp. 49–54, 2002 (Chinese).

Review Article

Integrating Photovoltaic Systems in Power System: Power Quality Impacts and Optimal Planning Challenges

Aida Fazliana Abdul Kadir,¹ Tamer Khatib,² and Wilfried Elmenreich²

¹ *Industrial Power Engineering, Faculty of Electrical Engineering, Universiti Teknikal Malaysia Melaka, 75300 Melaka, Malaysia*

² *Institute of Networked & Embedded Systems/Lakeside Labs, Alpen-Adria-Universität Klagenfurt, 9020 Klagenfurt, Austria*

Correspondence should be addressed to Tamer Khatib; tamer_khat@hotmail.com

Received 2 May 2014; Accepted 7 August 2014; Published 17 August 2014

Academic Editor: Hui Shen

Copyright © 2014 Aida Fazliana Abdul Kadir et al. This is an open access article distributed under the Creative Commons Attribution License, which permits unrestricted use, distribution, and reproduction in any medium, provided the original work is properly cited.

This paper is an overview of some of the main issues in photovoltaic based distributed generation (PVDG). A discussion of the harmonic distortion produced by PVDG units is presented. The maximum permissible penetration level of PVDG in distribution system is also considered. The general procedures of optimal planning for PVDG placement and sizing are also explained in this paper. The result of this review shows that there are different challenges for integrating PVDG in the power systems. One of these challenges is integrated system reliability whereas the amount of power produced by renewable energy source is consistent. Thus, the high penetration of PVDG into grid can decrease the reliability of the power system network. On the other hand, power quality is considered one of the challenges of PVDG whereas the high penetration of PVDGs can lead to more harmonic propagation into the power system network. In addition to that, voltage fluctuation of the integrated PVDG and reverse power flow are two important challenges to this technology. Finally, protection of power system with integrated PVDG is one of the most critical challenges to this technology as the current protection schemes are designed for unidirectional not bidirectional power flow pattern.

1. Introduction

The growing power demand has increased electrical energy production almost to its capacity limit. However, power utilities must maintain reserve margins of existing power generation at a sufficient level. Currently, transmission systems are reaching their maximum capacity because of the huge amount of power to be transferred. Therefore, power utilities have to invest a lot of money to expand their facilities to meet the growing power demand and to provide uninterrupted power supply to industrial and commercial customers [1]. The introduction of photovoltaic based distributed generation units in the distribution system may lead to several benefits such as voltage support, improved power quality, loss reduction, deferment of new or upgraded transmission and distribution infrastructure, and improved utility system reliability [2]. PVDG is a grid-connected generation located near consumers regardless of its power capacity [3], is an alternative way to support power demand and overcome congested transmission lines.

The integration of PVDG into a distribution system will have either positive or negative impact depending on the distribution system operating features and the PVDG characteristics. PVDG can be valuable if it meets at least the basic requirements of the system operating perspective and feeder design [4]. According to [5], the effect of PVDG on power quality depends on its interface with the utility system, the size of DG unit, the total capacity of the PVDG relative to the system, the size of generation relative to load at the interconnection point, and the feeder voltage regulation practice [6].

Figure 1 shows a schematic diagram of a grid-connected PV system which typically consists of a PV array, a DC link capacitor, an inverter with filter, a step-up transformer, and a power grid [5]. The DC power generated from the PV array charges the DC link capacitor. The inverter converts the DC power into AC power, which has a sinusoidal voltage and frequency similar to the utility grid. The diode blocks the reverse current flow through the PV array. The transformer steps up the inverter voltage to the nominal value of the grid

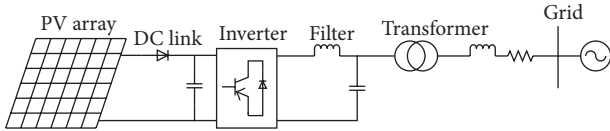


FIGURE 1: Schematic diagram of a grid-connected PV system.

voltage and provides electrical isolation between the PV system and the grid. The harmonic filter eliminates the harmonic components other than the fundamental electrical frequency.

One of the growing power quality concerns that degrade the performance of power systems is harmonic distortion. The main causes of harmonic distortion are due to the proliferation of power electronic devices like computer, television, energy saving lamps, adjustable-speed drives, arc furnaces, and power converters. Harmonic distortion is also caused by nonlinearity of equipment such as transformer and rotating machines [7]. These harmonic currents may create greater losses in the loads which consecutively require derating of the load, overheating of neutral conductor, overheating of transformer, and malfunction of protective devices [8]. Another power quality problem arises at the interface between PVDG inverters and the grid is harmonic resonance phenomenon. Harmonic resonance phenomena will occur at a resonant frequency where the inductive component is equal to the capacitive component. Harmonic resonance which has been found to be an increasingly common problem at the interface between PVDG inverters and the grid depends on the number of PVDG units. The effect of harmonic resonance not only presents a severe power quality problem but also can trip protection devices and cause damage to sensitive equipment [9].

On the other hand, it is well known that PVDG needs to be installed at the distribution system level of the electric grid and located close to the load centre. Studies are usually conducted to evaluate the impact of PVDG on harmonic distortion, power loss, voltage profile, short circuit current, and power system reliability before placing it in a distribution system. To reduce power losses, improve system voltage, and minimize voltage total harmonic distortion (THD_v), appropriate planning of power system with the presence of DG is required. Several considerations need to be taken into account such as the number and the capacity of the PVDG units, the optimal PVDG location, and the type of network connection. The installation of PVDG units at nonoptimal locations and with nonoptimal sizes may cause higher power loss, voltage fluctuation problem, system instability, and amplification of operational cost [10].

2. Power Quality Impact of PVDG

The integration of PVDG in power systems can alleviate overloading in transmission lines, provide peak shaving, and support the general grid requirement. However, improper coordination, location, and installation of PVDG may affect

the power quality of power systems [11]. Most conventional power systems are designed and operated such that generating stations are far from the load centers and use the transmission and distribution system as pathways. The normal operation of a typical power system does not include generation in the distribution network or in the customer side of the system. However, the integration of PVDG in distribution systems changes the normal operation of power systems and poses several problems which include possible bi-directional power flow, voltage variation, breaker noncoordination, alteration in the short circuit levels, and islanding operation [2, 6]. Therefore, studies are required to address the technical challenges caused by DG integration in distribution systems. The interconnection device between the DG and the grid must be planned and coordinated before connecting any DG [12].

2.1. Harmonic Impact of PVDG. Harmonic is a sinusoidal component of a periodic wave or a quantity which has a frequency that is an integral multiple of the fundamental frequency [13]. Harmonic distortion is caused by the nonlinearity of equipment such as power converters, transformer, rotating machines, arc furnaces, and fluorescent lighting [7]. PVDG connected to a distribution system may introduce harmonic distortion in the system depending on the power converter technology. A power quality study was performed on a PV system to estimate the effect of inverter-interfaced PVDG on the quality of electric power [14]. The experimental results indicate that the values of total harmonic distortion THD_i depend on the output power of the inverter. This dependence decreases proportionally with reduced power converter rating.

Another factor that influences harmonic distortion in a power system is the number of PVDG units connected to the power system. The interaction between grid components and a group of PVDG units can amplify harmonic distortion [15]. In addition, PVDG placement also contributes to harmonic distortion levels in a power system. DG placement at higher voltage circuit produces less harmonic distortion compared with PVDG placement at low voltage level [16]. On the customer side, the increasing use of harmonic-producing equipment such as adjustable speed drives may create problems, such as greater propagation of harmonics in the system, shortened lifetime of electronic equipment, and motor and wiring overheating. In addition, harmonics can flow back to the supply line and affect other customers at the PCC. Therefore, harmonic mitigation strategies for power systems must be measured, analyzed, and identified [1].

2.2. Harmonic Resonance in a Power System with PVDG. Resonance occurs in a power system when the capacitive elements of the system become exactly equal to the inductive elements at a particular frequency. Depending on the parallel or series operation, it may form parallel or series resonance. At a given location, when a system forms a parallel resonance, it exhibits high network impedance, whereas for a series resonance, it presents a low network impedance path [17].

With increasing PVDG penetration in the power grid, harmonic resonance is becoming a crucial issue in power systems [18]. Harmonic resonance can occur at the interconnection point of individual or multiple PVDG units to the grid because of impedance mismatch between the grid and the inverters. Dynamic interaction between grid and inverter output impedance can lead to harmonic resonance in grid current and/or voltage which occurs at certain frequencies. The effect of harmonic resonance presents severe power quality problems such as tripping of protection devices and damage to sensitive equipment because of overvoltage or overcurrent [18].

A study investigated the harmonic interaction between multiple PVDG units and a distributed network and found that high penetration levels of PVDG units increase harmonic emission significantly even though the PV inverters each meet IEC 61000-3-2 specifications. Parallel and series resonance phenomena between the network and PV inverters were found to be responsible for unexpected high current and voltage distortion levels in the network [19].

2.3. Effect of PVDG on Voltage Variation. The operating voltages in a distribution system are not always within required voltage ranges because of load variations along the feeders, the action of tap changers of the substation transformers, and the switching of capacitor banks or reactors. This results in voltage variations, which may be defined as the deviations of a voltage from its nominal value [19]. Disturbances classified as short-duration voltage variations are voltage sag, voltage swell, and short interruption, whereas disturbances classified as long-duration voltage variations include sustained interruption, undervoltage, and overvoltage [20].

With the growing electricity demand in distribution systems, the voltage tends to drop below its tolerable operating limits along distribution feeders with the increase of loads. Thus, the distribution system infrastructure should be upgraded to solve voltage drop problems [21]. The integration of PVDG units in a distribution system can improve the voltage profile as voltage drop across feeder segments is reduced because of reduced power flow through the feeder. However, if the power generated by PVDG is greater than the local demand at the PCC, the surplus power flows back to the grid. The excess power from DG may produce reverse power flow in the feeder and may create voltage rise at the feeder [22]. Some studies investigated methods of controlling voltage rise caused by PVDG connection into distribution systems. Borges and Falcão (2006) analyzed multiple sources of PVDG together with the operation of voltage regulators and concluded that the power injected by the PVDG unit should be identified to obtain system voltages within the allowed limits at the PVDG connection bus [23]. Chen et al. (2012) presented two voltage control techniques in a distribution feeder through system planning and equipment control [24]. System planning techniques were employed in the system design and planning stages whereas equipment control techniques were used to regulate the bus voltages along a feeder during real-time operation.

With high DG penetration at low voltage level, a violation may occur in the upper voltage limit. Therefore, a solution is needed to reduce the overvoltage caused by DG. Demirok et al. (2010) addressed the overvoltage problem by applying distributed reactive power regulation and active power curtailment strategies at the DG inverters [25]. An approach for charging and discharging control of the storage system (lead-acid batteries) is applied to regulate the storage capacity effectively. An adaptive voltage control scheme which uses an on-load tap changer and automatic voltage control relay was proposed to increase the output capacity of DG without violating voltage limits [24].

3. Maximum Allowable Penetration Level of PVDG

Several studies have been conducted to investigate the impacts of high PVDG penetration in distribution systems by considering various constraints. Kirawanich and O'Connell (2003) performed a simulation to investigate the harmonic impact of a PVDG on a typical commercial distribution system [26]. The results showed that even at the most vulnerable lateral tap points in the system under worst-case conditions, the voltage THD did not exceed the IEEE Standard 519 limit for up to 40% saturation of commercial distribution system with DG units. A similar study performed by Pandi et al. (2013) concluded that the maximum PVDG penetration levels based on an optimal DG size and locations on the 18-bus and 33-bus radial distribution systems are 66.67% and 33.53%, respectively [27].

Other studies focused on the maximum allowable penetration level of DG units by considering the transient stability limit [28]. Azmy and Erlich (2005) investigated the impact of utilizing selected DG units with different penetration levels on various forms of power system stability [28]. The simulation result showed that the voltage deviation decreases significantly with 28.3% DG penetration. Moreover, it is reported that the maximum penetration level of DG, without violating the transient stability limit, is 40% of the total connected load [28].

Another factor that may limit the penetration level of DG in a typical distribution system is the steady-state voltage rise. Celli et al. (2009) developed a method for evaluating the critical value of DG penetration level by considering DG siting and sizing [29]. The result showed that the limit of the DG penetration level in a distribution system was 40% to 50%. A similar study was conducted by Chen et al. (2012) to clarify what would happen to a distribution system if customers were allowed to install DG units freely on their premises and DG units became widespread [30]. The major factor that led to overvoltage and undervoltage was the surplus DG power in localized areas of the secondary network, which caused the tripping of the network protectors.

Germany and Italy have a very strong PV system penetration. By 2012, the installed PV capacity reached 32 GW and 16 GW, respectively. More than 20% of the capacity installed is connected to the distribution voltage network. In Germany—specifically—63% of the PVDG is connected

to the household voltage level. The integration of this big amount of PVDG makes challenges to the power system. For example, in case of have a large share of PVDG units that switch off simultaneously may increase the grid frequency up to 50.2 Hz. However, this problem has been addressed in Germany by requiring the back-fitting of installations with a nominal power above 10 kW. In addition to that, voltage regulation within tolerable limits is another challenge faced. Storage has been identified as a possible solution for providing flexibility to the power system and could possibly generate value streams from flexibility. However the feasibility of such a solution is remains challenging. A number of authors assess how storage could overcome the technical challenges of PV integration. For example, the battery can be optimally sized in order to avoid overvoltage caused inverter disconnection [31–36].

4. Optimal Placement and Sizing of PVDG

Voltage variation and harmonic distortion are two major disturbances in distribution systems. The voltage drop occurs because of increasing electricity demand, thereby indicating the need to upgrade the distribution system infrastructure. Studies have indicated that approximately 13% of the generated power is consumed as losses at the distribution level [37]. To mitigate voltage variation and harmonic distortion in distribution systems, several strategies were applied, such as the use of passive and active power filters to mitigate harmonic distortion and the application of custom power controllers to mitigate voltage variation problems. However, these mitigation strategies require investment. Therefore, to improve voltage profile and eliminate harmonic distortion in a distribution system with PVDG, a noninvasive method is proposed, which involves appropriate planning of PVDG units and determining optimal placement and sizing of PVDG units.

Before installing PVDG units in a distribution system, a feasibility analysis has to be performed. PVDG owners are requested to present the type, size, and location of their PVDG [27]. The power system is usually affected by the installation of PVDG. Therefore, the allowable PVDG penetration level must comply with the harmonic limits. Thus, optimal placement and sizing of DG is important because installation of DG units at optimal places and with optimal sizes can provide economic, environmental, and technical advantages such as power losses reduction, power quality enhancement, system stability, and lower operational cost [11].

Several methods have been applied to determine the optimal location and size of PVDG in a distribution system. The analytical method used for optimal PVDG placement and sizing is only accurate for the model developed, and it can be very complicated for solving complex systems. The power flow algorithm [10] has been used to find the optimum PVDG size at each load bus by assuming that each load bus can have a PVDG unit. However, this method is ineffective because it requires a large number of load flow computations. Analytical methods can also be used to place the PVDG

in radial or meshed systems [38]. In this method, separate expressions for radial and meshed systems are required, and complex procedures based on the phasor current are applied to solve the PVDG placement problem. However, this method only determines the optimum PVDG placement and not the optimum PVDG size as it considers a fixed PVDG size.

The metaheuristic method is also used in optimal placement and sizing of DG in distribution systems. This method applies an iterative generation process which can act as a lead for its subordinate heuristics to find the optimal or near-optimal solutions of the optimization problem [39]. It combines different concepts derived from artificial intelligence to improve performance. Some of the techniques that adopt metaheuristics concepts include genetic algorithm (GA), Tabu search, particle swarm optimization (PSO), ant colony optimization (ACO), and gravitational search algorithm (GSA).

The implementation of the general optimization technique for solving the optimal placement and sizing of PVDG problem is depicted in Figure 2. A multiobjective function is formulated to minimize the total losses, average total voltage harmonic distortion, (THD_v) and voltage deviation in a distribution system. The procedures for implementing the general optimization algorithm for determining optimal placement and sizing of PVDG are described as follows.

- (i) Obtain the input network information such as bus, line, and generator data.
- (ii) Randomly generate initial positions within feasible solution combination, such as the PVDG location, PVDG size in the range of 40% to 50% of the total connected loads, and PVDG controllable bus voltage in the range of 0.98 p.u to 1.02 p.u.
- (iii) Improve the optimization algorithm using the optimal parameters such as population size, number of dimension, and maximum iteration.
- (iv) Run loadflow and harmonic loadflow to obtain the total power loss, average THD_v and voltage deviation.
- (v) Calculate the fitness function.
- (vi) Check the bus voltage magnitude and THD_v constraints. If both exceed their limits, repeat step (iv).
- (vii) Update the optimization parameters.
- (viii) Repeat the process until the stopping criteria are achieved and the best solution is obtained.

5. Conclusion

This paper describes an overview of the relevant aspects related to PVDG and the impacts it might have on the distribution system. This paper evolves the background of PVDG and its impacts on power quality and the maximum allowable penetration level of PVDG connected to a distribution system. The implementation of the general optimization technique for solving the optimal placement and sizing of PVDG problem with multiobjective functions

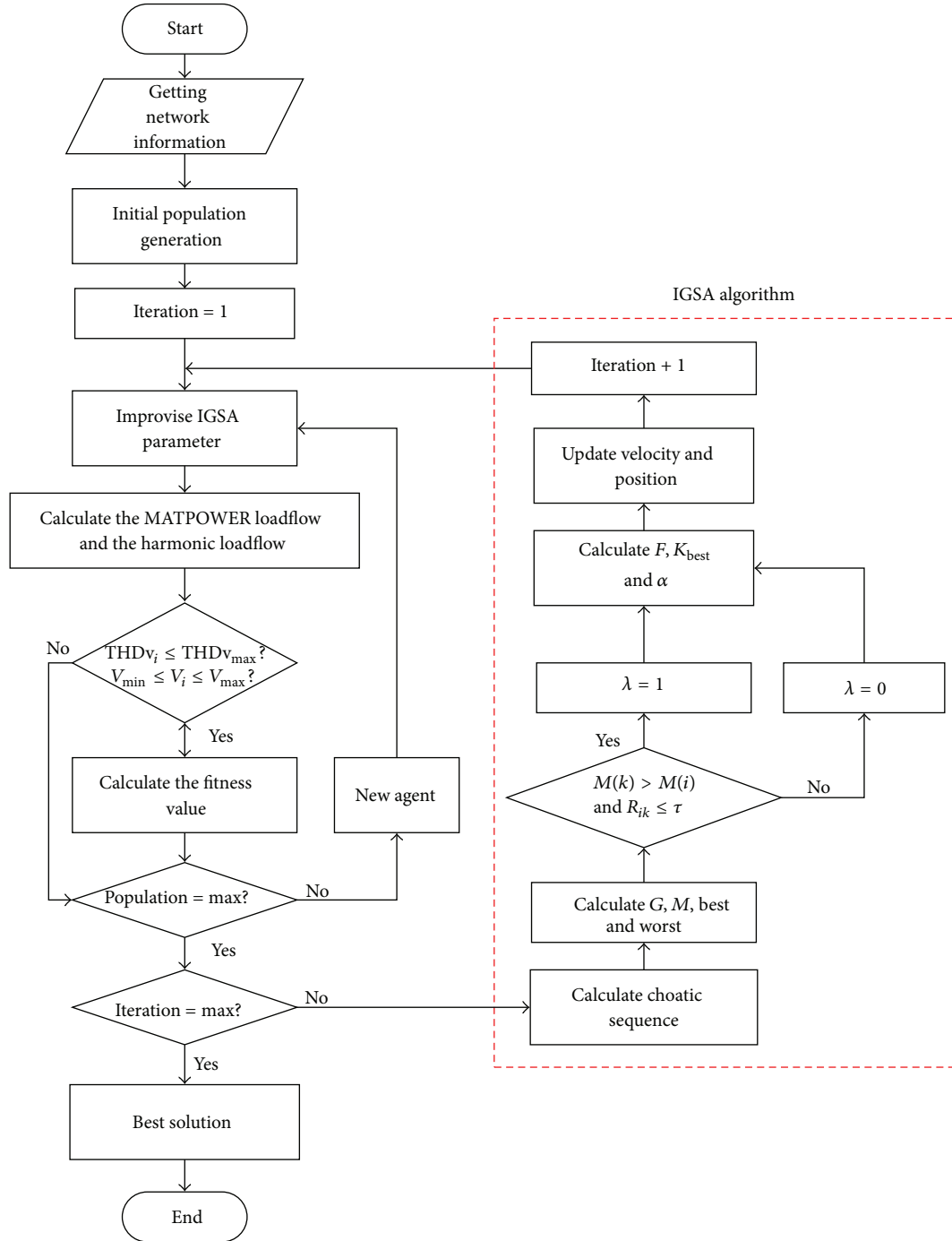


FIGURE 2: Flowchart of the general optimization technique for determining optimal placement and sizing of PVDG in a distribution system.

such as minimization of losses, THDv, and voltage deviation is explained. The multiobjective functions are considered as the technical benefits factors for optimal planning PVDG in the distribution system. It is concluded that there are great opportunities and benefits such as technical, economical, and environmental benefits are offered when installing PVDG in a distribution system. However, there are some technical issues and challenges come up when incorporating PVDG in a distribution system. These issues and challenges concluded

by several researchers need to be assessed for proper PVDG planning and operation in the distribution network. These issues are as follows.

- (i) **Reliability:** the amount of power produced by renewable energy source based PVDG is not consistent like wind and solar source. Thus, the high penetration of PVDG into grid can decrease the reliability of the power system network.

- (ii) Power quality: the high penetration of PVDGs can lead to more harmonic propagation into the power system network, increase the losses, and possibly decrease the equipment life time.
- (iii) Voltage fluctuation: it is a significant issue for high penetration level of PVDG. This issue desires to be critically considered in integrate inconsistent sources. For example, the fluctuation of solar source in supplying power to the load will caused overvoltage or undervoltage. The voltage fluctuation is very bad impact on the sensitive equipment.
- (iv) Reverse powerflow: incorporating PVDG in the system causes malfunctions of protection systems as they are configured by the unidirectional form.
- (v) System frequency: the unbalances between supply and demand will result to the deviations from the system nominal frequency. The high penetration of PVDG affects system frequency and makes the process of control more complicated.
- (vi) Protection schemes: the common distribution networks are configured in the radial form. Thus, the protections system is designed accordingly to the unidirectional flow patterns. However, the integrating of PVDG changes the flow into bidirectional and needs additional safety equipment and resizing of the network such as grounding, short-circuit, breaking capacity, and supervisory control and data acquisition (SCADA) systems.
- (vii) Islanding protection: anti-islanding protection schemes presently implement the PVDGs to remove immediately for grid faults through loss of grid (LOG) protection system. This significantly decreases the advantages of PVDG deployment. For avoiding disconnection of PVDGs during LOG, several islanding protection schemes are being developed. The biggest challenge for the islanding protection schemes is the protection coordination of distribution systems with bidirectional fault current flows.

Conflict of Interests

The authors hereby confirm that there is no conflict of interests in the paper with any third party.

Acknowledgments

This work is supported by Universiti Teknikal Malaysia Melaka under research Grant number PJP/2013/FKE (24C)/S01255. Part of the authors is supported by the research cluster Lakeside Labs funded by the European Regional Development Fund, the Carinthian Economic Promotion Fund (KWF), and the state of Austria under Grant 20214|22935|34445 (Project Smart Microgrid).

References

- [1] A. M. Borbely and J. F. Kreidel, *Distributed Generation: The Power Paradigm for the New Millennium*, CRC Press, New York, NY, USA, 2001.
- [2] P. P. Barker and R. W. de Mello, "Determining the impact of distributed generation on power systems. I. Radial distribution systems," in *Proceedings of the IEEE Power Engineering Society Summer Meeting*, vol. 3, pp. 1645–1656, Seattle, Wash, USA, 2000.
- [3] M. Z. C. Wanik, *Dynamic simulation and intelligent management of distributed generation [Ph.D. thesis]*, Duisburg-Essen University, Essen, Germany, 2011.
- [4] M. Begovic, "Sustainable energy technologies and distributed generation," in *Proceedings of the IEEE Power Engineering Society Summer Meeting*, pp. 540–545, July 2001.
- [5] P. A. Daly and J. Morrison, "Understanding the potential benefits of distributed generation on power delivery systems," in *Proceedings of the Rural Electric Power Conference*, pp. A21–A213, Little Rock, Ark, USA, May 2001.
- [6] S. Kim, J. Jeon, C. Cho, E. Kim, and J. Ahn, "Modeling and simulation of a grid-connected PV generation system for electromagnetic transient analysis," *Solar Energy*, vol. 83, no. 5, pp. 664–678, 2009.
- [7] K. W. Louie, P. Wilson, R. A. Rivas, A. Wang, and P. Buchanan, "Discussion on power system harmonic analysis in the frequency domain," in *Proceedings of the IEEE PES Transmission and Distribution Conference and Exposition: Latin America (TDC '06)*, 6, p. 1, August 2006.
- [8] "IEEE recommended practices and requirements for harmonic control in electrical power systems," IEEE Std 519-1992, IEEE, 1993.
- [9] X. Chen and J. Sun, "A study of renewable energy system harmonic resonance based on a DG test-bed," in *Proceeding of the 26th Annual IEEE Applied Power Electronics Conference and Exposition (APEC'11)*, pp. 995–1002, Fort Worth, Tex, USA, March 2011.
- [10] N. S. Rau and Y. M. Wan, "Optimum location of resources in distributed planning," *IEEE Transactions on Power Systems*, vol. 9, no. 4, pp. 2014–2020, 1994.
- [11] N. Jenkins and G. Strbac, "Effects of small embedded generation on power quality," in *Proceedings of the IEE Colloquium on Issues in Power Quality*, pp. 6/1–6/4, Coventry, UK, November 1995.
- [12] R. Saint and N. R. Friedman, "The application guide for distributed generation interconnection," in *Proceedings of the IEEE Rural Electric Power Conference*, pp. D2/1–D2/5, Colorado Springs, Colo, USA, May 2002.
- [13] IEEE, "IEEE Std. 519-1992," in *IEEE Recommended Practices and Requirements for Harmonic Control in Electrical in Electrical Power System*, IEEE, 1992.
- [14] M. Sidrach-De-Cardona and J. Carretero, "Analysis of the current total harmonic distortion for different single-phase inverters for grid-connected pv-systems," *Solar Energy Materials and Solar Cells*, vol. 87, no. 1–4, pp. 529–540, 2005.
- [15] M. C. Benhabib, J. M. A. Myrzik, and J. L. Duarte, "Harmonic effects caused by large scale PV installations in LV network," in *Proceedings of the 9th International Conference on Electrical Power Quality and Utilisation (EPQU'07)*, pp. 1–6, Barcelona, Spain, October 2007.
- [16] J. Arrillaga and N. R. Watson, *Power System Harmonics*, John Wiley & Sons, New York, NY, USA, 2003.

- [17] F. Wang, J. L. Duarte, and M. A. M. Hendrix, "Analysis of harmonic interactions between DG inverters and polluted grids," in *Proceedings of the IEEE International Energy Conference and Exhibition (EnergyCon '10)*, pp. 194–199, December 2010.
- [18] M. McGranaghan, S. Peele, and D. Murray, "Solving harmonic resonance problems on the medium voltage system," in *Proceedings of the 19th International Conference on Electricity Distribution*, pp. 1–4, 2007.
- [19] M. H. J. Bollen, "What is power quality?" *Electric Power Systems Research*, vol. 66, no. 1, pp. 5–14, 2003.
- [20] T. Chen, L. Chiang, and N. Yang, "Examination of major factors affecting voltage variation on distribution feeders," *Energy and Buildings*, vol. 55, pp. 494–499, 2012.
- [21] A. A. Eajal and M. E. El-Hawary, "Optimal capacitor placement and sizing in unbalanced distribution systems with harmonics consideration using particle swarm optimization," *IEEE Transactions on Power Delivery*, vol. 25, no. 3, pp. 1734–1741, 2010.
- [22] A. Casavola, G. Franzè, D. Menniti, and N. Sorrentino, "Voltage regulation in distribution networks in the presence of distributed generation: a voltage set-point reconfiguration approach," *Electric Power Systems Research*, vol. 81, no. 1, pp. 25–34, 2011.
- [23] C. L. T. Borges and D. M. Falcão, "Optimal distributed generation allocation for reliability, losses, and voltage improvement," *International Journal of Electrical Power and Energy Systems*, vol. 28, no. 6, pp. 413–420, 2006.
- [24] L. Chen, S. Qi, and H. Li, "Improved adaptive voltage controller for active distribution network operation with distributed generation," in *Proceedings of the 47th International Universities Power Engineering Conference (UPEC '12)*, pp. 1–5, London, UK, September 2012.
- [25] E. Demirok, D. Sera, R. Teodorescu, P. Rodriguez, and U. Borup, "Evaluation of the voltage support strategies for the low voltage grid connected PV generators," in *Proceedings of the 2nd IEEE Energy Conversion Congress and Exposition (ECCE '10)*, pp. 710–717, September 2010.
- [26] P. Kirawanich and R. M. O'Connell, "Potential harmonic impact of microturbines on a commercial power distribution system," in *Proceeding of the IEEE Power Engineering Society General Meeting*, vol. 2, July 2003.
- [27] V. R. Pandi, H. H. Zeineldin, W. Xiao, and A. F. Zobaa, "Optimal penetration levels for inverter-based distributed generation considering harmonic limits," *Electric Power Systems Research*, vol. 97, pp. 68–75, 2013.
- [28] A. M. Azmy and I. Erlich, "Impact of distributed generation on the stability of electrical power systems," in *Proceedings of the IEEE Power Engineering Society General Meeting*, pp. 1056–1063, IEEE, June 2005.
- [29] G. Celli, E. Ghiani, S. Mocci, and F. Pilo, "Multi-objective programming to maximize the penetration of distributed generation in distribution networks," in *Proceedings of the 20th International Conference and Exhibition on Electricity Distribution (CIRED '09)*, pp. 1–5, Prague, Czech Republic, June 2009.
- [30] P. Chen, R. Salcedo, Q. Zhu et al., "Analysis of voltage profile problems due to the penetration of distributed generation in low-voltage secondary distribution networks," *IEEE Transactions on Power Delivery*, vol. 27, no. 4, pp. 2020–2028, 2012.
- [31] A. Zucker and T. Hinchliffe, "Optimum sizing of PV-attached electricity storage according to power market signals—a case study for Germany and Italy," *Applied Energy*, vol. 127, pp. 141–155, 2014.
- [32] S. Chowdhury, U. Sumita, A. Islam, and I. Bedja, "Importance of policy for energy system transformation: diffusion of PV technology in Japan and Germany," *Energy Policy*, vol. 68, pp. 285–293, 2014.
- [33] J. Boemer, K. Burges, P. Zolotarev, J. Lehner, P. Wajant, and M. Fuerst, "Overview of German grid issues and retrofit of photovoltaic power plants in Germany for the prevention of frequency stability problems in abnormal system conditions of the ENTSO-E region continental Europe," in *Proceedings of the 1st International Workshop on Integration of Solar Power into Power Systems*, Aarhus, Denmark, 2011.
- [34] J. Tant, F. Geth, D. Six, P. Tant, and J. Driesen, "Multiobjective battery storage to improve PV integration in residential distribution grids," *IEEE Transactions on Sustainable Energy*, vol. 4, no. 1, pp. 182–191, 2013.
- [35] L. Hirth, "The market value of variable renewables: the effect of solar wind power variability on their relative price," *Energy Economics*, vol. 38, pp. 218–236, 2013.
- [36] A. Purvins, I. T. Papaioannou, and L. Debarberis, "Application of battery-based storage systems in household-demand smoothening in electricity-distribution grids," *Energy Conversion and Management*, vol. 65, pp. 272–284, 2013.
- [37] O. Amanifar and G. M. E. Hamedani, "Optimal distributed generation placement and sizing for loss and THD reduction and voltage profile improvement in distribution systems using Particle Swarm Optimization and sensitivity analysis," *International Journal on Technical and Physical Problems of Engineering*, vol. 3, pp. 47–53, 2011.
- [38] H. L. Willis, "Analytical methods and rules of thumb for modeling DG-distribution interaction," in *Proceedings of the IEEE Power Engineering Society Summer Meeting*, pp. 1643–1644, July 2000.
- [39] I. H. Osman and J. P. Kelly, *Meta-Heuristics: Theory and Applications*, Kluwer Academic Publishers, New York, NY, USA, 1996.

Research Article

SiO₂ Antireflection Coatings Fabricated by Electron-Beam Evaporation for Black Monocrystalline Silicon Solar Cells

Minghua Li,¹ Hui Shen,² Lin Zhuang,² Daming Chen,² and Xinghua Liang³

¹ School of Electrical Engineering, Guangdong Mechanical & Electrical College, Guangzhou 510515, China

² Institute for Solar Energy Systems, Guangdong Provincial Key Laboratory of Photovoltaic Technologies, State Key Laboratory of Optoelectronic Materials and Technologies, Sun Yat-sen University, Guangzhou 510006, China

³ Key Laboratory of Automobile Components and Vehicle Technology in Guangxi, Guangxi University of Science and Technology, Liuzhou 545006, China

Correspondence should be addressed to Hui Shen; shenhui1956@163.com

Received 1 May 2014; Revised 14 July 2014; Accepted 18 July 2014; Published 17 August 2014

Academic Editor: Tao Xu

Copyright © 2014 Minghua Li et al. This is an open access article distributed under the Creative Commons Attribution License, which permits unrestricted use, distribution, and reproduction in any medium, provided the original work is properly cited.

In this work we prepared double-layer antireflection coatings (DARC) by using the SiO₂/SiN_x:H heterostructure design. SiO₂ thin films were deposited by electron-beam evaporation on the conventional solar cell with SiN_x:H single-layer antireflection coatings (SARC), while to avoid the coverage of SiO₂ on the front side busbars, a steel mask was utilized as the shelter. The thickness of the SiN_x:H as bottom layer was fixed at 80 nm, and the varied thicknesses of the SiO₂ as top layer were 105 nm and 122 nm. The results show that the SiO₂/SiN_x:H DARC have a much lower reflectance and higher external quantum efficiency (EQE) in short wavelengths compared with the SiN_x:H SARC. A higher energy conversion efficiency of 17.80% was obtained for solar cells with SiO₂ (105 nm)/SiN_x:H (80 nm) DARC, an absolute conversion efficiency increase of 0.32% compared with the conventional single SiN_x:H-coated cells.

1. Introduction

For high-efficiency solar cells, antireflection coating (ARC) is very important for improving the performance of solar cells since it ensures a high photocurrent output by minimizing incident light reflectance on the top surface [1–4]. At present, hydrogen containing silicon nitride (SiN_x:H) thin film deposited by plasma enhanced chemical vapour deposition (PECVD) is widely used as ARC and passivation layer for crystalline silicon solar cells [5, 6]. However, the single-layer antireflection coatings (SARC) used in silicon solar cells still cause considerable optical reflectance loss in a broad range of the solar spectrum. Therefore, double-layer antireflection coatings (DARC) which consist of heterostructure materials such as MgF₂/ZnS [3, 7], MgF₂/BN [8], Al₂O₃/TiO₂ [9–11], and MgF₂/CeO₂ [12] are considered to be a more effective design in decreasing the reflection in a broad wavelength range for the high efficiency solar cells fabrication. These DARC are not common because of process

complexity, which could affect their mass production process. Though SiN_x:H/SiN_x:H [13] shows unique combination of good electronic and optical properties, it has disadvantages of high absorption in the UV region reducing of the short-circuit current of the cell. The SiO₂/SiN_x:H DARC are a promising design to improve solar cells efficiency due to its advantages in both surface passivation and antireflection properties. The simulation on the SiO₂/SiN_x:H DARC was carried out by optimizing their refractive index and film thickness [14]. Kim et al. [15] have investigated the conversion efficiency improvement of monocrystalline silicon solar cell with double layer antireflection coating consisting of SiO₂/SiN_x:H deposited by PECVD. And the solar cells with DARC showed the better efficiency as 17.57% and 17.76%, compared with 17.45% for single SiN_x:H ARC.

In this paper, we present a novel process method that DARC consisting of SiN_x:H and SiO₂ films were deposited via PECVD and an electron-beam evaporation technique, respectively. The thickness of SiN_x:H films as the bottom

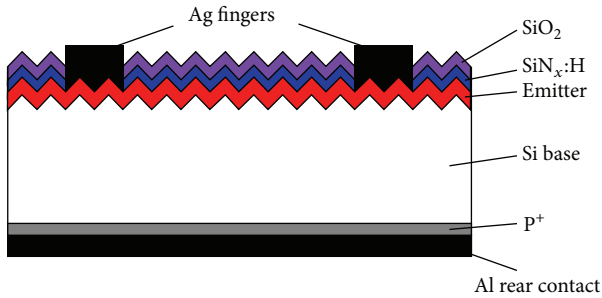


FIGURE 1: Schematic of the solar cell with $\text{SiO}_2/\text{SiN}_x\text{:H}$ DARC.

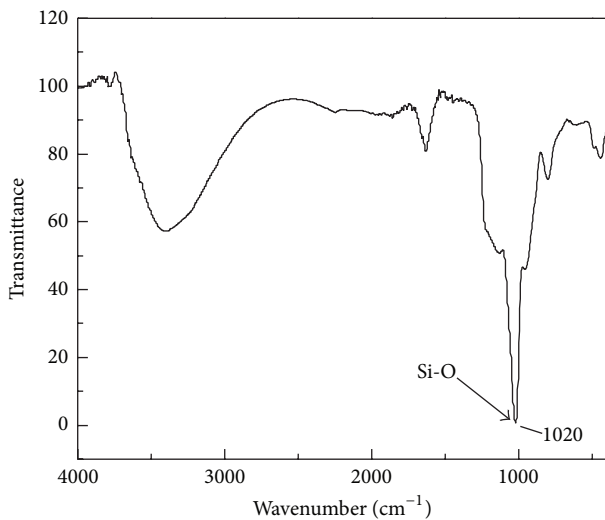


FIGURE 2: FTIR transmission spectra of SiO_2 thin film.

layer is kept at 80 nm, which is optimum for SARC. By simply varying the thickness of the SiO_2 layer as the top layer covering the conventional solar cell, monocrystalline silicon solar cells with different $\text{SiO}_2/\text{SiN}_x\text{:H}$ DARC are fabricated.

2. Experiment

Boron doped monocrystalline wafers, with a thickness of 160 μm , a size of 125 mm \times 125 mm, and a resistivity in the range of 1~3 Ωcm , have been used for all experiments. After standard cleaning and alkaline texturization, a standard POCl_3 emitter diffusion in a quartz tube led to a sheet resistivity of 60 Ω/\square . The wafers were coated with a $\text{SiN}_x\text{:H}$ layer in a PECVD (Centrotherm) system. The refractive index of $\text{SiN}_x\text{:H}$ was adjusted by controlling the NH_3/SiH_4 gas flow ratio. The thickness of the $\text{SiN}_x\text{:H}$ layer was 80 nm. After a standard front and back side screen printing process, the contact formation was performed by a firing through process. Then, the solar cells with $\text{SiN}_x\text{:H}$ SARC were performed. To prepare the $\text{SiO}_2/\text{SiN}_x\text{:H}$ DARC, SiO_2 thin films were deposited on the prepared solar cell with $\text{SiN}_x\text{:H}$ SARC by electron-beam evaporation. Considering of the SiO_2 layer on busbars may lead to contact issue in I - V test, we used steel mask on the top of busbars as shelter during e-beam

evaporation. High purity SiO_2 (99.99%) granules were used as the source material for evaporation and the source-to-substrate distance was 50 cm. The substrates temperature was controlled at 200°C. High purity oxygen (99.99%) was introduced into the chamber to maintain a pressure of 3.0×10^{-2} Pa and used as reactive gas during the deposition. The deposition rate was controlled using a quartz crystal sensor placed near the substrate, and set as $\sim 2 \text{ \AA/s}$. The thicknesses of the SiO_2 as top layer were 105 nm and 122 nm, respectively. Finally, the solar cells with different $\text{SiO}_2/\text{SiN}_x\text{:H}$ coatings were obtained. The structure of the solar cell with $\text{SiO}_2/\text{SiN}_x\text{:H}$ DARC is schematically shown in Figure 1.

The Fourier transform infrared spectroscopy (FTIR) measurement for the SiO_2 thin film has been made at 25°C using a Thermo Nicolet 6700 FTIR spectrometer. The refractive index of the $\text{SiN}_x\text{:H}$ and SiO_2 films were measured by a n&k analyzer 1200. Spectral reflectance and external quantum efficiency (EQE) measurements were performed by a solar cell spectral response measurement system (PV measurement, QEX7). In addition, the I - V characteristics of the solar cells were measured using a Berger I - V tester on a solar cell production line. All measurements were conducted under the standard test conditions (AM1.5G spectrum, 100 mW/cm^2 , 25°C). Prior to the measurements, the simulator was calibrated with a reference monocrystalline silicon solar cell, which was calibrated by the Fraunhofer ISE. All electrical parameters are presented as the average value of ten cells in the study.

3. Results and Discussion

3.1. SiO_2 Thin Film Characterization. XPS was applied to determine the chemical state of the Si and O elements, which can confirm the presence of SiO_2 layer in DARC. XPS analysis for SiO_2 film has been reported in our group [16].

In order to get a qualitative spectra of SiO_2 thin film compositions, we have performed Fourier transform infrared spectroscopy (FTIR) analysis. The samples were prepared on the aluminium thin film with 300 nm thickness on the glass substrate, which deposited by e-beam evaporation. We adopt reflection method to measure the sample. The spectra are presented in Figure 2. The band in the 1040–1150 cm^{-1} range is assigned to the stretching vibration mode Si–O [17, 18]. For the supplement of oxygen during the SiO_2 deposition, a clear increase of Si–O intensity peak (1020 cm^{-1}) is observed for the SiO_2 layer, which is related to the high oxygen content in this layer.

3.2. Optical Property. The color of the solar cell depends heavily on thickness of its ARC-layer. Figures 3(a) and 3(b) show the photographs of silicon solar cells with single $\text{SiN}_x\text{:H}$ SARC and SiO_2 (105 nm)/ $\text{SiN}_x\text{:H}$ (80 nm) DARC, respectively. Two kinds of coatings have good uniformity. It is notable that the front surface color of the solar cells changed from dark blue to black, indicating that there was a lower reflectance loss in the DARC, as shown in Figure 3(b).

The reflectance spectrum was measured to characterize the reflectance loss. Figure 4 depicts the reflectance spectra

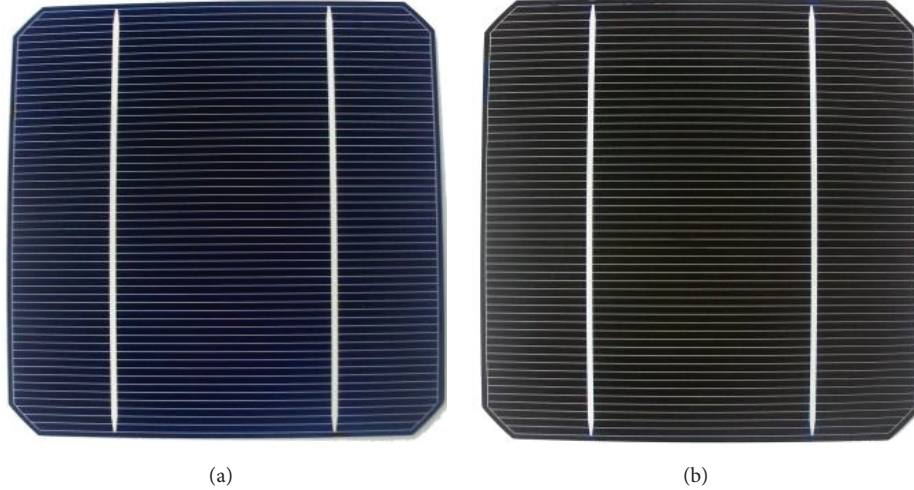


FIGURE 3: Photographs of monocrystalline silicon solar cells with (a) $\text{SiN}_x\text{:H}$ (80 nm) SARC and (b) SiO_2 (105 nm)/ $\text{SiN}_x\text{:H}$ (80 nm) DARC.

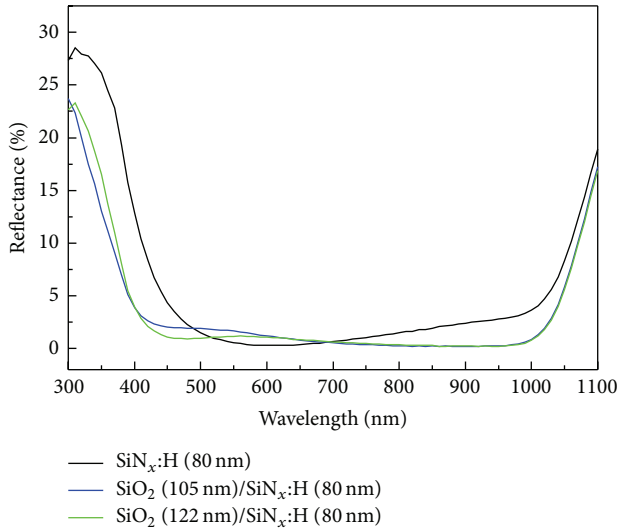


FIGURE 4: Reflectance curve for the single-layer ARC and double-layer ARC samples.

of solar cells with $\text{SiO}_2/\text{SiN}_x\text{:H}$ DARC and $\text{SiN}_x\text{:H}$ SARC, respectively. Compared with the $\text{SiN}_x\text{:H}$ SARC, $\text{SiO}_2/\text{SiN}_x\text{:H}$ layer stacks show lower reflectance in the range 300–450 nm. The amorphous SiO_2 coating is transparent in the measured wavelength range. It is obvious that the reflectance of the $\text{SiN}_x\text{:H}$ layer stack is dependent on the thickness of the SiO_2 coatings. With the thickness of SiO_2 in the $\text{SiO}_2/\text{SiN}_x\text{:H}$ stack increasing, the reflectance changes correspondingly. A similar simulation trend was also reported by Aguilar et al. [19]. In our work, the lowest reflectance was obtained while the thickness of SiO_2 was 105 nm in the $\text{SiO}_2/\text{SiN}_x\text{:H}$ stack, which is nearly consistent with previous simulation results. The value of calculated weighted reflectance is 1.72%.

It is acknowledged that a reduction in light of around 30% resulted from the reflectance at the Si and air interface [20]. ARC means an optically thin dielectric layer designed

TABLE 1: Summary of the average electrical parameters of the different ARC stacks compared with $\text{SiN}_x\text{:H}$ SARC solar cells (AM1.5G, 100 mW/cm^2 , 25°C).

Samples	Efficiency (%)	FF (%)	J_{sc} (mA/cm^2)	V_{oc} (mV)
$\text{SiN}_x\text{:H}$ (80 nm)	17.48	76.82	36.74	621.6
SiO_2 (105 nm)/ $\text{SiN}_x\text{:H}$ (80 nm)	17.80	77.58	37.77	621.3
SiO_2 (122 nm)/ $\text{SiN}_x\text{:H}$ (80 nm)	17.55	76.64	37.29	620.8

to suppress reflection by interference effects. By using DARC with $\lambda/4$ design, with growing indices from air to silicon, the minimum in reflection is broader in wavelength range. The measured refractive indices of $\text{SiN}_x\text{:H}$ and SiO_2 were 2.1 and 1.46 at 633 nm wavelength, respectively. Thus, the optimal thickness for each layer in term of their refractive indices can be obtained.

EQE data was collected for wavelengths in the range of 300–1100 nm to determine the spectral response of the solar cells, as shown in Figure 5(a); no significant differences in the infrared wavelength range were observed among these cells. On the other hand, the EQE of cells with DARC is higher than that with $\text{SiN}_x\text{:H}$ SARC in the range 300–450 nm wavelength. It was also shown that SiO_2 (105 nm)/ $\text{SiN}_x\text{:H}$ (80 nm) stack coatings has the highest improvement in short wavelength. IQE data was collected for wavelengths in the range of 300–1100 nm, as shown in Figure 5(b); EQE and IQE curves have the similar trends.

3.3. Solar Cell Results. The solar cells fabricated with novel $\text{SiO}_2/\text{SiN}_x\text{:H}$ stacks were tested and compared to conventional solar cells with $\text{SiN}_x\text{:H}$ SARC, as shown in Table 1. All data in Table 1 are the average values of ten samples. With the thickness of SiO_2 thin films varied, the conversion efficiency of the cells changed. Table 1 shows the conversion efficiency of the cells with SiO_2 (105 nm)/ $\text{SiN}_x\text{:H}$ (80 nm) DARC reached 17.80%, which was 0.32% (absolute) higher than solar cells

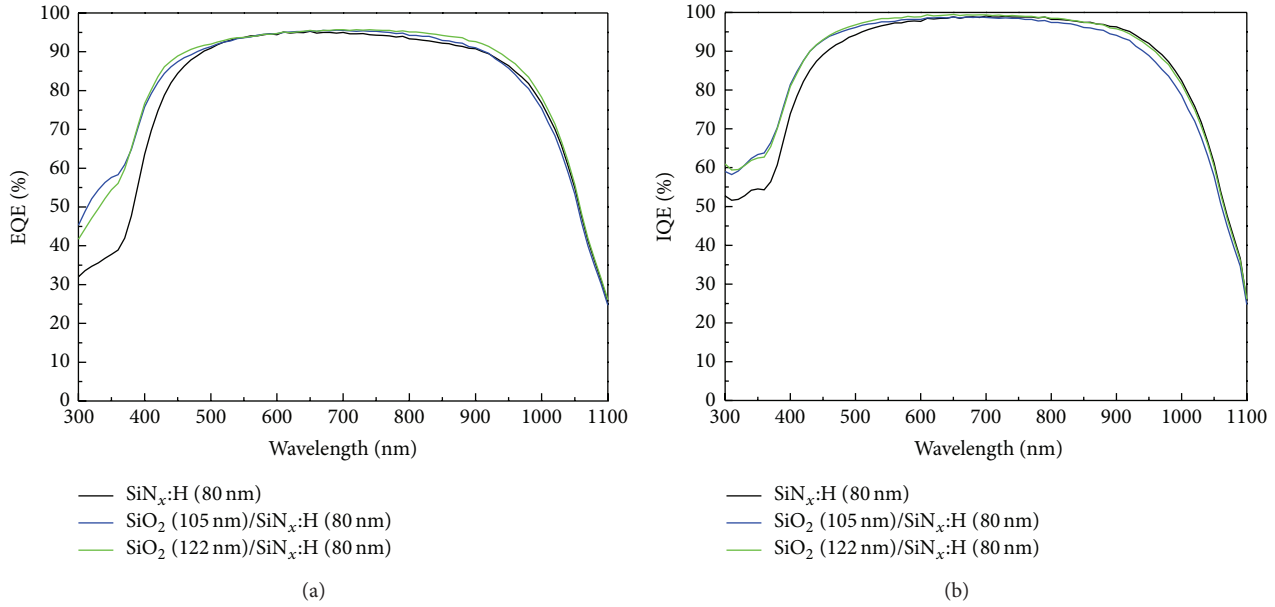
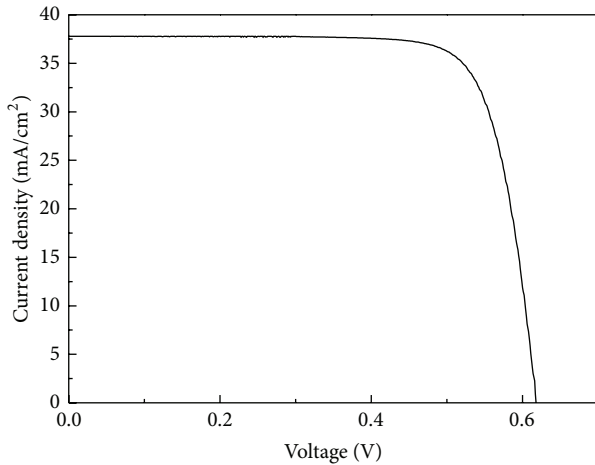


FIGURE 5: EQE and IQE of the single layer ARC and double layer ARC solar cells.



Area = 154.83 cm² FF = 77.58%
 V_{oc} = 621.3 mV Efficiency = 17.80%
 J_{sc} = 37.77 mA/cm²

FIGURE 6: J - V characteristics of the solar cell with SiO₂ (105 nm)/SiN_x:H (80 nm) DARC (AM1.5 G, 100 mW/cm², 25° C).

with SiN_x:H SARC. The fill factor of each group is nearly the same, while the V_{oc} shows small degradation for solar cells, which probably caused by the surface damages during the e-beam evaporation.

Correspondingly, the highest short-circuit current density (J_{sc}) was also obtained. It is demonstrated that the conversion efficiency of cells with DARC is dependent on the thickness of SiO₂ coatings, the same as the dependence of reflectance and EQE. Figure 6 shows the J - V characteristic of the solar cell with SiO₂ (105 nm)/SiN_x:H (80 nm) DARC.

4. Conclusions

In this work, SiO₂/SiN_x:H DARC were deposited on monocrystalline silicon solar cells. The results show that the SiO₂/SiN_x:H DARC have a lower reflectance compared with the SiN_x:H SARC. Accordingly, solar cells with SiO₂/SiN_x:H DARC exhibit a higher EQE and IQE in the short wavelengths of 300–450 nm. Due to current density improvement, the conversion efficiency of 17.80% was obtained for solar cells with DARC, 0.32% (absolute) higher than that of cells with single SiN_x:H coatings.

Conflict of Interests

The authors declare that there is no conflict of interests regarding the publication of this paper.

Acknowledgments

This work was funded by the Building Fund (no. 13-051-38) and Opening Project (nos. 2012KFMS04 and 2013KFM01) of Guangxi Key Laboratory of Automobile Components and Vehicle Technology. This work was also funded by the talent introduction project of Guangdong Mechanical & Electrical College. The authors would like to thank Ms. Qianzhi Zhang (Instrumental Analysis & Research Center, Sun Yat-sen University) for her help with FTIR measurement.

References

- [1] M. A. Green, "Third generation photovoltaics: ultra-high conversion efficiency at low cost," *Progress in Photovoltaics: Research and Applications*, vol. 9, no. 2, pp. 123–135, 2001.
- [2] J. Yoo, S. K. Dhungel, and J. Yi, "Properties of plasma enhanced chemical vapor deposited silicon nitride for the application in

- multicrystalline silicon solar cells," *Thin Solid Films*, vol. 515, no. 12, pp. 5000–5003, 2007.
- [3] D. Bouhafs, A. Moussi, A. Chikouche, and J. M. Ruiz, "Design and simulation of antireflection coating systems for optoelectronic devices: application to silicon solar cells," *Solar Energy Materials and Solar Cells*, vol. 52, no. 1-2, pp. 79–93, 1998.
- [4] S.-C. Chiao, J.-L. Zhou, and H. A. Macleod, "Optimized design of an antireflection coating for textured silicon solar cells," *Applied Optics*, vol. 32, no. 28, pp. 5557–5560, 1993.
- [5] B. Swatowska and T. Stapinski, "Amorphous hydrogenated silicon-nitride films for applications in solar cells," *Vacuum*, vol. 82, no. 10, pp. 942–946, 2008.
- [6] A. G. Aberle, "Overview on SiN surface passivation of crystalline silicon solar cells," *Solar Energy Materials and Solar Cells*, vol. 65, no. 1, pp. 239–248, 2001.
- [7] J. Zhao, A. Wang, P. Altermatt, and M. A. Green, "Twenty-four percent efficient silicon solar cells with double layer antireflection coatings and reduced resistance loss," *Applied Physics Letters*, vol. 66, no. 26, pp. 3636–3638, 1995.
- [8] A. Alemu, A. Freundlich, N. Badi, C. Boney, and A. Bensaoula, "Low temperature deposited boron nitride thin films for a robust anti-reflection coating of solar cells," *Solar Energy Materials and Solar Cells*, vol. 94, no. 5, pp. 921–923, 2010.
- [9] D. J. Aiken, "High performance anti-reflection coatings for broadband multi-junction solar cells," *Solar Energy Materials and Solar Cells*, vol. 64, no. 4, pp. 393–404, 2000.
- [10] J. Daniel, "Antireflection coating design for series interconnected multi-junction solar cells," *Progress in Photovoltaics: Research and Application*, vol. 8, pp. 563–570, 2000.
- [11] B. G. Lee, J. Skarp, V. Malinen, S. Li, S. Choi, and H. M. Branz, in *Proceedings of the IEEE Photovoltaic Specialists Conference*, Austin, Tex, USA, 2012.
- [12] S. E. Lee, S. W. Choi, and J. Yi, "Double-layer anti-reflection coating using MgF₂ and CeO₂ films on a crystalline silicon substrate," *Thin Solid Films*, vol. 376, no. 1-2, pp. 208–213, 2000.
- [13] Y. Lee, D. Gong, N. Balaji, Y.-J. Lee, and J. Yi, "Stability of SiN_x/SiN_x double stack antireflection coating for single crystalline silicon solar cells," *Nanoscale Research Letters*, vol. 7, article 50, 2012.
- [14] P. Doshi, G. E. Jellison Jr., and A. Rohatgi, "Characterization and optimization of absorbing plasma-enhanced chemical vapor deposited antireflection coatings for silicon photovoltaics," *Applied Optics*, vol. 36, no. 30, pp. 7826–7837, 1997.
- [15] J. Kim, J. Park, J. H. Hong et al., "Double antireflection coating layer with silicon nitride and silicon oxide for crystalline silicon solar cell," *Journal of Electroceramics*, vol. 30, no. 1-2, pp. 41–45, 2013.
- [16] M. Li, L. Zeng, Y. Chen, L. Zhuang, X. Wang, and H. Shen, "Realization of colored multicrystalline silicon solar cells with SiO₂/SiN_x:H double layer antireflection coatings," *International Journal of Photoenergy*, vol. 2013, Article ID 352473, 8 pages, 2013.
- [17] P. V. Bulkin, P. L. Swart, B. M. Lacquet, and J. Non-Cryst, "Effect of process parameters on the properties of electron cyclotron resonance plasma deposited silicon-oxynitride," *Journal of Non-Crystalline Solids*, vol. 187, pp. 403–408, 1995.
- [18] S. K. Ghosh and T. K. Hatwar, "Preparation and characterization of reactively sputtered silicon nitride thin films," *Thin Solid Films*, vol. 166, no. C, pp. 359–366, 1988.
- [19] J. Aguilar, Y. Matsumoto, G. Romero, and M. Alfredo Reyes, "Optical mismatch in double AR coated c-Si, a simple theoretical and experimental correlation," in *Proceedings of the 3rd World Conference on Photovoltaic Energy Conversion*, pp. 1001–1004, Osaka, Japan, May 2003.
- [20] A. Luque and S. Hegedus, *Handbook of Photovoltaic Science and Engineering*, John Wiley & Sons, Chichester, UK, 2003.

Research Article

An Improved Method for Sizing Standalone Photovoltaic Systems Using Generalized Regression Neural Network

Tamer Khatib and Wilfried Elmenreich

Institute of Networked and Embedded Systems and Lakeside Labs, University of Klagenfurt, 9020 Klagenfurt, Austria

Correspondence should be addressed to Tamer Khatib; tamer_khat@hotmail.com

Received 14 May 2014; Revised 9 July 2014; Accepted 23 July 2014; Published 11 August 2014

Academic Editor: Dimitrios Karamanis

Copyright © 2014 T. Khatib and W. Elmenreich. This is an open access article distributed under the Creative Commons Attribution License, which permits unrestricted use, distribution, and reproduction in any medium, provided the original work is properly cited.

In this research an improved approach for sizing standalone PV system (SAPV) is presented. This work is an improved work developed previously by the authors. The previous work is based on the analytical method which faced some concerns regarding the difficulty of finding the model's coefficients. Therefore, the proposed approach in this research is based on a combination of an analytical method and a machine learning approach for a generalized artificial neural network (GRNN). The GRNN assists to predict the optimal size of a PV system using the geographical coordinates of the targeted site instead of using mathematical formulas. Employing the GRNN facilitates the use of a previously developed method by the authors and avoids some of its drawbacks. The approach has been tested using data from five Malaysian sites. According to the results, the proposed method can be efficiently used for SAPV sizing whereas the proposed GRNN based model predicts the sizing curves of the PV system accurately with a prediction error of 0.6%. Moreover, hourly meteorological and load demand data are used in this research in order to consider the uncertainty of the solar energy and the load demand.

1. Introduction

Photovoltaic systems are environment-friendly energy systems. Thus, PV system installation has been given a big concern in the last three decades. However, PV systems' high capital cost is considered one of the most important challenges to this technology, especially when it is compared with conventional power systems. Therefore, many research works are being conducted in order to propose methods for optimization of PV systems so as to provide reliable systems with minimal capital cost. In this context, Sharma et al. in [1] define PV system optimization as "the process for determining the cheapest combination of PV array and battery that will meet the load requirement with an acceptable availability level over the expected lifetime." As a fact, PV system performance depends on available solar energy and ambient temperature and, therefore, meteorological variables must be extensively studied in order to optimally size a PV system [2].

In the literature, works related to PV system sizing can be categorized into intuitive, numerical, and analytical methods. The intuitive method is defined according to [3] as conducting simplified calculation of the system size without

taking into account the random nature of solar radiation or establishing a relationship between the different subsystems. The method considers the use of solar energy data such as the lowest monthly average, average annual, or monthly solar energy. A major disadvantage of the intuitive method is that it may result in an over- or undersizing of the designed system which results in low reliability of the system or high cost of produced energy [3]. In the meanwhile, numerical method is defined as implementing system simulation for each time period considered. In this method, daily or hourly data are used and based on that the energy balance and flow of the system are calculated. The simulation method offers the advantage of being more accurate, and the evaluation of system availability can be approached in a quantitative manner. System availability in this case is defined as the load percentage satisfied by the PV system for long period of time [3]. The simulation method allows optimizing the energy and economic cost of the system. Simulation methods can be divided into two, namely, stochastic and deterministic methods. In the stochastic method, the uncertainty in solar energy and load demand is considered by simulating a random process modelling hourly solar radiation and load demand

records. Due to the difficulties in finding the hourly solar energy models [3–5], the deterministic simulation method considers the use of predefined load and meteorological data. As for the analytical method, the equations describing the PV system size as a function of reliability have to be developed. This method has the advantage of providing simple calculation of the PV system size, while the disadvantage is the difficulty in finding the coefficients of the equations which are location dependent [6, 7].

Due to the difficulty in calculating the optimum PV size by the simulation and analytical methods, artificial neural networks (ANN) are employed to overcome these limitations. For optimizing PV systems in many regions in Algeria, a combined numerical and ANN method has been used [8, 9]. In this method, the optimal PV sizing factors of the targeted sites are first calculated using the numerical method first. After that the ANN based model is utilized for predicting these factors using the geographical location coordinates. The developed ANN model has two input variables, namely, latitude and longitude, and two outputs, namely, the sizing factors for the PV array (C_A) and the storage battery (C_s), respectively. The ANN model helps in simplifying the calculation of the sizing factors but its limitation is that it can only determine the optimum size of PV system at one reliability level or loss of load probability (LLP). In [10], the analytical method is used to obtain a large data set for optimum sizes of a PV system at different LLPs and this data set is used to train an ANN to predict the optimum size of the PV array in terms of the optimum storage battery, LLP, and “yearly cleanses index.” The main drawback of this method is that the ANN model predicts the optimum PV array size depending on the optimum storage battery capacity which is not explained as to how it is calculated. In [9], the same combined numerical and ANN method presented in [11] has been used but this time it is used for generating the sizing curves at different LLPs for certain sites in Algeria. Two ANN models have been developed in which the first ANN model has four inputs which are latitude, longitude, altitude, and LLP and thirty outputs representing the thirty possible C_A values. After predicting the C_A , the C_s is calculated and then the sizing curve is predicted by the second ANN model. In this method, the sizing curve is predicted by ANN only after determining the optimum pair of C_A and C_s , thus making the procedure laborious and impractical.

To overcome the limitations of the abovementioned methods in determining optimal sizing of PV systems, we propose an improved approach using a general regression neural network (GRNN) to predict the PV array and battery capacities in terms of LLP, latitude, and longitude. By using the GRNN model, the calculation for the optimum PV size of a standalone PV (SAPV) system can be automated and improved without the need for extensive mathematical calculations or graphical analysis techniques.

2. Analytical Method for Sizing SAPV System

The background theory and formulation used in the analytical method for sizing SAPV system as proposed in [7]

are described in this section. The analytical method is based on a PV system energy model and a long term of meteorological data such as solar energy and ambient temperature. In general, a typical SAPV system consists of a PV module/array, power conditioner comprising charge controller and maximum power point tracking controller, storage battery, inverter, and load. A PV module collects energy from the sun and converts it to DC power which then is handled by a power conditioner to supply loads. The energy produced by a PV array is given by

$$E_{PV} = A_{PV} \cdot E_{\text{sun}} \cdot \eta_{PV} \cdot \eta_{\text{inv}} \cdot \eta_{\text{wire}}, \quad (1)$$

where A_{PV} is the area of the PV module/array and E_{sun} is daily solar irradiation. η_{PV} , η_{inv} , and η_{wire} are efficiencies of PV module, inverter, and conductors, respectively.

PV module efficiency depends on cell temperature and it can be given as function of reference efficiency (η_{ref}) which is provided in the data sheet, cell temperature, (T_C) and standard testing temperature (T_{ref}) as illustrated below

$$\eta_{PV} = \eta_{\text{ref}} [1 - \beta_{\text{ref}} (T_C - T_{\text{ref}})]. \quad (2)$$

β_{ref} is a factor and it can be given by

$$\beta_{\text{ref}} = \frac{1}{T_o - T_{\text{ref}}}. \quad (3)$$

As for cell temperature, it can be calculated using ambient temperature as follows:

$$T_C = T_a + \frac{\text{NOCT} - 20}{800} G_{\text{ref}}, \quad (4)$$

where T_a is the ambient temperature, G_{ref} is the standard testing solar radiation, and NOCT is the nominal operation cell temperature.

The difference between the energy at the front end of a PV system E_{PV} and at the load side is given by

$$E_D = \sum_{i=1}^{8760} (E_{PV} - E_L), \quad (5)$$

where E_L is the load energy demand.

E_D may have a positive value ($E_{PV} > E_L$) or a negative value ($E_{PV} < E_L$). In case of having E_D positive, there is an excess in energy in the system. In the meanwhile, if E_D is negative then there will be an energy deficit. Excess energy is usually stored in batteries in order to be used in the deficit time. The energy deficit is defined as the disability of the PV system to fulfil the load demand at a specific time.

System availability (reliability) is an important issue to be considered in designing of PV system. 100% availability of a PV system means that the system is able to cover the load demand all the year time without shortages. Consequently, 99% availability means that the system is not able to cover the load demand in 88 hours during one year time. This means that high PV system availability leads to high reliability and vice versa. However, high reliable PV system results high initial cost and, thus, it is not feasible to consider very high

availability rates in designing PV system. The availability of a PV system can be as a loss of load probability (LLP) index. LLP is defined as the ratio of annual energy deficit to annual load demand and it is given by

$$LLP = \frac{\sum_{i=1}^{8760} \text{Energy deficits}_i}{\sum_{j=1}^{8760} \text{Energy demand}_j}. \quad (6)$$

In [7], an analytical method is presented for optimal sizing of a standalone PV system. This method is represented by two empirical equations between PV array sizing ratio (C_A) and battery sizing ratio (C_s) and system reliability LLP. In [7], the authors assumed that the relation between C_A and LLP can be expressed by two exponential terms while the relation between C_A and C_s is linear as follows:

$$\begin{aligned} \text{optimum } C_A &= c_1 e^{c_2 LLP} + c_3 e^{c_4 LLP}, \\ \text{optimum } C_s &= c_5 C_A + c_6. \end{aligned} \quad (7)$$

The sizing ratios C_A and C_s are calculated as follows:

$$\begin{aligned} C_A &= \frac{C_{PV}}{C_L}, \\ C_s &= \frac{C_B}{C_L}, \end{aligned} \quad (8)$$

where C_B and C_{PV} are battery capacity and PV array capacity at specific load, respectively, and C_L is the load demand.

The optimization process presented in [7] starts by defining some initial values for load demand, PV efficiency, charging efficiency, inverter efficiency, and conductor efficiency. After that, daily solar irradiation for the targeted site is utilized in order to calculate the expected output power of the system. After that, a design space that contains a set of PV array area values is initiated. Based on each PV array area value and the defined load demand, C_A is then calculated. Then, E_D is calculated using (5). Subsequently, arrays of deficit and excess energies are constructed. At this point, at each specific PV array area, LLP, C_s , and C_A are calculated and stored in arrays. Consequently this loop is repeated until the maximum value of PV array area is reached. Finally, plots of LLP versus C_A and C_s versus C_A are constructed and from these plots, curve fitting equations are derived using the MATLAB fitting toolbox to find the coefficients of (7).

3. GRNN for Sizing SAPV System

Artificial neural networks (ANNs) are nonalgorithmic information processing systems which are able to learn and generalize the relationship between input and output variables from the recorded data. In this work we apply a GRNN model to improve the method presented in [7]. The aim of the proposed GRNN model is to predict the sizing curves directly without the need to run any iterative simulation and to abandon the need for calculating models coefficient. A schematic diagram of the basic architecture of a GRNN is shown in Figure 1. The network has several layers: the input,

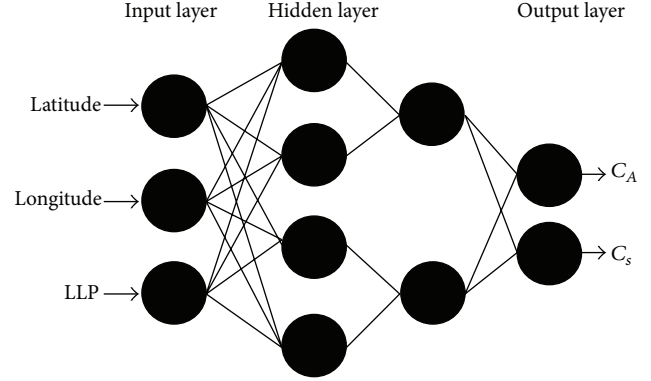


FIGURE 1: Topology of the GRNN used to predict the optimum size of a SAPV.

hidden, and output layers. Each layer is interconnected by connection strengths, called weights.

A generalized regression neural network (GRNN) is a probabilistic neural network consisting of an input layer, a hidden layer, a pattern/summation layer, and a decision node. Each predictor variable has a corresponding input neuron. The input values standardize the input values by subtracting the median and scaling the value to the interquartile range. The input layer feeds the hidden neuron layers where each training pattern is represented by a hidden neuron. In the pattern layer, there are only two neurons, a denominator summation unit and a numerator summation unit. The denominator summation unit adds up the weights of the values coming from each of the hidden neurons. The numerator summation unit adds up the weights of the values multiplied by the actual target value for each hidden neuron. The decision node divides the values accumulated by the numerator summation unit by the value in the denominator summation unit and produces the predicted target value of the GRNN. The advantage of GRNNs is simplicity, fast training, good approximation also with smaller training sets, and, thus, high efficiency in comparison to other networks [12].

In general, there is no rule to determine the optimum number of hidden nodes in the hidden layer without training several networks and estimating the generalization error of each one. Large number of hidden nodes resulted in high generalization error due to the overfitting and high variance. In the meanwhile, low number of hidden units causes large training and generalization error due to underfitting and high statistical bias [13]. Anyways, there are some “rules of thumb” for selecting the number of the hidden nodes in the literature. Blum in [14] suggests that the number of neurons in the hidden layer is supposed to be somewhere between the input layer size and the output layer size. Swingler in [15] and Berry and Linoffin [16] claim that one does not require more than twice the number of the inputs. In addition, Boger and Guterman in [17] suggest that the number of the hidden nodes can be 70–90% of the number of the input nodes. Caudill and Butler in [18] recommended that the number of hidden nodes should be equal to the number of the inputs

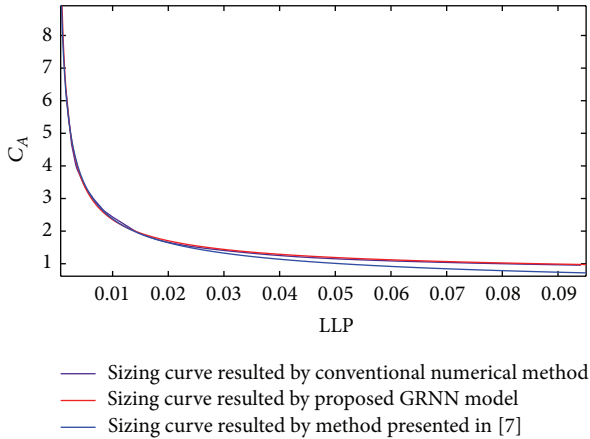


FIGURE 2: PV array sizing curve.

plus the number of the outputs multiplied by (2/3). Based on these recommendations the recommended number of the hidden layer for our model is in the range of 2 to 4 hidden neurons. In this paper we used 4 hidden nodes.

In this research, three variables are used as input parameters for the input nodes of the input layer, latitude, longitude, and LLP. Two nodes are at the output layer, namely, C_A , C_s , which are the optimum sizing ratios of the PV array and battery. We used the data set from [7] to train the ANN with the Levenberg-Marquardt backpropagation algorithm. The analytical method proposed in [7] is used to design PV system at 11 reliability levels (LLP (0–10%)) for each year of each station. The training of the proposed model is done utilizing MATLAB “nftool” and using 75% of the provided data set. These data were divided into three parts 70% for training, 15% for internal validation, and 15% for internal training.

4. Results and Discussion

As mentioned before, in [7], five sites are considered in the conducted optimization. In this research, the developed GRNN is trained by using four of these sites, namely, Johor Baharu, Kuching, Ipoh, and Alor Setar, while the fifth site which is Kuala Lumpur is used for testing the developed model. Figure 2 shows a comparison of sizing curves for the PV array obtained by numerical simulation, equations presented in [7], and the developed GRNN.

Figure 2 indicates that the GRNN model is more accurate in predicting the size of the PV array than the results based on the equations presented in [7]. The average mean absolute percentage error values were 1.2% and 5.1%, respectively. Using the GRNN, the difficulty of calculating the coefficients in the equations proposed by Khatib et al. [7] is avoided. Figure 3 shows the predicted storage battery by GRNN compared to the one calculated by the numerical simulation. The prediction accuracy was very high which indicates the utility of the use of GRNN in sizing PV systems.

From these figures, it is concluded that the proposed model is able to predict system sizing curve using only the

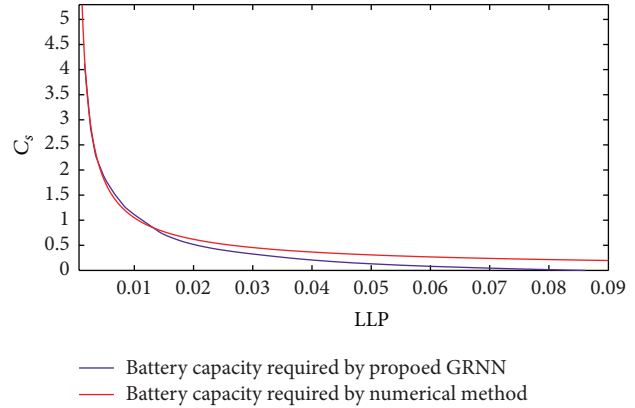


FIGURE 3: Battery capacity at different LLP.

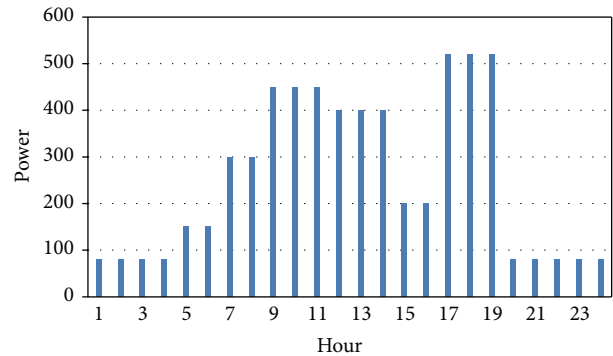


FIGURE 4: Simulated load demand.

location coordinates as well as the loss of load probability which can be considered as an advantage when it is compared to other ANN based models such as the models presented in [8–11]. Anyway, to validate the proposed method in terms of system reliability a design example is conducted in this paper considering the proposed method and some previously published methods. In [5, 7] optimization of PV system is done for Malaysia. However to validate the optimization results both authors designed a PV system supplying a 2.215 kWh/day load being located at Kuala Lumpur at 0.01 LLP. However, Shen in [5] did not generalize his results for other load demands while Khatib et al. in [7] did not consider the uncertainty of solar energy and the variation of the load demand. Therefore, to prove the validity of the proposed procedure and to avoid the limitations of [5, 7] an hourly load demand occurring at 24 hours and hourly solar energy data are used. In order to model the respective load demand of a typical remote area, we consider a larger load of 6.130 kWh/day in this paper. Figure 4 shows the temporal distribution of the simulated load demand. In this paper the hourly model of PV system in [19] is used to validate the proposed method.

Based on the developed ANN, the optimum sizing ratios for the considered site (Kuala Lumpur) are $C_A = 2.02$ and $C_s = 0.793$. We calculate the size of the PV based on the assumption that the used PV module has 200 Wp

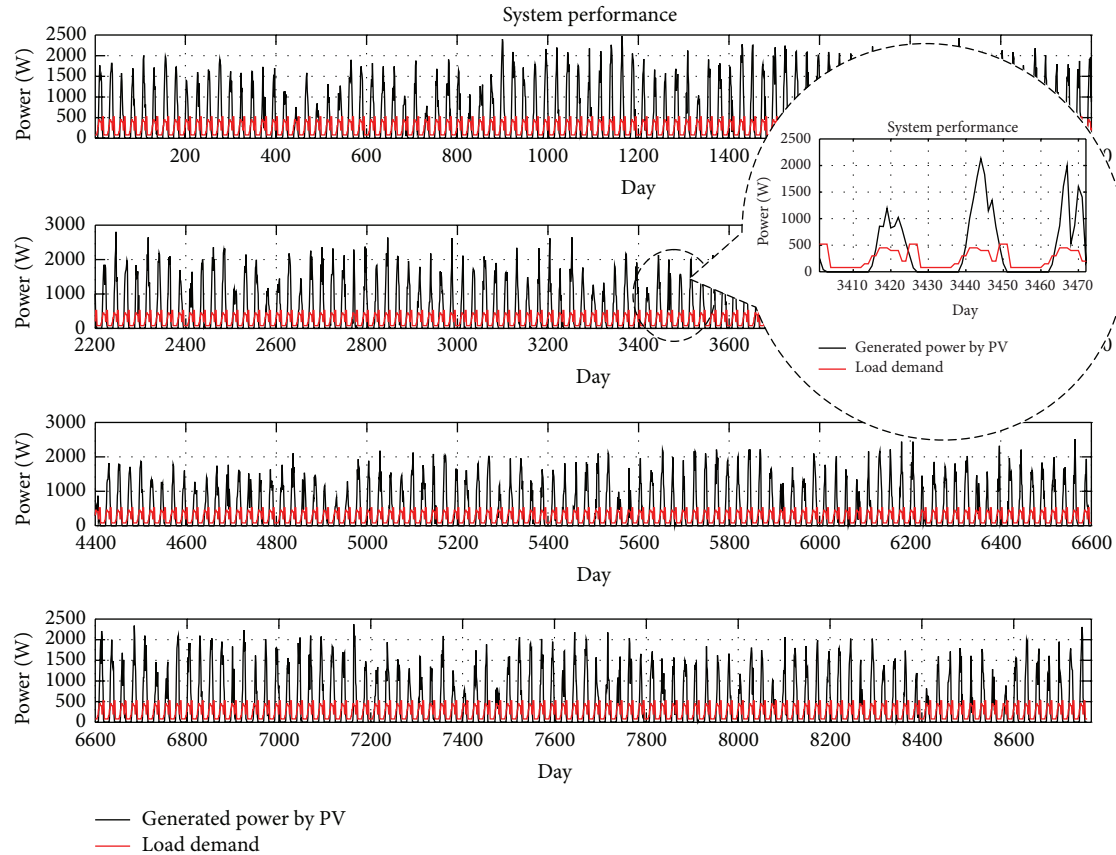


FIGURE 5: Generated power by the designed system.

rated power, 1.4 m^2 area, and 16% conversion efficiency (as reference value) and the rated battery voltage operates on 12 volts with a charging efficiency of 80% and an inverter conversion efficiency of 90%. The required PV array and battery capacities are 2.5 kWp and $324 \text{ Ah}/12 \text{ V}$, respectively. The power generated by the proposed photovoltaic system is calculated with respect to the load (see Figure 5). The average power generated by the designed PV array is 1.075 kW . This power is supposed to cover the load demand while the excess power is used to charge the battery. In the case of fully charged batteries, the excess power will be dumped using a dumping load. Figure 6 shows the power balance of the system in which negative power indicates that the battery is used to supply the load, while the positive net power indicates that this power has to be used in charging the battery or to be dumped. Figure 7 shows the net power which needs to be dumped. The sum of the dumped energy per year is 1757 kWh .

Figure 8 shows the state of charge (SOC) of the battery storage for a year (1–8760 hours). A SOC value of 1.0 indicates that the battery is not used while SOC value of less than 1.0 means that the battery is used. As indicated in the figure, the battery periodically supplies power to cover the load demand during the night time. Through one year, the battery reaches its allowable minimum SOC (0.2) 87 times. Figure 9 shows the loss of load days. The figure shows the percentage of covered load demand during loss of load days. During

a year, the load is lost for 87 hours which corresponds to 99% availability during one year. Note that most of load loss incidences happen in January, February, and December. From the figure, the loss of load probability is 0.5%.

In [7], the authors used the same sizing ratios and location to design a PV system to supply a 2.215 kWh/day load considering a 1% LLP. The authors used to simulate this designed system daily solar radiation values and daily averages of load demand. According to [7], the LLP of the designed system is 0.95%, while in this research the use of hourly solar radiation and load demand resulted in a 0.5% LLP despite that we aimed to design at it 1%. This slight difference can be due to the differences in the used metrological data. From these points two conclusions can be stated. First, the proposed sizing ratio for Malaysia in [5, 7] and in this paper is proven even by considering the uncertainty in solar energy and variation in the load demand. In addition, the using of hourly meteorological data and load demand definitely yields more accurate optimization but it could cause a slight oversizing in certain cases.

5. Conclusion

An ANN model is used to facilitate the use of a developed method for sizing PV system for Malaysia. The proposed

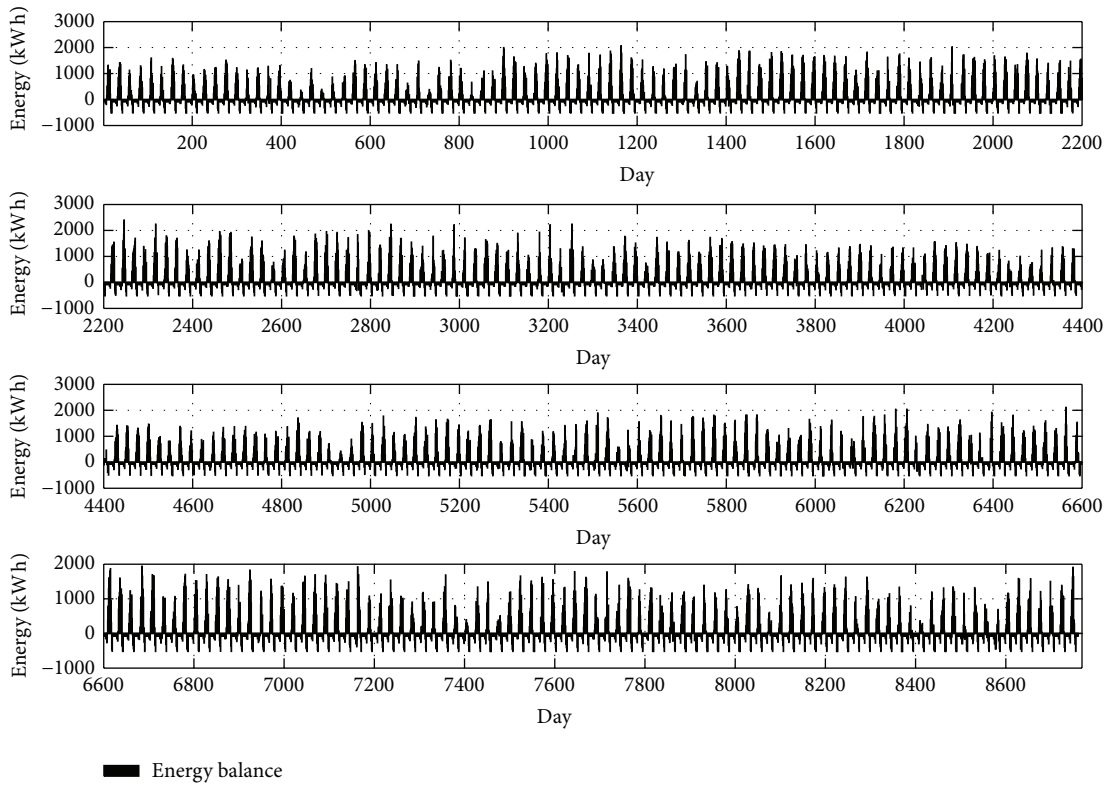


FIGURE 6: Energy balance for designed PV system.

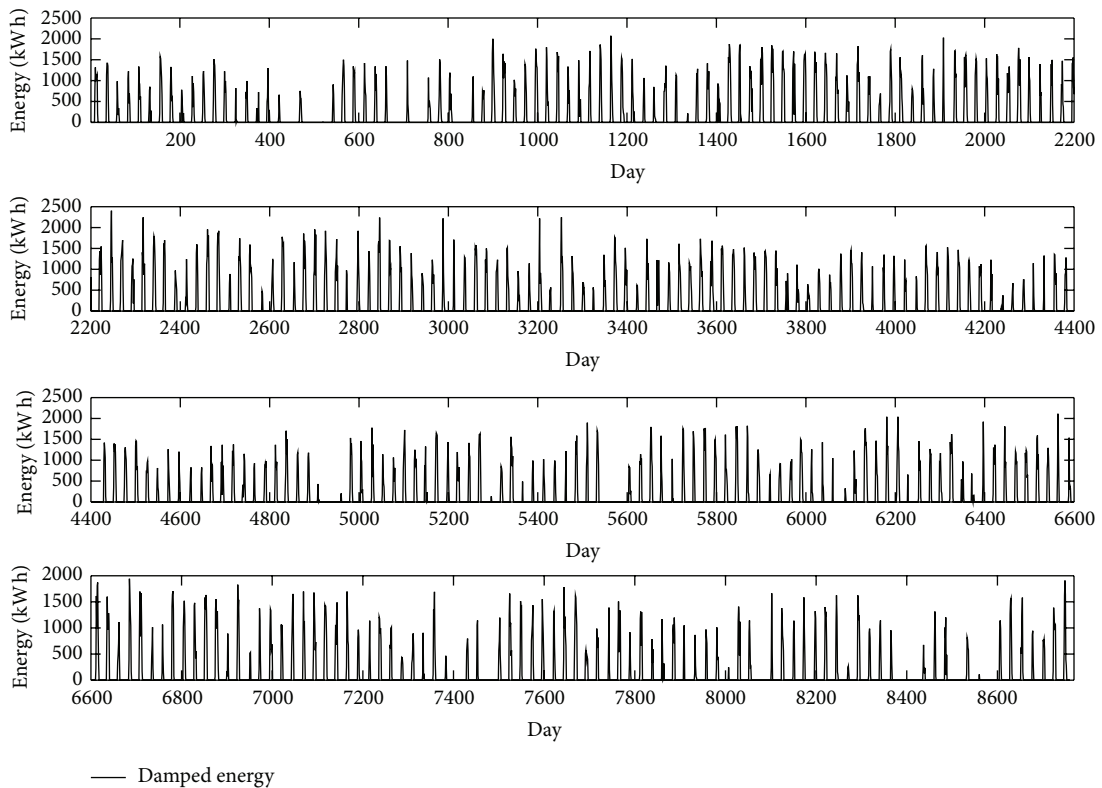


FIGURE 7: Damped power for the designed PV system.

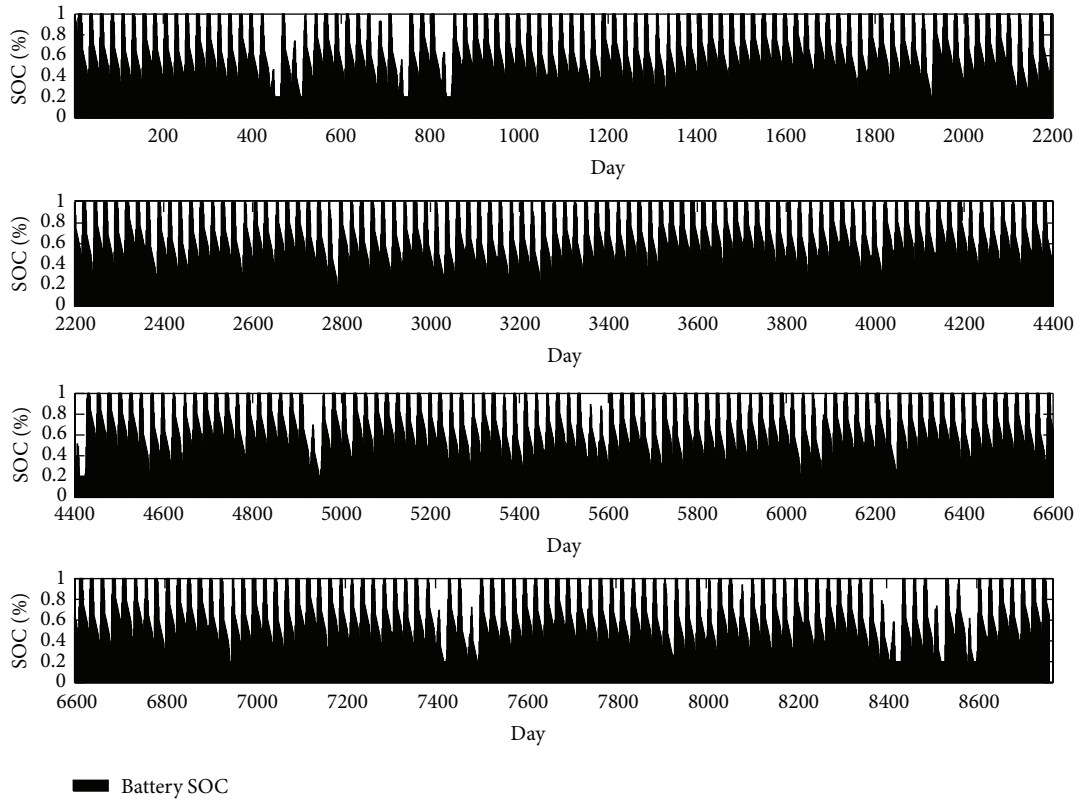


FIGURE 8: Battery storage SOC for the designed PV system.

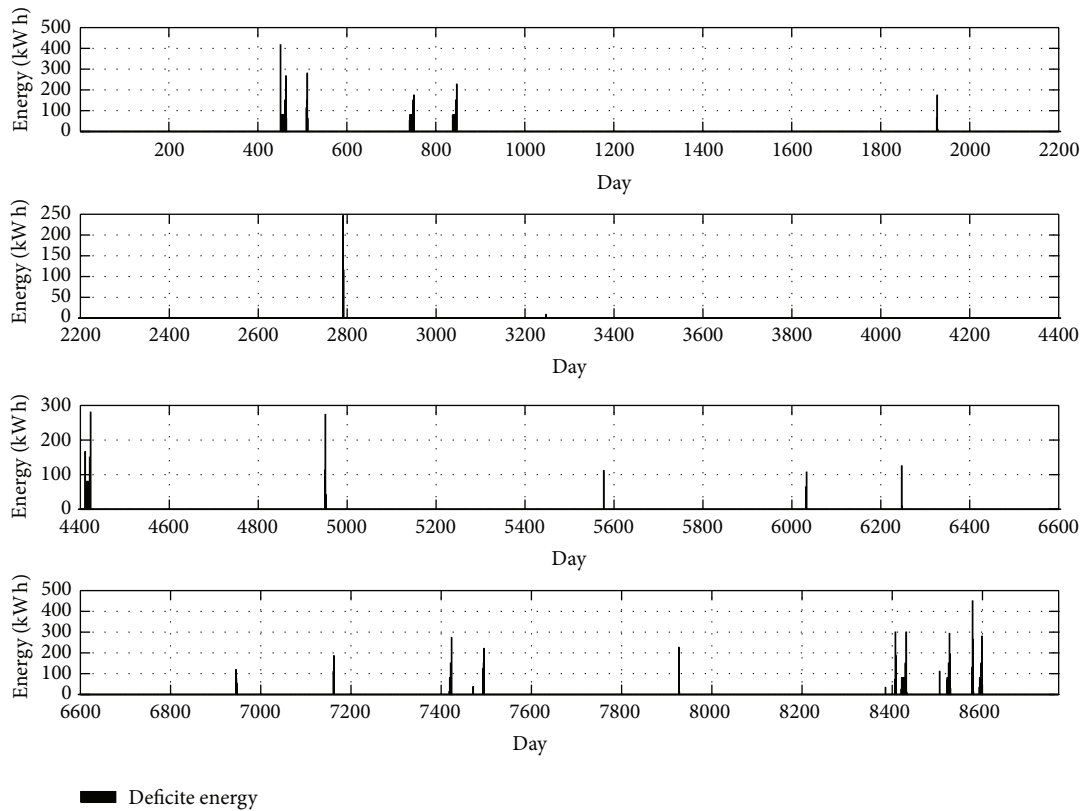


FIGURE 9: Loss of load days for the designed PV system.

ANN model predicts the size of the PV system in terms of LLP, latitude, and longitude. The developed ANN model showed high accuracy in predicting the PV system size whereas the MAPE is 0.6%. However, to ensure the validity of the proposed method, a designed example for a specific load is conducted considering the uncertainty in the solar radiation and the variation of the load demand. To validate the designed system we used a simulation based on hourly solar radiation and load demand. As a result, the LLP of the designed system is found to be 0.5% which indicates a sufficiently high reliability of the designed system.

Conflict of Interests

The authors declare that there is no conflict of interests regarding the publication of this paper.

Acknowledgments

This work is supported by Lakeside Labs, Klagenfurt, Austria, and funded by the European Regional Development Fund (ERDF) and the Carinthian Economic Promotion Fund (KWF) under Grants KWF 20214|23743|35470 (Project MONERGY) and 20214|22935|34445 (Project Smart Microgrid).

References

- [1] V. K. Sharma, A. Colangelo, and G. Spagna, "Photovoltaic technology: basic concepts, sizing of a stand alone photovoltaic system for domestic applications and preliminary economic analysis," *Energy Conversion and Management*, vol. 36, no. 3, pp. 161–174, 1995.
- [2] T. Khatib, A. Mohamed, and K. Sopian, "A review of photovoltaic systems size optimization techniques," *Renewable and Sustainable Energy Reviews*, vol. 22, pp. 454–465, 2013.
- [3] M. Sidrach-de-Cardona and L. M. López, "A simple model for sizing stand alone photovoltaic systems," *Solar Energy Materials and Solar Cells*, vol. 55, no. 3, pp. 199–214, 1998.
- [4] A. Hadj Arab, B. Ait Driss, R. Amimeur, and E. Lorenzo, "Photovoltaic systems sizing for Algeria," *Solar Energy*, vol. 54, no. 2, pp. 99–104, 1995.
- [5] W. X. Shen, "Optimally sizing of solar array and battery in a standalone photovoltaic system in Malaysia," *Renewable Energy*, vol. 34, no. 1, pp. 348–352, 2009.
- [6] T. Markvart, A. Fragaki, and J. N. Ross, "PV system sizing using observed time series of solar radiation," *Solar Energy*, vol. 80, no. 1, pp. 46–50, 2006.
- [7] T. Khatib, A. Mohamed, K. Sopian, and M. Mahmoud, "A new approach for optimal sizing of standalone photovoltaic systems," *International Journal of Photoenergy*, vol. 2012, Article ID 391213, 9 pages, 2012.
- [8] A. Mellit, M. Benganem, A. H. Arab, and A. Guessoum, "An adaptive artificial neural network model for sizing stand-alone photovoltaic systems: application for isolated sites in Algeria," *Renewable Energy*, vol. 30, no. 10, pp. 1501–1524, 2005.
- [9] A. Mellit, "ANN-based GA for generating the sizing curve of stand-alone photovoltaic systems," *Advances in Engineering Software*, vol. 41, no. 5, pp. 687–693, 2010.
- [10] L. Hontoria, J. Aguilera, and P. Zufiria, "A new approach for sizing stand alone photovoltaic systems based in neural networks," *Solar Energy*, vol. 78, no. 2, pp. 313–319, 2005.
- [11] A. Mellita and M. Benganem, "Sizing of stand-alone photovoltaic systems using neural network adaptive model," *Desalination*, vol. 209, no. 1–3, pp. 64–72, 2007.
- [12] C. H. Dagli, A. L. Buczak, J. Ghosh, M. J. Embrechts, O. Ersoy, and S. Kercel, *Intelligent Engineering Systems Through Artificial Neural Network*, ASME, 2000.
- [13] S. Geman, E. Bienenstock, and R. Doursat, *Neural Networks and the Bias/Variance*, 1992.
- [14] A. Blum, *Neural Networks in C++*, John Wiley & Sons, New York, NY, USA, 1992.
- [15] K. Swingler, *Applying Neural Networks: A Practical Guide*, Academic Press, London, UK, 1996.
- [16] M. Berry and G. Linoff, *Data Mining Techniques*, John Wiley & Sons, New York, NY, USA, 1997.
- [17] Z. Boger and H. Guterman, "Knowledge extraction from artificial neural networks models," in *Proceedings of the 1997 IEEE International Conference on Systems, Man, and Cybernetics. Part 3 (of 5)*, pp. 3030–3035, Orlando, Fla, USA, October 1997.
- [18] M. Caudill and C. Butler, *Understanding Neural Networks: Computer Explorations*, vol. 1 of *Basic Networks*, The MIT Press, Cambridge, Mass, USA, 1993.
- [19] T. Khatib and W. Elemenreich, "Novel simplified hourly energy flow models for photovoltaic power systems," *Energy Conversion and Management*, vol. 79, pp. 441–448, 2014.

Research Article

Seismic and Power Generation Performance of U-Shaped Steel Connected PV-Shear Wall under Lateral Cyclic Loading

Hongmei Zhang,¹ Jinzhi Dong,¹ Yuanfeng Duan,² Xilin Lu,¹ and Jinqing Peng³

¹ State Key Laboratory of Disaster Reduction in Civil Engineering, Tongji University, Shanghai 200092, China

² College of Civil Engineering and Architecture, Zhejiang University, Hangzhou 310058, China

³ Renewable Energy Research Group, Department of Building Services Engineering, The Hong Kong Polytechnic University, Hong Kong

Correspondence should be addressed to Yuanfeng Duan; ceyfduan@zju.edu.cn

Received 2 May 2014; Accepted 12 May 2014; Published 6 August 2014

Academic Editor: Hui Shen

Copyright © 2014 Hongmei Zhang et al. This is an open access article distributed under the Creative Commons Attribution License, which permits unrestricted use, distribution, and reproduction in any medium, provided the original work is properly cited.

BIPV is now widely used in office and residential buildings, but its seismic performance still remained vague especially when the photovoltaic (PV) modules are installed on high-rise building facades. A new form of reinforced concrete shear wall integrated with photovoltaic module is proposed in this paper, aiming to apply PV module to the facades of high-rise buildings. In this new form, the PV module is integrated with the reinforced concrete wall by U-shaped steel connectors through embedded steel plates. The lateral cyclic loading test is executed to investigate the seismic behavior and the electric and thermal performance with different drift angles. The seismic behavior, including failure pattern, lateral force-top displacement relationship, and deformation capacity, was investigated. The power generation and temperature variation on the back of the PV module and both sides of the shear wall were also tested. Two main results are demonstrated through the experiment: (1) the U-shaped steel connectors provide enough deformation capacity for the compatibility of the PV module to the shear wall during the whole cyclic test; (2) the electricity generation capacity is effective and stable during this seismic simulation test.

1. Introduction

Solar energy is clean and renewable energy. At present, using solar energy to generate electricity has been concerned by a growing number of researchers. According to the report of International Energy Agency, there will be one-fifth of the whole global energy produced by solar system by 2050 and a rise of 60% is anticipated by the end of this century [1]. Since buildings consume more than 30% energy in the world, the building-integrated photovoltaic (BIPV) technology which integrates photovoltaic (PV) modules with building envelopes, such as roofs, vertical facades, or windows, becomes a popular application form [2, 3]. One of the most attractive characteristics of BIPV is the conversion of the buildings from an energy consumer with a proportion of 30%~60% to an energy producer by themselves without occupying land [4-6]. Moreover, PV integrated buildings offer considerable scope for energy-demand offsets and reduction of greenhouse (GHG) emissions and achieve

local use of electricity to avoid transmission and distribution investments and the associated losses [7]. In the latest 5 years, BIPV becomes one of the fastest growing segments of the solar industry all over the world with a predicted capacity growth of over 50% from 2011 to 2017 [8].

For the envelope of high-rise buildings, the area of facades is much larger than that of roofs, although the angle of inclination is not the best one in terms of power generation when integrating PV modules on these buildings. According to related studies, the unit power generation capacity of the PV modules on building facades is also considerable comparing with that of roofs [9, 10]. And the total power generation value of the PV on building facades is far more than that of roofs. According to current studies, the facade photovoltaic systems can be classified into three basic types including facades-integrated cladding, curtain walls, and structural glazing [7], and the integration manners, materials, characteristics, and typical cases for each type of system were investigated. Han et al. [11] evaluated the outdoor performance of a naturally

ventilate double-sided PV facade through field monitoring from a small scale test rig. Research results indicated that the heat gain from facade in summer could be substantially reduced and additional electrical power can also be generated from such facade as a byproduct. Yang et al. conducted an experiment to evaluate the cooling load component contributed by building-integrated PV walls and showed that the PV wall can reduce the corresponding cooling load components by 33%–50% [12]. Peng et al. conducted an investigation on the annual thermal performance of a photovoltaic wall mounted on a multilayer facade [13]. The results indicated that the south-facing PV wall could reduce heat gain through the envelope by 51% in summer in Hong Kong. And an optimal thickness for the air gap of south-facing PV wall (0.06 m) is recommended in Hong Kong in terms of the overall thermal performance. Bloem [14] and Sun et al. [15] studied the electrical and thermal performance evaluation of photovoltaic (PV) systems integrated as cladding components of the buildings. The optimum designs suggestions were put out through the researches. Azadian and Radzi [6] categorized four main barriers and gave suggestions to enhance the efficiency of generating and maintaining power. Related researches also indicate the PV module integrated building facade has great benefit in energy and resources saving [16–21].

Although various research on PV wall have been conducted, seldom research are focused on the safety and power generation performance of BIPV systems when and after earthquakes hit. As known to us, China is a country with frequent earthquakes. The cost of high-rise buildings becomes very huge. Therefore, the new constructed buildings must meet the need of both energy saving and seismic safety especially in high-rise buildings. Currently, the PV modules of building facades are designed as nonstructural components attached to the building envelope. As a special nonstructural component, the PV facades of high-rise buildings may cause secondary disaster during earthquake, if the PV system is not properly designed. The seismic design of nonstructural components has been attract more and more attentions. Special requests are given in building seismic design by ASCE 7-10 [22] and the Chinese Code GB 50011-2010 [23]. But, current nonstructural requests are not so clear and not proper to PV component. Actually, PV system has the property of producing electricity that is excellent disaster prevention and mitigation solution to the earthquake hit area. However, the reliability of power supply for disaster relief after earthquake also depends on the proper seismic design [24].

Shear wall is one of the most widely used structural members in the high-rise buildings due to its high lateral bearing capacity and energy dissipation capacity [25–29]. According to the related engineering installation atlas of BIPV, the PV module is installed on building walls by bolts and steel beams, but even this installation atlas form has not been evaluated in terms of seismic safety. Moreover, expansion anchor bolt has been proved not so reliable under seismic action.

As we have seen, BIPV has been applied worldwide, while the structural property especially the seismic behavior has

not been evaluated. Current BIPV forms are seldom applied on structural facades especially on high-rise structures for its safety consideration. With the consideration of seismic safety and material saving, a new kind of PV facade form, an integrated PV module with shear walls, called U-shaped steel connected PV integrated shear wall (U-PV-SW), is proposed according to the current PV installation forms. As a possible PV facade application form, this U-PV-SW is designed in detail here. To clarify the construction procedure and evaluate the structural property and the electricity-generation capacity, a U-PV-SW model was made and tested. The design and installation measure are simulated by model construction. The seismic behavior and power generation capacity are evaluated under the reversed low cyclic loading test. And the temperature variation of the PV module and walls is tested simultaneously.

2. Design and Construction of the U-PV-SW

A U-shaped steel connected PV module integrated shear wall is designed in this study. The PV module was mounted on the predesigned embedded steel plates of the shear wall by bolts and U-shaped steel connectors. In this design, a multicrystalline silicon (mc-Si) PV module with maximum efficiency of 15% was chosen here. The dimensions and details of the PV module are shown in Figure 1. The total weight of PV module is 18.6 kg. The electrical and mechanical characteristics are listed in Table 1. The shear wall was designed as common structure member with embedded columns according to Chinese Code for Seismic Design of Buildings (GB 50011-2010) and Code for Design of Concrete Structures (GB 50010-2010) [23, 30]. Four steel plates with dimensions 143 mm × 110 mm × 8 mm are fixed on the shear wall which is designed according to request of embedded element in Chinese Code for Design of Steel Structures (GB 50017-2003) [31]. The embedded plates were welded with reinforcements cage of the shear wall by four D8 (diameter = 8 mm) reinforcements before the concrete were casted. Then, the U-shaped steel connectors were welded on the embedded steel plate so as to be fixed on the reinforced concrete shear wall. Since the PV module is applied on high-rise structures, we chose steel instead of aluminum alloy as the connector material. The dimensions of shear wall and embedded plates and U-shaped connectors are shown in Figure 2.

Commonly, concrete shear walls are designed as a ductile member and often failed at the corner as concrete crush and steel bar buckling after earthquake hit. Under this consideration, the embedded steel plates are located away from the critical area so as to avoid the connection failure caused by corner concrete crush.

The U-shaped connectors were welded to the embedded steel plates after the shear wall concrete was casted, see Figure 2(a). There is a 15 mm × 12 mm preformed hole on the U-shaped connector to connect PV module by bolts; see Figure 2(b). The PV module was connected to the connectors by four D8 (diameter = 8 mm) bolts. Since the main structural response under earthquake is lateral deformation, the holes on the U shape connector can provide relative movement space between bolts and connector like most bolt

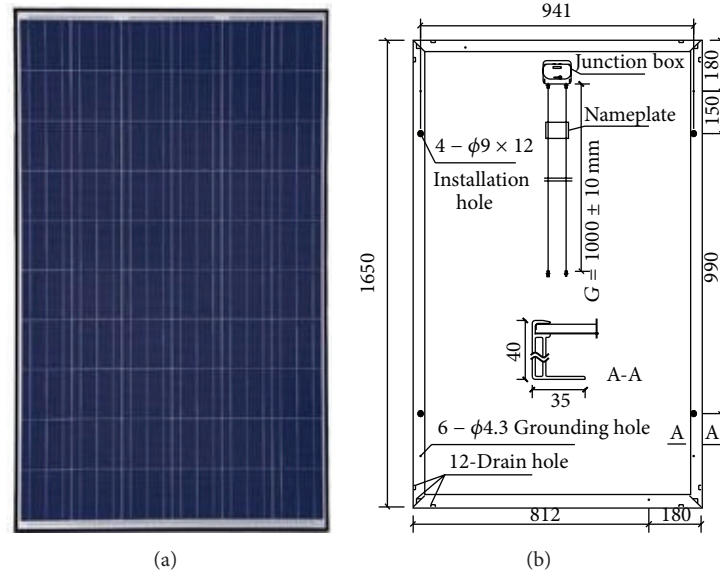


FIGURE 1: Dimension and details of the PV module (unit: mm). (a) Front view. (b) Back view.

TABLE 1: The PV module specifications.

Solar panel model	TSM-PC05A.08
Electrical characteristics (STC)	
Peak power Watts- P_{MAX} (W_p)	260
Power output tolerance- P_{MAX} (%)	0~+3
Maximum power voltage- V_{MPP} (V)	30.6
Maximum power current- I_{MPP} (A)	8.50
Open circuit voltage- V_{OC} (V)	38.2
Short circuit current- I_{SC} (A)	9.0
Mechanical characteristics	
Solar cells	Multicrystalline 156 × 156 mm
Cell orientation	60 cells (6 × 10)
Module dimensions	1650 × 992 × 40 mm
Weight	18.6 kg
Glass	High transparency solar glass 3.2 mm
Frame	Black anodized aluminum alloy
J-box	IP65 rated
Cables	Photovoltaic technology cable 4.0 mm ² , 1000 mm
Connector	Original MC4

connected steel elements. Moreover, the installation error can also be adjusted by the enlarged hole.

Figure 3 shows the installation details of the U-PV-SW (U-shaped steel connected PV integrated shear wall). Firstly, the U-shaped steel connectors were welded in the predesigned position of embedded plates. Then, the PV module was connected to the steel connectors by four bolts. Some pieces of rubber gaskets (HS=45) with a thickness of 3 mm were placed between the bolts and PV module as dampers to reduce the collision. The thickness of the air gap between the PV modules and the facade has a significant influence on the thermal performance of PV wall [11, 13]. In

this paper, the air gap was determined to be about 0.075 m for Shanghai weather conditions.

The construction procedure was simulated through the model fabrication. The embedded element is fixed on the shear wall smoothly, and the U shape connector was also welded on the embedded plates conveniently, but it takes a little bit time. If it can be installed by bolt or locked directly, the installation period can be reduced obviously. When installing the PV module with the U-shaped connector, the bolt needs to be screwed carefully. If the space of the U shape connector is larger, the bolt connecting will be easier or use lock form.

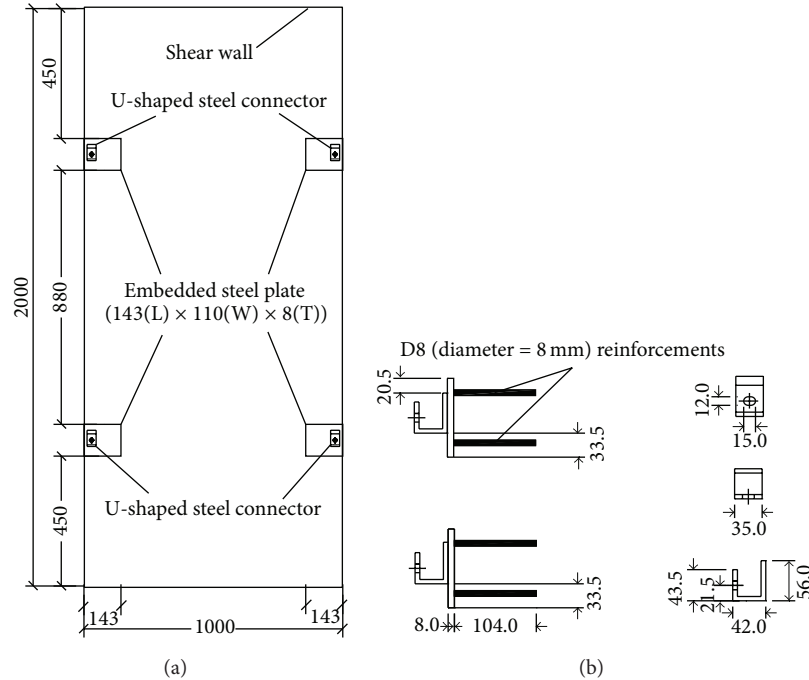


FIGURE 2: Details of shear wall, embedded plate, and U-shaped connector. (a) Shear wall and embedded steel plate. (b) U-shaped steel connector (unit: mm).

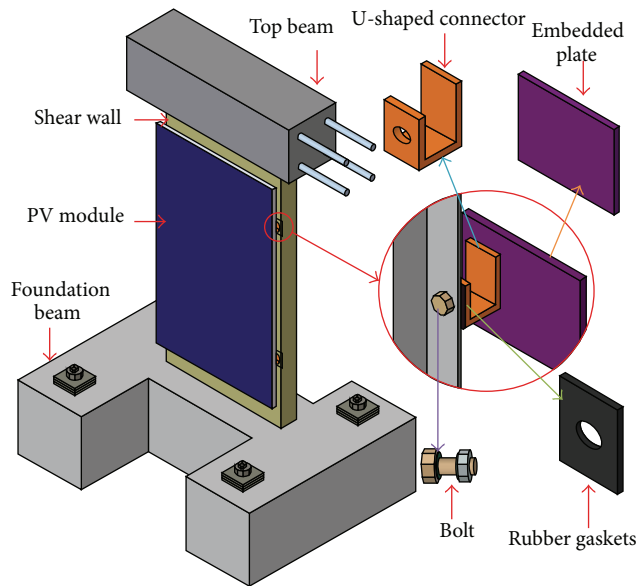


FIGURE 3: Installation details of U-SW-PV.

Through this installation simulation, several suggestions can be made. (1) The connector can be bolted or locked with the shear wall; (2) the bolt screw space needs to be considered when installing the PV module with the connector; and a lock form connection is preferable.

3. Experimental Investigation

3.1. Test Specimen. The specimen labeled as U-PV-SW was modeled and tested in this study. The shear wall of this specimen was designed as 1/2 scaled shear wall of the typical

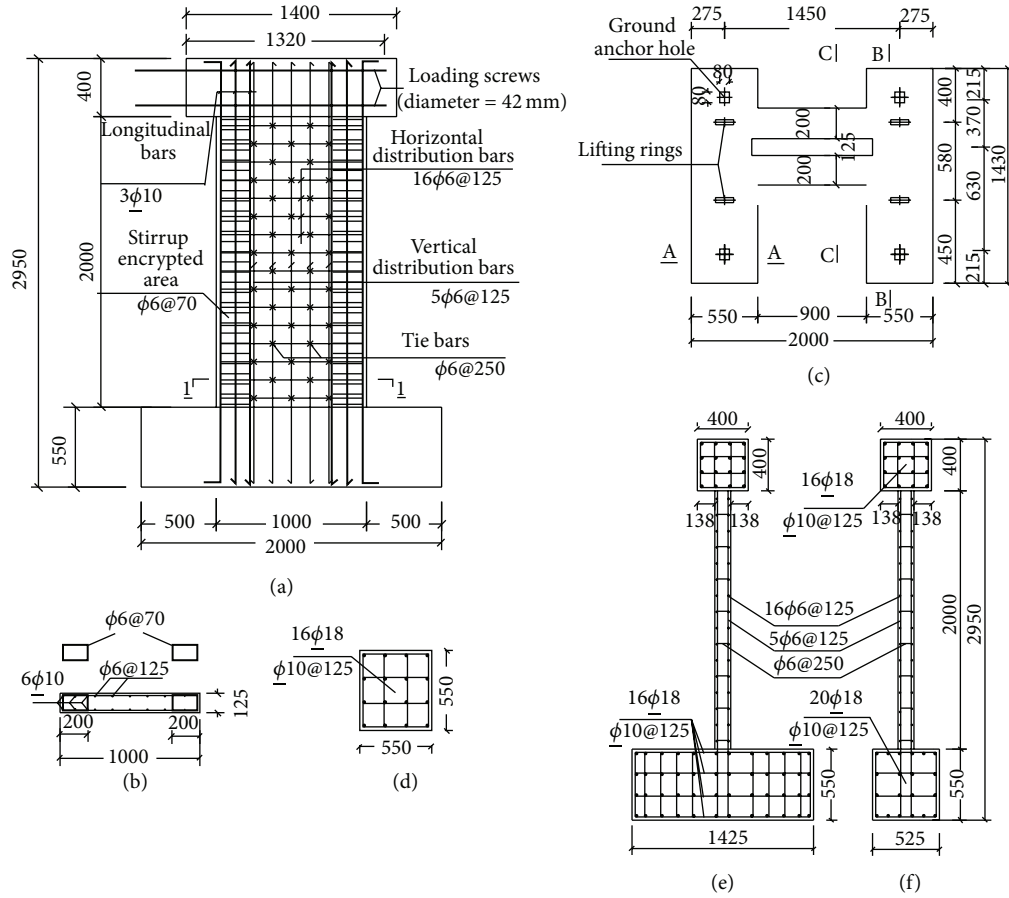


FIGURE 4: Dimension and details of specimen, U-SW-PV-1 (unit: mm). (a) Elevation view. (b) Section 1-1. (c) Plan view of foundation beam. (d) Section A-A. (e) Section B-B. (f) Section C-C.

story of a high-rise structure. Figure 4 shows the details of the specimen. The shear wall is 2000 mm in height, 1000 mm in length, and 125 mm in thickness. The aspect ratio (i.e., height-to-width ratio) of the shear wall is 2.0. A reinforced concrete foundation beam with a cross-section of 550 mm by 550 mm was casted together with the wall, through which the specimen was securely clamped to the reaction floor by 4 large size bolts. The reinforced concrete top beam with a cross-section of 400 mm by 400 mm was casted as well, through which the horizontal loads were applied to the wall.

As shown in Figures 4(a) and 4(b), the reinforcement details of the shear wall and the boundary elements were designed according to the provision of Chinese codes GB 50011-2010 [23] and GB50010-2010 [31]. The reinforcement of the foundation and top beams was designed strong enough to ensure the beams will not be damaged during the test, and there was no damage in the process of the actual test. Figures 4(d), 4(e), and 4(f) present the reinforcing details of these beams, respectively.

3.2. Material Property. The concrete of C40 is adopted in the specimen making (nominal cubic compressive strength $f_{cu,d} = 40$ MPa, and design value of axial compressive strength $f_{c,d} = 19.1$ MPa). Actual cubic compressive strength $f_{cu,t}$ of the concrete was tested by cubes of 150 mm ×

TABLE 2: (a) Material properties of concrete. (b) Material properties of steels.

(a)			
Strength grade	C40		
Test cubic compressive strength, $f_{cu,t}$ (N/mm ²)	37.7		
Test axial compressive strength, f_{ct} (N/mm ²)	28.3		
Young's modulus, E_s (N/mm ²)	33800		
(b)			
	HPB 235 (φ6)	HRB335 (Φ10)	Q235 (steel plate)
Yield strength, $f_{y,t}$ (N/mm ²)	297.7	451.7	425.5
Ultimate strength, $f_{u,t}$ (N/mm ²)	430	545	440.6
Young's modulus, E_s (N/mm ²)	2.0×10^5	1.6×10^5	1.8×10^5

150 mm × 150 mm concrete blocks and the results are listed in Table 2(a). And the actual value of axial compressive strength of concrete $f_{c,t}$ was tested on a prism with dimension of 300 mm × 100 mm × 100 mm. It is worth noting that the actual

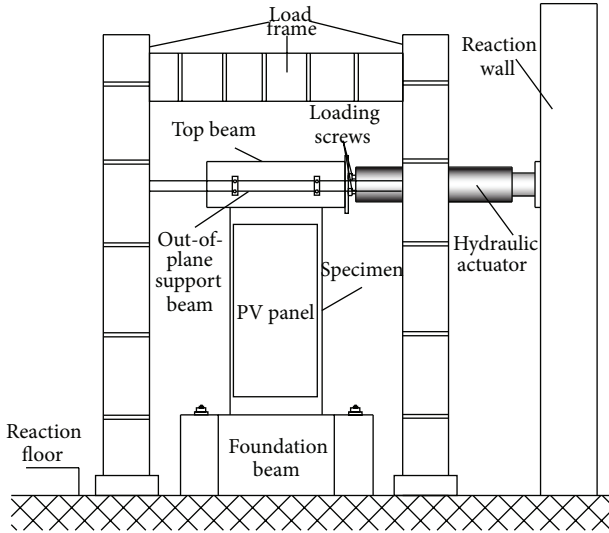


FIGURE 5: Test setup.

value of axial compressive strength of concrete $f_{c,t}$ was about 0.75 times of $f_{c,u,t}$ in consistent with the value of 0.76, which is recommended by the Chinese Code for Design of Concrete Structures (GB50010-2010) [31].

Four steel embedded plates were made with the steel of grade Q235 (nominal yield strength $f_y = 235$ MPa, design value of yield strength $f_{y,d} = 215$ MPa). There were two types of reinforcements in the shear wall, and their strength grades were HPB235 ($f_y = 235$ MPa) and HRB335 ($f_y = 335$ MPa), respectively. The actual test values of both steel plates and reinforcements are listed in Table 2(b). The bolts of D8 are used to connect U shape steel connector and PV module (nominal ultimate strength of D8 bolts, $f_u = 400$ MPa, and the ratio $f_y/f_u = 0.8$).

3.3. Test Setup, Loading Program, and Instruments. Figure 5 shows the test setup, where the specimen was located in the steel frame. The foundation beam was clamped to the floor by bolts. The top beam was connected to a hydraulic actuator in the horizontal direction by four loading screws (diameter = 42 mm). Several rollers with out-of-plane support beams were set on both sides of the top beam of the shear wall to prevent out-of-plane deformation during the whole test. The low cyclic lateral load was acted by the actuator mounted horizontally to the reaction wall. The horizontal loading point (i.e., the mid-height of the top beam) was 2200 mm above the base of the wall, so the shear span ratio of the wall was 2.2.

Figure 6 shows the loading history of the test, which was controlled by displacement. Before the specimen was yield, the displacement was increased by 1 mm with each cycle. After the specimen was yield, the displacement was increased as by 2 mm with every three cycles. The ultimate displacement was designed as 40 mm, while, in order to ensure the safety of the specimen, and the last two loading sequence (37 mm and 40 mm) was maintained only one cycle. In each loading sequence, the specimen was pushed first and then pulled by the actuator. The test was terminated when the loading

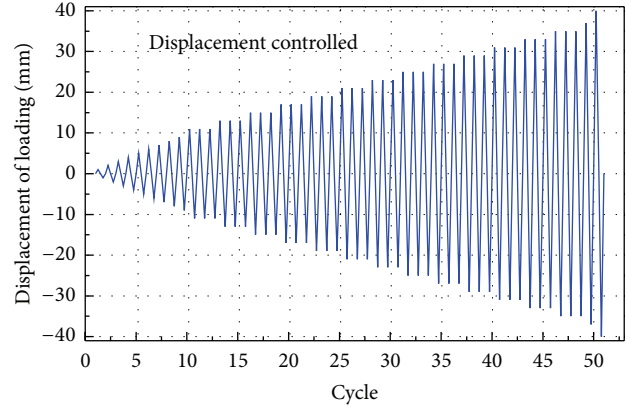


FIGURE 6: Loading sequence.

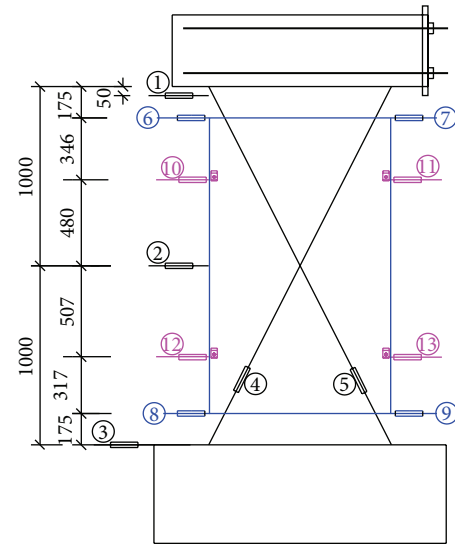


FIGURE 7: Location details of LVDTs.

displacement reached 40 mm, (40 mm is 1/50 of the height of the specimen). It is regarded that a structure may collapse when the story drift angle exceeds the criterion of 1/50 [23].

During the experiment of the specimen, several sensors and data acquisition system were employed to collect the structural behavior information. The sensors in the actuators were used to measure the lateral load and top displacement of the specimen. The LVDTs (linear variable different transformers) were used to measure the global and local deformations of the shear wall. Figure 7 gives out the location of the LVDTs distributed on the specimen. Three LVDTs (LVDTs 1# to 3#) were used to measure the displacement variation along the height of the wall. One pair of intercrossed LVDTs (LVDTs 4# and 5#) measured the shear deformation of the wall. Two pairs of horizontal LVDTs (LVDTs 6# to 9#) measured the lateral displacement along the height of the PV module in both left and right sides. Another two pairs of horizontal LVDTs (LVDTs 10# to 13#) were employed to measure the lateral displacement of the four connectors. In addition, several strain gauges were stuck on the steel bars

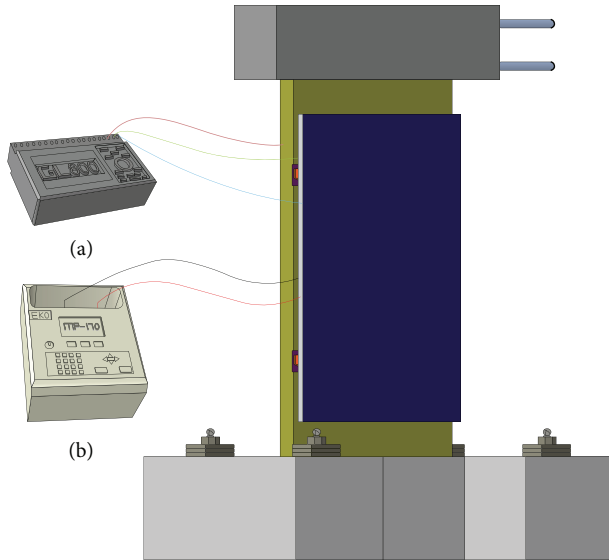


FIGURE 8: Instruments for measuring temperature and electricity. (a) GRAPHTEC midi logger GL800. (b) EKO MP-170.

of the shear wall to measure the vertical, horizontal strain variation during the test.

Figure 8 shows the instruments for measuring temperatures and electricity performance of the PV module. As the test was conducted in winter, the sunshine is not so rich, and artificial sunshine environment was established in the laboratory by using several high-power halogen lamps, which were equally spaced to ensure the uniform of irradiance (see Figure 9). The artificial lighting system was consisted by four 500 W halogen lamps in the middle height of the PV module and four 1000 W halogen lamps at the upper and bottom height of the PV module. The position was fixed during the whole testing process to confirm the same lighting condition. Three thermocouples were used to measure and record the temperature variation of U-SW-PV. Two of them were stocked on the internal and external surfaces of the shear wall. Another one was stuck on the back surface of the PV module. The temperature data of the three thermocouples was collected by a data logger (GRAPHTEC midi logger GL800, see Figure 8).

The power generation behavior of PV module was tested by *I-V* tracer (EKO MP-170, made in Japan). The voltage and current variation curve, the maximum power— P_{MAX} , the voltage at the maximum power point— V_{MPP} , and current at the maximum power point— I_{MPP} were also recorded by the *I-V* curve tracer. Actual test setup and instruments are shown in the Figure 9.

4. Experimental Results

4.1. Seismic Performance of U-SW-PV

4.1.1. Overview. The typical development of the observed damage was shown in Figure 10. Initial horizontal cracks appeared at the bottom of both sides of the wall when the top displacement reached 8 mm, as shown in Figure 10(a).

Subsequently, the outmost longitudinal reinforcement of the boundary element became yield according to the tested steel bar property. Next, the diagonal cracks were generally observed immediately after the initial yielding of the outmost longitudinal bars. And Figure 10(b) shows the cracks on the shear wall when the drift angle is 1/120 (that is a safety limit under severe earthquake according to Chinese seismic code). And the PV module still remained perfect at this moment (see Figure 10(c)). With the increasing of the horizontal loading, new horizontal and diagonal cracks developed fast, and the maximum width of the cracks were near 2 mm. Then, it is observed that the concrete cover at the bottom of the shear wall became crushed. Following the concrete cover spalling, the stirrups and longitudinal reinforcements were exposed, and the bars buckled or broke finally.

4.1.2. Damage and Failure Pattern

(1) Shear Wall. The shear wall of the U-SW-PV specimen experienced reinforcements local buckling and concrete compressive crushing. The damage process can be divided into elastic stage, plastic stage, and severe failure stage. (1) The elastic stage started from the initial loading to the yield state of the specimen. In the elastic stage, the top drift angle of the specimen is within 1/200, which meets the requirement of the Chinese seismic code (i.e. 1/1000). Drift angle is defined as the ratio of the lateral top displacement to the height of the shear wall. When the drift angle is 1/200, the strain of the reinforcements indicated the steel bars at the outer edges of the bottom of the wall also yielded. (2) After the specimen yielded, cracks and concrete spalling developed fast with the increasing of the loading. And the longitudinal bars came to be exposed. When the drift angle reached 1/116, the lateral force reached the peak value. (3) Then, it is the severe failure stage, which started from the specimen reaching the peak load to the specimen's almost collapse. In the end, the longitudinal bars fractured and the concrete in the plastic hinge area was crushed extremely.

(2) Connection. The embedded plates and the U-shaped connector have not subjected any damage during this test (see Figure 11). Only tiny cracks appeared on the concrete around the embedded steel plates, and no concrete spalling or crushing was observed. Figure 11 demonstrates the details of the specimen after the test finished. From this figure, we can see the U-shaped connectors remained perfect when the specimen reaches the ultimate state.

(3) PV Module. The PV module is installed on the shear wall by 4 U shape steel connectors. There is no any physical damage found during and after the cyclic lateral loading test. The tempered glass, the solar cells, and the aluminum alloy frame were still in perfect physical condition.

4.1.3. Lateral Force-Top Displacement Relationship and the Deformation Capacity. The relationship curves of the lateral force and the top displacement of the shear wall, including the hysteresis loop curves and the envelope curve, are shown in Figures 12(a) and 12(b), respectively. The hysteresis loop

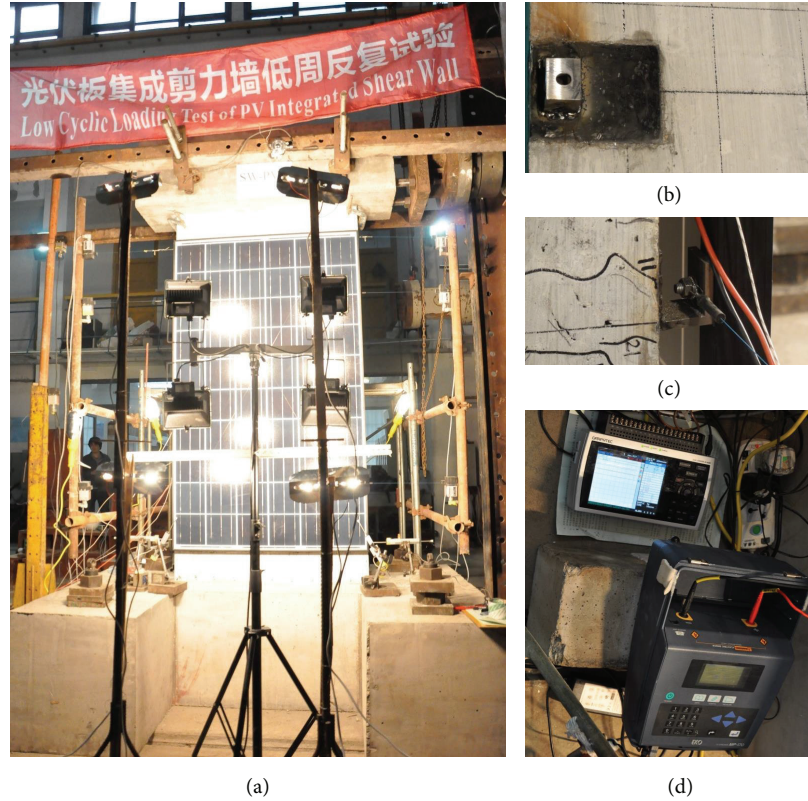


FIGURE 9: The real test setup and instruments for U-SW-PV-1. (a) Test setup. (b) Connection of U-shaped connector and embedded steel plate. (c) Connection of U-shaped connector and PV module. (d) Instruments (GL800 and EKO MP-170).

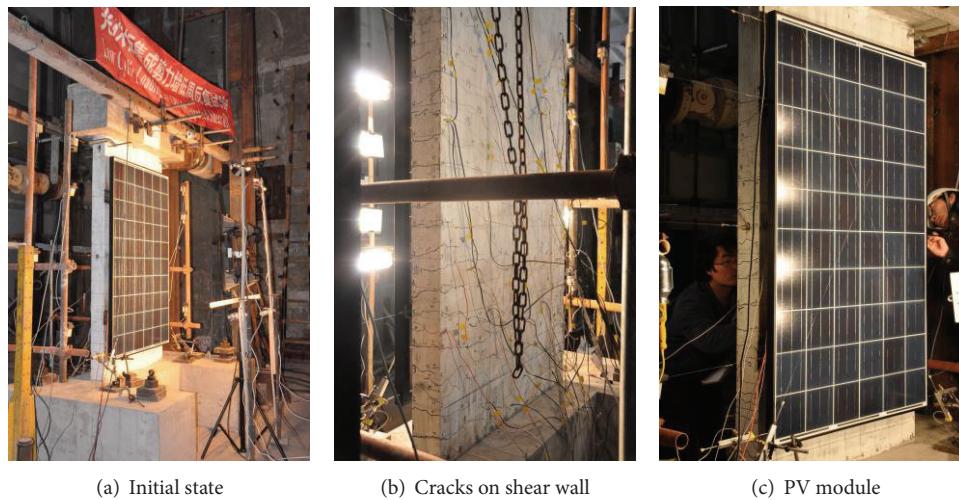


FIGURE 10: Typical damage development. (a) No damage (drift angle: 1/1000). (b) Cracks on shear wall (drift angle: 1/120). (c) No damage on PV module (drift angle: 1/120).

curves of the wall appeared as reversed “S” and were similar to the same type shear walls [25–29]. The yielding and ultimate state are illustrated in Figure 13. The hysteresis curves of the shear wall are almost linear and the residual drift angle is less than 1/1000. When the shear wall is yield, the loading stiffness is apparently decreased, and the lateral bearing force is still increased. When the drift angle increases to 1/120 (i.e., the drift angle limit for the RC shear wall structure subjected to an

earthquake specified by code GB50011-2010 [23]), the residual drift angle of unloading is about 1/400. With the increase of the loading level, the hysteretic loops became plumper until the specimen failed.

The displacement ductility coefficient is defined as

$$\mu_{\Delta} = \frac{\Delta_u}{\Delta_y}. \quad (1)$$

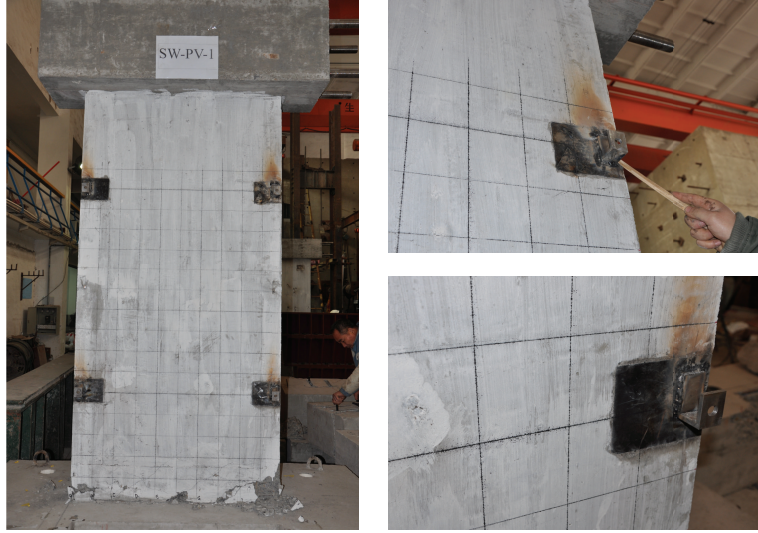


FIGURE 11: Damage details of the U-shaped connectors when the specimen reached its ultimate state.

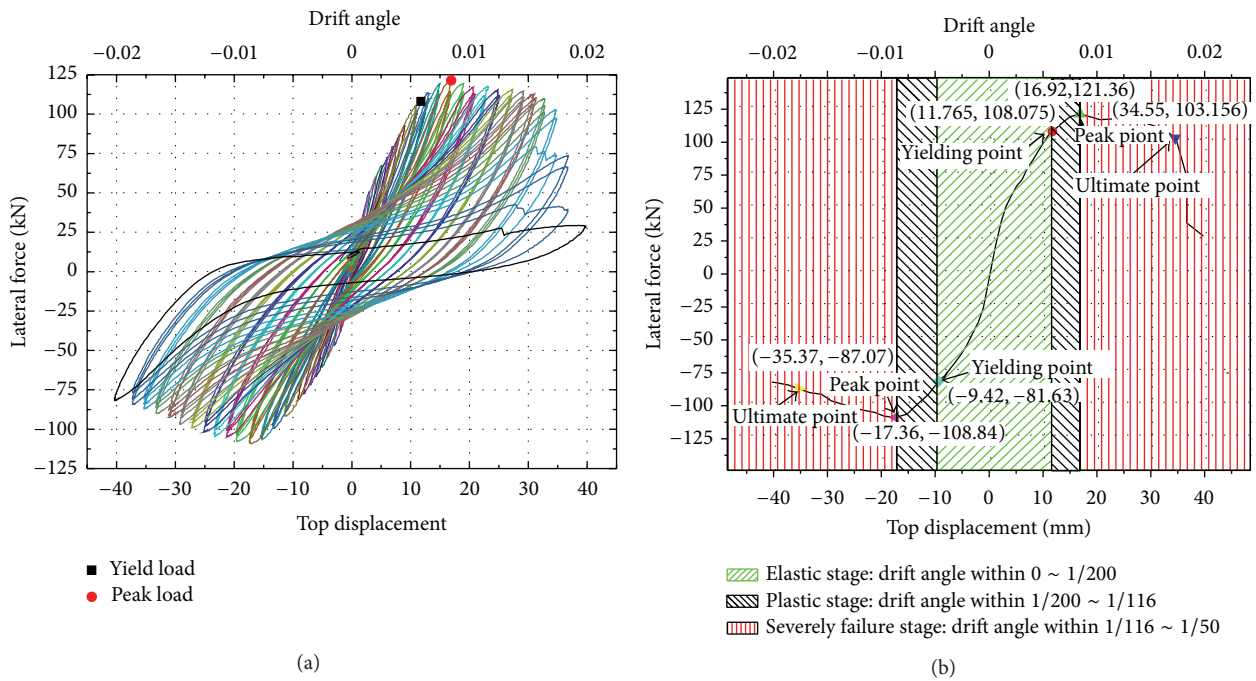


FIGURE 12: Lateral force-top displacement curve of the shear wall. (a) Hysteresis loop curves. (b) Envelope curve.

Here, Δ_u and Δ_y are ultimate displacement and yield displacement, respectively. The ultimate drift angle is

$$\theta_u = \frac{\Delta_u}{H}, \quad (2)$$

where “ H ” is the height of the LVDT 1# to the wall basement. The ultimate drift angle θ_u is the average value of the pulling and pushing directions. The critical deformation values are listed in Table 3.

4.2. Seismic, Electricity Generation, and Temperature Performance

4.2.1. Seismic Performance. Glass is the main carrier of PV module, so the PV module integrated building facades can be considered as a special type of curtain wall. According to the Chinese Technical Code for Glass Curtain Wall Engineering (JGJ 102-2003) [32], the ultimate story drift angle limit value in the glass curtain wall is three times of the elastic drift angle limit of the main structure in seismic design. Since the elastic story drift angle limit value of shear wall structure is 1/1000,

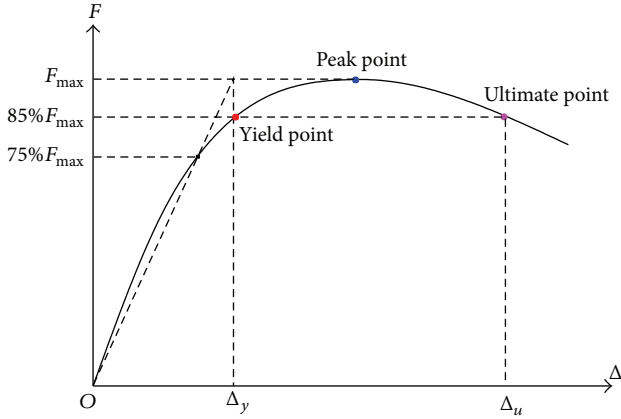


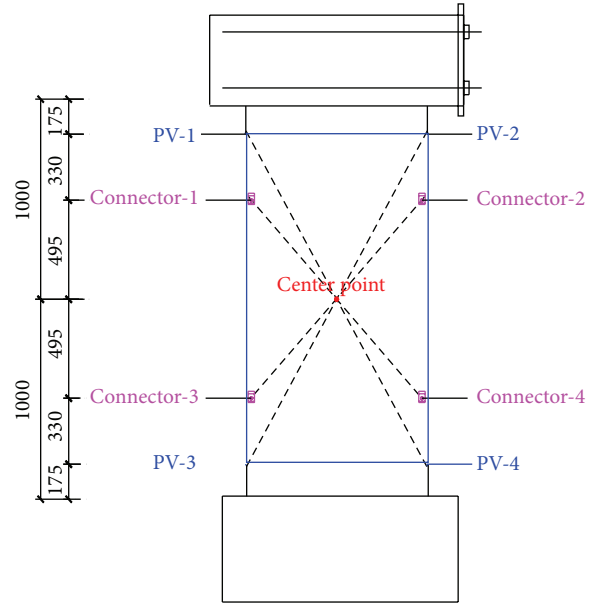
FIGURE 13: Definition of yielding and ultimate state of the shear wall. (Note: yield point is the point on the curve with the same abscissa with the intercross point of the horizontal line at peak point and the connecting line between 75% peak point and origin; ultimate point is the point on the curve when the lateral force decreases to 85% of the maximum value).

TABLE 3: Critical deformation and ductility coefficient.

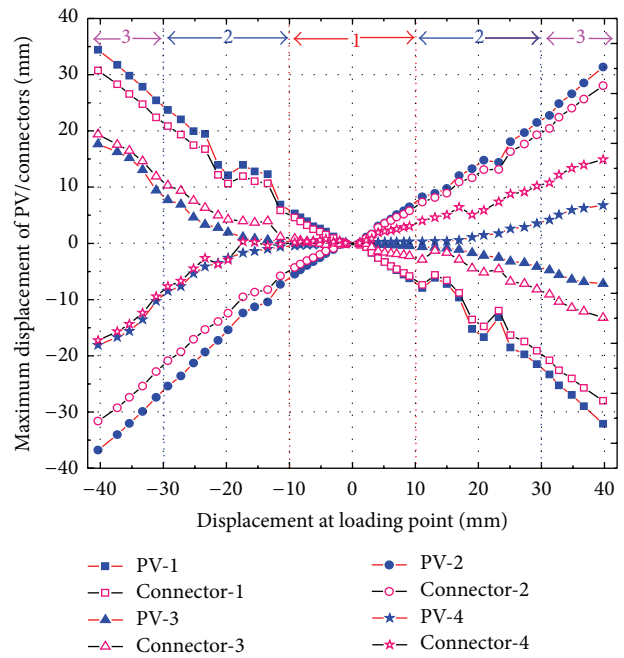
Specimen	U-SW-PV	Description
Yield disp. Δ_y (mm)	11.77/9.42	Push/pull
Ultimate disp. Δ_u (mm)	34.55/35.37	Push/Pull
Ultimate drift ratio θ_u	1/56	Average
Disp. ductility ratio μ_Δ	3.345	Average

thus the ultimate limit value of PV module is 3/1000, which is a relatively conservative design value to actual damage value.

To test the deformation of the PV module during the cyclic lateral loading procedure, the maximum horizontal displacements of PV module and U-shaped connectors in every loading cycle were monitored and recorded by LVDTs (i.e., LVDTs 6[#] to 9[#] for PV module and LVDTs 10[#] to 13[#] for U-shaped connectors, see Figure 7). The locations of measurement points were shown in Figure 14(a), and the maximum displacements were shown in Figure 14(b). The curves in Figure 14(b) were the connection line of the maximum displacements during every loading cycle. Accordingly, three deformation stages were divided here. The first is the absolute elastic deformation. In this stage, the shear wall drift angle is about 1/200, and the PV module and connectors were basically in linear state. When the absolute displacements are between 10 and 20 mm, the shear wall was in the damage developing stage (second stage). And, in this stage, the envelope curves appeared obvious fluctuation. With the development of the cracks and the yielding of the longitudinal reinforcement, the deformation of the shear wall came into nonlinear state, which did not keep linear deformation relationship with the PV module. The last deformation stage is defined by the absolute displacements between 30 and 40 mm. In this stage, the curves of the lower position (PV 3, 4 and connectors 3, 4, as shown in Figure 14(a)) were obviously nonlinear due to the severe damage of the shear wall foot.



(a)



(b)

FIGURE 14: The maximum horizontal displacements of PV module and U-shaped connectors. (a) Location of deformation monitors. (b) The maximum horizontal displacements.

To illustrate the deformation compatibility of the shear wall and the PV module, the drift angle development of the shear wall and the PV module are drawn in Figure 15. In this figure, the difference of the drift angle during the whole loading process (presented by 1) can be observed. Since the loading was added on the beam of the shear wall, the drift angle development of the shear wall is the most obvious. The drift angle development of the PV module is in accordance

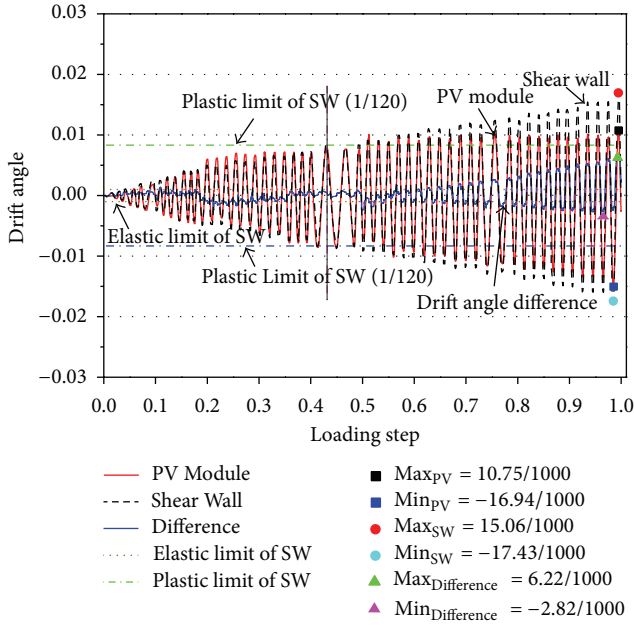


FIGURE 15: The displacement difference between the PV module and the shear wall.

with that of the shear wall at first; to be exact, the two curve matched with each other before the shear wall came into the limit value of plastic drift angle (i.e., 1/120 [23]).

From Figure 15, we can find that, with the increase of lateral load, the drift angle of the shear wall grows up gradually (the maximum drift angle is 15.06/1000), while the growth of the PV module drift angle is not so obvious (the maximum drift angle is 10.75/1000). The difference of the drift angle of the shear wall and PV module was also drawn out in Figure 15. With the increase of the lateral displacement, the difference of the two drift angle grew up gradually. The minimum difference of the drift angle is 2.82/1000 when the shear wall is in severe damage stage (i.e., no collapse stage according to China code [23]). However, when the shear wall failed, the value is 6.22/1000. The growth of the difference of the two drift angle indicates that the incompatibility of the PV module and the shear wall became obvious with the plastic development of the specimen.

The investigation of the drift angle development can provide the following information. (1) According to Chinese seismic design code [23], the U-PV-SW is exactly perfect before the drift angle reaches 1/1000 (1/1000 is the critical limit of elastic state of shear structures in Chinese Seismic Code) and did not collapse or get severely damaged before the drift angle reaches 3/1000 and 1/120 (3/1000 and 1/120 is the critical limit of plastic state of glass curtain wall and shear wall structures in Chinese Seismic Code); (2) the drift of the PV module is in accordance with that of the shear wall before the drift angle reaches 1/120; (3) when the drift angle of the shear wall is over the plastic limit of Chinese seismic code (i.e., 1/120), the difference of the two-drift angle became more and more obvious. The maximum difference of the two-drift angle is 6.22/1000, which indicates that deformation of the

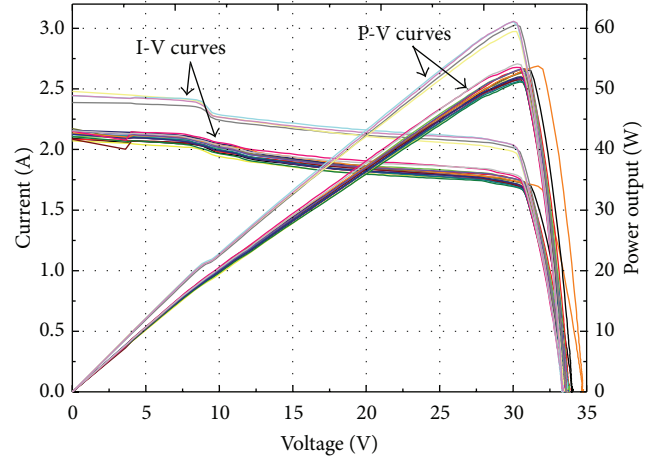


FIGURE 16: The *I-V* curves and *P-V* curves of the PV module.

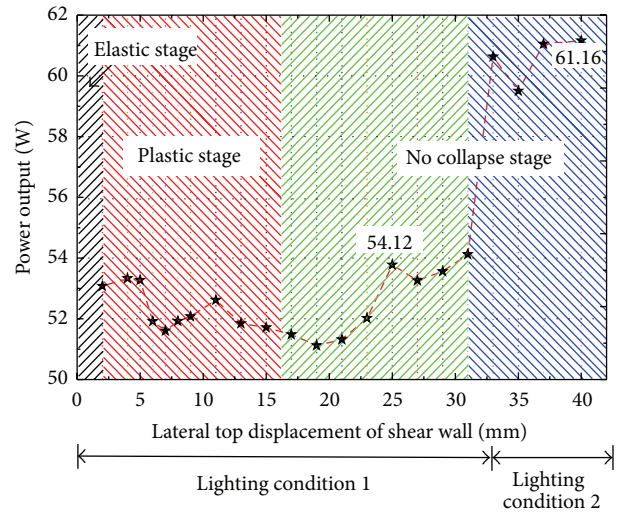


FIGURE 17: Maximum power output of PV module.

shear wall and the PV module is obviously inconsistent at the large deformation stage.

4.2.2. Electricity Generation Performance. The *I-V* curves and *P-V* curves of the PV module during the whole test process is shown in Figure 16. The artificial lighting environment was established before the test. The *I-V* and *P-V* data of the PV module were measured and recorded by the EKO MP-170 *I-V* curve tracer before and during the whole cyclic test. It is worth noting that the voltage of the artificial lighting power supply became higher than before when the socket was changed to another one after the lateral top displacement reached 33 mm for circuit problem. So, the artificial lighting condition can be divided into two stages as seen in Figures 16 and 17. So, the generated power in the first lighting condition is far less than the second lighting condition. The curves of both *I-V* and *P-V* are also obviously different under the two lighting conditions as shown in Figure 16.

TABLE 4: Electric power output of the PV module under the two artificial lighting conditions.

Power (W)	Elastic stage	Plastic stage	No collapse stage	
			Condition 1	Condition 2
Average value	53.029	52.256	52.584	60.585
Percentage	100%	98.54%	99.16%	/

Note:

① The percentage was defined as the average power output ratio to that of elastic stage.

② According to Chinese seismic code [23], the drift angle of elastic stage is within 1/1000 and the plastic ultimate stage is 1/120.

The maximum power outputs of the PV module were shown in Figure 17. Because the temperature of the experimental environment is relatively cold, and the test was conducted in the indoor laboratory, the artificial lighting is employed to simulate the sunshine, as shown in Figure 9. Under the artificial lighting conditions, the current and the voltage generated by the PV module were collected. The average maximum power generated by the PV module was around 52.45 W under the first lighting condition (the lateral top displacement of shear wall is within 1 mm to 31 mm). And the average maximum power was up to around 60.58 W under the second lighting condition (the lateral top displacement of shear wall is within 31 mm to 40 mm). The electric power output performance of the PV module under the two artificial lighting conditions is listed in Table 4. In this table, the power generation performance is compared under different specimen drift angle with the same lighting condition.

From Figures 16 and 17 and Table 4, we can find that the power generation performance keeps stable under cyclic movement, and the power capacity is not obviously influenced by the failure of the shear wall. To be exact, the power output in plastic stage is 98.54% compared to the elastic stage and 99.16% in “no collapse” stage (severe damage stage).

4.2.3. Temperature Variation. As mentioned above, the temperature sensors were stuck on internal and external surface of the shear wall center and the back of the PV module center. The temperature variation of the back surface of PV module and the internal and external surfaces of shear wall during the whole test process were monitored and shown in Figures 18 and 19. In addition, the temperature difference curve between the back of PV module and external surface of shear wall was drawn in Figure 18, and the temperature difference curve between the external and internal surface of shear wall was drawn in Figure 19.

During the whole test, the ambient temperature was around 7°C (Dec 26, 2013, Shanghai). The test was conducted from 8:30 am to 14:30 pm, and there was a break in lunch time. The temperature was measured through the whole process of the cyclic test. According to the measurement results, the temperature of PV module rose fast under the artificial lighting and maintained around 40°C soon. The temperature of the external surface of the wall increased from 8°C to 15.9°C. The temperature of the external surface of the shear wall increased obviously at first and then came to increase slowly. It rose from 7.7°C at 8:35 am to 10.7°C at 9:38 (rose 3°C/1 h) and rose from 14.6°C at 13:08 to 15.1°C at 14:08 (rose

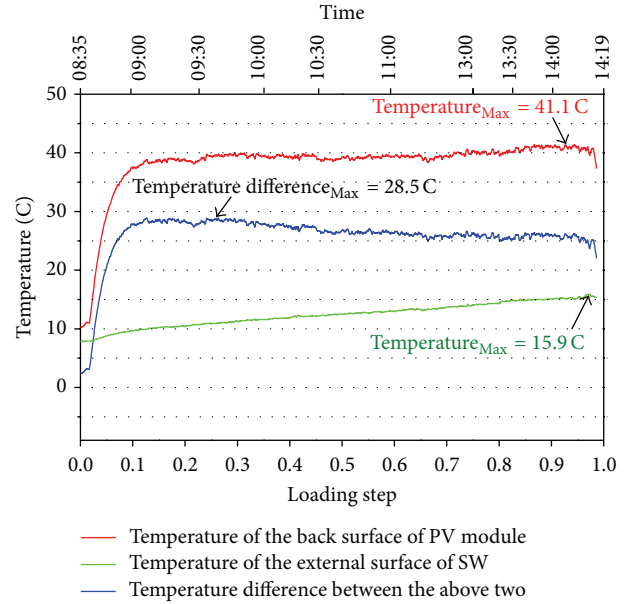


FIGURE 18: The temperature data of PV module and the external surface of shear wall.

0.5°C/1 h). Therefore, the temperature tends to be basically constant.

Figure 19 shows the temperature of shear wall in both external and internal surfaces. The temperature of internal surface of the shear wall increased with the cyclic experiment process, and its final temperature reached up to 13.6°C at 14:19 pm. The temperature difference between the external and internal surface was maintained around 2°C during most of the test process.

Each temperature curve in Figures 18 and 19 showed that the temperature variation was not obviously influenced by specimen drift state or damage development state, and the PV module and the shear wall tend to maintain at a certain temperature value under the irradiation condition.

5. Discussions

This paper investigated the seismic, electricity generation, and thermal performance of the U-shaped steel connected PV module integrated shear wall (U-PV-SW), as well as the construction procedure. From the above tested results,

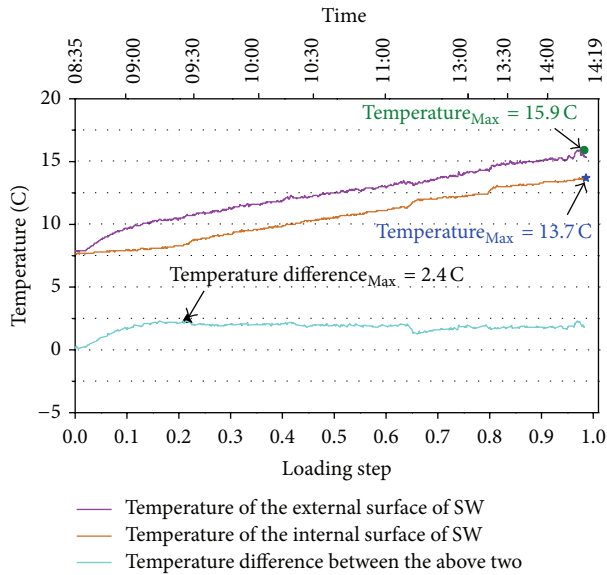


FIGURE 19: The temperature data of the shear wall in both internal and external surfaces.

the U-PV-SW demonstrates the applicability to be used in residential or office buildings.

(1) *Seismic Performance.* The failure pattern of the shear wall demonstrates that the damage pattern has not been obviously influenced by the integrated PV module. The critical failure pattern is also at the bottom corner as concrete crushing and steel bars buckling. It is almost the same as the tests the authors had conducted for the similar shear walls [27–30]. The drift angle of the shear wall is 1/200 and 1/116, which meets the requirement of Chinese seismic design code [23]. As Chinese seismic design code gives out the limits at elastic stage and plastic stage, these two limits of shear structures are 1/1000 and 1/120. Actually, these two limits are applied to confirm no damage at frequent earthquake and no collapse at severe earthquake. According to this idea, the U-PV-SW specimen absolutely meet the requirement for it has no damage before the drift angle is 1/200 and does not collapse till the specimen reached the ultimate state, when the drift angle is close to 1/50.

The PV module is integrated to the shear wall by U-shaped steel connector. Because the main component of PV module is a brittle material, the connector is designed to have enough deformation capacity to prevent the large deformation of PV module when the shear wall gets under severe earthquake. The tested result indicates the PV module and the U shape steel connector suffered no visible damage during the whole seismic simulation test. The drift angle of PV module is basically in accordance with that of the shear wall when the shear wall is within plastic stage. And it is not increased as obviously as that of the shear wall in “no collapse” (severe damage) state. The maximum drift angle of the PV module is 10.75/1000, and that of the shear wall is 15.06/1000. The drift angle difference is about 1/200 when the specimen reached the ultimate state. Therefore, the U shape connector plays an important role in reducing the deformation of the PV

module when the shear wall has severe lateral deformation. The electricity generation efficiency also provides evidence to perfect condition of the PV module. According to Chinese seismic design of glass curtain wall [32], the drift angle limit is 3/1000, while the PV module is not damaged when the drift angle is 10.75/1000, which is far more than that of the required limit value. Therefore, even if the PV integrated shear wall structures are designed according to the current code, it meets the deformation limit requirement.

An important issue is noted here. The drift angle of shear wall is 1/120 under severe earthquake in Chinese seismic design code, and the drift angle limit of glass curtain wall is 3/1000 (about 1/333), which is far less than that of shear wall. If we design the PV integrated shear wall structure with the limit of 3/1000, it will be too strict for the structures and will result in much waste. Two ways are suggested to address this issue. One is to design the connector with enough deformation capacity and vibration reduction effect. The other is to amend the deformation limit of PV system. Both of the two ways need to be investigated for the seismic design.

(2) *Electricity Generation Efficiency.* The electricity generation variation is monitored in the same irradiation condition during the whole seismic simulation test. The collected results are divided into three stages. And the electricity generation at each stage is almost at the same condition. That indicates the electricity generation capacity is not influenced by the lateral deformation of the PV module, and the condition of the PV module is still perfect after the test.

These results indicate that, after severe earthquake hit, the PV module integrated on the buildings can be with perfect condition to continue to generate electricity, so to improve the earthquake rescue capacity by necessary power supply. That is important for life safety and earthquake relief.

(3) *Thermal Performance.* Under the artificial irradiation, the highest temperature of PV module reached 41.1°C, and those of the external and internal shear wall surface tend to be maintained at 15.9°C and 13.7°C. The temperature difference of the external and internal shear wall surface was maintained at 2°C. As known to us, shear wall is a kind of structural member with good insulation performance; with external and internal insulation construction layer, the thermal performance can also be improved. So, applying the PV system to high-rise shear wall structures has both electricity generation capacity and obvious energy saving effect. The maximum temperature difference between shear wall external surface and PV module back is 28.5°C. So, the tested temperature variation provides the evidence that the temperature increase can be obviously reduced by the existence of the air gap. The flowing air can reduce the growth of the building temperature, and, on the other hand, it can ensure that the electricity generation capacity is not influenced by the temperature increase.

(4) *Construction Convenience.* The construction procedure of the U-shaped steel connected PV module integrated shear wall is practiced in this experimental study. The embedded element can be fixed in shear wall conveniently. But, the bolt

method is preferable to the weld method considering the convenience of the installation of the U-shaped steel connector. And the U-shaped connector needs to be optimized with the shape and dimension to install or change the PV modules. However, to allow the deformation incompatibility between the PV module and the shear wall, the optimized connector needs to have enough deformation capacity.

6. Conclusions

This paper proposed a U-shaped steel connected PV integrated shear wall (U-PV-SW). A lateral cyclic loading test was carried out to evaluate the seismic, electricity generation, and thermal performance. The findings and conclusions can be summarized as follows.

- (1) The seismic performance of the shear wall of the U-PV-SW is not obviously influenced by the integrated PV module. And the PV module is in accordance with the shear wall within the plastic drift limitation in Chinese seismic code. The U-shaped connector has obvious deformation capacity to reduce the drift angle of PV module by 1/200, compared with that of the shear wall at the ultimate stage.
- (2) The electricity generation capacity is not influenced by the lateral deformation of the PV module. The power output is almost the same at different deformation stages according to the shear wall seismic design limit. And, with the U-shaped flexible connection, the condition of the PV module is perfect till the completion of the test.
- (3) The temperature increase can be obviously reduced by the existence of the air gap. According to the tested result, the maximum temperature difference between shear wall external surface and PV module back is 28.5°C.
- (4) The construction practice indicates the U-shaped connector needs to be further improved to meet the requirement of easy construction, optimal air gap, and the effective deformation capacity.

Applying the BIPV technology to high-rise buildings needs to meet the requirement of the seismic design code. The design code of glass curtain wall is not adequate for the design of PV module system and should be improved in future PV system design. The connector form still needs to be optimized considering the seismic safety and efficient service performance of both the PV and shear wall.

Conflict of Interests

The authors declare that there is no conflict of interests regarding the publication of this paper.

Acknowledgments

This work was financially supported by Hong Kong, Macao and Taiwan Science & Technology Cooperation Program of

China (2012DFH70130), National Natural Science Foundation of China (51178426), Fundamental Research Funds of the Central Universities, and Zhejiang Provincial Natural Science Foundation of China (LR13E080001).

References

- [1] F. Diner, "The analysis on photovoltaic electricity generation status, potential and policies of the leading countries in solar energy," *Renewable and Sustainable Energy Reviews*, vol. 15, no. 1, pp. 713–720, 2011.
- [2] J. Peng, L. Lu, and H. Yang, "An experimental study of the thermal performance of a novel photovoltaic double-skin facade in Hong Kong," *Solar Energy*, vol. 97, pp. 293–304, 2013.
- [3] S. Barkaszi and J. Dunlop, "Discussion of strategies for mounting photovoltaic arrays on rooftops," in *Proceedings of the International Solar Energy Conference*, pp. 333–338, Washington, DC, USA, 2001.
- [4] S. Mekhilef, R. Saidur, and A. Safari, "A review on solar energy use in industries," *Renewable and Sustainable Energy Reviews*, vol. 15, no. 4, pp. 1777–1790, 2011.
- [5] P. Braun and R. R  ther, "The role of grid-connected, building-integrated photovoltaic generation in commercial building energy and power loads in a warm and sunny climate," *Energy Conversion and Management*, vol. 51, no. 12, pp. 2457–2466, 2010.
- [6] F. Azadian and M. A. M. Radzi, "A general approach toward building integrated photovoltaic systems and its implementation barriers: a review," *Renewable and Sustainable Energy Reviews*, vol. 22, pp. 527–538, 2013.
- [7] D. K. Prasad and M. Snow, *Designing with Solar Power: A Source Book for Building Integrated Photovoltaics (BiPV)*, Images Publishing, 2005.
- [8] V. Delisle and M. Kummert, "A novel approach to compare building-integrated photovoltaics/thermal air collectors to side-by-side PV modules and solar thermal collectors," *Solar Energy*, vol. 100, pp. 50–65, 2014.
- [9] M. A. Shameri, M. A. Alghoul, K. Sopian, M. F. M. Zain, and O. Elayeb, "Perspectives of double skin facade systems in buildings and energy saving," *Renewable and Sustainable Energy Reviews*, vol. 15, no. 3, pp. 1468–1475, 2011.
- [10] National building standard design Atlas, "Building solar photovoltaic systems design and installation (10J908-5)," Beijing, China, 2010.
- [11] J. Han, L. Lu, J. Peng, and H. Yang, "Performance of ventilated double-sided PV facade compared with conventional clear glass facade," *Energy and Buildings*, vol. 56, pp. 204–209, 2013.
- [12] H. Yang, J. Burnett, and J. Ji, "Simple approach to cooling load component calculation through PV walls," *Energy and Buildings*, vol. 31, no. 3, pp. 285–290, 2000.
- [13] J. Peng, L. Lu, H. Yang, and J. Han, "Investigation on the annual thermal performance of a photovoltaic wall mounted on a multi-layer facade," *Applied Energy*, vol. 112, pp. 646–656, 2013.
- [14] J. J. Bloem, "Evaluation of a PV-integrated building application in a well-controlled outdoor test environment," *Building and Environment*, vol. 43, no. 2, pp. 205–216, 2008.
- [15] L. Sun, L. Lu, and H. Yang, "Optimum design of shading-type building-integrated photovoltaic claddings with different surface azimuth angles," *Applied Energy*, vol. 90, no. 1, pp. 233–240, 2012.

- [16] J. Q. Peng, L. Lu, H. Yang, and J. Han, "Investigation on the annual thermal performance of a photovoltaic wall mounted on a multi-layer façade," *Applied Energy*, vol. 112, pp. 646–656, 2013.
- [17] G. E. Lau, G. H. Yeoh, V. Timchenko, and R. K. K. Yuen, "Natural convection in a PV-integrated double-skin façade using Large-Eddy simulation," *Procedia Engineering*, vol. 14, pp. 3277–3284, 2011.
- [18] T. T. Chow, G. Pei, L. S. Chan, Z. Lin, and K. F. Fong, "A comparative study of PV glazing performance in warm climate," *Indoor and Built Environment*, vol. 18, no. 1, pp. 32–40, 2009.
- [19] G. Fraisse, K. Johannes, V. Trillat-Berdal, and G. Achard, "The use of a heavy internal wall with a ventilated air gap to store solar energy and improve summer comfort in timber frame houses," *Energy and Buildings*, vol. 38, no. 4, pp. 293–302, 2006.
- [20] D. Wang, X. Guan, and S. Zhang, "Experimental study on PV solar wall," *Advanced Materials Research*, vol. 250–253, pp. 3134–3138, 2011.
- [21] H.-C. Sung, S. Cheng, C. Y. Huang, and C. Chan, "An empirical study on a variety of solar panels in BIPV power conversion applications," in *Proceedings of the 19th International Workshop on Active-Matrix Flatpanel Displays and Devices: TFT Technologies and FPD Materials (AM-FPD '12)*, pp. 297–300, Ryukoku University, Kyoto, Japan, July 2012.
- [22] ASCE, "Minimum design loads for building and other structures," ASCE 7-10, New York, NY, USA, 2010.
- [23] Ministry of Construction of the People's Republic of China, *Code for Seismic Design of Buildings (GB 50011-2010)*, China Architecture & Building Press, Beijing, China, 2010.
- [24] H. Li, S. Xiao, and L. Huo, "Damage investigation and analysis of engineering structures in the Wenchuan earthquake," *Journal of Building Structures*, vol. 4, pp. 10–19, 2008.
- [25] H. Zhang, X. Lu, and X. Wu, "Experimental study and numerical simulation of the reinforced concrete walls with different stirrup in the boundary element," *Journal of Asian Architecture and Building Engineering*, vol. 9, no. 2, pp. 447–454, 2010.
- [26] Y. Zhou, D. Zhang, Z. Huang, and D. Li, "Deformation capacity and performance-based seismic design for reinforced concrete shear walls," *Journal of Asian Architecture and Building Engineering*, vol. 13, no. 1, pp. 209–215, 2014.
- [27] H. Zhang, X. Lu, J. Li, and L. Liang, "Cyclic load experiment study on the laminated composite RC walls with different concrete ages," *Structural Engineering and Mechanics*, vol. 36, no. 6, pp. 745–758, 2010.
- [28] H. M. Zhang, X. L. Lu, Y. F. Duan, and J. B. Li, "Experimental study and numerical simulation of partially prefabricated laminated composite RC walls," *Advances in Structural Engineering*, vol. 14, no. 5, pp. 967–979, 2011.
- [29] H. M. Zhang, X. L. Lu, Y. F. Duan et al., "Experimental study on failure mechanism of RC walls with different boundary elements under vertical and lateral loads," *Advances in Structural Engineering*, vol. 17, no. 3, pp. 361–379, 2014.
- [30] Ministry of Construction of the People's Republic of China, *Code for Design of Concrete Structures (GB 50010-2010)*, China Architecture & Building Press, Beijing, China, 2010.
- [31] Ministry of Construction of the People's Republic of China, *Code for design of steel structures (GB 50017-2003)*, China Planning Press, Beijing, China, 2003.
- [32] Ministry of Construction of the People's Republic of China, *Technical Code for Glass Curtain Wall Engineering (JGJ 102-2003)*, China Architecture & Building Press, Beijing, China, 2003.

Research Article

A Newton-Based Extremum Seeking MPPT Method for Photovoltaic Systems with Stochastic Perturbations

Heng Li,^{1,2} Jun Peng,^{1,2} Weirong Liu,^{1,2} Zhiwu Huang,^{1,2} and Kuo-Chi Lin³

¹ School of Information Science and Engineering, Central South University, Changsha 410075, China

² Hunan Engineering Laboratory for Advanced Control and Intelligent Automation, Changsha 410075, China

³ Department of Mechanical and Aerospace Engineering, University of Central Florida, Orlando, FL 32816, USA

Correspondence should be addressed to Jun Peng; pengj@csu.edu.cn

Received 2 May 2014; Revised 6 July 2014; Accepted 6 July 2014; Published 24 July 2014

Academic Editor: Dimitrios Karamanis

Copyright © 2014 Heng Li et al. This is an open access article distributed under the Creative Commons Attribution License, which permits unrestricted use, distribution, and reproduction in any medium, provided the original work is properly cited.

Microcontroller based maximum power point tracking (MPPT) has been the most popular MPPT approach in photovoltaic systems due to its high flexibility and efficiency in different photovoltaic systems. It is well known that PV systems typically operate under a range of uncertain environmental parameters and disturbances, which implies that MPPT controllers generally suffer from some unknown stochastic perturbations. To address this issue, a novel Newton-based stochastic extremum seeking MPPT method is proposed. Treating stochastic perturbations as excitation signals, the proposed MPPT controller has a good tolerance of stochastic perturbations in nature. Different from conventional gradient-based extremum seeking MPPT algorithm, the convergence rate of the proposed controller can be totally user-assignable rather than determined by unknown power map. The stability and convergence of the proposed controller are rigorously proved. We further discuss the effects of partial shading and PV module ageing on the proposed controller. Numerical simulations and experiments are conducted to show the effectiveness of the proposed MPPT algorithm.

1. Introduction

Recent years have seen a growing interest in the research of solar energy, which is mainly due to the advantages solar energy has over traditional fossil energies, including safety, sustainable source of energy, less environment pollution, and numerous market potentials. As the main available solar technology, photovoltaic array has been widely used in satellites and spacecrafts, solar vehicles, and domestic power supply; see [1, 2] and the references therein.

The process of guiding a photovoltaic array to its maximum power point is called maximum power point tracking. Due to the inherent nature of photovoltaic cells, the power-voltage curves of PV cells depend nonlinearly on temperature and irradiation intensity; see [3–5]. This fact, however, means that the operating current or voltage that maximizes the output power will change with environmental conditions. To maintain the maximum output power regardless of environmental parameters, one common way is to design MPPT

control system to regulate operating current or voltage to the maximum output power point.

With the rapid development of embedded technology, microcontroller based MPPT control system has been the dominated approach in current photovoltaic systems [5]. This approach is favoured because researchers and engineers prefer to program elegant and advanced MPPT algorithms rather than design complicated and expensive MPPT control circuits.

There are a number of MPPT control algorithms that have been proposed in the literature, among which the two primary algorithms are incremental conductance (IncCond) algorithm [5] and perturb and observe (PO) algorithm [6]. In PO algorithms, a step perturbation is added into the control signal and used to monitor the direction of changes in power. PO has been a commercial algorithm because of its ease of implementation. The main drawback of PO algorithm is that it will oscillate at the maximum power point. Also, it has been shown that PO fails to track the rapidly changing

irradiance [7]. The IncCond algorithm tracks the maximum power point by comparing the instantaneous and incremental conductances of the PV array. Thus it can track the rapidly changing irradiance. However, the harmonic components of array voltage and current need to be measured and used to adjust the reference voltage, which implies that errors at the maximum power point occur due to the low precision sensors used [8].

A promising new MPPT algorithm is the method of extremum seeking (ES) control; see [9–12]. As a model-free, real-time optimization method, ES is well suited for applications with unknown or partly known dynamics and external perturbations, such as photovoltaic systems [11]. ES uses perturbation signals (either from external disturbances or from converter ripples) as probing signals to estimate the gradient of the power map and then update the control signal according to the estimation [12]. It has been shown that ES has the advantages of both rigorously provable convergence and simplicity of hardware implementation [13]. However, existing extremum seeking MPPT controllers still suffer from the following two limitations.

- (i) In existing extremum seeking MPPT controllers, perturbation signals are generally assumed to be periodic. On the one hand, the assumption is rather ideal since external disturbances are typically unknown and stochastic; on the other hand, the requirement of orthogonality makes periodic ES difficult to extend to multivariable cases.
- (ii) In existing extremum seeking MPPT controllers, the convergence speed is typically defined by the gradient of power map of PV systems, which implies that control systems will be highly influenced by unknown and changing environmental conditions. To construct a practical MPPT control system, the convergence of MPPT controller should be user-assignable rather than being dependent on environmental conditions.

Thus the aim of this paper is to provide an improved extremum seeking MPPT control algorithm to solve these problems. Recent progress in stochastic averaging theory has made it possible to consider more general stochastic perturbations when designing extremum seeking controllers; see [14, 15]. In [14], Liu and Krstic provide a systematic design of extremum seeking when stochastic perturbations exist and prove the stability of the stochastic extremum seeking via a developed stochastic averaging theory. The theoretical part of this paper is based on the findings of [14, 15] and we further propose a Newton-based stochastic extremum seeking MPPT controller considering physical features of photovoltaic systems. We conduct extensive simulations and experiments to show the effectiveness of the proposed control algorithm.

The remainder of the paper is organized as follows. In Section 2, preliminary knowledge about photovoltaic modelling and maximum power point tracking is introduced. In Section 3, a new Newton-based stochastic extremum seeking MPPT controller is designed. The tracking performance of the proposed controller is evaluated in Section 4. We conclude the paper in Section 5.

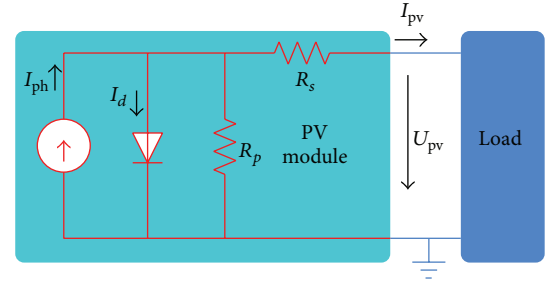


FIGURE 1: The equivalent electrical circuit of a photovoltaic module.

2. Photovoltaic Modelling and MPPT

In this section, we will introduce some preliminary knowledge about PV array and MPPT. A photovoltaic array typically consists of several photovoltaic modules connected in series or parallel to obtain the desired output voltage and current. Thus we first introduce the electrical characteristics of PV modules. More detailed background information can be found in [16].

A photovoltaic module can be seen as a black box that produces a current I_{pv} at a voltage U_{pv} . The inside of that black box can be described by an electric circuit with 4 components, as shown in Figure 1.

- (i) Current source: this is the source of the photo current, which can be denoted by

$$I_{ph} = S \cdot H \cdot \xi, \quad (1)$$

where S is the module area, H is the intensity of incoming light, and ξ is the response factor.

- (ii) Diode: this nonlinear element reflects the dependence on the band gap and losses to recombination. It is characterized by the reverse current I_d .
- (iii) Shunt resistor R_p : it represents losses incurred by conductors.
- (iv) Serial resistor R_s : it also represents losses incurred by nonideal conductors.

The relationship between current I_{pv} and voltage U_{pv} of a photovoltaic module is then expressed by

$$I_{pv} = I_{ph} - I_d \left[\exp \left(\frac{U_{pv} + I_{pv} R_s}{U_T} \right) - 1 \right] - \frac{U_{pv} + I_{pv} R_s}{R_p}, \quad (2)$$

where $U_T = qkT/e$ with ideality factor q , temperature T , Boltzmann constant $k = 1.38e^{-23}$, and the elementary charge $e = 1.602e^{-19}$.

Then the output power P_{pv} of a photovoltaic module is denoted by

$$P_{pv} = U_{pv} I_{pv} = f(U_{pv}), \quad (3)$$

where function $f(\cdot)$ is determined by manufacturing and environmental parameters, such as module area S , irradiance

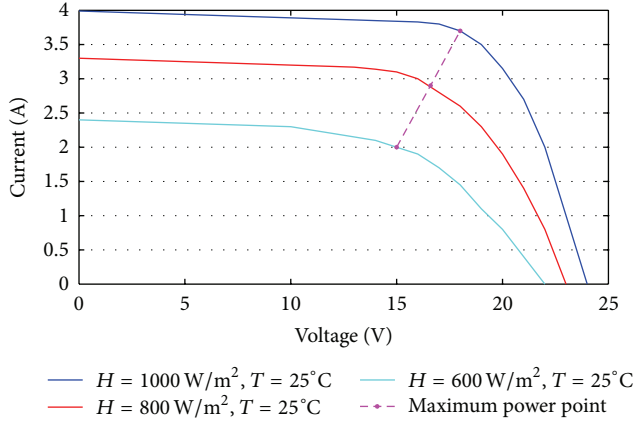


FIGURE 2: I - V characteristics of KC65T PV module at various irradiance levels.

H , response factor ξ , and temperature T , and thus is generally unknown or partially known *a priori*.

Figure 2 shows the I - V characteristics of the KC65T photovoltaic module at various irradiance levels; see the datasheet of KC65T [18]. With light varying its intensity throughout the day, the maximum power point moves to different voltages and currents. Thus a MPPT control system is typically adopted between the photovoltaic module and the load to adjust the output voltage or current and maintain the maximum power output.

The schematic of a photovoltaic MPPT control system with stochastic perturbations is shown in Figure 3. The photovoltaic panel converts solar energy to electrical energy via the photovoltaic effect. A MPPT control system is designed between the photovoltaic panel and load to optimize the conversion efficiency. The adopted MPPT control system consists of three components: MPPT controller, DC-DC driver, and DC-DC converter. The proposed MPPT system can be either voltage control or current control depending on which one is used as the control variable of the MPPT controller. In this paper, we design the MPPT control system with voltage control, but the proposed method is also suited to current control cases.

As the DC-DC driver and converter are relatively mature in electrical industry, the main work in MPPT control system is the design of MPPT control algorithm. Such a research interest has continued for decades, since even small improvements in performance can lead to great economic benefits. Though considerable progress has been made in this field, the following two problems have not been effectively solved:

- (i) how to optimize the output power with unknown power map when stochastic external disturbances exist;
- (ii) how to assign the convergence speed by designers rather than unknown power map.

3. MPPT Controller Design

In this section, we propose a new Newton-based stochastic extremum seeking MPPT controller to handle the above two difficulties. The proposed controller not only inherits the advantages of classical extremum seeking in model-free optimization but also shows its distinctive features in dealing with stochastic perturbations and assigning convergence rates. In what follows, we will introduce the control structure, implementation, and stability analysis of the proposed controller. Some further discussions will be provided in Section 3.5.

3.1. Controller Structure. In order to illustrate the motivation of designing Newton-based extremum seeking MPPT controller, we first introduce the application of classical gradient-based extremum seeking in MPPT of photovoltaic systems. Figure 4 shows the control structure of a gradient-based extremum seeking MPPT controller.

As shown in Figure 4, τ is the duty cycle of PWM waves, η is the stochastic perturbation, and \widehat{U}_{pv} is the estimation of desired voltage that optimizes the power map. The model of DC-DC driver and converter can be simplified as follows:

$$\tau = g(U_{pv}, \widehat{U}_{pv}), \quad (4)$$

$$U_{pv} = \ell(\tau). \quad (5)$$

The maximum power point (MPP) of the photovoltaic system is defined as

$$P_{pv}^* = f(U_{pv}^*) = f(\ell(\tau^*)) \triangleq \max P_{pv}, \quad (6)$$

where U_{pv}^* , τ^* are the desired voltage and duty cycle at the MPP.

We then denote the voltage estimation error \widetilde{U}_{pv} by

$$\widetilde{U}_{pv} = \widehat{U}_{pv} - U_{pv}^*. \quad (7)$$

For the purpose of illustration, assume that the power map $f(\cdot)$ is of the quadratic form; then the averaged system is obtained by

$$\dot{\widetilde{U}}_{pv} = kH\widetilde{U}_{pv}, \quad (8)$$

where H is the second derivative (Hessian) of the power map. Equation (8) shows that the convergence rate is governed by the unknown Hessian H , which is highly influenced by environmental conditions, such as irradiance and temperature.

A practical MPPT control system often requires that the convergence of the controller should be designer-assignable. We next show that this goal can be realized with the Newton-based extremum seeking.

If the power map is known, the following Newton optimization algorithm can be used to find the maximum power point:

$$\frac{dP_{pv}}{dt} = -\left(\frac{d^2 f(U_{pv})}{dU_{pv}^2}\right)^{-1} \frac{df(U_{pv})}{dU_{pv}}. \quad (9)$$

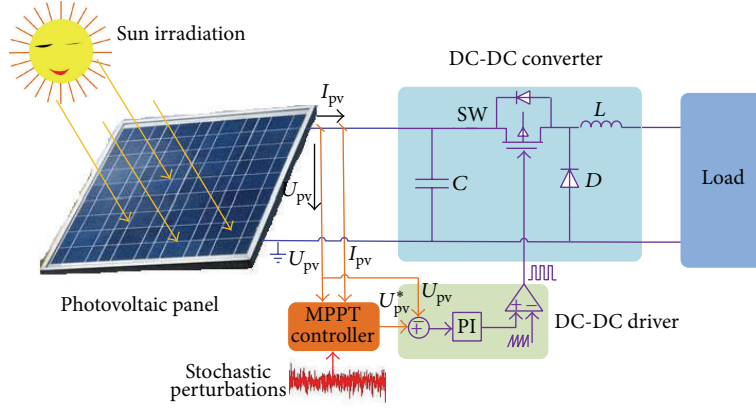


FIGURE 3: The schematic of a photovoltaic MPPT control system with stochastic perturbations.

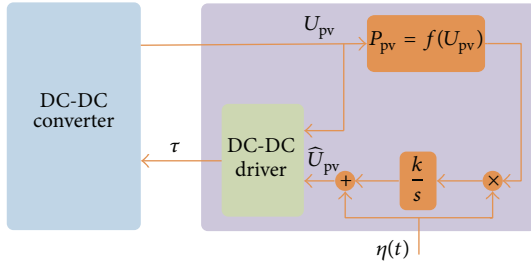


FIGURE 4: The structure of gradient-based extremum seeking MPPT controller.

If $f(\cdot)$ is unknown, then an estimator is needed to approximate $df(x)/dx$ and $d^2f(x)/dx^2$. Then the purpose of the controller design is to combine the Newton optimization algorithm (9) with estimators of the first and second derivatives of power map to achieve the maximum power point tracking.

Let \widehat{G} be the estimation of the first-order derivative, \widehat{H} the estimation of the second-order derivative, and Γ the estimation of inverse of second derivative. Then we propose a Newton-based stochastic extremum seeking MPPT controller in Figure 5. As shown in Figure 5, the first-order derivative of f is estimated by $\widehat{G} = P_{pv}M(\eta)$ and the second-order derivative of f is estimated by $\widehat{H} = P_{pv}N(\eta)$. It is typically difficult to derive $\Gamma = 1/\widehat{H}$ directly when \widehat{H} is close to zero. Instead, a dynamic estimator $\dot{\Xi} = -h\Xi + h\widehat{H}$ is employed to approximate Γ .

We rewrite the proposed control algorithm in state space as

$$\begin{aligned} U_{pv} &= g(\tau), \\ \tau &= \ell(U_{pv}, \widehat{U}_{pv}), \\ \dot{\widehat{U}}_{pv} &= -k\Gamma M(\eta) P_{pv}, \\ \dot{\Gamma} &= h\Gamma - h\Gamma^2 N(\eta) P_{pv}, \end{aligned} \quad (10)$$

where η is a general stochastic signal and $S(\eta) = a \sin(\eta)$, $M(\eta)$, and $N(\eta)$ are the output of signal generator Ψ with the original signal η .

Remark 1. The signal generator outputs $M(\cdot)$, $N(\cdot)$ play an important role in the Newton-based stochastic extremum seeking, since they are used to estimate the first-order and second-order derivative of power map $f(\cdot)$, respectively. Theoretically, they can be any bounded and odd continuous functions. However, considering the practical stability of the photovoltaic system, we choose $M(\cdot)$, $N(\cdot)$ by following the design principle in [19] as

$$\begin{aligned} M(\eta) &= \frac{1}{aW_0(q)} \sin(\eta), \\ N(\eta) &= \frac{1}{a^2W_0^2(\sqrt{2}q)} (\sin^2(\eta) - W_0(q)), \end{aligned} \quad (11)$$

where variables $W_0(q)$ and $W_1(q)$ are defined as follows:

$$\begin{aligned} W_0^2(\sqrt{2}q) &= 2(W_1(q) - W_0^2(q)), \\ W_0(q) &= \frac{1}{2} (1 - e^{-q^2}), \\ W_1(q) &= \frac{3}{8} - \frac{1}{2} e^{-q^2} + \frac{1}{8} e^{-4q^2}. \end{aligned} \quad (12)$$

3.2. Controller Implementation. In this subsection, we provide a detailed flow chart of the implementation of the proposed Newton-based extremum seeking MPPT method, as shown in Figure 6. The basic idea of the controller implementation is that the controller measures the output voltage and current and then computes the output power. Then the first derivative and second derivative of the power map are estimated, respectively, based on the product of output power and stochastic signals. If the termination criterion is satisfied, go to the next iteration. If not, regulate the duty cycle and output voltage to update the output power and go to the next iteration.

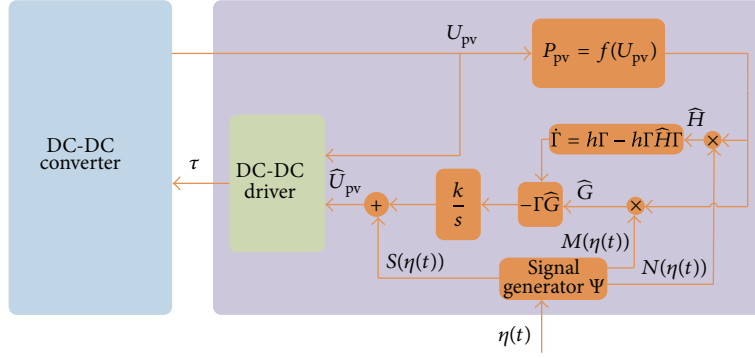


FIGURE 5: The structure of Newton-based extremum seeking MPPT controller.

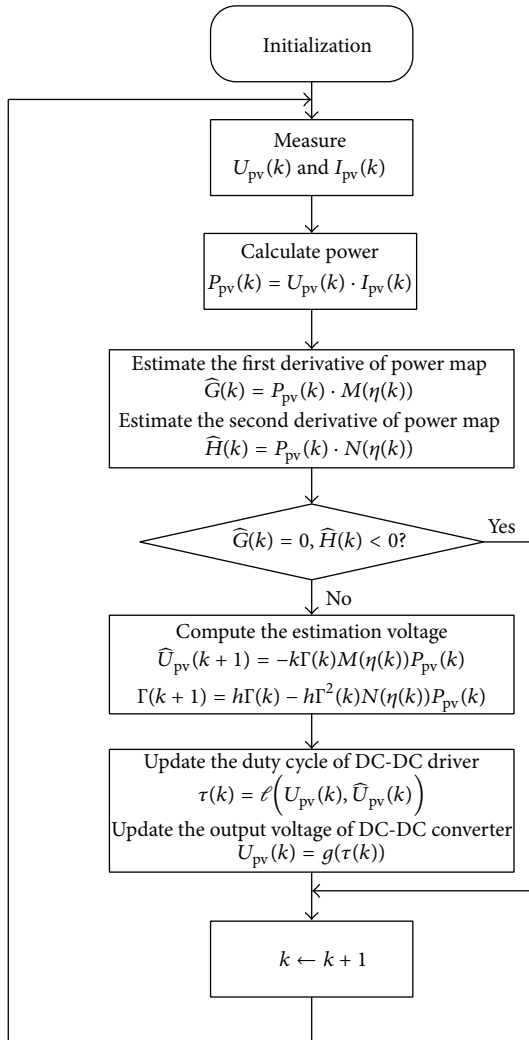
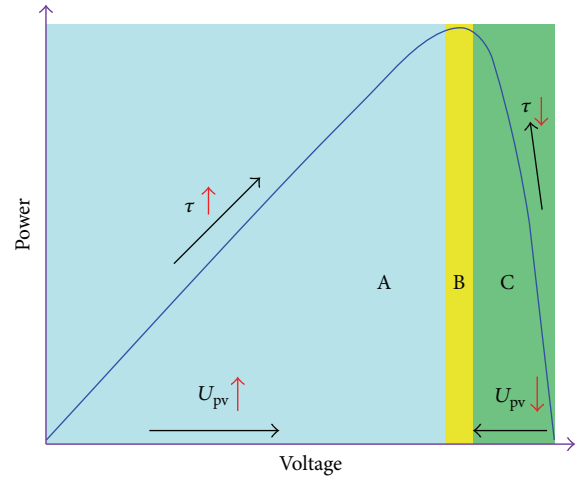


FIGURE 6: Flow chart of the Newton-based extremum seeking MPPT method.

3.3. *A Heuristic Analysis.* In this subsection, we provide a heuristic analysis of the Newton-based extremum seeking MPPT controller. This illustrative analysis will be helpful


 FIGURE 7: Three different regions of an illustrative P - V curve.

in understanding the proposed MPPT algorithm. A more rigorous stability analysis is provided in Section 3.4.

In the I - V characteristics of a PV module, there are three different regions, namely, current source region, MPP region, and voltage source region [20]. These three regions correspond to the regions A, B, and C in the P - V curve, as shown in Figure 7. We will introduce the actions of the MPPT controller in these three regions and explain how the MPPT is achieved.

The update of control signal τ in (10) can be further simplified as

$$\tau(k+1) = \tau(k) + \Delta\tau(k), \quad (13)$$

where $\Delta\tau(k)$ is the update of the control signal τ in one iteration.

In what follows, we will introduce the update of control input τ and output voltage U_{pv} in the following three different regions.

Region A. In this region, the first derivative of the power map $dP_{pv}/dU_{pv} > 0$ and the second derivative $d^2P_{pv}/dU_{pv}^2 < 0$. Then the Newton optimization algorithm (9) turns to be

$$\frac{dP_{pv}}{dt} = -\left(\frac{d^2f(U_{pv})}{dU_{pv}^2}\right)^{-1} \frac{df(U_{pv})}{dU_{pv}} > 0, \quad (14)$$

which means that the update of the control signal $\Delta\tau > 0$. Then the duty cycle τ in (10) is increasing. The larger τ will drive the DC-DC converter to produce larger voltage U_{pv} and then U_{pv} will move in the direction of converging to the desired voltage U_{pv}^* .

Region B. At the MPP, the first derivative $dP_{pv}/dU_{pv} = 0$ and the second derivative $d^2P_{pv}/dU_{pv}^2 < 0$. Then the Newton optimization algorithm (9) is

$$\frac{dP_{pv}}{dt} = -\left(\frac{d^2f(U_{pv})}{dU_{pv}^2}\right)^{-1} \frac{df(U_{pv})}{dU_{pv}} = 0, \quad (15)$$

which means that the change of control signal $\Delta\tau = 0$. Then the control input τ and output voltage U_{pv} keep stable at the desired τ^* and U_{pv}^* , which implies that the MPPT is realized.

Region C. In this region, the first derivative of the power map $dP_{pv}/dU_{pv} < 0$ and the second derivative $d^2P_{pv}/dU_{pv}^2 < 0$. Then the Newton optimization algorithm (9) turns to be

$$\frac{dP_{pv}}{dt} = -\left(\frac{d^2f(U_{pv})}{dU_{pv}^2}\right)^{-1} \frac{df(U_{pv})}{dU_{pv}} < 0, \quad (16)$$

which means that the change of control signal $\Delta\tau < 0$. Then the duty cycle τ in (10) is decreasing. The smaller τ will drive the DC-DC converter to produce smaller voltage U_{pv} and then U_{pv} will move in the direction of converging to the desired voltage U_{pv}^* .

3.4. Stability Analysis. Stability is a basic requirement of a practical control system. In this subsection, we analyze the stability of the proposed MPPT algorithm using stochastic averaging theory. Then the main theoretical contribution of this paper is concluded as follows.

Theorem 2. Consider the photovoltaic MPPT control system shown in Figure 3 with DC-DC driver (4), DC-DC converter (5), and unknown power map (3). Assume that the output power P_{pv} reaches its maximum P_{pv}^* at the desired control input τ^* and desired voltage U_{pv}^* . Then under the control law (10) for the update of τ , the stability of the closed-loop system is guaranteed. Moreover, the output power P_{pv} exponentially converges to the maximum power P_{pv}^* , which implies that the maximum power point tracking is achieved.

Proof. We assume that the stochastic perturbation $\eta(t)$ considered in this paper has invariant distribution $\mu(dx) = (1/\sqrt{\pi}q)e^{-x^2/q^2}dx$. Denote the estimation error $\tilde{\tau} = \hat{\tau} - \tau^*$, $\tilde{\Gamma} = \hat{\Gamma} - \Gamma^{-1}$. Then the error system can be denoted by

$$\begin{aligned} \dot{\tilde{\tau}} &= -k(\tilde{\Gamma} + H^{-1})M(\eta)f(g(\tau^* + \tilde{\tau} + a\sin(\eta))), \\ \dot{\tilde{\Gamma}} &= h(\tilde{\Gamma} + H^{-1}) \\ &\quad - h(\tilde{\Gamma} + H^{-1})^2N(\eta)f(g(\tau^* + \tilde{\tau} + a\sin(\eta))). \end{aligned} \quad (17)$$

For simplicity, a quadratic power map is considered:

$$f(\ell(\tau)) = f^* + \frac{f''(\ell(\tau^*))}{2}(\tau - \tau^*)^2 = f^* + \frac{H}{2}(\tau - \tau^*)^2. \quad (18)$$

Then the error system can be simplified as

$$\begin{aligned} \dot{\tilde{\tau}} &= -k(\tilde{\Gamma} + H^{-1})M(\eta)\left(f^* + \frac{H}{2}(\tilde{\tau} + a\sin(\eta))^2\right), \\ \dot{\tilde{\Gamma}} &= h(\tilde{\Gamma} + H^{-1}) \\ &\quad - h(\tilde{\Gamma} + H^{-1})^2N(\eta)\left(f^* + \frac{H}{2}(\tilde{\tau} + a\sin(\eta))^2\right). \end{aligned} \quad (19)$$

To guarantee the stability of closed-loop system, the generated stochastic signals $M(\eta)$ and $N(\eta)$ are chosen as

$$\begin{aligned} M(\eta) &= \frac{1}{aW_0(q)}\sin(\eta), \\ N(\eta) &= \frac{1}{a^2W_0^2(\sqrt{2}q)}(\sin^2(\eta) - W_0(q)), \end{aligned} \quad (20)$$

where $W_0^2(\sqrt{2}q) = 2(W_1(q) - W_0^2(q))$; variables $W_0(q)$ and $W_1(q)$ are defined as follows:

$$\begin{aligned} W_0(q) &= \frac{1}{2}(1 - e^{-q^2}), \\ W_1(q) &= \frac{3}{8} - \frac{1}{2}e^{-q^2} + \frac{1}{8}e^{-4q^2}. \end{aligned} \quad (21)$$

Then we obtain the average system

$$\begin{aligned} \dot{\tilde{\tau}}^{\text{ave}} &= -k(\tilde{\tau}^{\text{ave}} - \tilde{\Gamma}^{\text{ave}}H\tilde{\tau}^{\text{ave}}), \\ \dot{\tilde{\Gamma}}^{\text{ave}} &= -h(\tilde{\Gamma}^{\text{ave}} - h(\tilde{\Gamma}^{\text{ave}})^2H). \end{aligned} \quad (22)$$

Thus, according to the stochastic averaging theory [14], system (22) has a locally exponentially stable equilibrium at $(\tilde{\tau}^{\text{ave}}, \tilde{\Gamma}^{\text{ave}}) = (0, 0)$. When $\tilde{\tau} \rightarrow 0$, we have $\tau \rightarrow \tau^*$ and then $P_{pv} \rightarrow P_{pv}^*$. Thus the maximum power point tracking is realized. This completes the proof. \square

Remark 3. From the equilibrium equation (22), we can find that the convergence of closed-loop system is totally determined by parameters k and h , which implies that, in the design of control algorithm (10), the convergence rate can be arbitrarily assigned by the designer with an appropriate choice of k and h . Generally speaking, relatively large k and h will lead to a good convergence rate, but too large k and h will also result in oscillations during the convergence. Hence, k and h should be chosen by fully considering both the dynamic and the steady responses.

3.5. Further Discussions. Besides the stability property discussed above, there are some more issues that should be considered in the implementation of MPPT controllers, such as tracking efficiency, effects of partial shading, and PV module ageing effects. In what follows, we will discuss these topics that may be helpful in the application of the proposed MPPT method.

(1) Tracking Efficiency. Tracking efficiency has been the most important consideration of the MPPT method in many commercial applications. The tracking efficiency of a MPPT algorithm can be calculated by the following equation [6]:

$$\eta_T = \frac{\int_0^t P_{pv}(t) dt}{\int_0^t P_{\max}(t) dt}, \quad (23)$$

where $P_{pv}(t)$ is the measured power produced by the PV array under the control of MPPT algorithm and $P_{\max}(t)$ is the theoretical maximum power that the array can produce.

The discrete definition of the tracking efficiency can be denoted by [21]

$$\eta_T = \frac{1}{n} \sum_{k=0}^n \frac{P_{pv}(k)}{P_{\max}(k)}, \quad (24)$$

where n is the number of samples.

Tracking efficiency evaluates the overall performance of a MPPT algorithm. In the next section, we will verify the tracking efficiency of the proposed MPPT method with numerical results.

(2) Effects of Partial Shading. The partial shading effect has received much attention recently in the implementation of MPPT controller, which is partly due to the rapid development of building integrated photovoltaics (BIPV) [22]. As the BIPV is commonly installed on the rooftop, it typically suffers from partial shading due to the space limitation, clouds, and so forth.

When a PV system is subjected to partial shading, the P - V curve often exhibits a global extremum and several local extremums, as shown in Figure 8. Hence, in order to track the global MPP of power map, the adopted MPPT algorithm should have a global convergence. However, from (22) we find that the proposed controller is locally stable at the MPP, which implies that it may get trapped at local extremums and may not be a good choice for PV systems under partial shading. Fortunately, several global or semiglobal extremum

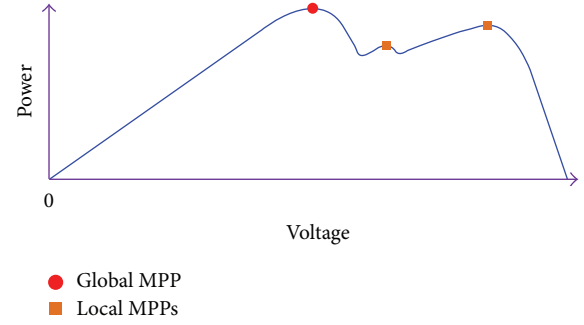


FIGURE 8: An illustrative P - V curve for PV systems under partial shading.

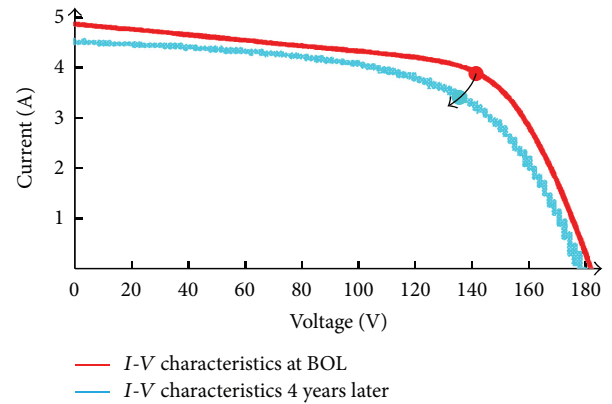


FIGURE 9: Degradation of 20 a-Si modules after 4 years of operation in [17].

seeking control designs have been available; see [23–25] for more information.

(3) Effects of PV Module Ageing. Reliability and lifetime of PV modules are key factors to PV system performance and are mainly dominated by the PV module ageing effect [26]. In order to separate the ageing effect from the irradiance and temperature, it is necessary to evaluate the Beginning of Life (BOL) performance. Then the deviations between the experimental data and BOL performance explain the ageing of the PV system [17].

Figure 9 shows the degradation of 20 a-Si modules after 4 years of operation in the literature [17]. We can find that the MPP declines slowly during the 4-year time. Mathematically, the maximum power point tracking for an ageing PV system is essentially an optimization process for a slowly varying unknown cost function [13]. The proposed Newton-based extremum seeking MPPT controller optimizes the power map with real-time measurements and calls for no knowledge of model information. Thus it can deal with the PV module ageing effect well.

4. Tracking Performance Evaluation

In this section, we provide several simulation and experiment results to show the effectiveness of the proposed MPPT

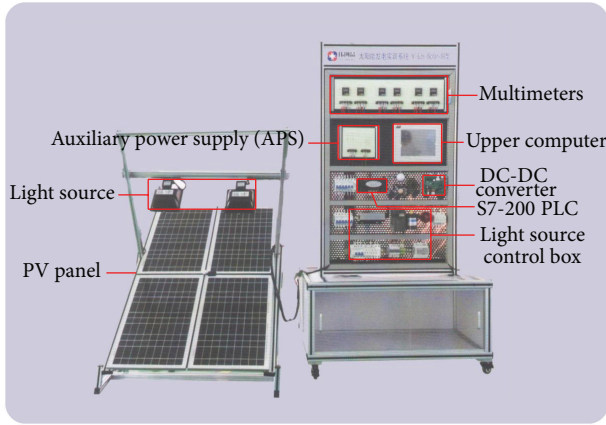


FIGURE 10: The experiment setup of the light source-driven photovoltaic MPPT system.

algorithm. In order to evaluate the tracking performance of the proposed MPPT algorithm under arbitrary desired irradiance, we adopt the light source-driven photovoltaic MPPT system, as shown in Figure 10.

In Figure 10, there are two incandescents working as the irradiation source. The KC65T-PV panel converts the solar energy to electrical energy via the photovoltaic effect. The Siemens S7-200 PLC works as the MPPT controller, driving the DC-DC converter and regulating the output voltage of the converter. The upper computer is used to collect and store experimental data and multimeters are used to display the measurements. The light source control box is used to regulate the irradiation intensity of light sources.

In what follows, we will provide simulation examples and experiment results to illustrate the tracking performance of the proposed MPPT algorithm under uniform irradiance and nonuniform irradiance cases, respectively. The data sheets of KC65T photovoltaic module under different irradiance conditions are shown in Tables 1 and 2; see [18] for detailed information.

4.1. Tracking under Uniform Irradiance. In this subsection, we consider the tracking performance evaluation of the proposed MPPT algorithm under the uniform irradiance. A simulation and an experiment are provided, respectively, to illustrate the implementation of the algorithm. The simulation is conducted in MATLAB/Simulink and the parameter setting of the proposed control algorithm is shown in Table 3. For simplicity, we adopt only one KC65T PV module in the simulation.

Figure 11 shows the simulation results of the proposed MPPT algorithm under uniform irradiance of 800 W/m^2 at 25°C . The convergence of the maximum power point is shown in Figure 11(a). The output power oscillates in the direction of MPP which is detected by the product of the power and perturbations. We can see that the output power converges to the MPP within 5 s. The output power in the steady state is about 46.1 W, whereas the maximum power of the PV

TABLE 1: Data sheet of KC65T at 800 W/m^2 , 25°C .

Maximum power (P_{\max})	47.7 W
Maximum power voltage (U_{mpp})	15.5 V
Maximum power current (I_{mpp})	3.08 A

TABLE 2: Data sheet of KC65T at 1000 W/m^2 , 25°C .

Maximum power (P_{\max})	65.3 W
Maximum power voltage (U_{mpp})	17.4 V
Maximum power current (I_{mpp})	3.75 A

TABLE 3: Parameter setting of the proposed MPPT controller.

Parameter	Value
a	0.1
k	1
h	0.08
q	40

module is 47.7 W. Then the simulated tracking efficiency of the proposed MPPT algorithm is about 96.6%.

Figure 12 shows the comparison between the proposed Newton-based extremum seeking MPPT method and classical extremum seeking MPPT method. We compare the tracking performance of the two MPPT methods in terms of tracking efficiency and convergence time. The numerical comparison of the two MPPT methods is shown in Table 4.

In addition to the simulations, experiments on the light source-driven photovoltaic MPPT system are conducted for the purpose of verification. The irradiance is set to be 800 W/m^2 and the temperature is about $23\sim 27^\circ\text{C}$. The PV panel comprises four KC65T PV modules, with two modules connected in parallel and two in series.

The experiment results of the proposed MPPT algorithm are shown in Figures 13 and 14. From Figure 13(a), we can see that the output power converges to the MPP within 6 s. The average power at steady state is about 178 W, whereas the maximum power is 190.8 W; then the tracking efficiency is about 93.2%.

4.2. Tracking under Nonuniform Irradiance. In this subsection, we will consider the tracking performance of the proposed MPPT algorithm under nonuniform irradiance with an abrupt change from 800 W/m^2 to 1000 W/m^2 at 10 s. For the purpose of comparison, we also provide the experiment results of the classical gradient-based extremum seeking MPPT method under the same experimental conditions.

Figure 15 shows the experiment results of the proposed Newton-based extremum seeking MPPT method under the nonuniform irradiance. It is shown in Figure 15(a) that the new MPP is located within 2 s. The new steady power is about 243 W, while the maximum power is 261.2 W; then the tracking efficiency is about 93%.

Figure 16 shows the experiment results of the classical gradient-based extremum seeking MPPT method under the

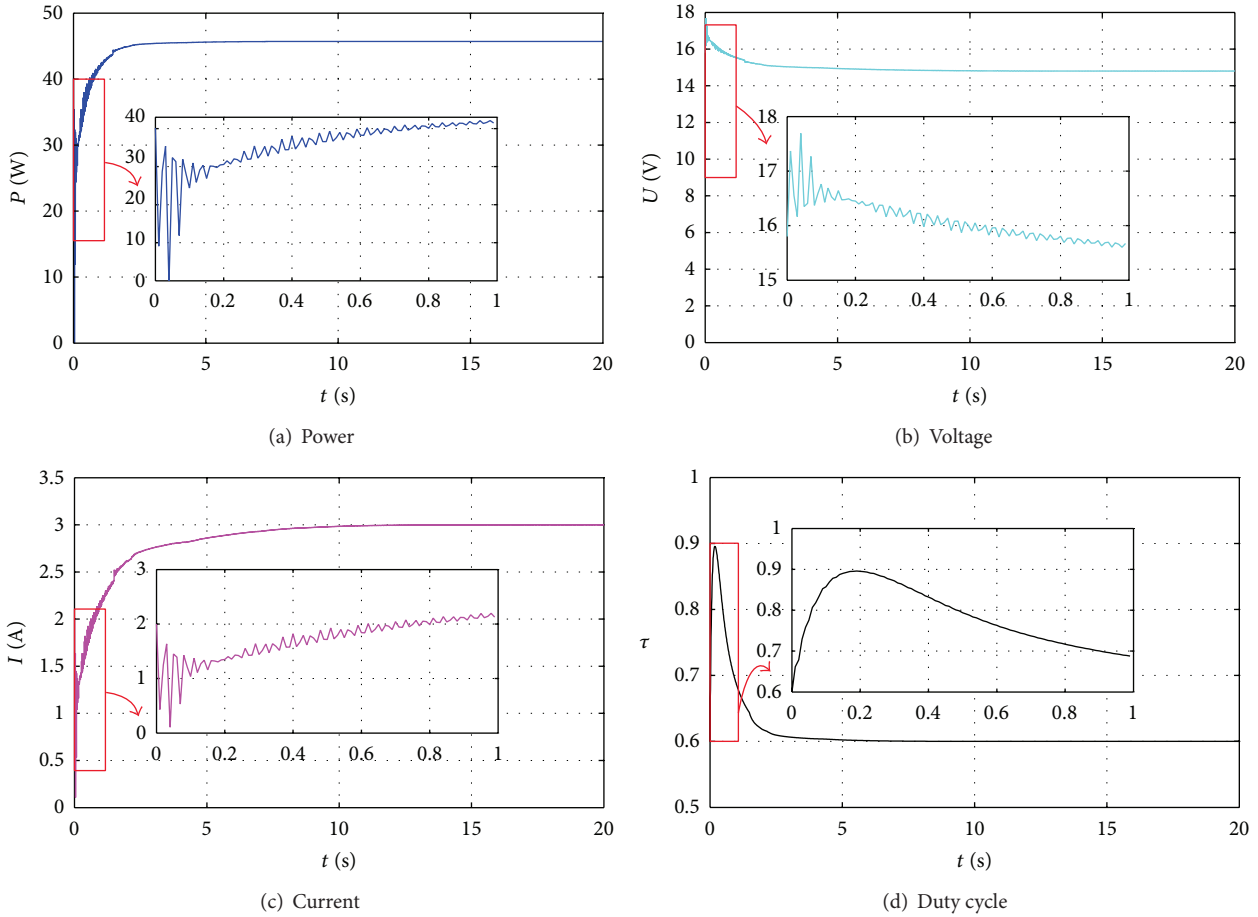


FIGURE 11: Simulation results of the proposed MPPT method under uniform irradiance of 800 W/m^2 at 25°C .

TABLE 4: The simulated comparison of the two methods.

MPPT method	Efficiency	Convergence
Newton-based ES MPPT	96.6%	<4 s
Gradient-based ES MPPT	92.1%	>6 s

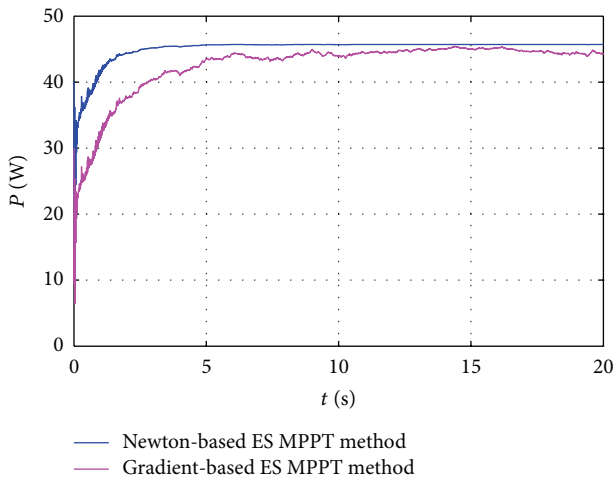


FIGURE 12: The comparison between the proposed MPPT method and classical extremum seeking MPPT method.

nonuniform irradiance. It is shown in Figure 16(a) that the new MPP is located within 4 s. The new steady power is about 231 W, while the maximum power is 261.2 W; then the tracking efficiency is about 88.4%.

In order to illustrate the effectiveness of the proposed MPPT method more intuitively, we provide the numerical comparison between the proposed algorithm and classical extremum seeking MPPT algorithm under different irradiance. Figures 17 and 18 show the comparison of the two methods under irradiance 800 W/m^2 and irradiance 1000 W/m^2 , respectively. We can see that the proposed method shows its superiority in both tracking efficiency and convergence rate.

5. Concluding Remark

In this paper, we propose a new Newton-based extremum seeking MPPT algorithm for photovoltaic systems. The proposed algorithm benefits the following advantages: it calls for no knowledge of the power map; it has a good tolerance of stochastic perturbations and its convergence rate can be totally designer-assignable. The stability and convergence of the proposed MPPT controller are rigorously proved with stochastic averaging theory. Some topics related to applications are discussed, such as partial shading effects and PV

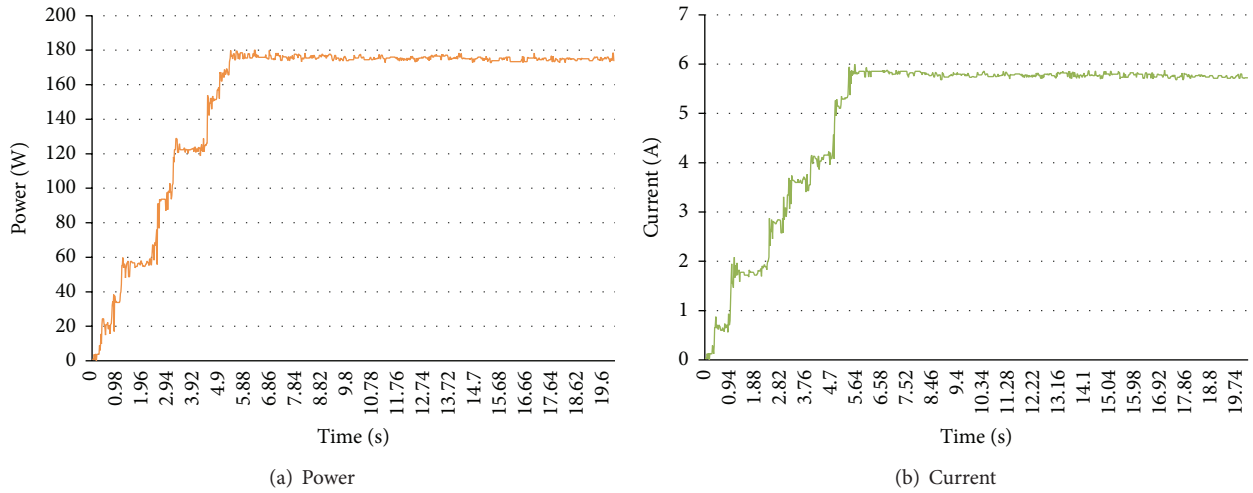


FIGURE 13: Experiment results of output power and current collected in the upper computer.

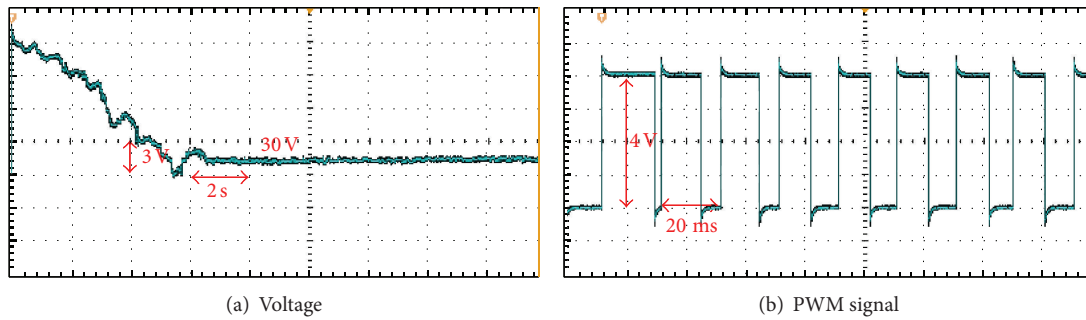


FIGURE 14: Experiment results of output voltage and PWM signal measured in the oscilloscope.

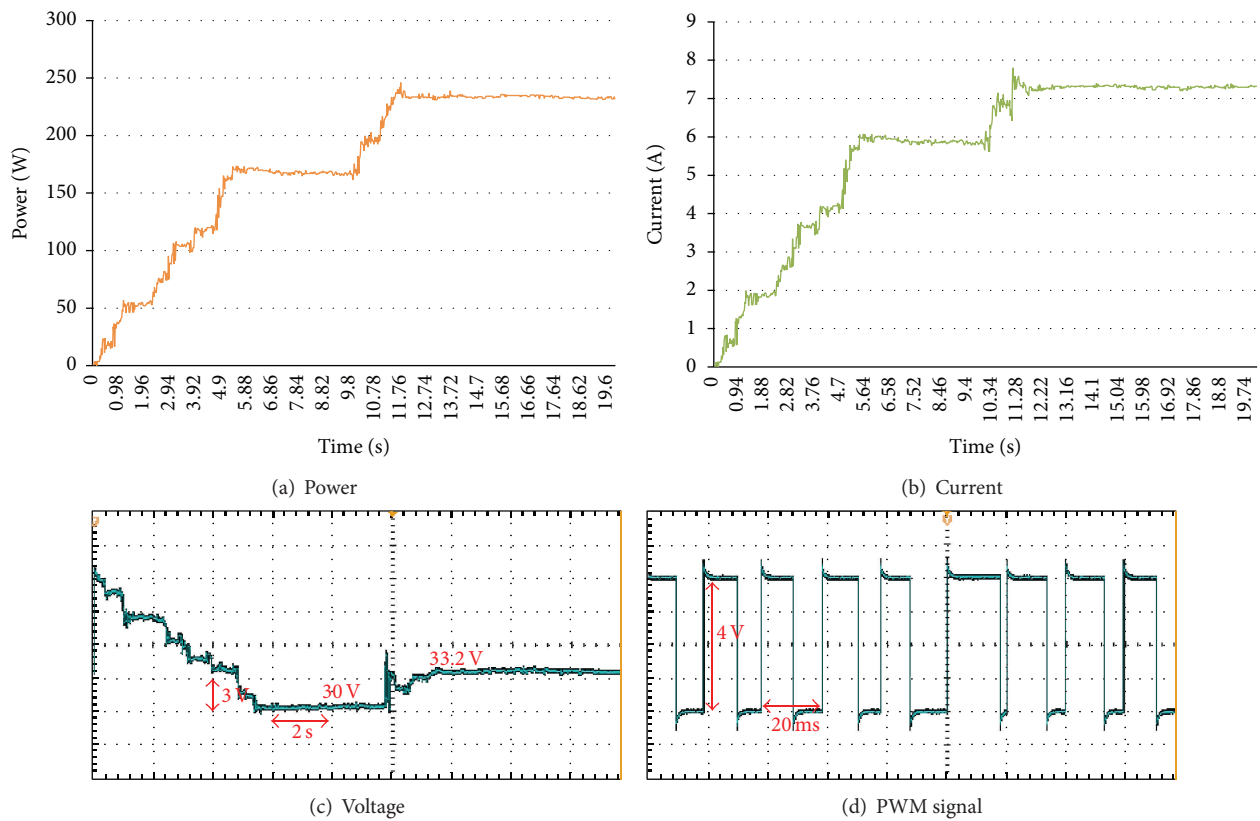


FIGURE 15: Tracking performance of the Newton-based extremum seeking MPPT algorithm under nonuniform irradiance.

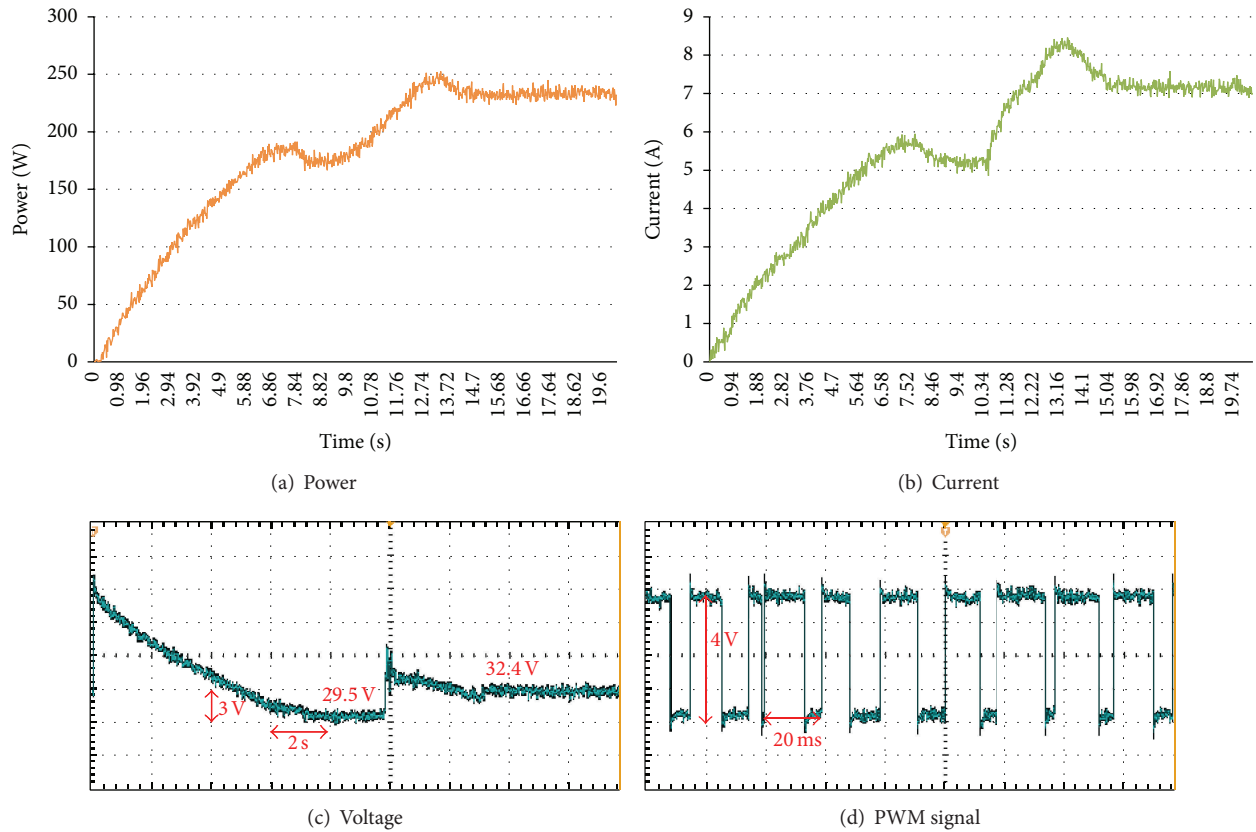


FIGURE 16: Tracking performance of the gradient-based extremum seeking MPPT algorithm under nonuniform irradiance.

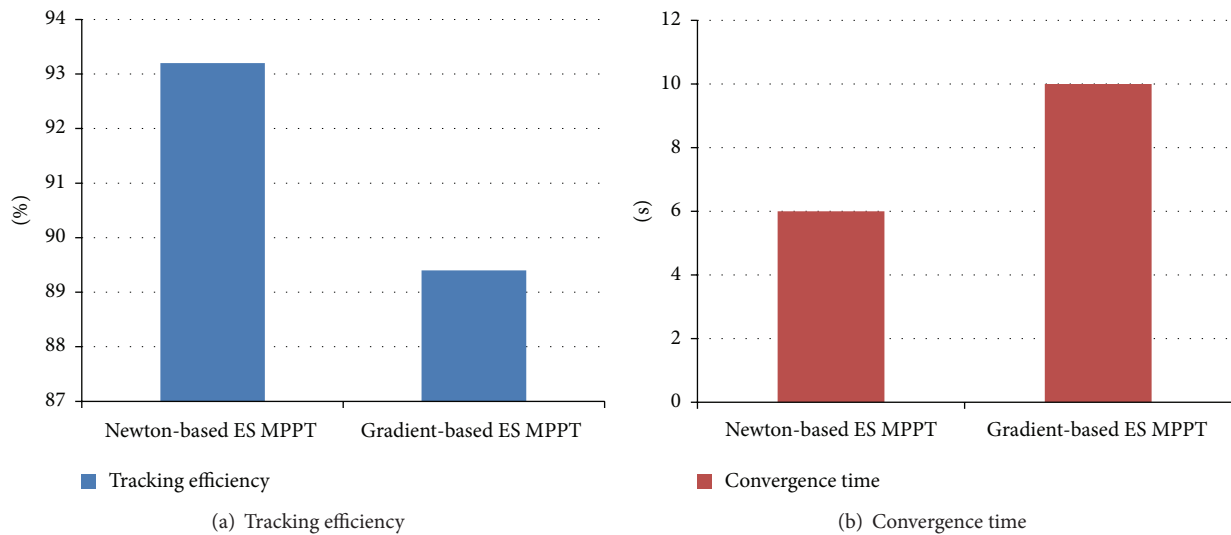


FIGURE 17: The numerical comparison between the proposed MPPT algorithm and classical extremum seeking MPPT algorithm under irradiance 800 W/m^2 .

module ageing effects. Simulation and experiment results are provided to show the effectiveness of the proposed method.

It is also worth mentioning that both the Newton-based ES and gradient-based ES belong to the so-called static

extremum seeking, which requires that the power map of photovoltaic systems is rather slower than extremum seeking. When irradiance changes quickly, the tracking performance of ES MPPT algorithms will be worse. In order to propose

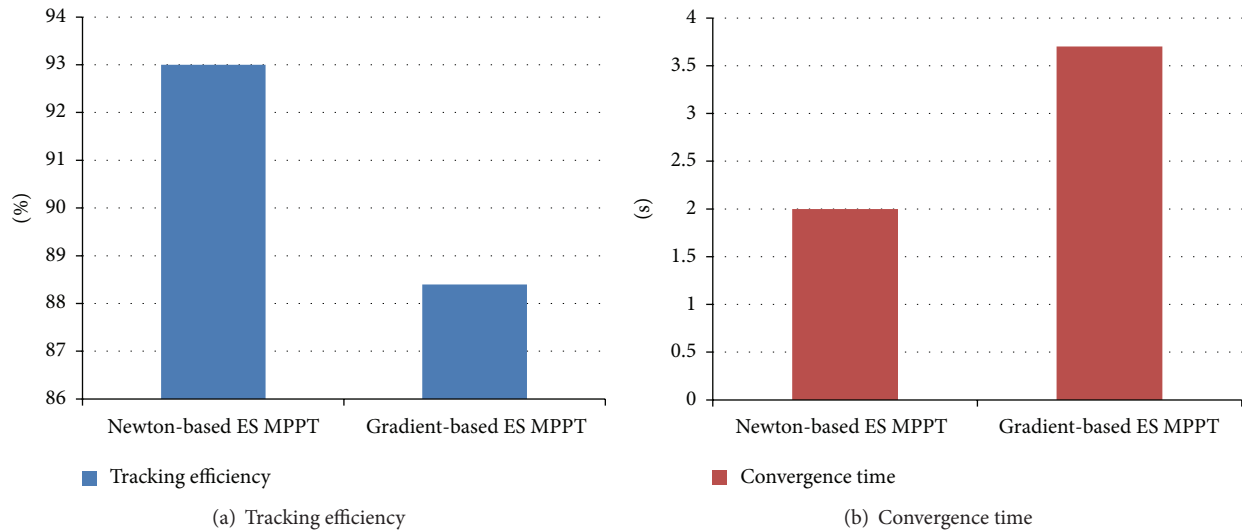


FIGURE 18: The numerical comparison between the proposed MPPT algorithm and classical extremum seeking MPPT algorithm under irradiance 1000 W/m².

a commercial ES MPPT algorithm, we will further investigate the dynamic extremum seeking and its applications in maximum power point tracking in future work.

Conflict of Interests

The authors declare that there is no conflict of interests regarding the publication of this paper.

Acknowledgments

The authors would like to thank the anonymous reviewers for their valuable comments. This work is supported by the National Natural Science Foundation of China (Grant nos. 61071096 and 61379111), the Fundamental Research Funds for the Central Universities of Central South University, and Hunan Provincial Innovation Foundation for Postgraduate.

References

- [1] E. F. Camacho, M. Berenguel, F. R. Rubio, and D. Martinez, *Control of Solar Energy Systems*, Springer, 2012.
- [2] E. F. Camacho, M. Berenguel, and F. R. Rubio, *Advanced Control of Solar Plants*, Springer, 1997.
- [3] T. Esum and P. L. Chapman, "Comparison of photovoltaic array maximum power point tracking techniques," *IEEE Transactions on Energy Conversion*, vol. 22, no. 2, pp. 439–449, 2007.
- [4] V. Salas, E. Olías, A. Barrado, and A. Lázaro, "Review of the maximum power point tracking algorithms for stand-alone photovoltaic systems," *Solar Energy Materials and Solar Cells*, vol. 90, no. 11, pp. 1555–1578, 2006.
- [5] K. H. Hussein, I. Muta, T. Hoshino, and M. Osakada, "Maximum photovoltaic power tracking: an algorithm for rapidly changing atmospheric conditions," *IEE Proceedings: Generation, Transmission and Distribution*, vol. 142, no. 1, pp. 59–64, 1995.
- [6] D. P. Hohm and M. E. Ropp, "Comparative study of maximum power point tracking algorithms," *Progress in Photovoltaics: Research and Applications*, vol. 11, no. 1, pp. 47–62, 2003.
- [7] T. Kawamura, K. Harada, Y. Ishihara et al., "Analysis of MPPT characteristics in photovoltaic power system," *Solar Energy Materials and Solar Cells*, vol. 47, no. 1–4, pp. 155–165, 1997.
- [8] C. Hua, J. Lin, and C. Shen, "Implementation of a DSP-controlled photovoltaic system with peak power tracking," *IEEE Transactions on Industrial Electronics*, vol. 45, no. 1, pp. 99–107, 1998.
- [9] R. Leyva, C. Alonso, I. Queinnec, A. Cid-Pastor, D. Lagrange, and L. Martínez-Salamero, "MPPT of photovoltaic systems using extremum-seeking control," *IEEE Transactions on Aerospace and Electronic Systems*, vol. 42, no. 1, pp. 249–258, 2006.
- [10] S. L. Brunton, C. W. Rowley, S. R. Kulkarni, and C. Clarkson, "Maximum power point tracking for photovoltaic optimization using ripple-based extremum seeking control," *IEEE Transactions on Power Electronics*, vol. 25, no. 10, pp. 2531–2540, 2010.
- [11] H. Yau and C. Wu, "Comparison of extremum-seeking control techniques for maximum power point tracking in photovoltaic systems," *Energies*, vol. 4, no. 12, pp. 2180–2195, 2011.
- [12] A. Ghaffari, M. Krstić, and S. Seshagiri, "Extremum seeking for wind and solar energy applications," *ASME Dynamic Systems & Control Magazine*, pp. 13–21, 2014.
- [13] D. Dochain, M. Perrier, and M. Guay, "Extremum seeking control and its application to process and reaction systems: a survey," *Mathematics and Computers in Simulation*, vol. 82, no. 3, pp. 369–380, 2011.
- [14] S. Liu and M. Krstic, "Stochastic averaging in continuous time and its applications to extremum seeking," *IEEE Transactions on Automatic Control*, vol. 55, no. 10, pp. 2235–2250, 2010.
- [15] S. Liu and M. Krstic, "Newton-based stochastic extremum seeking," *Automatica*, vol. 50, no. 3, pp. 952–961, 2014.
- [16] <http://www.greenrhinoenergy.com/solar/>.
- [17] A. Abete, F. Scapino, F. Spertino, and R. Tommasini, "Ageing effect on the performance of a-Si photovoltaic modules in a grid connected system: experimental data and simulation

- results,” in *Proceedings of the Conference Record of the 28th IEEE Photovoltaic Specialists Conference*, pp. 1587–1590, Anchorage, Alaska, USA, 2000.
- [18] <http://www.kyocerasolar.com/assets/001/5170.pdf>.
- [19] S. Liu and M. Krstic, *Stochastic Averaging and Stochastic Extremum Seeking*, Springer, London, UK, 2012.
- [20] P. Bhatnagar and R. K. Nema, “Maximum power point tracking control techniques: state-of-the-art in photovoltaic applications,” *Renewable and Sustainable Energy Reviews*, vol. 23, pp. 224–241, 2013.
- [21] A. Reza Reisi, M. Hassan Moradi, and S. Jamasb, “Classification and comparison of maximum power point tracking techniques for photovoltaic system: a review,” *Renewable and Sustainable Energy Reviews*, vol. 19, pp. 433–443, 2013.
- [22] K. Ishaque and Z. Salam, “A review of maximum power point tracking techniques of PV system for uniform insolation and partial shading condition,” *Renewable & Sustainable Energy Reviews*, vol. 19, pp. 475–488, 2013.
- [23] Y. Tan, D. Nešić, I. M. Y. Mareels, and A. Astolfi, “On global extremum seeking in the presence of local extrema,” *Automatica*, vol. 45, no. 1, pp. 245–251, 2009.
- [24] F. Esmailzadeh Azar, M. Perrier, and B. Srinivasan, “A global optimization method based on multi-unit extremum-seeking for scalar nonlinear systems,” *Computers and Chemical Engineering*, vol. 35, no. 3, pp. 456–463, 2011.
- [25] W. H. Moase and C. Manzie, “Semi-global stability analysis of observer-based extremum-seeking for Hammerstein plants,” *IEEE Transactions on Automatic Control*, vol. 57, no. 7, pp. 1685–1695, 2012.
- [26] R. Khatri, S. Agarwal, I. Saha, S. K. Singh, and B. Kumar, “Study on long term reliability of photo-voltaic modules and analysis of power degradation using accelerated aging tests and electroluminescence technique,” *Energy Procedia*, vol. 8, pp. 396–401, 2011.

Review Article

A Review of Solar Photovoltaic Concentrators

**Mehrdad Khamooshi,¹ Hana Salati,¹ Fuat Egelioglu,¹ Ali Hooshyar Faghiri,¹
Judy Tarabishi,¹ and Saeed Babadi²**

¹ *Department of Mechanical Engineering, Faculty of Engineering, Eastern Mediterranean University, Famagusta, North Cyprus, Via Mersin 10, Turkey*

² *Department of Electrical and Computer Engineering, University of Concordia, Montreal, QC, Canada H4B 1R6*

Correspondence should be addressed to Mehrdad Khamooshi; mehrdadkhamooshi@yahoo.com

Received 5 March 2014; Revised 12 April 2014; Accepted 26 April 2014; Published 19 June 2014

Academic Editor: Dimitrios Karamanis

Copyright © 2014 Mehrdad Khamooshi et al. This is an open access article distributed under the Creative Commons Attribution License, which permits unrestricted use, distribution, and reproduction in any medium, provided the original work is properly cited.

Throughout the recent centuries, the limits of using energy resources due to the cost and environmental issues became one of the scientists' concerns. Because of the huge amount of energy received by the Earth from the sun, the application of photovoltaic solar cells has become popular in the world. The photovoltaic (PV) efficiency can be increased by several factors; concentrating photovoltaic (CPV) system is one of the important tools for efficiency improvement and enables for a reduction in the cell area requirement. The limits of the PV area can reduce the amount of absorbing irradiation; CPV systems can concentrate a large amount of sunlight into a smaller one by applying lenses or curved and flat mirrors. However, the additional costs on concentrating optics and cooling systems made CPV less common than nonconcentrated photovoltaic. This paper reviews the different types of PV concentrators, their performance with advantages and disadvantages, concentration ratio, acceptance angle, brief comparison between their efficiencies, and appropriate cooling system.

1. Introduction

As the fossil fuels are reducing gradually in our planet, solar photovoltaic systems and technology are becoming a promising option for electricity generation. The amount of solar power output is about 166 PW out of which 85 PW reaches the Earth. This shows not only that solar power is well over 500 times our current world 15 TW power consumption, but also that all other sources are less than 1% of solar power output [1–3]. The radiation, that is, not reflected or scattered and reaches the surface directly is called direct or beam radiation and the scattered radiation reaching the ground is called diffuse radiation [4]. Basically, the role of concentration photovoltaic systems is to collect both beam and scattered irradiation, which do not reach the photovoltaic cells. Besides photovoltaic, the concentrator also has other applications such as thermal power applications [5–7], lighting systems [8–10], pumping of solar lasers [11–15], hydrogen production [16–18], and other applications. Although Parida et al. [19] performed a fundamental review study on the solar photovoltaic technologies and McConnell

et al. [20] reviewed market aspects of solar concentrators, there is no complete review on concentrated photovoltaic technologies. The aim of this study is therefore to review different CPV technologies and their other characteristics such as performance, advantages, disadvantages, and appropriate cooling system.

2. Solar Concentrators

In a simple description, the idea of CPV is using optical devices with cheap and suitable technology to concentrate the light on small and highly efficient photovoltaic solar cells. Hence, the cost will be reduced by means of replacing the cell surface with cheaper optical devices [21]. There are some advantages and disadvantages solar concentrator systems have over flat plate systems for large installations. Table 1 obtained from the [22] shows some advantages of CPV.

Solar concentrators are classified by their optical characteristics such as the concentration factor, distribution of illumination, focal shape, and optical standard. Concentration

TABLE I: Advantages of concentrating over flat-plate systems for large PV installations [22].

Lower cost	GaAs dish concentrators are projected to produce electricity at 7.4 cents/kWh by 2010, whereas thin-film modules are projected to be at 9.6 cents/kWh. If thin-film module prices come down from the assumed \$75/m ² to \$35/m ² at 12% efficiency (29 cents/W), then thin-film electricity cost would equal GaAs dish cost.
Superior efficiency	Concentrators are the only option to have system efficiencies over 20%. This reduces land utilization as well as area related costs.
Higher annual capacity factor	Tracking provides for improved energy output. Once the expense of tracking is incurred with flat-plates, the leap to installing concentrator modules is small.
Less materials availability issues	Concentrators use standard construction materials for the bulk of their requirements. Flat-plate systems have serious concerns over material availability: silicon feedstock, or indium in the case of CuInSe ₂ .
Less toxic material use	Many thin-film concepts use quite toxic materials such as cadmium, and so forth.
Ease of recycling	The trend in modern mass-product manufacturing is to make a product as recyclable as possible. Concentrators are composed mainly of easily recyclable materials, steel, aluminum, and plastic. Recycling flat-plate modules will be much more difficult.
Ease of rapid manufacturing capacity scale-up	Existing semiconductor manufacturing capacity is more than sufficient to supply projected cell requirements. The remaining manufacturing is comprised of rather standard mechanical components. This greatly reduces capital requirements compared to flat-plate.
High local manufacturing content	Aside from the cells, the remaining content of concentrator systems can be manufactured worldwide, and close to the final point-of-use.

factor X , which is also known as the number of suns, is the ratio of the mean radiant flux density on a receiver area G_x compared to the average normal global irradiance G [23]:

$$X = \frac{G_x}{G}. \quad (1)$$

The classification based on the concentration factor includes the following conditions [24]:

- (i) low concentration (LCPV): (1–40 x),
- (ii) medium concentration (MCPV): (40–300 x),
- (iii) high concentration (HCPV): (300–2000 x).

Also the efficiencies of different PV cells can be obtained from the following [25]:

$$\eta = \frac{P_{\max}}{Ar E_e}, \quad (2)$$

where η is efficiency, P_{\max} is the ratio of the optimal electric power delivered by the PV cell, Ar is the area of the PV cell exposed to sunlight, and solar irradiance received by the PV is E_e .

Higher tracker tolerances, passive heat sinks, lower cost optics, reduced manufacturing costs, and reduced installation precision made LCPV more simple compared to HCPV [26]. The experimental findings by Butler et al. [27] show that LCPV has the potential to harvest more energy when using standard Si solar cells in a basic concentration configuration as used in this study. However, Pérez-Higueras et al. [24] stated that high concentrator photovoltaic technology is still in a deployment stage, but the cells and modules efficiency data offered by their manufacturing companies, as well as

the measuring experiments carried out by several research centers, forecast an attractive short-term increment in their efficiency, which means that these systems could be profitable in economical and energy terms in a short period of time. This fact represents a potential alternative to flat module photovoltaic systems in the energy generation market.

Based on the Pérez-Higueras et al. study [24], Table 2 shows different HCPV efficiencies in the laboratories and in commercials.

They are also classified in two other optical categories: (1) imaging optical concentrators, which means the image formed on the receiver by the optical concentrators [28] and (2) nonimaging optical concentrators: the receiver is not concerned with forming an image on it by optical concentrators [29].

2.1. Overview on Different Models. During past decades, a lot of developments have been made on designing different models of solar concentrators. Experts analyzed these models through these decades and there have been some changes in their design. This part presents different models of concentrators.

2.1.1. Fresnel Lenses. Fresnel lenses recently have been one of the best choices due to their noble properties such as small volume, light weight, as well as mass production with low cost [30]. In early Fresnel lenses, glass was replaced by polymethylmethacrylate (PMMA), discovered by Augustin Jean Fresnel, with optical characteristics almost the same as glass including good transmissivity and resistance to sunlight; it is the suitable material choice for the manufacturing of Fresnel lenses [31, 32]. A Fresnel lens is a flat optical

TABLE 2: Different HCPV efficiencies recorded in Laboratories and commercials [24].

	Efficiency (%)	Suns	Type	Description
Laboratories efficiencies				
1	41.6	364	GaInP/GaInAs/Ge	Lattice-matched
2	41.1	454	GaInP/GaInAs/Ge	Lattice-mismatched
3	40.8	326	GaInP/GaInAs/GaInAs	Inverted monolithic
4	40.7	240	GaInP/GaInAs/Ge	Lattice-mismatched
5	37.2	500	nGaP/InGaAs/Ge	Lattice-matched
Commercials efficiencies				
1	39	500	Multijunction	http://www.emcore.com
2	38.5	500	Multijunction	http://www.spectrolab.com
3	35	500	Multijunction	http://www.spirecorp.com
4	35	300	Multijunction	http://www.azurspace.com
5	27	100	Silicon	http://www.amonix.com

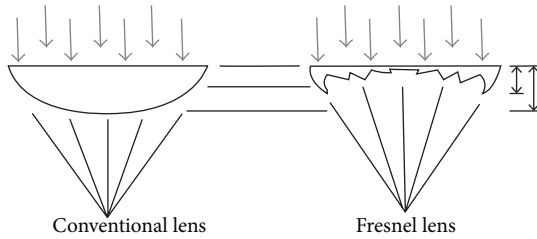


FIGURE 1: Conventional lens and Fresnel lens [30].

component where the bulk material is eliminated because the surface is made up of many small concentric grooves. These grooves individually act as prisms since each groove is approximated by a flat surface that reflects the curvature at that position of the conventional lens [33]. Figure 1 shows the schematic view of conventional lens and Fresnel lens.

The concentration of flux is represented as follows [34]:

$$C_{\max} = \frac{n^2}{\sin \theta \sin \psi}, \quad (3)$$

where C_{\max} represents the maximum concentration of optical flux (unitless); n is the real component of the refractive index (unitless); and θ (acceptance angle along the plane of the azimuth) and ψ (the acceptance angle of the altitude) are the acceptance angles.

Briefly, concentrated solar energy applications using Fresnel lens systems are in following categories: thermal application, thermal heating, solar cooking [5, 35, 36], photocatalytic [37], solar building [38], solar-pumped laser [39–41], lighting [42, 43], and surface modification of metallic materials [33, 44–46].

There are two main types of Fresnel lenses which are circular and linear. For the circular category, Nakata et al. [47] described a 300 W polar axis tracking concentrator with 36 circular Fresnel lenses (40×40) and designed cells to obtain the uniform distribution. As a result, the optical efficiency of the lens is 83% and the output power becomes about 50% greater than that of the commercial lens, an experimental and analytical method used by Harmon [48] to

determine the efficiency and intensity variations of a circular Fresnel lens as a solar concentrator. Using a photovoltaic scanning technique, the experimental part and simulation are constructed to model the behavior of the lens. According to the results, the lens is an inefficient concentrator with losses that begin at 20% and rise to about 80% as the focal distance decreases.

A research done by Whitfield et al. [49] compares Point-focus Fresnel lens, two-axis tracking, and the use of the housing as heat Sink with other models which include linear Fresnel lens, solid CPC secondary's, and two-axis tracking. Linear Fresnel lens system has the advantage of being simple and totally enclosed yet is more costly than some of the others. The point-focus Fresnel lens has the advantage of having potential for simple mass-produced optics but its serious problem is the loss of efficiency at higher concentration. Optical properties of flat linear Fresnel lenses manufactured from glass are presented by Franc et al. [50] and the behavior of these lenses in perpendicular and inclined beams of rays is discussed.

2.1.2. Quantum Dot Concentrator. Quantum dot concentrator (QDC) is a nontracking concentrator that includes three main parts; transparent flat sheet of glass or plastic doped with quantum dots (QDs), reflective mirrors placed on three different edges and the back surface, and a PV cell which is attached to the exit aperture. As it is shown in Figure 2 when the sun radiation hits the surface of concentrator, a part of the radiation will be refracted by a fluorescent material and absorbed by quantum dots (QDs); photons are reemitted isotropically at a lower frequency and guided to the PV cell [25]. The size of quantum dots, which are made of nanostructures, typically varies from tens to hundreds of nanometers in size [51].

Research done by Mičić et al. [52] has shown that QDs are capable of absorbing light over an extremely broad wavelength range and the absorption spectra also depicts the spectral shift to higher energy as QD size decreases. The main advantages of QDC are the following: they are without any tracking system, they can concentrate both diffuse and direct radiations [53], due to the geometries of these

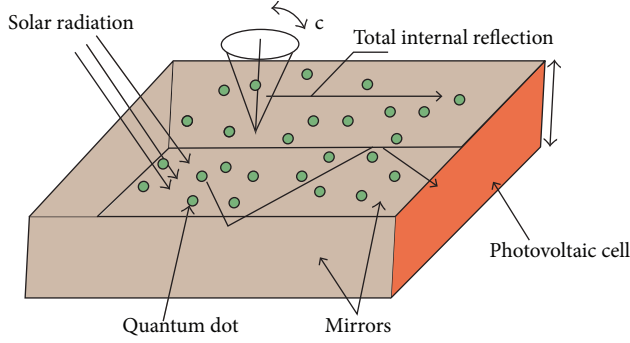


FIGURE 2: Principle of the QDC [25].

concentrators, they have less problems of heat dissipation [25], and sheets are inexpensive and are suitable architectural components [54]. Developing QDCs was restricted by the stringent requirements of the luminescent dyes such as high quantum efficiency, suitable absorption spectra and red shifts, and illumination stability [55, 56]. The problems of organic dyes can settle by replacing them with QDs which have the advantages of less degradation and high luminescence [57]. Schüler et al. [58] proposed that quantum dot containing nanocomposite coatings might be an alternative for the production of planar quantum dot solar concentrators. The concentration ratios of QDCs are completely discussed by Gallagher et al. [25] who determined concentration ratios of different types by comparative analysis. A maximum comparative concentrating factor (MCCF) was determined at specific solar intensities using (4):

$$\text{MCCF} = \frac{P_{\text{dev-max}}}{P_{\text{max-ref}}}, \quad (4)$$

where $P_{\text{dev-max}}$ is the power maximum for the test device and $P_{\text{ref-max}}$ is the power maximum for the reference devices.

2.1.3. Parabolic Concentrator. The solar parabolic trough collector is the most recognized technology due to its high dispatchability and low unit cost. In parabolic trough concentrators, the parabolic shaped mirror focuses sunlight on the receiver tube which is placed at the focal point of parabola [59]. Reflectivity of the mirror, incident angle, tracking error, intercept factor, as well as absorptivity of the receiver, are the factors which can affect the performance of the parabolic trough concentrator [60]. Additionally, Riffelmann et al. [61] mentioned the image quality of the mirror, slope error, and collector assembly, as the factors which the optical efficiency of a parabolic trough collector depends on.

In order to enhance the concentration efficiency of the parabolic trough, Omer and Infield [62] discussed the two-stage concentration of the parabolic trough collector. This design provides an efficient concentration of the incident solar radiation without any frequent tracking system. The performance of the parabolic trough collector depends on receiver design and heat loss from the receiver [60, 63–68]. The heat loss can increase by different tools; one of them is inserting porous inserts in the inner surface of the receiver.

The porous inserts increase the heat transfer rate by (1) increasing the effective fluid thermal conductivity, (2) enhancing mixing between the fluid and receiver wall, and (3) lowering thermal resistance by developing a thinner hydrodynamic boundary layer [59]. Figure 3 shows a schematic view of a parabola.

The concentration ratio of the Parabolic concentrator can be obtained from (5) [69, 70]:

$$C = \frac{\sin \phi_R}{\pi \sin \theta_\alpha} \quad (5)$$

$$\tan\left(\frac{\phi_R}{2}\right) = \frac{2y_s}{4f} = \frac{y_s}{2f},$$

where θ_α is half the acceptance angle, ϕ_R is the rim angle, and f is focus length.

2.1.4. Compound Parabolic Concentrator (CPC). Compound parabolic concentrators (CPCs) are designed to efficiently collect and concentrate distant light sources with some acceptance angle. Figure 4 illustrates the configuration of CPC.

The geometrical concentration ratio and theoretical maximum possible concentration ratio of the CPC are obtainable from (6) [71, 72]:

$$\text{CR} = \frac{A_a}{A_r} \quad (6)$$

$$\text{CR}_{\text{max,3D}} = \frac{1}{\sin^2(1/2)\theta_{\text{max}}},$$

where A_a , A_r , and θ_{max} are the aperture area, receiver area, and maximum acceptance angle, respectively.

CPCs can be in both 2-dimensional and 3-dimensional configuration. Suzuki and Kobayashi's [73] study on 2-D CPC is about the optimum acceptance angle of the concentrator with the declination angle of ± 23.5 on the celestial hemisphere for direct radiation and uniform irradiance for diffuse radiation. The results indicate that the optimum half-acceptance angle is 26 degrees irrespective of the change in the diffuse radiation fraction. It was also found that almost all over the Earth, a common CPC is an optimum application for many solar collecting systems.

Senthilkumar et al. [74] performed substantial research work in order to improve the performance of the two-dimensional compound parabolic concentrator (2D CPC). They found out that the three-dimensional compound parabolic concentrator (3D CPC) is more efficient than the 2D CPC because of the higher concentration ratio. Yehezkel et al. [75] analyzed the losses due to reflection properties and calculated the effect of these losses on concentration ratio. They estimated reflection losses using an empirical linear model to facilitate design and system optimization by analytical methods without resorting to a ray-tracing procedure.

Khalifa and Al-Mutawalli [76] did an experimental study on effects of two-axis sun tracking on thermal performance of CPC in two different modes; in the first, a batch feeding

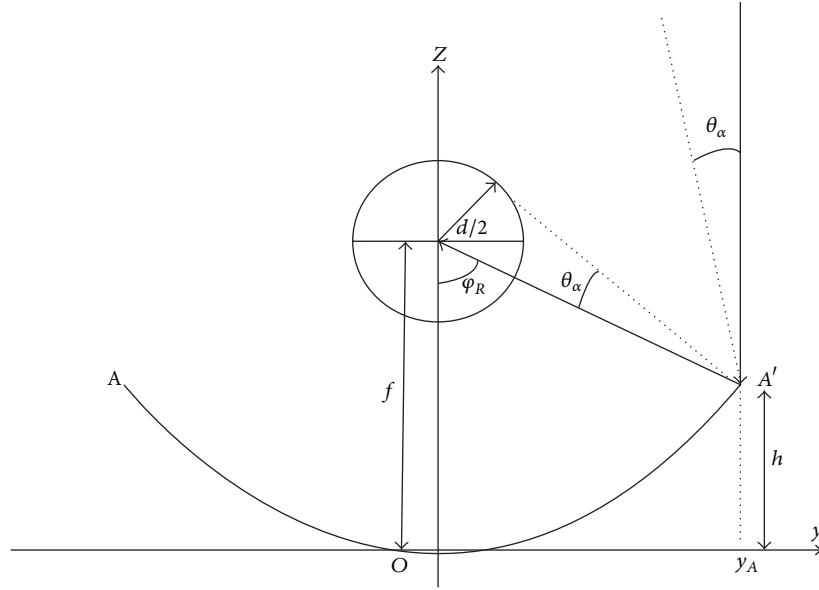


FIGURE 3: Schematic view of the parabola.

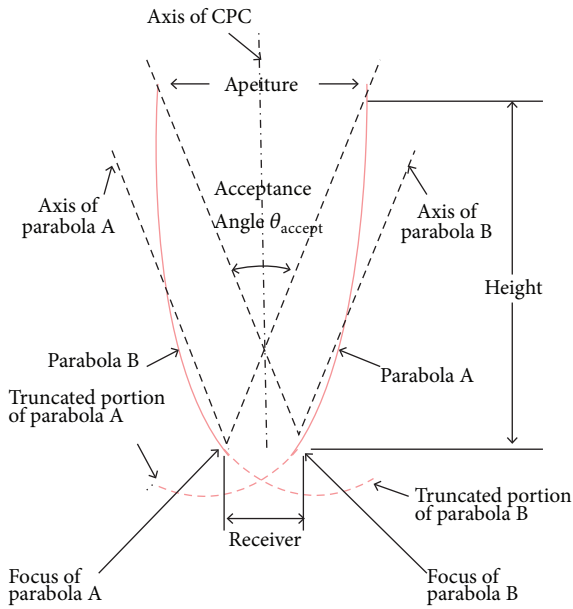


FIGURE 4: Cross section of a nontruncated CPC [132].

was used where no flow through the collector was allowed whereas in the second, different steady water flow rates were used. The results led us to the conclusion that the energy gain of a CPC collector can be increased by using two-axis tracking systems. The best improvement was achieved when the flow rate was in the range of 25 to 45 kg/hr.

Mallick et al. [77] designed a novel nonimaging asymmetric compound parabolic photovoltaic concentrator (ACPPVC) with different numbers of PV strings connected in series experimentally characterized under outdoor conditions both with and without concentrators which indicated that the use of an ACPPVC increased the maximum power

point by 62% when compared to a similar nonconcentrating PV panel.

2.1.5. Dielectric Totally Internally Reflecting Concentrator (DTIRC). Dielectric totally internally reflecting concentrator (DTIRC) which was suggested by Ning et al. [78] is one of the most important nonimaging optical concentrators. In addition to the solar application, these lenses were proposed for IR detection [79] and optical wireless communication systems [80, 81].

As shown in Figure 5, DTIRCs consist of three main parts: a curved front surface, a totally internally reflecting profile, and an exit aperture [81].

The important factor for rays to reach the exit aperture is to be within the designed acceptance angle of the concentrator. When a set of rays hits the front curved surface at the acceptance angle, it is refracted and directed to the exit aperture. Ning et al. [82] discussed two-stage photovoltaic concentrators with Fresnel lenses as primaries and dielectric totally internally reflecting nonimaging concentrators as secondaries. The results indicated that two-stage concentrator suggests higher concentration and more uniform flux distribution on the photovoltaic cell than the point focusing Fresnel lens alone. Muhammad-Sukki et al. [83] described designing a dielectric totally internally reflecting concentrator (DTIRC). They used maximum concentration method (MCM) which was outlined with the simulation to optimize the design of the concentrator. The results from MATLAB simulations indicate that MCM offers a higher geometrical concentration gain, with a slight increase in the concentrator size.

The advantages of DTIRC over compound parabolic concentrator are higher efficiency, higher concentration ratio, flux tailoring, and work without any needs of cooling features. However, DTIRC itself cannot efficiently pass all of

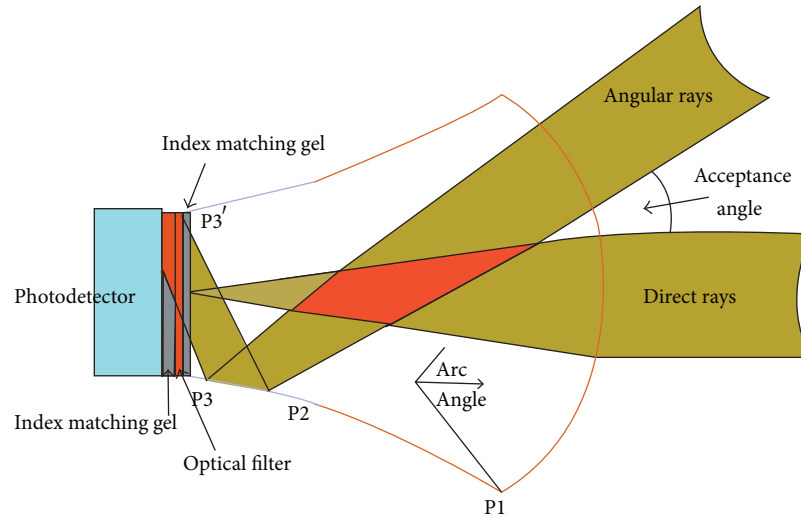


FIGURE 5: Side view of a DTIRC [81].

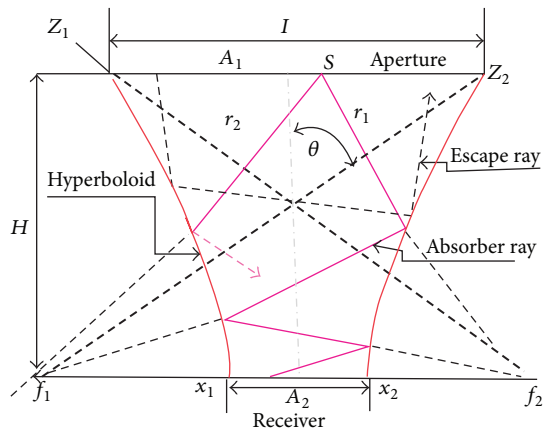


FIGURE 6: 2-D Hyperboloid concentrator [86].

the solar energy that it accepts into a lower index media [84]. Muhammad-Sukki et al. [85] present a study about a mirror symmetrical dielectric totally internally reflecting concentrator (MSDTIRC) which is a new type of DTIRC. They presented a method for calculating concentration gain of the mentioned system.

2.1.6. Hyperboloid Concentrator. Figure 6 shows two dimensional hyperboloid concentrators. Incident rays on the aperture enter the hyperboloid concentrator and either reach the receiver or reflect back out of the concentrator [86]. This kind of concentrator is also called the elliptical hyperboloid concentrator. A 3-D figure of an elliptical hyperboloid concentrator is showed in Figure 7.

The advantage of this concentrator is that it is very compact, since only a truncated version of the concentrator needs to be used. Because of this factor, it is mainly used as a secondary concentrator [87]. Garcia-Botella et al. [29] found out that the one-sheet hyperbolic concentrator is an ideal 3D

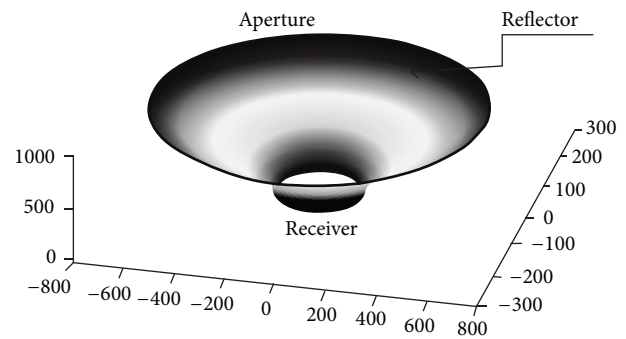


FIGURE 7: 3-D elliptical hyperboloid concentrator.

asymmetric concentrator as its shape does not disturb the flow lines of an elliptical disk. It also does not need a tracking system where two different acceptance angles, transversal and longitudinal direction, are needed.

Sellami et al. [88] designed a 3-D concentrator and coined the Square elliptical hyperboloid (SEH) to be integrated in either glazing windows or facades for photovoltaic application. This configuration can collect both diffuse and direct beam. They also found that optical efficiency depends on the size of the SHE.

It has been shown that the 3-D solar concentrator acquired from the hyperboloid has the ability of concentrating all the entering rays [89] such as the trumpet concentrator, which is composed of a revolution of hyperbolic type and was considered as an ideal concentrator [90].

Chen et al. [91] investigated a solar concentrator containing primary paraboloidal and secondary hyperboloidal mirrors by using the ray tracing method to obtain higher concentration ratio. The results indicated that such a method can increase the concentration of solar flux twice when concentration tracking errors exist.

Saleh Ali et al. [92] presented a study about designing a static 3-D solar elliptical hyperboloid concentrator (EHC).

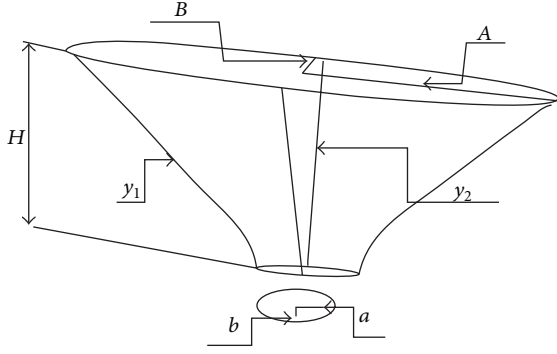


FIGURE 8: Geometrical parameters of an elliptical hyperboloid concentrator [92].

They proposed some equation for designing hyperboloid concentrators [92], based on Figure 8.

The design of hyperboloid concentrators is based on the following equations:

$$\begin{aligned} \frac{x^2}{a^2} + \frac{y^2}{b^2} - \frac{z^2}{c^2} &= 1, \\ y_1 &= \left[\left\{ \left(\frac{x^2}{a^2} \right) - 1 \right\} \times \{H^2 \times (CR - 1)\} \right]^{0.5}, \\ A &= (CR \times (a)^2)^{0.5}, \\ y_2 &= \left[\left\{ \left(\frac{x^2}{b^2} \right) - 1 \right\} \times \{H^2 \times (CR - 1)\} \right]^{0.5}, \\ B &= (CR \times (b)^2)^{0.5}, \\ CR &= \frac{A_p}{A_r}. \end{aligned} \quad (7)$$

2.1.7. RR, XX, XR, RX, and RXI. These configurations represent the new concentrators which achieved the theoretical maximum acceptance angle concentration and it was concluded that they may be useful for high concentration cells [93].

In these designs “R” denotes refraction, “X” denotes reflection, and “I” denotes internal reflection [94]. The design methods of all these concentrators are basically similar to each other. RXI designs can almost describe other models as shown in Figure 9; rays that impinge on the concentrator aperture, within the acceptance angle, are directed to the receiver by means of one refraction, one reflection, and one total internal reflection [95].

Minano et al. [96] investigated the performance of RX and the results indicated that when the angular spread of the input bundle is small, the performance of the rotational RX is acceptable. An analysis of the RX concentrator performed by Benitez and Minano [97] stated that when the field of view is small (less than 6 degrees full angle), even for concentrations up to 95% of the theoretical maximum, its

imaging performance is similar (in MTF terms) to that of normal incidence of an $f/3.7$ planoconvex spherical lens with optimum defocusing. This image capability is suitable for receivers. Minano et al. [98] explored a research for RX and RXI concentrators. Their results had shown that when the acceptance angle of the concentrator is less than 5 degrees (for a source at infinity), its performance in 3D is very good. Also, the RX shown in their analysis had been designed for a finite source and the RXI for a source at infinity.

3. Tables of Properties

Table 3 shows the advantages and disadvantages of the different types of solar concentrators.

Based on Peterina et al.’s [99] study Table 4 represents different kinds of CPV modules and their typical size and power.

Swanson [22] performed a review study on the characteristics of concentrated photovoltaic systems which approached the economical aspects of the systems. Table 5 summarized Swanson’s study which represents different CPV with their characteristics.

For the cost comparison of different CPV systems Table 6 which is obtained from Whitfield et al. [49] presents some CPV systems with their cost.

4. Appropriate Cooling Systems

Cooling of photovoltaic cells under concentrated illumination is one of the major problems during designing them. The photovoltaic cell efficiency decreases with increasing temperature or due to nonuniform temperature [100–109]. Also, cell degradation will occur if the temperature exceeds certain limits [102].

The thermal properties of the coolant are another important factor for choosing the right cooling system. Thermal properties of air make it less efficient compared to water which results in more parasitic power [110]. Also, the coolant or working fluid should be compatible, which means that it should not attack or corrode the envelope or wick and there is no chemical reaction between the working fluid and the envelope or wick structure that liberates noncondensable gas (NCG) [111].

Heat pipes are popular and interesting technology with the aim of cooling the PV modules especially under concentration. A heat pipe is a vacuum tight device consisting of a working fluid and a wick structure [111]. The working fluid transfers the additional and the rejected heat by condensation processes. Heat pipes are usually made of aluminum or copper; Table 7 shows the compatible working fluid for copper and aluminum based on refs. [111–113].

Akbarzadeh and Wadowski [114] made reports on a parabola-trough that uses heat pipes for cooling. Each cell is mounted vertically on the end of a thermosyphon which is made of a flattened copper pipe with a finned condenser area. The cell temperature does not go beyond 46°C on sunny days with the concentration ratio of 20 suns; the reports show that

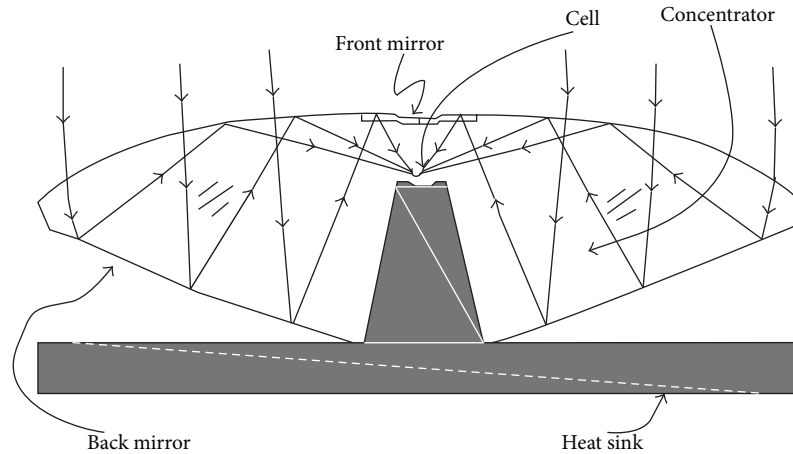


FIGURE 9: RXI concentrator cross-section [93].

TABLE 3: Advantages and disadvantages of solar concentrators.

Type of concentrator	Advantages	Reference	Disadvantages	Reference
Fresnel lens	(i) Small volume (ii) Light weight (iii) Mass production	[30]	(i) Imperfection on the edges of the facets, causing the rays to be improperly focused at the receiver (ii) Possibility of lost light due to incidence on the draft facet (iii) Luminance is necessarily reduced in order to minimize the upper disadvantages	[133, 134]
Quantum dot concentrator	(i) Nontracking concentrator (ii) Have less problems of heat dissipation (iii) Sheets are inexpensive and are suitable architectural components	[25, 54]	Developing QDCs was restricted by stringent requirements of the luminescent dyes	[55, 56]
Parabolic trough	Make efficient use of direct solar radiation	[135]	(i) Use only direct radiation (ii) high cost (iii) low optical and quantum efficiencies	[135]
Compound parabolic concentrator	Most of radiation within the acceptance angle can transmit trough the output aperture into receivers	[136]	Needs good tracking system in order to get maximum efficiency	[137]
Dielectric totally internally reflecting concentrator	(i) Higher efficiency and concentration ratio than CPC (ii) Work without any needs of cooling features	[84]	Cannot efficiently pass all of the solar energy that it accepts into a lower index media	[84]
Hyperboloid concentrator	Very compact	[87]	Need to introduce lens at the entrance aperture to work effectively	[87]
RR, XX, XR, RX, and RXI	(i) Achieving the theoretical maximum acceptance angle concentration (ii) High concentration (iii) Lighter weight (iv) Less expensive tracking system	[93, 138]	The size of the cell must be kept to minimum to reduce shadowing effect	[138]

the temperature will pass 84°C without fluid in the cooling system.

Horne presents a cooling system for a paraboloidal dish which focuses the light onto cells [115]. Water is sent to the receiver by a central pipe. It then flows behind the cells. By applying this method, not only does the water cool the cells, but it also acts as a filter by absorbing a significant amount of UV radiation that would otherwise reach the cells. Russell

patented a heat pipe cooling system for linear Fresnel lenses in which each of them focuses the light onto a string of cells placed along the length of a heat pipe of circular cross-section; the panel is formed by several pipes mounted next to each other [116] (Figure 10).

Thermal energy is extracted from the heat pipe by an internal coolant circuit where inlet and outlet are on the same pipe end ensuring a uniform temperature along the pipe.

TABLE 4: Description of CPV modules.

CPV Type	Optics	Cell type	C. Ratio	Cooling	Tracking	Size	Power
Point focus	Fresnel	Silicon III-V	$50 < x < 500$	Passive	Two axis	215 m ²	25 kW
Large area point focus	Parabolic dish central tower	Silicon III-V	$150 < x < 500$	Active	Two_axis	14 m diameter, 135 m ²	24 kW
Linear system	Linear lens parabolic trough	Silicon III-V	$15 < x < 60$ $60 < x < 300$	Passive	One axis on parabolic	84 meter long and 250 m ² aperture	34 kW
Static systems	Non imaging device	Silicon	$1.5 < x < 10$	Passive	No tracking	—	—
Mini point focus	Small lens RXI device small parabolic	Silicon III-V	$300 < x < 1000$	Passive	Two_axis	2 m ²	200 W

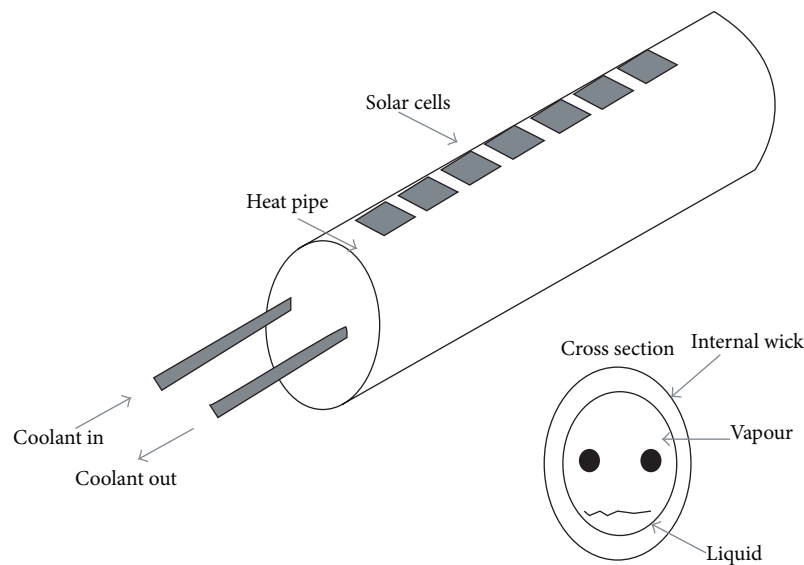


FIGURE 10: Heat pipe based cooling system [116].

Chenlo and Cid [106] described a linear Fresnel lens cooled by water flow through a galvanized steel pipe. The cells are soft soldered to a copper-aluminum-copper sandwich, which is in turn soldered to the rectangular pipe which presents good electrical and thermal models for uniform and nonuniform cell illumination.

Du et al. [117] proposed an experimental analysis of a water cooled concentrated photovoltaic system with the concentration ratio of 8.5. The water cooler was composed of an aluminum plate with two pipes which were attached at the back of the solar module. They showed that increasing the flow rate of water had a relation with increasing the efficiency of the module and CPV systems performed better with cooling systems.

Two different cooling systems were compared by Farahat [118] for the aim of cooling high concentration photovoltaic systems. Water cooling systems and heat pipe techniques were compared and recommended the heat pipe cooling method as the best method for HCPV.

Geng et al. [119] performed both numerical and experimental studies on cooling the high concentration photovoltaic by applying oscillating heat pipes as the cooling system. Their numerical study analyzed the temperature

distribution under different heat flux and some other outdoor conditions. Their results demonstrated that using heat pipes was a reliable, simple, uniform, and costless cooling method. Also, oscillating heat pipes need no air fan or pump and have no power consumption which makes them suitable for HCPV systems.

Chong and Tan [120] discussed a study on applying an automotive radiator as the active cooling system of the dense-array concentrator photovoltaic system. They employed a computational fluid dynamic (CFD) to perform a flow and heat transfer analysis for the cooling system of the mentioned CPV. For evaluation and feasibility of the study, they set up an experimental procedure with the concentration ratio of 377 suns. They observed that by applying the cooling system when the temperature of the cell reduced from 59.4°C to 37.1°C, the efficiency successfully improved from 22.39% to 26.86%.

During the past decades, heat sinks became popular devices for cooling processes. Many researchers conducted studies about using heat sink for cooling CPV systems.

Karathanassis et al. [121] conducted a study about optimizing the microchannel, plate-fin heat sink suitable for the cooling of a linear parabolic trough concentrating photovoltaic/thermal (CPVT) system. Their results showed that

TABLE 5: Different CPV projects with specifications [22, 87].

Companies/institutions	Type of concentrator	Type of focus	Concentration ratio	Tracking system	Cooling system	Efficiency	Cost	Reference
Sun power corporation	Fresnel lens	Point	25-400	—	—	27%	—	[22]
Solar research corporation	Parabolic dish	Point	239	Yes	Yes	22%	—	[139]
Photovoltaics International	Fresnel lens	Linear	10	Yes	—	12.7%	4-6 cent kwh (110 MW/yr production rate)	[140]
Polytechnical University of Madrid	Flat concentration devices (RXI)	point	1000	No	—	—	Low cost (need no tracking system due to high acceptance angle)	[141]
Fraunhofer-Institut für Solare Energiesysteme	Parabolic and trough	Linear and point	214	yes	yes	77.5%	—	[142]
Entech	Fresnel lenses	Linear	20	Yes	—	15%	7-15 cent Kwh (30 MW/yr production rate)	[143]
BP Solar and the Polytechnical University of Madrid	Parabolic trough	Linear	38	Yes	Yes	13%	13 cent kwh (15 MW/yr production rate)	[144]
Australian National University	Parabolic trough	Linear	30	Yes	—	15%	—	[145]
AMONIX and Arizona Public Service	Fresnel lens	Point	250	Yes	Yes	24%	—	[146]

TABLE 6: Comparative analysis of different CPV systems from economic aspects [49].

Primary concentrator	Secondary concentrator	Tracking system	Concentration ratio	Cost \$/W _p
Point focus Fresnel lens	No	Gimbals	36	1.48
Cylindrical paraboloid	Point-focus CPC	Polar	65	1.78
Linear Fresnel lens	Solid CPC	Gimbals	37	2.02
Curved TIR lens	No	Polar	28	1.97
Curved Fresnel lens	No	Polar	15	2.18
V-trough, screen printed	No	Polar	2	4.31

The costs given in the table are for cells, optical systems, mountings, and trackers only, including construction costs; balance of system costs are omitted as they are similar for all types of collector. The cost in \$/W_p is for collectors at operating temperature and, for concentrators, is based on direct beam irradiance of 850 W/m²; the cost for the flat plate is based on a total irradiance of 1000 W/m² [49].

TABLE 7: Fluids compatible with copper and aluminum, based on heat pipe life tests.

	Copper	Aluminum
Compatible	(i) Water	(i) Ammonia
	(ii) Methanol	(ii) Acetone
	(iii) Ethanol	(iii) Toluene
		(iv) n-Butane
		(v) n-pentane
		(vi) n-heptane
Incompatible	(i) Ammonia	(i) Water
	(ii) Acetone	(ii) Methanol, other alcohols
		(iii) Benzene (carcinogen)
		(iv) Naphthalene

microchannel heat sinks are ideal high heat flux dissipation as they achieve thermal resistance values as low as 0.0082 K/W. Also, their 1-D model could predict the flow and conjugate heat transfer inside a microchannel.

Do et al. [122] proposed a thermal resistance correlation as a design tool of a natural convective heat sink with plate-fins for concentrating photovoltaic (CPV). Different experimental investigations were also done for various heat sink geometries, input powers, and inclination angles. Their correlation could predict the effect of inclination angles and fin spacing. The optimized fin spacing was highly dependent on the inclination angle and temperature difference for specific geometry.

Edenburn did an analysis for a point focus Fresnel lens array under passive cooling system [123]. The cooling device is made up of linear fins on all available heat sink surfaces. The passive heat sink keeps the cell temperature below 150°C even on extreme days at a concentration level of about 90 suns.

Natarajan et al. [124] elaborated a numerical investigation of solar temperature of concentrated PV using Fresnel lenses with a concentration ratio of 10x with and without a passive cooling system. The simulation results showed that a number of four fins of 1 mm thickness and 5 mm height were favorable for the mentioned CPV.

By applying water as working fluid, Kumar and Reddy [125] investigated properties of porous disc receivers by different porosities. Empirical correlations were developed

to determine the Nusselt number and friction factor for the porous disc receiver. Satyanarayana et al. [126] developed different porous enhanced receiver configurations to increase the heat transfer rate. Drabiniok and Neyer [127] proposed an experimental study about special cooling systems of PB cells on the basis of a bionic method using a porous compound polymer foil. The foil was laminated directly on silicon substrates providing good thermal contact with the water cooled down by evaporation. A temperature reduction of up to 11.7°C was observed and the presented system was capable of self-regulating the water flow and the resulting cooling rate by its direct dependency on environmental conditions like temperature and air velocity.

Sun et al. [128] performed an experimental study about heat dissipation of linear concentrating photovoltaic by applying a direct liquid-immersion cooling method using dimethyl silicon oil. The results showed that the temperature of the cell rose from 0 to 35 increasing linearly with oil temperature. The cooling capacity of the direct liquid-immersion cooling made this method favorable, and the average cell temperature and heat transfer temperature difference could be maintained in the range between 20–31°C and 5–16°C, respectively, at a direct normal irradiance of about 910 W/m², 15°C silicon oil inlet temperature, and Re numbers varying from 13,602 to 2720. Finally, they reported no significant efficiency degradation and the electrical performance was considered to be stable after 270 days of silicon oil immersion.

Teo et al. [129] did an experimental study on analyzing the effect of active cooling systems on the efficiency of the PV modules. They applied parallel arrays of ducts with inlet/outlet modified designs for uniform airflow distribution which attached to the back of the module. The efficiency increased from 8-9% to 12% and 14% by using the active cooling system.

Ji et al. [130] performed a numerical and experimental study on using a jet impingement/channel receiver for cooling densely packed PV cells under a paraboloidal dish concentrator. They had shown that the proposed system has the desirable working performance and was of good application potential for the cooling of PV cells exposed to a high heat flux.

Brideau and Collins [131] could increase the heat transfer coefficient between the PV cells and air by using an impinging

TABLE 8: Main characteristics of different cooling system.

Type	Description	Reference
Heat pipe	(i) Simple (ii) Reliable (iii) Uniform (iv) Costless (v) Needs no air fan, pump, or energy consumption (vi) Suitable for HCPV	[118, 119]
Microchannels	(i) Low thermal resistance (ii) Low power requirement (iii) Ability to remove a large amount of heat in a small area	[102, 147]
Forced air	(i) Less efficient than water (ii) More parasitic power	[110]
Porous	High temperature reduction with appropriate attachment	[127]
Impinging jet	Applying the coolant for hybrid system	[131]

jet with the aim of proposing a hybrid PV/T system. Table 8 shows the main description of different cooling systems.

5. Conclusion

Environmental issues and energy saving concerns have always been a major global problem. CPV systems are special technology due to their capability of producing electricity with high efficiency. A review of solar photovoltaic concentrators' technologies and their characteristics and properties such as their fundamental functions, efficiencies, concentration ratio, tracking systems, cooling systems, and brief comparison in some parts is presented. Choosing the complete CPV containing the concentrator, tracking system, and cooling system is highly dependent on some limitation factors such as the climate conditions, geographical conditions, budget limits, and space limits. Consequently, for choosing an appropriate CPV system, considerations can be made by using the summarized information provided in Tables 3–8 by assuming the limitation factors.

Tables 3–6 present the main and specific characteristics of different concentrated photovoltaic systems and Tables 7–8 summarize some factors for choosing the appropriate cooling system.

Through this review paper, we introduced solar concentrated photovoltaic systems in a detailed description in order to provide some main information for scientists and manufactures to improve the CPV technology and to optimize the efficiencies. Finally, it will draw wider interest to the use of concentrated photovoltaic technology.

Conflict of Interests

The authors declare that there is no conflict of interests regarding the publication of this paper.

Acknowledgment

The authors gratefully acknowledge Dr. Kiyan Parham, the lecturer of Mechanical Engineering Department in Eastern

Mediterranean University, for his valuable help for searching the literature.

References

- [1] D. Abbott, "Keeping the energy debate clean: how do we supply the world's energy needs?" *Proceedings of the IEEE*, vol. 98, no. 1, pp. 42–66, 2010.
- [2] P. E. Glaser, "Power from the sun: its future," *Science*, vol. 162, no. 3856, pp. 857–861, 1968.
- [3] B. Mendoza, "Total solar irradiance and climate," in *Fundamentals of Space Environment Science*, V. Jatenco-Pereira, A. C.-L. Chian, J. F. Valdes-Galicia, and M. A. Shea, Eds., pp. 882–890, 2005.
- [4] H. Mousazadeh, A. Keyhani, A. Javadi, H. Mobli, K. Abrinia, and A. Sharifi, "A review of principle and sun-tracking methods for maximizing solar systems output," *Renewable and Sustainable Energy Reviews*, vol. 13, no. 8, pp. 1800–1818, 2009.
- [5] A. Lewandowski and D. Simms, "An assessment of linear Fresnel lens concentrators for thermal applications," *Energy*, vol. 12, no. 3–4, pp. 333–338, 1987.
- [6] J. O'Gallagher and R. Winston, "Performance model for two-stage optical concentrators for solar thermal applications," *Solar Energy*, vol. 41, no. 4, pp. 319–325, 1988.
- [7] J. Xiao, X. Wei, Z. Lu, W. Yu, and H. Wu, "A review of available methods for surface shape measurement of solar concentrator in solar thermal power applications," *Renewable and Sustainable Energy Reviews*, vol. 16, no. 5, pp. 2539–2544, 2012.
- [8] D. Feuermann, J. M. Gordon, and M. Huleihil, "Light leakage in optical fibers: experimental results, modeling and the consequences for remote lighting and solar concentrator systems," in *Nonimaging Optics: Maximum Efficiency Light Transfer VI*, R. Winston, Ed., pp. 65–75, August 2001.
- [9] A. Garcia-Botella, D. Vazquez, and E. Bcrnabeu, "A new concentrator-collimator lighting system using LED technology," *Journal of the Illuminating Engineering Society*, vol. 29, no. 2, pp. 135–140, 2000.
- [10] A. García-Botella, D. Vázquez, and E. Bernabeu, "Geometric and thermal design for a new concentrator-collimator lighting system based on LED technology," *Metrologia*, vol. 37, no. 5, pp. 607–610, 2000.

- [11] H. Arashi, D. Cooke, and H. Naito, "Fivefold increase in solar laser output with a nonimaging concentrator," *Japanese Journal of Applied Physics I: Regular Papers & Short Notes & Review Papers*, vol. 34, no. 9A, pp. 4795–4798, 1995.
- [12] H. Arashi, Y. Kaneda, and M. Ishigame, "A solar-pumped laser using a large solar concentrator," in *Clean and Safe Energy Forever*, T. Horigome, K. Kimura, T. Takakura, T. Nishino, and I. Fujii, Eds., vol. 1–3, pp. 445–449, Pergamon Press, 1990.
- [13] S. A. Bakhramov, S. D. Payziyev, S. I. Klychev, A. K. Kasimov, and A. A. Abdurakhmanov, "Laser on the big solar concentrator," in *Proceedings of the 2nd International Conference on Advanced Optoelectronics and Lasers (CAOL '05)*, I. A. Sukhoivanov, Ed., vol. 1, pp. 109–111, September 2005.
- [14] V. Krupkin, G. Thompson, A. Yogev, and M. Oron, "Compound parabolical concentrator as pumping device for solid state solar lasers," in *8th Meeting on Optical Engineering in Israel: Optical Engineering and Remote Sensing*, M. Oron, I. Shladov, and Y. Weissman, Eds., vol. 1971 of *Proceedings of SPIE*, pp. 400–407, December 1992.
- [15] M. Lando, J. Kagan, and B. Linyekin, "38-watt Nd:YAG laser pumped by a 6.85 m² target-aligned solar concentrator," in *Electro-Optics and Microelectronics*, R. Lavi and E. Azoulay, Eds., pp. 33–36, 2000.
- [16] W. Villasmil and A. Steinfeld, "Hydrogen production by hydrogen sulfide splitting using concentrated solar energy—thermodynamics and economic evaluation," *Energy Conversion and Management*, vol. 51, no. 11, pp. 2353–2361, 2010.
- [17] A. Z'Graggen, P. Haueter, G. Maag, M. Romero, and A. Steinfeld, "Hydrogen production by steam-gasification of carbonaceous materials using concentrated solar energy—IV. Reactor experimentation with vacuum residue," *International Journal of Hydrogen Energy*, vol. 33, no. 2, pp. 679–684, 2008.
- [18] A. Z'Graggen, P. Haueter, G. Maag, A. Vidal, M. Romero, and A. Steinfeld, "Hydrogen production by steam-gasification of petroleum coke using concentrated solar power—III. Reactor experimentation with slurry feeding," *International Journal of Hydrogen Energy*, vol. 32, no. 8, pp. 992–996, 2007.
- [19] B. Parida, S. Iniyan, and R. Goic, "A review of solar photovoltaic technologies," *Renewable and Sustainable Energy Reviews*, vol. 15, no. 3, pp. 1625–1636, 2011.
- [20] R. McConnell, S. Kurtz, and M. Symko-Davies, "Concentrator photovoltaic technologies," *Refocus*, vol. 6, no. 4, pp. 35–39, 2005.
- [21] A. Luque and V. Andreev, *Concentrator Photovoltaics*, Springer, Heidelberg, Germany, 2007.
- [22] R. M. Swanson, "The promise of concentrators," *Progress in Photovoltaics: Research and Applications*, vol. 8, no. 1, pp. 93–111, 2000.
- [23] V. Andreev, V. D. Romyantsev, and V. A. Grilikhes, *Photovoltaic Conversion of Concentrated Sunlight*, John Wiley & Sons, Chichester, UK, 1997.
- [24] P. Pérez-Higueras, E. Muñoz, G. Almonacid, and P. G. Vidal, "High Concentrator PhotoVoltaics efficiencies: present status and forecast," *Renewable and Sustainable Energy Reviews*, vol. 15, no. 4, pp. 1810–1815, 2011.
- [25] S. J. Gallagher, B. Norton, and P. C. Eames, "Quantum dot solar concentrators: electrical conversion efficiencies and comparative concentrating factors of fabricated devices," *Solar Energy*, vol. 81, no. 6, pp. 813–821, 2007.
- [26] J. Lushetsky, *Accelerating Innovation in Solar Technologies Overview of the DOE Solar Energy Technology Program*, US Department of Energy: Solar Energy Technologies Program, 2008.
- [27] B. A. Butler, E. E. van Dyk, F. J. Vorster, W. Okullo, M. K. Munji, and P. Booyesen, "Characterization of a low concentrator photovoltaics module," *Physica B: Condensed Matter*, vol. 407, no. 10, pp. 1501–1504, 2012.
- [28] R. Winston, J. J. O'Gallagher, and R. Gee, "Nonimaging solar concentrator with uniform irradiance," in *Nonimaging Optics and Efficient Illumination Systems*, R. Winston and R. J. Koshel, Eds., pp. 237–239, August 2004.
- [29] A. Garcia-Botella, A. A. Fernandez-Balbuena, D. Vázquez, and E. Bernabeu, "Ideal 3D asymmetric concentrator," *Solar Energy*, vol. 83, no. 1, pp. 113–117, 2009.
- [30] W. T. Xie, Y. J. Dai, R. Z. Wang, and K. Sumathy, "Concentrated solar energy applications using Fresnel lenses: a review," *Renewable and Sustainable Energy Reviews*, vol. 15, no. 6, pp. 2588–2606, 2011.
- [31] R. Leutz and A. Suzuki, *Nonimaging Fresnel Lenses: Design and Performance of Solar Concentrators*, Springer, Berlin, Germany, 2001.
- [32] R. Leutz, A. Suzuki, A. Akisawa, and T. Kashiwagi, "Developments and designs of solar engineering Fresnel lenses," in *Proceedings of the Symposium on Energy Engineering*, Hong Kong, 2000.
- [33] C. Sierra and A. J. Vázquez, "High solar energy concentration with a Fresnel lens," *Journal of Materials Science*, vol. 40, no. 6, pp. 1339–1343, 2005.
- [34] D. C. Miller and S. R. Kurtz, "Durability of Fresnel lenses: a review specific to the concentrating photovoltaic application," *Solar Energy Materials and Solar Cells*, vol. 95, no. 8, pp. 2037–2068, 2011.
- [35] E. Lorenzo and A. Luque, "Fresnel lens analysis for solar energy applications," *Applied Optics*, vol. 20, no. 17, pp. 2941–2945, 1981.
- [36] M. M. Valmiki, P. Li, J. Heyer et al., "A novel application of a Fresnel lens for a solar stove and solar heating," *Renewable Energy*, vol. 36, no. 5, pp. 1614–1620, 2011.
- [37] J. M. Monteagudo and A. Durán, "Fresnel lens to concentrate solar energy for the photocatalytic decoloration and mineralization of orange II in aqueous solution," *Chemosphere*, vol. 65, no. 7, pp. 1242–1248, 2006.
- [38] Y. Chen, "The continuous production of fresnel lens and a discussion on its application in solar building Chen Yike," in *Proceedings of ISES World Congress 2007*, D. Y. Goswami and Y. W. Zhao, Eds., vol. 1–5, pp. 323–326, 2007.
- [39] T. Ohkubo, T. Yabe, K. Yoshida et al., "Solar-pumped 80 W laser irradiated by a Fresnel lens," *Optics Letters*, vol. 34, no. 2, pp. 175–177, 2009.
- [40] T. Yabe, B. Bagheri, T. Ohkubo et al., "100 W-class solar pumped laser for sustainable magnesium-hydrogen energy cycle," *Journal of Applied Physics*, vol. 104, no. 8, Article ID 083104, 2008.
- [41] T. Yabe, T. Ohkubo, S. Uchida et al., "High-efficiency and economical solar-energy-pumped laser with Fresnel lens and chromium codoped laser medium," *Applied Physics Letters*, vol. 90, no. 26, Article ID 261120, 2007.
- [42] Y. Tripanagnostopoulos, C. Siabekou, and J. K. Tonui, "The Fresnel lens concept for solar control of buildings," *Solar Energy*, vol. 81, no. 5, pp. 661–675, 2007.
- [43] A. Tsangrassoulis, L. Doulos, M. Santamouris et al., "On the energy efficiency of a prototype hybrid daylighting system," *Solar Energy*, vol. 79, no. 1, pp. 56–64, 2005.

- [44] C. Sierra, E. Michie, and A. J. Vázquez, "Production improvement of NiAl coatings achieved by self-propagating high-temperature synthesis with concentrated solar energy," *Revista de Metalurgia*, pp. 469–474, 2005.
- [45] C. Sierra and A. J. Vázquez, "NiAl coatings on carbon steel by self-propagating high-temperature synthesis assisted with concentrated solar energy: mass influence on adherence and porosity," *Solar Energy Materials and Solar Cells*, vol. 86, no. 1, pp. 33–42, 2005.
- [46] C. Sierra and A. J. Vázquez, "NiAl coating on carbon steel with an intermediate Ni gradient layer," *Surface & Coatings Technology*, vol. 200, no. 14–15, pp. 4383–4388, 2006.
- [47] Y. Nakata, N. Shibuya, T. Kobe, K. Okamoto, A. Suzuki, and T. Tsuji, "Performance of circular Fresnel lens photovoltaic concentrator," *Japanese Journal of Applied Physics*, vol. 19, pp. 75–78, 1980.
- [48] S. Harmon, "Solar-optical analyses of a mass-produced plastic circular Fresnel lens," *Solar Energy*, vol. 19, no. 1, pp. 105–108, 1977.
- [49] G. R. Whitfield, R. W. Bentley, C. K. Weatherby et al., "The development and testing of small concentrating PV systems," *Solar Energy*, vol. 67, no. 1–3, pp. 23–34, 1999.
- [50] F. Franc, V. Jirka, M. Malý, and B. Nábělek, "Concentrating collectors with flat linear fresnel lenses," *Solar and Wind Technology*, vol. 3, no. 2, pp. 77–84, 1986.
- [51] D. Gerion, F. Pinaud, S. C. Williams et al., "Synthesis and properties of biocompatible water-soluble silica-coated CdSe/ZnS semiconductor quantum dots," *Journal of Physical Chemistry B*, vol. 105, no. 37, pp. 8861–8871, 2001.
- [52] O. I. Mičić, H. M. Cheong, H. Fu et al., "Size-dependent spectroscopy of InP quantum dots," *Journal of Physical Chemistry B*, vol. 101, no. 25, pp. 4904–4912, 1997.
- [53] R. Reisfeld and C. K. Jorgensen, "Luminescent solar concentrators for energy conversion," *Structure and Bonding*, vol. 49, pp. 1–36, 1982.
- [54] K. Barnham, J. L. Marques, J. Hassard, and P. O'Brien, "Quantum-dot concentrator and thermodynamic model for the global redshift," *Applied Physics Letters*, vol. 76, no. 9, pp. 1197–1199, 2000.
- [55] V. Wittwer, K. Heidler, A. Zastrow, and A. Goetzberger, "Theory of fluorescent planar concentrators and experimental results," *Journal of Luminescence*, vol. 24–25, no. 2, pp. 873–876, 1981.
- [56] A. Goetzberger, W. Stahl, and V. Wittwer, "Physical limitations of the concentration of direct and diffuse radiation," in *Proceedings of the 6th European Photovoltaic Solar Energy Conference*, Reidel, Dordrecht, The Netherlands, 1985.
- [57] A. P. Alivisatos, "Perspectives on the physical chemistry of semiconductor nanocrystals," *The Journal of Physical Chemistry*, vol. 100, no. 31, pp. 13226–13239, 1996.
- [58] A. Schüler, M. Python, M. V. del Olmo, and E. de Chambrier, "Quantum dot containing nanocomposite thin films for photoluminescent solar concentrators," *Solar Energy*, vol. 81, no. 9, pp. 1159–1165, 2007.
- [59] K. R. Kumar and K. S. Reddy, "Effect of porous disc receiver configurations on performance of solar parabolic trough concentrator," *Heat and Mass Transfer*, vol. 48, no. 3, pp. 555–571, 2012.
- [60] J. A. Clark, "An analysis of the technical and economic performance of a parabolic trough concentrator for solar industrial process heat application," *International Journal of Heat and Mass Transfer*, vol. 25, no. 9, pp. 1427–1438, 1982.
- [61] K.-J. Riffelmann, A. Neumann, and S. Ulmer, "Performance enhancement of parabolic trough collectors by solar flux measurement in the focal region," *Solar Energy*, vol. 80, no. 10, pp. 1303–1313, 2006.
- [62] S. A. Omer and D. G. Infield, "Design and thermal analysis of a two stage solar concentrator for combined heat and thermoelectric power generation," *Energy Conversion and Management*, vol. 41, no. 7, pp. 737–756, 2000.
- [63] M. A. Al-Nimr and M. K. Alkam, "A modified tubeless solar collector partially filled with porous substrate," *Renewable Energy*, vol. 13, no. 2, pp. 165–173, 1998.
- [64] K. R. Kumar and K. S. Reddy, "Thermal analysis of solar parabolic trough with porous disc receiver," *Applied Energy*, vol. 86, no. 9, pp. 1804–1812, 2009.
- [65] S. D. Odeh, G. L. Morrison, and M. Behnia, "Modelling of parabolic trough direct steam generation solar collectors," *Solar Energy*, vol. 62, no. 6, pp. 395–406, 1998.
- [66] K. S. Reddy, K. R. Kumar, and G. V. Satyanarayana, "Numerical investigation of energy-efficient receiver for solar parabolic trough concentrator," *Heat Transfer Engineering*, vol. 29, no. 11, pp. 961–972, 2008.
- [67] K. S. Reddy and G. V. Satyanarayana, "Numerical study of porous finned receiver for solar parabolic trough concentrator," *Engineering Applications of Computational Fluid Mechanics*, vol. 2, no. 2, pp. 172–184, 2008.
- [68] Q.-C. Zhang, K. Zhao, B.-C. Zhang et al., "New cermet solar coatings for solar thermal electricity applications," *Solar Energy*, vol. 64, no. 1–3, pp. 109–114, 1998.
- [69] A. Rabl, *Active Solar Collectors and Their Applications*, Oxford University Press, New York, NY, USA, 1985.
- [70] F. Kreith and J. E. Kreider, *Principles of Solar Engineering*, McGraw-Hill, New York, NY, USA, 1978.
- [71] J. A. Duffie and W. A. Beckman, *Solar Engineering of Thermal Processes*, John Wiley & Sons, Hoboken, NJ, USA, 2006.
- [72] F. Kreith and J. E. Kreider, *Principles of Solar Engineering*, Hemisphere Publishing Corporation, Washington, DC, USA, 1978.
- [73] A. Suzuki and S. Kobayashi, "Yearly distributed insolation model and optimum design of a two dimensional compound parabolic concentrator," *Solar Energy*, vol. 54, no. 5, pp. 327–331, 1995.
- [74] S. Senthilkumar, K. Perumal, and P. S. S. Srinivasan, "Construction and performance analysis of a three dimensional compound parabolic concentrator for a spherical absorber," *Journal of Scientific and Industrial Research*, vol. 66, no. 7, pp. 558–564, 2007.
- [75] N. Yehezkel, J. Appelbaum, A. Yogeve, and M. Oron, "Losses in a three-dimensional compound parabolic concentrator as a second stage of a solar concentrator," *Solar Energy*, vol. 51, no. 1, pp. 45–51, 1993.
- [76] A.-J. N. Khalifa and S. S. Al-Mutawalli, "Effect of two-axis sun tracking on the performance of compound parabolic concentrators," *Energy Conversion and Management*, vol. 39, no. 10, pp. 1073–1079, 1998.
- [77] T. K. Mallick, P. C. Eames, T. J. Hyde, and B. Norton, "The design and experimental characterisation of an asymmetric compound parabolic photovoltaic concentrator for building façade integration in the UK," *Solar Energy*, vol. 77, no. 3, pp. 319–327, 2004.
- [78] X. Ning, R. Winston, and J. O'Gallagher, "Dielectric totally internally reflecting concentrators," *Applied Optics*, vol. 26, no. 2, pp. 300–305, 1987.

- [79] X. H. Ning, "Application of nonimaging optical concentrators to infrared energy detection," in *Nonimaging Optics: Maximum Efficiency Light Transfer*, vol. 1528 of *Proceedings of SPIE*, p. 88, 1991.
- [80] R. Ramirez-Iniguez and R. Green, "Elliptical and parabolic totally internally reflecting optical antennas for wireless infrared communications," in *Proceedings of the IrDA/IEE/IEEE Conference on Optical Wireless*, Warwick University, 2003.
- [81] R. Ramirez-Iniguez and R. J. Green, "Optical antenna design for indoor optical wireless communication systems," *International Journal of Communication Systems*, vol. 18, no. 3, pp. 229–245, 2005.
- [82] X. H. Ning, J. O'Gallagher, and R. Winston, "Optics of two-stage photovoltaic concentrators with dielectric second stages," *Applied Optics*, vol. 26, no. 7, pp. 1207–1212, 1987.
- [83] F. Muhammad-Sukki, R. Ramirez-Iniguez, S. G. McMeekin, B. G. Stewart, and B. Clive, "Optimised dielectric totally internally reflecting concentrator for the solar photonic optoelectronic transformer system: maximum concentration method," in *Knowledge-Based and Intelligent Information and Engineering Systems*, R. Setchi, I. Jordanov, R. J. Howlett, and L. C. Jain, Eds., vol. 6279 of *Lecture Notes in Computer Science*, pp. 633–641, Springer, Berlin, Germany, 2010.
- [84] M. F. Piszczor and R. P. Macosko, "A high-efficiency refractive secondary solar concentrator for high temperature solar thermal applications," Technical Memorandum, NASA, 2000.
- [85] F. Muhammad-Sukki, S. H. Abu-Bakar, R. Ramirez-Iniguez et al., "Mirror symmetrical dielectric totally internally reflecting concentrator for building integrated photovoltaic systems," *Applied Energy*, vol. 113, pp. 32–40, 2014.
- [86] I. M. S. Ali, T. K. Mallick, P. A. Kew, T. S. O'Donovan, and K. S. Reddy, "Optical performance evaluation of a 2-D and 3-D novel hyperboloid solar concentrator," in *Proceedings of the 11th World Renewable Energy Congress*, Abu Dhabi, UAE, 2010.
- [87] F. Muhammad-Sukki, R. Ramirez-Iniguez, S. G. McMeekin, B. G. Stewart, and B. Clive, "Solar concentrators," *International Journal of Applied Sciences*, vol. 1, no. 1, pp. 1–15, 2010.
- [88] N. Sellami, T. K. Mallick, and D. A. McNeil, "Optical characterisation of 3-D static solar concentrator," *Energy Conversion and Management*, vol. 64, pp. 579–586, 2012.
- [89] A. García-Botella, A. Á. Fernández-Balbuena, D. Vázquez, E. Bernabeu, and A. González-Cano, "Hyperparabolic concentrators," *Applied Optics*, vol. 48, no. 4, pp. 712–715, 2009.
- [90] J. M. Gordon, "Complementary construction of ideal nonimaging concentrators and its applications," *Applied Optics*, vol. 35, no. 28, pp. 5677–5682, 1996.
- [91] C.-F. Chen, C.-H. Lin, H.-T. Jan, and Y.-L. Yang, "Design of a solar concentrator combining paraboloidal and hyperbolic mirrors using ray tracing method," *Optics Communications*, vol. 282, no. 3, pp. 360–366, 2009.
- [92] I. M. Saleh Ali, T. Srihari Vikram, T. S. O'Donovan, K. S. Reddy, and T. K. Mallick, "Design and experimental analysis of a static 3-D elliptical hyperboloid concentrator for process heat applications," *Solar Energy*, vol. 102, pp. 257–266, 2014.
- [93] J. C. Minano, J. C. Gonzalez, and I. Zanesco, "Flat high concentration devices," in *Proceedings of the 24th IEEE Photovoltaic Specialists Conference*, vol. 1-2, pp. 1123–1126, IEEE, New York, NY, USA, December 1994.
- [94] R. Winston, J. C. Minano, and P. Benitez, *Nonimaging Optics*, Elsevier Academic Press, San Diego, Calif, USA, 2005.
- [95] J. C. Minano, J. C. Gonzalez, and P. Benitez, "A high-gain, compact, nonimaging concentrator: RXI," *Applied Optics*, vol. 34, no. 34, pp. 7850–7856, 1995.
- [96] J. C. Minano, P. Benitez, and J. C. Gonzalez, "RX: a nonimaging concentrator," *Applied Optics*, vol. 34, no. 13, pp. 2226–2235, 1995.
- [97] P. Benitez and J. C. Minano, "Analysis of the image formation capability of RX concentrators," in *Nonimaging Optics: Maximum Efficiency Light Transfer III*, R. Winston, Ed., vol. 2538, pp. 73–84, 1995.
- [98] J. C. Minano, J. C. Gonzalez, and P. Benitez, "New nonimaging designs: the RX and the RXI concentrators," in *Nonimaging Optics: Maximum-Efficiency Light Transfer II*, R. Winston and R. L. Holman, Eds., vol. 2016 of *Proceedings of SPIE*, pp. 120–127, 1993.
- [99] I. Peterina, A. B. Cueli, J. Díaz, J. Moracho, and A. R. Lagunas, "CENER experience testing CPV modules," *Energetica Internacional*, no. 123, 2012.
- [100] V. L. Dalal and A. R. Moore, "Design considerations for high-intensity solar cell," *Journal of Applied Physics*, vol. 48, no. 3, p. 8, 1977.
- [101] D. J. Mbeue, H. C. Card, and D. C. Card, "A model of silicon solar cells for concentrator photovoltaic and photovoltaic/thermal system design," *Solar Energy*, vol. 35, no. 3, pp. 247–258, 1985.
- [102] A. Royne, C. J. Dey, and D. R. Mills, "Cooling of photovoltaic cells under concentrated illumination: a critical review," *Solar Energy Materials and Solar Cells*, vol. 86, no. 4, pp. 451–483, 2005.
- [103] G. Sala, "Cooling of solar cells," in *Cells and Optics for Photovoltaic Concentration*, A. Hilger, Ed., pp. 239–267, Adam Hilger, Bristol, UK, 1989.
- [104] I. Anton, G. Sala, and D. Pachon, "Correction of the Voc vs. temperature dependence under non-uniform concentrated illumination," in *Proceedings of the 17th European Photovoltaic Solar Energy Conference*, pp. 156–159, Munich, Germany, 2001.
- [105] A. Cheknane, B. Benyoucef, and A. Chaker, "Performance of concentrator solar cells with passive cooling," *Semiconductor Science and Technology*, vol. 21, no. 2, pp. 144–147, 2006.
- [106] F. Chenlo and M. Cid, "A linear concentrator photovoltaic module: analysis of non-uniform illumination and temperature effects on efficiency," *Solar Cells*, vol. 20, no. 1, pp. 27–39, 1987.
- [107] A. Luque, G. Sala, and J. C. Arboiro, "Electric and thermal model for non-uniformly illuminated concentration cells," *Solar Energy Materials and Solar Cells*, vol. 51, no. 3-4, pp. 269–290, 1998.
- [108] R. K. Mathur, D. R. Mehrotra, S. Mittal, and S. R. Dhariwal, "Thermal non-uniformities in concentrator solar cells," *Solar Cells*, vol. 11, no. 2, pp. 175–188, 1984.
- [109] R. W. Sanderson, D. T. O'Donnell, and C. E. Backus, "The effects of nonuniform illumination and temperature profiles on silicon solar cells under concentrated sunlight," in *Proceedings of the 14th IEEE Photovoltaic Specialists Conference (PVSC '80)*, pp. 431–436, January 1980.
- [110] A. D. Kraus and A. Bar-Cohen, *Design and Analysis of Heat Sinks*, John Wiley & Sons, New York, NY, USA, 1st edition, 1995.
- [111] W. G. Anderson, P. M. Dussinger, D. B. Sarraf, and S. Tamanna, "Heat pipe cooling of concentrating photovoltaic cells," in *Proceedings of the 33rd IEEE Photovoltaic Specialists Conference (PVSC '08)*, May 2008.

- [112] P. D. Dunn and D. A. Reay, *Heat Pipes*, Elsevier Science, Tarrytown, NY, USA, 4th edition, 1994.
- [113] W. G. Anderson, "Intermediate temperature fluids for heat pipes and LHPs," in *Proceedings of the 5th International Energy Conversion Engineering Conference (IECEC '07)*, AIAA, St. Louis, Mo, USA, 2007.
- [114] A. Akbarzadeh and T. Wadowski, "Heat pipe-based cooling systems for photovoltaic cells under concentrated solar radiation," *Applied Thermal Engineering*, vol. 16, no. 1, pp. 81–87, 1996.
- [115] W. E. Horne, "Solar energy system," US patent no. 5269851, 1993.
- [116] R. F. Russell, "Uniform temperature heat pipe and method of using the same," US patent no. 4320246, 1982.
- [117] B. Du, E. Hu, and M. Kolhe, "Performance analysis of water cooled concentrated photovoltaic (CPV) system," *Renewable and Sustainable Energy Reviews*, vol. 16, no. 9, pp. 6732–6736, 2012.
- [118] M. A. Farahat, "Improvement the thermal electric performance of a photovoltaic cells by cooling and concentration techniques," in *Proceedings of the 39th International Universities Power Engineering Conference (UPEC '04)*, pp. 623–628, September 2004.
- [119] W.-G. Geng, L. Gao, M. Shao, and X.-Y. Li, "Numerical and experimental study on cooling high-concentration photovoltaic cells with oscillating heat pipe," *International Journal of Low-Carbon Technologies*, vol. 7, no. 3, pp. 168–173, 2012.
- [120] K.-K. Chong and W.-C. Tan, "Study of automotive radiator cooling system for dense-array concentration photovoltaic system," *Solar Energy*, vol. 86, no. 9, pp. 2632–2643, 2012.
- [121] I. K. Karathanassis, E. Papanicolaou, V. Belessiotis, and G. C. Bergeles, "Multi-objective design optimization of a micro heat sink for Concentrating Photovoltaic/Thermal (CPVT) systems using a genetic algorithm," *Applied Thermal Engineering*, vol. 59, no. 1–2, pp. 733–744, 2013.
- [122] K. H. Do, T. H. Kim, Y.-S. Han, B.-I. Choi, and M.-B. Kim, "General correlation of a natural convective heat sink with plate-fins for high concentrating photovoltaic module cooling," *Solar Energy*, vol. 86, no. 9, pp. 2725–2734, 2012.
- [123] M. W. Edenburn, "Active and passive cooling for concentrating photovoltaic arrays," in *Proceedings of the 14th Photovoltaic Specialists Conference*, pp. 771–776, San Diego, Calif, USA, January 1980.
- [124] S. K. Natarajan, T. K. Mallick, M. Katz, and S. Weingaertner, "Numerical investigations of solar cell temperature for photovoltaic concentrator system with and without passive cooling arrangements," *International Journal of Thermal Sciences*, vol. 50, no. 12, pp. 2514–2521, 2011.
- [125] K. R. Kumar and K. S. Reddy, "Investigation of heat transfer characteristics of line focus receiver with porous disc inserts for solar parabolic trough concentrator," in *Proceedings of the 20th National and 9th International ISHMT-ASME Heat and Mass Transfer Conference*, Mumbai, India, 2010.
- [126] G. V. Satyanarayana, K. R. Kumar, and K. S. Reddy, "Numerical study of porous enhanced receiver for solar parabolic trough collector," in *Proceedings of the 3rd International Conference on Solar Radiation and Day Lighting*, New Delhi, India, 2007.
- [127] E. Drabiniok and A. Neyer, "Bionic micro porous evaporation foil for photovoltaic cell cooling," *Microelectronic Engineering*, vol. 119, pp. 65–69, 2014.
- [128] Y. Sun, Y. Wang, L. Zhu, B. Yin, H. Xiang, and Q. Huang, "Direct liquid-immersion cooling of concentrator silicon solar cells in a linear concentrating photovoltaic receiver," *Energy*, vol. 65, pp. 264–271, 2014.
- [129] H. G. Teo, P. S. Lee, and M. N. A. Hawlader, "An active cooling system for photovoltaic modules," *Applied Energy*, vol. 90, no. 1, pp. 309–315, 2012.
- [130] J. Ji, Y. Wang, T.-T. Chow, H. Chen, and G. Pei, "A jet impingement/channel receiver for cooling densely packed photovoltaic cells under a paraboloidal dish solar concentrator," *Heat Transfer Research*, vol. 43, no. 8, pp. 767–778, 2012.
- [131] S. A. Brideau and M. R. Collins, "Development and validation of a hybrid PV/Thermal air based collector model with impinging jets," *Solar Energy*, vol. 102, pp. 234–246, 2014.
- [132] C. A. Mgbemene, J. Duffy, H. Sun, and S. O. Onyegegbu, "Electricity generation from a compound parabolic concentrator coupled to a thermoelectric module," *Journal of Solar Energy Engineering*, vol. 132, no. 3, 2010.
- [133] P. D. Menghani, R. R. Udawant, A. M. Funde, and S. V. Dingare, "Low pressure steam generation by solar energy with fresnel lens: a review," *IOSR Journal of Mechanical and Civil Engineering*, vol. 5, pp. 60–63, 2013.
- [134] O. E. Miller, J. H. Mcleod, and W. T. Sherwood, "Thin sheet plastic Fresnel lenses of high aperture," *Journal of the Optical Society of America*, vol. 41, no. 11, p. 8, 1951.
- [135] S. Malato, J. Blanco, A. Vidal, and C. Richter, "Photocatalysis with solar energy at a pilot-plant scale: an overview," *Applied Catalysis B: Environmental*, vol. 37, no. 1, pp. 1–15, 2002.
- [136] G.-L. Dai, X.-L. Xia, C. Sun, and H.-C. Zhang, "Numerical investigation of the solar concentrating characteristics of 3D CPC and CPC-DC," *Solar Energy*, vol. 85, no. 11, pp. 2833–2842, 2011.
- [137] E. Hossain, R. Muhida, A. F. Dzulkipli, and K. A. A. Rahman, "Solar cell efficiency improvement using compound parabolic concentrator and an implementation of sun tracking system," in *Proceedings of the 11th International Conference on Computer and Information Technology (ICCIT '08)*, vol. 1–2, pp. 723–728, December 2008.
- [138] A. Terao, W. P. Mulligan, S. G. Daroczi et al., "A mirror-less design for micro-concentrator modules," in *Proceedings of the 28th IEEE Photovoltaic Specialists Conference*, pp. 1416–1419, 2000.
- [139] J. B. Lasich, A. Cleeve, N. Kaila et al., "Close-packed cell arrays for dish concentrators," in *Proceedings of the 24th IEEE Photovoltaic Specialists Conference*, pp. 1938–1941, December 1994.
- [140] N. Kaminar, J. McEntree, P. Stark, and D. Curchod, "SEA 10X concentrator development progress," in *Proceedings of the 22nd IEEE Photovoltaic Specialists Conference*, pp. 529–532, October 1991.
- [141] J. L. Alvarez, M. Hernandez, P. Benitez, and J. C. Minano, "Experimental measurements of RXI concentrators for photovoltaic applications," in *Proceedings of the 2nd World Conference and Exhibition on Photovoltaic Solar Energy Conversion*, Vienna, Austria, 1998.
- [142] M. Brunotte, A. Goetzberger, and U. Blieske, "Two-stage concentrator permitting concentration factors up to 300X with one-axis tracking," *Solar Energy*, vol. 56, no. 3, pp. 285–300, 1996.
- [143] M. J. O'Neill and A. J. McDanal, "Fourth-generation concentrator system: from the lab to the factory to the field," in *Proceedings of the 24th IEEE Photovoltaic Specialists Conference*, pp. 816–819, December 1994.
- [144] G. Sala, J. C. Arboiro, A. Luque et al., "480 kW peak EUCLIDES concentrator power plant using parabolic troughs," in *Proceedings of the 2nd World Conference and Exhibition on Photovoltaic Solar Energy Conversion*, Vienna, Austria, 1998.

- [145] A. W. Blakers and J. Smeltink, "The ANU PV/trough concentrator system," in *Proceedings of the 2nd World Conference on Photovoltaic Solar Energy Conversion*, Vienna, Austria, 1998.
- [146] V. Garboushian, S. Yoon, G. Turner, A. Gunn, and D. Fair, "A novel high-concentration PV technology for cost competitive utility bulk power generation," in *Proceedings of the 1st World Conference on Photovoltaic Energy Conversion*, pp. 1060–1063, Waikoloa, Hawaii, USA, December 1994.
- [147] D. B. Tuckerman and R. F. W. Pease, "High-performance heat sinking for VLSI," *Electron Device Letters*, vol. 2, no. 5, pp. 126–129, 1981.

Research Article

A Simple Approach in Estimating the Effectiveness of Adapting Mirror Concentrator and Tracking Mechanism for PV Arrays in the Tropics

**M. E. Ya'acob,¹ H. Hizam,^{1,2} H. Abdul Rahman,³ W. Z. Wan Omar,³
Myo Than Htay,⁴ and A. H. M. A. Rahim⁵**

¹ Department of Electrical & Electronic Engineering, Faculty of Engineering, Universiti Putra Malaysia, 43400 Serdang, Selangor, Malaysia

² Centre of Advanced Power and Energy Research (CAPER), Universiti Putra Malaysia, 43400 Serdang, Selangor, Malaysia

³ Centre of Electrical Energy Systems, Universiti Teknologi Malaysia, 81310 Johor Bahru, Malaysia

⁴ Department of Electrical and Electronic Engineering, Faculty of Engineering, Shinshu University, Nagano 380-8553, Japan

⁵ Department of Electrical Engineering, King Fahd University of Petroleum & Minerals, P.O. Box 349, Dhahran 31261, Saudi Arabia

Correspondence should be addressed to M. E. Ya'acob; fendyupm@gmail.com

Received 25 November 2013; Revised 16 April 2014; Accepted 12 May 2014; Published 2 June 2014

Academic Editor: Hui Shen

Copyright © 2014 M. E. Ya'acob et al. This is an open access article distributed under the Creative Commons Attribution License, which permits unrestricted use, distribution, and reproduction in any medium, provided the original work is properly cited.

Mirror concentrating element and tracking mechanism has been seriously investigated and widely adapted in solar PV technology. In this study, a practical in-field method is conducted in Serdang, Selangor, Malaysia, for the two technologies in comparison to the common fixed flat PV arrays. The data sampling process is measured under stochastic weather characteristics with the main target of calculating the effectiveness of PV power output. The data are monitored, recorded, and analysed in real time via GPRS online monitoring system for 10 consecutive months. The analysis is based on a simple comparison of the actual daily power generation from each PV generator with statistical analysis of multiple linear regression (MLR) and analysis of variance test (ANOVA). From the analysis, it is shown that tracking mechanism generates approximately 88 Watts (9.4%) compared to the mirror concentrator which generates 144 Watts (23.4%) of the cumulative dc power for different array configurations at standard testing condition (STC) references. The significant increase in power generation shows feasibilities of implying both mechanisms for PV generators and thus contributes to additional reference in PV array design.

1. Introduction

In this work, the main target is to increase the daily energy generation from PV generators despite the fluctuating sun irradiance, G , which is the sole source of photonic effect in PV electricity conversion process. Research works around the globe were conducted to improve the energy production of solar PV modules under real operating conditions. Chen [1] reported that the installed capacity of the PV in Malaysia at the end of 2009 and 2010 is 1 MWp and 100 MWp, respectively. The potential Malaysian uptake of solar PV is set to increase with the estimated requirement of up to 6500 MW by 2030 [1]. Market research also pointed that solar PV would have the biggest share of Malaysia renewable energy installations

as the price of solar PV keeps going down. This is mainly due to technology maturity and economies of scale as more solar cell manufacturers come online.

The Government of Malaysia had officially started the fit-in-tariff (FiT) enactment of the renewable energy law on December 1, 2011, to encourage uptake of renewable energy projects in the country. In this scheme, solar PV received the highest FiT rate of up to RMI.77 per kWh energy production for projects approved in 2012. This rate is applicable for 21-year contract period. The rate for new projects will reduce by 8% per year, depending on the approval date of the project [2].

The local condition and environment at the targeted location for the application of the PV varies. This affects the

generation capability and the efficiency of the PV modules, which are generally calculated and solely extrapolated by per PV module characteristics, which are obtained from standard tests in the laboratory [3]. The energy generation quantity is not included, as this would depend on the duration of the sunshine and the quality of the sunlight incident onto the PV panel [4]. To increase the capability of the solar cells, solar tracking and solar light concentrations could be employed individually or in combination. Solar tracking basically employs mechanism that continually points the PV modules directly to the sun [5].

Mirror concentrating element and tracking mechanism has been seriously investigated and widely adapted in solar PV technology. In this study, a practical in-field method is conducted in Serdang, Selangor, Malaysia, by means of installing multiple solar systems: the first employing the 2-axis sun tracking system, the second employing mirror concentrating system, and the third employing a basic fixed system, a base system, to be used as comparator [6]. The mirror concentrator embedded in the $2 \times$ CPV technologies adopted V-through concept of configuration with enhancement in mirror concentration. Recent study by [7–11] which implies and enhances the optical efficiency of V-through technology in solar PV application creates alternative means of reducing the overall built-up area, quantity of module, and heat dissipation and thus significantly lowers down the installation cost. Climatic variables in most of the tropical based countries have significant effects on PV performance in generating sufficient and stabilized electricity to the normal grid [12–14] where radiation level (G) and temperature element (T) are the dominant factors in most of the PV efficiency calculations.

The duration of data sampling process is done for 10 consecutive months in the equatorial sun-belt region of uniform temperature-irradiance, high humidity-rainfall, and generally light wind weather characteristics. The data are monitored, recorded, and analysed in real time via general packet radio service (GPRS) which can be managed online via smart-pv.net. The analysis is based on standard testing conditions (STC) data per unit array generation where power contributions from mirror reflecting elements and tracking mechanism are practically analyzed. The STC, as defined in MS/IEC 61836 standards for the photovoltaic technology, reflects the reference values of the in-plane irradiance (G) of 1000 W/m^2 , PV cell junction temperature of 25° , and air mass (AM) of 1.5 value to be used during the quality testing of any PV device. A high quality, safe, and durable PV module delivers the expected rated power (W_p) withstanding extremely wide range of environmental conditions and is reputedly capable of delivering high energy yield over a period of time.

Statistical analysis applied for this work is multiple linear regression (MLR) by means of modelling the relationship between two or more explanatory variables. In this case the output power (P_{dc}) with the contributions from mirror and tracker element by fitting a linear equation to the observed data with the hypothesis of every value of the independent variable x_1 , x_2 is associated with the dependant variable y .

The common model for MLR with n given observations can be denoted by

$$y_i = \beta_0 + \beta_1 x_{i1} + \beta_2 x_{i2} + \varepsilon_i \quad \text{for } i = 1, 2, \dots, n. \quad (1)$$

The MLR technique observes the varying value of y_i by expressing the overall correlation as data = fit + residual, where the β represents the fit terminology and the ε for the residual or deviations of the observed and mean values of y_i . By adapting the analysis of variance (ANOVA) fitting model to the data sets, the analytical process of comparing the mean response values at different levels of the factor is simulated where the program computes a number of means and variances, dividing two variances and comparing the ratio to a handbook value to determine statistical significance [15, 16]. Each level of the factors is investigated to see if the response is significantly different from the response at other levels of the factor. The ANOVA provides a statistical test of whether or not the means of several groups are equal and therefore generalizes t -test to more than two groups for statistical significance. Some practical examples of ANOVA modelling for solar PV application are described in [17–20].

This paper reports the efforts by the authors to practically calculate the effectiveness of solar tracking and mirror based solar concentrating mechanism for electricity generation via simple comparison of recorded field data, where this information will be the additional reference in designing a PV array configuration installed in the tropics.

2. PV Pilot Plant Setup

The entire PV array installed at the site is connected directly to the nearest grid point (Feeder Pillar) which is linked to the main distribution board (MDB) for electricity distribution. The three different PV arrays are configured as shown in Figure 1 where each module is a series of 95 W CEEG monocrystalline modules with 17.05% practical conversion efficiency and the specifications are described in Table 1.

The air mass (AM) is the relative optical path length which light takes through the atmosphere normalized to the shortest possible path length with consideration of environmental blockage such as dust and particles. The site calculation is based on (2) with three time intervals of 9 am, 12 noon, and 3 pm for the duration of 7 days and projects the value of AM 1.4 or approximately 45° solar zenith angle comparable to air mass AM 1.5 global hemispherical defined by ASTM and IEC. Consider

$$AM = \left[1 + \left(\frac{s}{h} \right)^2 \right]^{0.5}, \quad (2)$$

where s is the shadow length and h is the object height.

DC power (in Watt) is calculated directly from PV array generation via online monitoring system <http://www.smart-pv.net> which adapts cloud database through general packet radio service (GPRS) on 3G cellular communication with global system for mobile communications. PV generator efficiency is calculated using

TABLE 1: Specifications of 1kWp PV generator system.

Fixed Flat PV (FF)	Tracking flat PV (TF)	Concentrating PV (CPV)
(i) Common flat PV array	(i) Dual-axis sun tracking	(i) Dual-axis sun tracking with mirror concentrator
(ii) Series connecting 12 units of CEEG 95 W monocrystalline module	(ii) Series connecting 12 units of CEEG 95 W monocrystalline module	(ii) Series connecting 6 units of CEEG 95 W monocrystalline module
(iii) Built-up area: 3.6 m × 2.4 m	(iii) Built-up area: 3.6 m × 2.4 m	(iii) Built-up area: 3.6 m × 2.4 m
(iv) Rated power: 1kW	(iv) Rated power: 1kW	(iv) Rated power: 1kW
(v) V_{oc} : 22.5 V × 12 = 270 V _{dc}	(v) V_{oc} : 22.5 V × 12 = 270 V _{dc}	(v) V_{oc} : 22.5 V × 6 = 135 V _{dc}
(vi) I_{sc} : 5.56 A _{dc}	(vi) I_{sc} : 5.56 A _{dc}	(vi) I_{sc} : 5.56 A _{dc}
(vii) P_{dc} : 1.5 kW (rated at STC)	(vii) P_{dc} : 1.5 kW (rated at STC)	(vii) P_{dc} : 0.75 kW (rated at STC)



Fixed flat (configured using 12 CEEG modules of 95 W)

(a)



Tracking flat (configured using 12 CEEG modules of 95 W)

(b)



2x CPV (configured using 6 CEEG modules of 95 W)

(c)

FIGURE 1: Overview of 3 types of PV generators installed at site.

(3) by implying factors of irradiation (G) and area (A) where the built-up area is 8.64 m² as follows:

$$\eta_{\text{gen}} = 100 * \left[\frac{P}{(G * A)} \right]. \quad (3)$$

The standard calculation for DC power is calculated using (4) where the values are based on the different types of PV arrays to produce the individual power outcome. The main element of calculating the contributions from mirror and tracking elements is done by means of a simple comparison of the recorded power output based on the actual data at site. Power from mirror concentrator (P_m) is calculated using (5)

and power from tracking mechanism (P_t) is calculated using (6). Consider

$$P_{dc} = I_{dc} \times V_{dc} \quad (4)$$

$$P_m = P_{CPV} - P_{TF} \quad (5)$$

$$P_t = P_{TF} - P_{FF}. \quad (6)$$

For (4) and (5), the ground condition during data sampling is the same at exact time sequence and is applying the same CEEG PV module specifications. For (6), the amount of PV module should be the same and as the tracking flat occupies twelve PV modules compared to the CPV which is configured

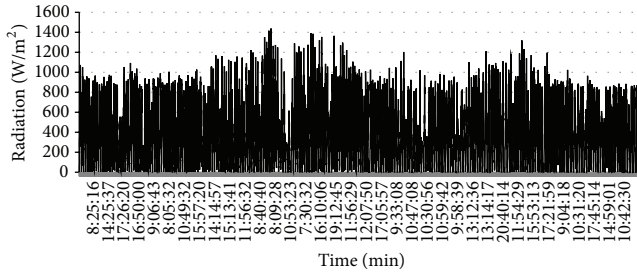


FIGURE 2: Radiation profile for 12,190 samples of field data.

using only six PV modules the approach is to divide P_{TF} with 2.

The data for three environment factors of radiation (G), wind speed (w), and ambient temperature (T_a) are captured and logged using 3-parameter weather station installed at site.

3. Results and Discussion

The radiation profile (in W/m^2) shown in Figure 2 is plotted for the whole monitoring period of 268 days operation with 12,190 data samples. The highest radiation level recorded during the sampling period was at $1438 W/m^2$ on 15 May 2012. The sun hours throughout the monitoring period are calculated at 3047.5 hours with 11.34 hours/day of sun radiation received which is relatively high and thus supports the 6 hours of direct sun each day all year round as claimed by Chen [1]. Figure 2 also indicates the time scale in x -axis (the time sequence of daily sun received at site) where if we segment the sun hours into 3 segments of 4 hours segment 2 (10.00 am to 2.00 pm) shows the highest radiation values compared to segment 1 (6.00 am to 10.00 am) and segment 3 (2.00 pm to 6.00 pm). The minimum recorded radiation started at the value of $3 W/m^2$ as early as 4.00 am for most of the days. The average radiation recorded for 15-minute interval during generation days is $339.7 W/m^2$.

The high value of radiation level at site is further supported based on the 2012 annual reports by the Meteorological Department of Malaysia where the mean daily global radiation was reported ranging from $16 MJ/m^2$ to $23 MJ/m^2$ as plotted in Figure 3.

From the report, it can be interpolated that the PV pilot plant in Universiti Putra Malaysia (UPM) receives a strong solar radiation of $17\text{--}18 MJ/m^2$ or $4.72\text{--}5 kWh/m^2$ daily. Haris [21, 22] supports this statement with yearly average global irradiance value of $1571 kWh/m^2$ or $4.3 kWh/m^2$ daily for Kuala Lumpur which is the closest reference to the project site. Figures 4 and 5 illustrate the ambient temperature (T_a) and wind speed (w) pattern at site throughout the monitoring period of 15-minute time intervals.

The recorded ambient temperature ranges from $22.2^\circ C$ up to $38.4^\circ C$ with an average value of $29.41^\circ C$, while wind speed flows from $0 m/s$ up to $8.9 m/s$ with average value of $1.27 m/s$. The wind profile is not very strong at the site due to the experience of having $0 m/s$ (no wind) for about 527 hours or 22 days throughout the monitoring period.

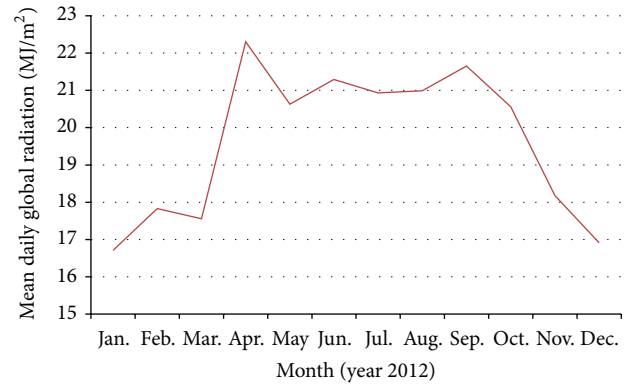


FIGURE 3: Monthly mean ambient temperature and mean daily global radiation for the year 2012 at KLIA, Sepang, Malaysia.

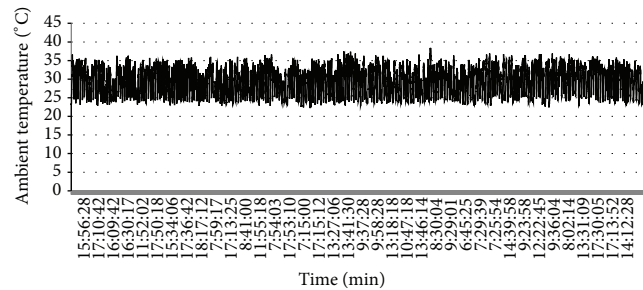


FIGURE 4: Ambient temperature pattern for 10 months.

The PV generator efficiency as in (3) is plotted as shown in Figure 6. From this calculation, the average values for 117 samples of data show that FF generator achieves efficiency of 10.04% and TF generator produces up to 10.78% which is the highest and the lowest efficiency value coming from CPV generator with 3.04%. In general, it can be denoted that the η_{gen} value contradicts the rated CEEG PV module efficiency of 17.05%.

As means of analysing mirror and tracker contribution, the power generation (in kilowatt) from mirror concentrator and tracking mechanism is plotted in Figure 7 for 62 data samples of standard testing conditions (STC) with 5% tolerance based on field measurement. Based on the field data collected, the ANOVA test as described in Table 2 is further calculated as statistical justification on the reliability of sample data used and to show correlation values of the mirror and tracker contribution. In this case, the CPV generator energy output (P_{dc}) is used as the dependent variable (y -parameter) as the generator has both mirror and tracking mechanism features. The mirror and tracking mechanism are classified as the independent variable (x -parameter).

At a sample time interval, the highest recorded power generated is from TF generator for 1.27 kW followed by 1.05 kW from FF generator and the least from CPV generator of 0.63 kW where the power generation heavily depended on the quantity of PV modules applied in each generator.

From the plotted data in Figure 8 and (4)–(6), the results showed that, for this site (Serdang, Malaysia), it is found that

TABLE 2: Summary output of MLR and ANOVA.

(a)

Regression statistics	
Multiple R	0.667607
R square	0.4457
Adjusted R square	0.42691
Standard error	0.062748
Observations	62

(b)

ANOVA					
	df	SS	MS	F	Sig F
Regression	2	0.186789	0.093395	23.72025	2.7573E - 08
Residual	59	0.232303	0.003937		
Total	61	0.419092			

(c)

	Coef	S.E	t Stat	P-value	Lower 95%	Upper 95%
Intercept	0.441245	0.026579	16.60135	6.63E - 24	0.38806074	0.494429
Tracker contribution	0.216826	0.076519	2.833624	0.00629	0.06371174	0.369939
Mirror contribution	1.078696	0.164241	6.56777	1.45E - 08	0.75005068	1.407341

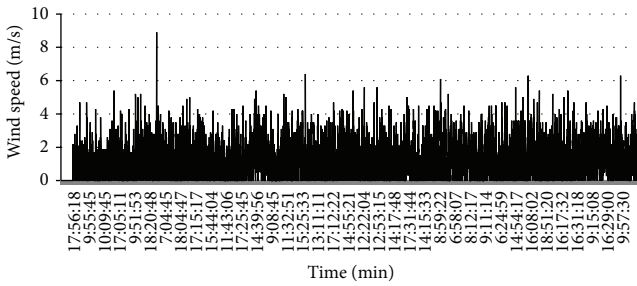


FIGURE 5: Wind profile throughout the monitoring period.

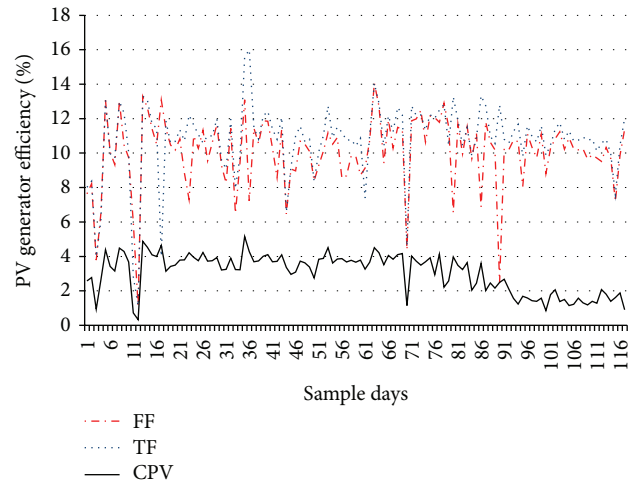


FIGURE 6: PV generator efficiency based on sampled field data.

the dual-axis tracking mechanism generates approximately 88 Watts/day or 9.4% of the TF cumulative power (with the FF generator as reference). The total generation throughout the sampling period coming from tracking mechanism reaches 5.49 kW out of the recorded 58.5 kW power output. The tracker generation seems unstable and sometimes experiencing rapid fluctuation mainly due to the sun angle of incident (AOI) and cloud shading factor. The mirror concentrating element generates approximately 8.93 kW out of 38.2 kW total power generation from CPV generator (with TF generator as reference). Based on daily average, the value can be converted as 144 Watts/day or 23.4% of the CPV cumulative power.

The increase of 14% in power generation shows significant feasibility of implying mirror mirror concentrator for PV generators with temperature increase within the allowable temperature range (-40°C to $+85^{\circ}\text{C}$) for the CEEG PV module. The crux finding of this work is statistically supported by means of MLR and ANOVA test. The power generation from mirror reflector is more stable and consistent compared to the tracking mechanism as shown in the line fit plot figures. General

observation suggests that the high generation from mirror reflector is due to the increase of incident light reflection on the PV module surface which would also increase the PV surface temperature.

Based on the statistical output, the correlation and coefficients involved are described in (7) with quite a low value standard error (SE) of 0.062% and sum of squared error (SSE) of 0.42%. The significance of correlations (R^2) between each factor is rather small with 0.45 values but this can be considered enough for statistical correlation based on the good F -test outcomes. Consider

$$P_{dc} = 0.44 + 0.22 * P_m + 1.07 * P_t \quad R^2 = 0.45. \quad (7)$$

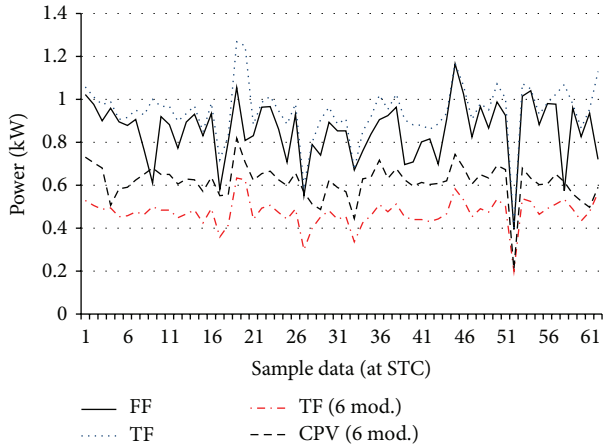


FIGURE 7: Power generation from each individual PV generator at STC conditions.

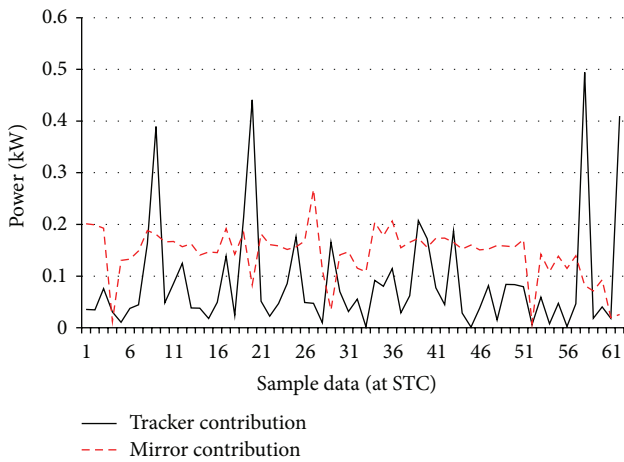


FIGURE 8: Power generation from mirror concentrator and tracking mechanism at site.

This study focuses on the comparison of power generation via adapting mirror concentrator and tracking mechanism on PV arrays with statistical approach using MLR and ANOVA as means of early findings based on the tropical pattern of Malaysia climate.

4. Conclusion

The drawbacks of presently practised method of adapting mirror concentrator and tracking mechanism for solar PV generator are analyzed for their genuine daily power contributions specifically in the tropical-ground conditions of Malaysia. PV generator systems rated at 1 kW with multiple configurations are taken as relative comparison for the sampling period of 10 consecutive months. Analysis shows that the mirror contribution is relatively high compared to the tracking mechanism with 14% daily increment and has a significant impact on the surface temperature of PV modules. The daily power increase by adapting both enhancement

techniques carries strong wattage of adapting PV technology in the tropics.

Nomenclature

- STC: Standard testing condition
($G = 1000 \text{ W/m}^2$, $T_a = 25^\circ\text{C}$, $\text{AM} = 1.5$)
- IEC: International Electrotechnical Commission
- ASTM: American Society for Testing and Materials
- NOCT: Nominal operating cell temperature
($G = 800 \text{ W/m}^2$, $T_a = 20^\circ\text{C}$, $\text{AM} = 1.0$)
- T : Absolute temperature in Kelvin
($\theta + 273.15 \text{ K}$)
- T_a : Ambient temperature
- G_{mea} : Measured solar irradiance (based on Pyranometer output)
- P_{rated} : Rated power for PV modules/generator
- P_{mpp} : Output power at maximum power point
- I_{mpp} : Current value at maximum power point
- V_{mpp} : Voltage value at maximum power point
- v : Wind speed (m/s)
- η : Efficiency
- A_{PV} : Aperture surface area of PV module (m^2)
- s : Length of shadow
- h : Length of object
- FF: Fixed flat PV generator
- TF: Tracking flat PV generator
- CPV: Concentrating PV generator.

Conflict of Interests

The authors affirm that the paper has been prepared in accordance with Instructions to Authors, that it has not been previously published, and that they have neither conflict of interests nor financial interests in the energy industry or any other institutional bodies.

Acknowledgments

The authors thank Sichuan Zhonghan Solar Power Co. Ltd. for the generous support throughout this project period. Furthermore, the authors delegate their thanks to the Research Management Centre (RMC), Universiti Putra Malaysia, for the approval of research funding under the Project Matching Grant (Vote no. 9300400) and Ministry of Higher Education, Malaysia, for the approval of Exploratory Research Grant Scheme (ERGS Vote no. 5527132).

References

- [1] W. N. Chen, "Solar photovoltaic—plug into the sun—part 1," in *MGCC Quarterly*, pp. 10–12, Malaysia-German Chamber of Commerce and Industry, Kuala Lumpur, Malaysia, 2010.
- [2] Anon, "Sustainable Energy Development Authority Malaysia FiT Dashboard," April 2013, <http://seda.gov.my/>.

- [3] A. International, *ASTM E948-09 Standard Test Method for Electrical Performance of Photovoltaic Cells Using Reference Cells under Simulated Sunlight*, ASTM International, West Conshohocken, Pa, USA, 2009.
- [4] H. Abdul Rahman, *Energy analysis based on simulation model for building integrated photovoltaic system for Malaysia [Ph.D. thesis]*, Faculty of Electrical Engineering, Universiti Teknologi Malaysia, Johor Bahru, Malaysia, 2012.
- [5] J. P. David, F. Floret, J. Guerin, J. C. Paiva, and L. Aiache, "Autonomous photovoltaic converter with linear focusing concentrator," *Solar Cells*, vol. 4, no. 1, pp. 61–70, 1981.
- [6] M. Effendy Ya'Acob, H. Hizam, M. T. Htay, M. A. M. Radzi, T. Khatib, and M. Bakri A, "Calculating electrical and thermal characteristics of multiple PV array configurations installed in the tropics," *Energy Conversion and Management*, vol. 75, pp. 418–424, 2013.
- [7] C. S. Solanki, C. S. Sangani, D. Gunashekar, and G. Antony, "Enhanced heat dissipation of V-trough PV modules for better performance," *Solar Energy Materials and Solar Cells*, vol. 92, no. 12, pp. 1634–1638, 2008.
- [8] R. Tang and X. Liu, "Optical performance and design optimization of V-trough concentrators for photovoltaic applications," *Solar Energy*, vol. 85, no. 9, pp. 2154–2166, 2011.
- [9] S. Riffat and A. Mayere, "Performance evaluation of v-trough solar concentrator for water desalination applications," *Applied Thermal Engineering*, vol. 50, no. 1, pp. 234–244, 2013.
- [10] S. Maiti, S. Banerjee, K. Vyas, P. Patel, and P. K. Ghosh, "Self regulation of photovoltaic module temperature in V-trough using a metal-wax composite phase change matrix," *Solar Energy*, vol. 85, no. 9, pp. 1805–1816, 2011.
- [11] K. K. Chong, K. G. Chay, and K. H. Chin, "Study of a solar water heater using stationary V-trough collector," *Renewable Energy*, vol. 39, no. 1, pp. 207–215, 2012.
- [12] S. R. Wenham, M. A. Green, M. E. Watt, and R. Corkish, "The characteristics of sunlight," in *Applied Photovoltaic*, pp. 3–25, Earthscan Publication, London, UK, 2nd edition, 2007.
- [13] K. E. Park, G. H. Kang, H. I. Kim, G. J. Yu, and J. T. Kim, "Analysis of thermal and electrical performance of semi-transparent photovoltaic (PV) module," *Energy*, vol. 35, no. 6, pp. 2681–2687, 2010.
- [14] J. P. Kim, H. Lim, J. H. Song, Y. J. Chang, and C. H. Jeon, "Numerical analysis on the thermal characteristics of photovoltaic module with ambient temperature variation," *Solar Energy Materials and Solar Cells*, vol. 95, no. 1, pp. 404–407, 2011.
- [15] R. C. Sprinthal and S. T. Fisk, *Basic Statistical Analysis*, Prentice Hall, Englewood Cliffs, NJ, USA, 1990.
- [16] D. C. Montgomery, G. C. Runger, and N. F. Hubele, *Engineering Statistics*, John Wiley & Sons, New York, NY, USA, 2009.
- [17] I. Mbamali, "An assessment of solar radiation patterns for sustainable implementation of solar home systems in nigeria," *American International Journal of Contemporary Research*, vol. 2, no. 6, 2012.
- [18] J. Leloux, L. Narvarte, and D. Trebosc, "Review of the performance of residential PV systems in France," *Renewable and Sustainable Energy Reviews*, vol. 16, no. 2, pp. 1369–1376, 2012.
- [19] D. Paul, D. Mukherjee, and S. R. B. Chaudhuri, "Assessing solar PV behavior under varying environmental conditions—a statistical approach," in *Proceedings of the 4th International Conference on Electrical and Computer Engineering (ICECE '06)*, pp. 217–220, December 2006.
- [20] G. Y. Obeng, H.-D. Evers, F. O. Akuffo, I. Braimah, and A. Brew-Hammond, "Solar photovoltaic electrification and rural energy-poverty in Ghana," *Energy for Sustainable Development*, vol. 12, no. 1, pp. 43–54, 2008.
- [21] A. H. Haris, "Grid-connected and building integrated photovoltaic: application status & prospect for Malaysia," *Master Builders Journal*, vol. 3, pp. 91–95, 2006.
- [22] A. Haris, *MBIPV Project: Catalyzing Local PV Market*, Finance & Investment Forum on PV Technology, Kuala Lumpur, Malaysia, 2008.

Research Article

Optimum Availability of Standalone Photovoltaic Power Systems for Remote Housing Electrification

Tamer Khatib and Wilfried Elmenreich

Institute of Networked & Embedded Systems/Lakeside Labs, University of Klagenfurt, P.O. Box B10a.2, 9020 Klagenfurt, Austria

Correspondence should be addressed to Tamer Khatib; tamer_khat@hotmail.com

Received 5 January 2014; Revised 15 April 2014; Accepted 29 April 2014; Published 8 May 2014

Academic Editor: Hongxing Yang

Copyright © 2014 T. Khatib and W. Elmenreich. This is an open access article distributed under the Creative Commons Attribution License, which permits unrestricted use, distribution, and reproduction in any medium, provided the original work is properly cited.

The availability of PV systems is discussed to determine the optimum availability at which standalone PV systems must be designed. Optimization methods and PV systems software, such as HOMER and PV.MY, were used for this purpose. Six PV systems with six availability levels were analyzed, in terms of wasted energy, cost of energy, battery usage, and power shortages, using real meteorological data. Results show that PV systems with 99% availability are recommended, because of their high reliability and favorably wasted energy.

1. Introduction

Considering that PV systems are clean, environment-friendly, and secure energy sources, PV system installation has played an important role worldwide. However, the drawback of PV systems is their high capital cost, compared to conventional energy sources. Currently, many studies were conducted that focus on the optimization of standalone PV systems, so that the number of PV modules, capacity of storage battery, and capacity of inverter were optimally selected. Standalone PV systems are widely used in remote areas without access to electricity grid. These systems had proven their feasibility, compared with conventional standalone power systems (e.g., diesel generators), especially for remote applications, because of the difficulty in accessing the remote areas and the cost of transportation. However, a PV system must be designed to meet the desired load demand at a defined level of availability [1].

Many sizing works for PV system can be found in the literature. Based on [1], three major PV-system-sizing procedures are available, namely, intuitive, numerical (simulation based), and analytical methods, in addition to some individual methods. However, most of these methods depend on system availability. For example, in [2], a well-completed optimization of PV systems in Algeria was implemented by dividing the regions into four zones using sky clearness

index. The optimization of PV systems was based on different levels of system availability and a simulation program which calculates the possible sizes of a PV system at a specific system availability and load demand. Thereafter, the optimum PV system configuration is selected based on system capital cost. In [3], an elegant optimization method for PV system was presented. A PV system mathematical model was developed to optimize its size based on well-defined solar energy data and load demand. The developed model contains models for PV array, storage battery, and charge regulator. However, the optimization considers the combined minimum cost with maximum system availability taking into account the uncertainty in solar energy and the variation in the demanded energy by the load.

The optimization of a PV system was done for three sites in the UK using the sizing curves derivation in [4]. To avoid any load interruption, the PV array size was designed based on the worst monthly average solar energy. As for finding the minimum storage requirement, the same method used in plotting the sizing curves of the PV array was used for the battery. The minimum storage requirement was calculated each year of the used historical data. However, PV array size was calculated based on the worst month method, which may cause oversizing in the PV generator, especially in months having average solar energy higher than the worst month. The considered system availability in this study was 100%.

In [5], an optimization of a PV system was presented based on long term solar radiation series for UK. In this study, the average of the obtained solar radiation series was calculated and divided in two climatic cycles. One of these climatic cycles contains days with average solar radiation equal to or higher than the calculated overall solar radiation average, whereas other climatic cycles contain days that have average solar radiation lower than the calculated overall average solar radiation. Thereafter, the necessary size of the PV generator and the storage battery was calculated based on all the climatic cycles to construct the general-sizing curve at specific system availability. Finally, the resultant sizing curve was fitted to an exponential function to derive a mathematical formula that can be used to calculate PV system size directly. In [6], a comprehensive sizing of standalone PV systems for Malaysia was presented. A simulation was performed, depending on the energy flow in a PV system [7]. By this simulation, the possible sizes of a PV/battery system at different system availabilities for five main locations were obtained and plotted to establish a mathematical correlation between PV array capacity and system availability and between PV array capacity and storage battery capacity. After calculating the coefficients for each region, the averages of these coefficients were calculated to establish a model for all Malaysia. From the examples of PV system optimization that were given, it can be concluded that the PV systems were designed at different levels of availability of 90% to 100%.

The main objective of the present paper is to study the effect of system availability on system size and cost to recommend an optimum availability level at which PV systems must be designed.

2. Standalone PV System Availability

Each standalone PV system, like any other power systems, has a specific level of availability. This reliability level affects system performance, production, feasibility, and investment [8–14]. According to the Sandia National Laboratory in [15], the availability of a standalone PV system can be defined as the percentage of time at which a power system is capable of meeting the load requirements. The number of hours that the system is available, divided by 8760 h, gives the annual system availability. A system with 95% availability is expected to meet the load requirement of 8322 h during an average year for the entire useful life of the system. An annual availability of 99% means that the system can operate the load for 8672 h of the 8760 h [15]. In [16], the PV system availability is defined as the percentage of time at which a PV system is capable of meeting the load requirements.

The availability of a PV system can be described by statistical values. In [17], the availability of PV systems is defined as a statistical value, called loss of load probability (LLP), which is given by

$$LLP = \frac{\sum_{i=1}^{8760} \text{EnergyDeficit}_i}{\sum_{j=1}^{8760} \text{LoadDemand}_j} \quad (1)$$

The numerator in (1) is the sum of the energy demanded which the PV system cannot cover in a year's time. On

the other hand, the denominator is the sum of the energy demanded in a year's time. After calculating the LLP, the availability (A) of the PV system can be expressed as

$$A = (1 - LLP) * 100\% \quad (2)$$

Some researchers used another statistical value to describe the availability of a PV system, namely, loss of power supply probability (LOSP). In [18, 19], LOSP is described as a probability function,

$$f_c = \text{SOC}(t) \leq \text{SOC}_{\min}; \quad \text{for } t \leq T, \quad (3)$$

where f_c is the probability that the state of charge at any accumulative time t within the time period T will be equal to or less than the minimum permissible level (SOC_{\min}).

According to this formula, the availability of a PV system can be calculated as

$$A = (1 - f_c) * 100\% \quad (4)$$

However, increasing PV system availability increases the size of the system and, consequently, the capital cost of the system. In [20], the effect of the availability of PV system on PV array cost is deeply studied. According to [20], the system size and cost increased rapidly while trying to obtain the last few percentages of availability. The relation between PV array cost (size) and system availability was almost linear until 80%, at which it became logarithmic thereafter. In addition, the Sandia National Laboratory, in [15], illustrated the relation between the peak sunshine hours of the system and the needed storage capacity for the system at two levels of system availability. According to [15], the storage needed from a PV system that has 99% availability is higher than that from a PV system with 95% availability. Moreover, the difference between the needed storage capacities becomes much higher as the number of peak sunshine hours becomes lower than 4.

Based on that, increasing availability of the PV system increased the size of the PV array and the needed storage capacity. On these bases, knowing the optimum availability at which the PV system must be designed is important. In [15], two levels of availability are recommended: 95% and 99%. However, these authors stated that the 95% availability is more recommended. Meanwhile, in [20], it is suggested that the nature of the load of the PV system determines its availability. For example, telecommunication repeater stations will be considered as a critical load. Thus, 99% availability is demanded, whereas other noncritical loads can be designed based on 95% availability. In [2], the availability of PV systems in the range of 90% to 100% is recommended. Meanwhile, in [3], the availability of PV systems in the range of 92% to 99.9% is recommended. In [4], it is recommended that PV systems must be designed at 100% availability. In addition, in [5], it is suggested that PV system availability must be higher than 95% and that an LLP value of zero cannot be assigned. In [6], the PV system availability in the range of 95% to 99% is recommended, whereas a 98% availability of PV system is recommended in [7]. Finally, the HOMER software, which is a widely used PV system optimization tool, designs standalone PV systems at 100% availability.

TABLE 1: Designed PV systems specification.

A	C_A (kWp)	C_B (Ah/12 V)	E_{PV} (kWh)	LOLH	E_D (kWh)	CoE (\$/kWh)	SOC _{80%}
100%	4.3	1316	6882	0	4645	0.6	7881
99%	2.5	324	4000	199	1789	0.27	2748
98%	2.3	270	3681	386	1491	0.25	2595
97%	2.2	260	3521	661	1368	0.24	2502
96%	2.1	250	3361	736	1217	0.23	2416
95%	2	240	3201	972	1090	0.22	2341

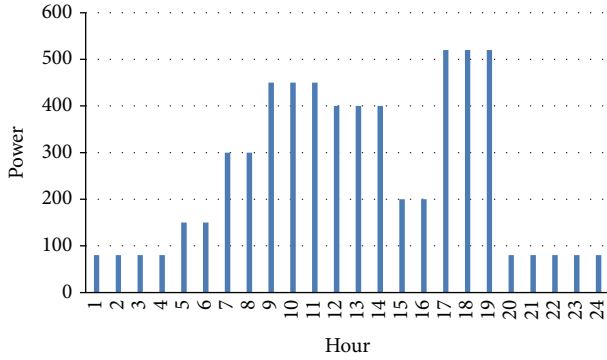


FIGURE 1: Simulated load demand.

On these bases, the availability of PV systems is mostly recommended in the range of 95% to 100%. However, an exact availability level is not yet determined even by the present study. A more specific availability level must be defined among the availability levels that are in the range of 95% to 100%. In the next section, a brief analysis of a PV system designed at six availability levels is performed to try to find the optimum availability at which PV systems must be designed.

3. Searching for the Optimum PV System Availability

In this section, a brief analysis of a PV system designed at six availability levels (95%, 96%, 97%, 98%, 99%, and 100%) is performed to find the best system availability at which PV systems must be designed. Figure 1 shows the used load demand. The total load demand was 6.135 kWh/day with a maximum power of 0.52 kW. The average load power was 0.255 kW and the load factor was 49%.

In this section, the method proposed by [6] was used to design the PV system at different availability levels. In addition, the tool presented in [21] was used to simulate these systems using hourly solar radiation and ambient temperature records for Kuala Lumpur City, Malaysia. The proposed method and the HOMER software were used to design the PV system at 100% availability. Then, the methods proposed in [6, 21] were used to design and analyze the designed PV systems

According to HOMER, a PV system with a 4 kWp PV array and 1500 Ah/12 V storage battery is needed to meet

the desired load demand at zero loss of load probability (100% availability). On the other hand, for the method in [6], a PV system with 4.3 kWp and 1316 Ah/12 V storage battery is needed to meet the desired load demand. The difference between the result given by HOMER and that by the proposed method is attributed to two reasons: the nature of the meteorological variable used and the specification assumption of the device. As for the former, the method in [6] used real hourly meteorological data, whereas HOMER used monthly averages and converted it into hourly data using embedded models. As for the latter, many differences exist in the defined specifications for the modeled devices, such as conversion efficiency of the PV module, charging efficiency of the battery, and other factors.

Table 1 shows the specifications and statistics of six PV systems designed at six availability levels. The table shows the availability level (A), PV array capacity (C_A), storage battery capacity (C_B), energy generated by the PV array in a year's time (E_{PV}), number of loss load hours (LOLH), damped energy (E_D), cost of energy generated by the PV system (CoE), and number of hours in the year that the SOC of the battery was higher than 80% (SOC_{80%}). As for LOLH, the simulation counted each hour within which an energy deficit occurs, despite the fact that some of the hourly demands can be partially covered.

From the table, the system with 100% availability consisted of a 4.3 kWp PV array and a 1316 Ah/12 V storage unit. The system generated 6882 kWh per year, whereas 4645 kWh was damped, which means that 67.5% of the energy generated was wasted. The cost of energy generated by such a system is 0.6 USD/kWh. In addition, the battery SOC was higher than 80% in about 89.9% of a year's time, which indicates that the battery was not the kind used during a year's time.

As for the system with 99% availability, a 2.5 kWp PV array and a 324 Ah/12 V storage battery are the recommended energy source sizes. In a year's time, 4000 kWh was generated, whereas 45% of this energy was damped. The cost of the energy generated by the system is 0.27 USD/kWh. The battery SOC in 31% of a year's time was higher than 80%, which means that the battery was well used compared with the previous case. The number of hours at which the system cannot meet the load demand was 199, which translates to 2.2% of a year's time.

As for the remaining system options, the performances of these systems were close to each other, whereas the needed PV array and battery capacity were in the range of 2.3 kWp to 2 kWp and 270 Ah/12 V to 240 Ah/12 V. The generated

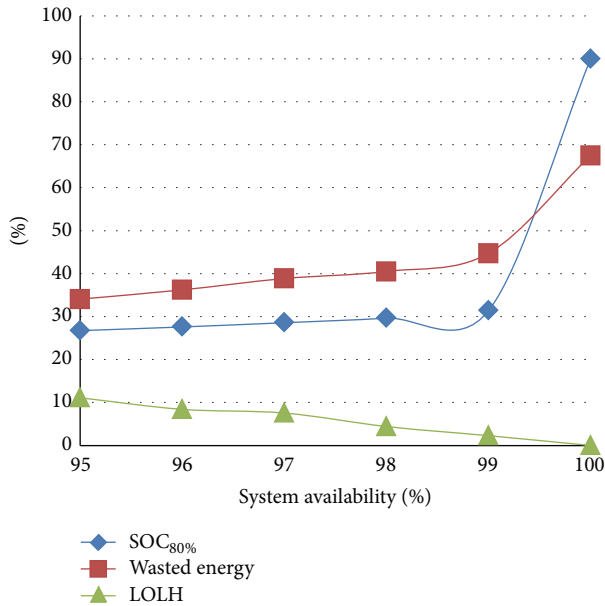


FIGURE 2: PV systems comparison.

energy was in the range of 3201 kWh/year to 3681 kWh/year, whereas the percentage damped energy was in the range of 34% to 40%. On the other hand, the cost of the energy generated by these systems was in the range of 0.22 USD/kWh to 0.25 USD/kWh, whereas the percentage of the days within which the battery SOC was higher than 80% was in the range of 28% to 30%. The LOLH values of these systems were in the range of 4.4% to 11.1%, which are high values, especially, compared with the previous systems.

Figure 2 shows a comparison among these systems in terms of wasted energy (damped energy-to-generated energy), battery usage (SOC_{80%} to the number of hours in a year's time), and LOLH percentage (LOLH to the number of hours in a year's time). The figure shows that systems with availability in the range of 99% to 95% had almost similar battery usages. Hence, systems with 98% to 99% availability are recommended in this regard. As for LOLH, systems with availability values in the range of 98 to 100 are recommended. Finally, systems with availability values in the range of 97% to 98% are recommended, in terms of wasted energy. On the basis of these results, systems with availability values of 98% and 99% are most recommended.

Referring to the CoE in Table 1, it is noted that, by using the system with 99% availability, the supplier lost 298 kWh/per year in damped energy, compared with the system with 98% availability. Moreover, the generation of energy costs the supplier 0.02 USD per kWh more, compared with the system with 98% availability. On the other hand, the LOLH value increased by 187 h in the system with 98% availability, compared with the system with 99% availability. Thus, despite the fact that the system with 98% availability was cheaper in terms of unit cost and damped energy, it is less reliable compared with the system with 99% availability. Upon this basis, PV systems with 99% availability are recommended due to their high reliability and favorable running costs.

4. Conclusion

Optimum PV system availability was studied and presented in this paper. Six PV systems with different reliability levels were studied using solar energy and ambient temperature records for Kuala Lumpur City, Malaysia. The performance analysis was in terms of wasted energy, cost of energy, battery usage, and power shortages using real meteorological data. The results show that PV systems with 99% availability are recommended due to their high reliability and favorably wasted energy.

Conflict of Interests

The authors declare that there is no conflict of interests regarding the publication of this paper.

Acknowledgments

This work is supported by Lakeside Labs, Klagenfurt, Austria, and funded by the European Regional Development Fund (ERDF) and the Carinthian Economic Promotion Fund (KWF) under Grant KWF 20214|23743|35470 (Project MON-ERGY) and 20214|22935|34445 (Project Smart Microgrid). The authors would like to thank Lizzie Dawes for proofreading the paper.

References

- [1] T. Khatib, A. Mohamed, and K. A. Sopian, "A review of photovoltaic systems size optimization techniques," *Renewable and Sustainable Reviews*, vol. 22, pp. 454–465, 2012.
- [2] A. H. Arab, B. A. Driss, R. Amimeur, and E. Lorenzo, "Photovoltaic systems sizing for Algeria," *Solar Energy*, vol. 54, no. 2, pp. 99–104, 1995.
- [3] G. B. Shrestha and L. Goel, "A study on optimal sizing of stand-alone photovoltaic stations," *IEEE Transactions on Energy Conversion*, vol. 13, no. 4, pp. 373–378, 1998.
- [4] A. Fragaki and T. Markvart, "Stand-alone PV system design: results using a new sizing approach," *Renewable Energy*, vol. 33, no. 1, pp. 162–167, 2008.
- [5] T. Markvart, A. Fragaki, and J. N. Ross, "PV system sizing using observed time series of solar radiation," *Solar Energy*, vol. 80, no. 1, pp. 46–50, 2006.
- [6] T. Khatib, A. Mohamed, K. Sopian, and M. Mahmoud, "A new approach for optimal sizing of standalone photovoltaic systems," *International Journal of Photoenergy*, vol. 2012, Article ID 391213, 7 pages, 2012.
- [7] P. Arun, R. Banerjee, and S. Bandyopadhyay, "Optimum sizing of photovoltaic battery systems incorporating uncertainty through design space approach," *Solar Energy*, vol. 83, no. 7, pp. 1013–1025, 2009.
- [8] P. Zhang, W. Li, S. Li, Y. Wang, and W. Xiao, "Reliability assessment of photovoltaic power systems: review of current status and future perspectives," *Applied Energy*, vol. 104, pp. 822–833, 2013.
- [9] R. Fucci, L. Lancellotti, and C. Privato, "A procedure for assessing the reliability of short circuited concentration photovoltaic systems in outdoor degradation conditions," *Microelectronics Reliability*, vol. 54, no. 1, pp. 182–187, 2014.

- [10] G. Zini, C. Mangeant, and J. Merten, "Reliability of large-scale grid-connected photovoltaic systems," *Renewable Energy*, vol. 36, no. 9, pp. 2334–2340, 2011.
- [11] R. M. Moharil and P. S. Kulkarni, "Reliability analysis of solar photovoltaic system using hourly mean solar radiation data," *Solar Energy*, vol. 84, no. 4, pp. 691–702, 2010.
- [12] J. K. Kaldellis, P. Koronakis, and K. Kavadias, "Energy balance analysis of a stand-alone photovoltaic system, including variable system reliability impact," *Renewable Energy*, vol. 29, no. 7, pp. 1161–1180, 2004.
- [13] V. Sharma and S. S. Chandel, "Performance and degradation analysis for long term reliability of solar photovoltaic systems: a review," *Renewable and Sustainable Energy Reviews*, vol. 27, pp. 753–767, 2013.
- [14] M. Lee, D. Soto, and V. Modi, "Cost versus reliability sizing strategy for isolated photovoltaic micro-grids in the developing world," *Renewable Energy*, vol. 69, pp. 16–24, 2014.
- [15] Sandia International Laboratory, *Standalone Photovoltaic Power Systems*, Sandia International Laboratory, Albuquerque, NM, USA, 1995.
- [16] T. Ball and V. Risser, "Stand-alone terrestrial photovoltaic power systems," in *Proceedings of the 20th IEEE Photovoltaic Specialists Conference*, Tutorial Notes, Las Vegas, Nev, USA, 1988.
- [17] P. Tsalides and A. Thanailakis, "Loss-of-load probability and related parameters in optimum computer-aided design of stand-alone photovoltaic systems," *Solar Cells*, vol. 18, no. 2, pp. 115–127, 1986.
- [18] E. Ofry and A. Braunstein, "The loss of power supply probability as a technique for designing standalone solar electrical (Photovoltaic) systems," *IEEE Transactions on Power Apparatus and Systems*, vol. 102, no. 5, pp. 1171–1175, 1983.
- [19] I. Abouzahr and R. Ramakumar, "Loss of power supply probability of stand-alone photovoltaic systems: a closed form solution approach," *IEEE Transactions on Energy Conversion*, vol. 6, no. 1, pp. 1–11, 1991.
- [20] S. R. Wenham, M. A. Green, and M. E. Watt, *Applied Photovoltaics*, Earthscan, London, UK, 2007.
- [21] T. Khatib, A. Mohamed, and K. Sopian, "A software tool for optimal sizing of PV systems in Malaysia," *Modelling and Simulation in Engineering*, vol. 2012, Article ID 969248, 16 pages, 2012.

Research Article

Superior Antireflection Coating for a Silicon Cell with a Micronanohybrid Structure

Hsi-Chien Liu¹ and Gou-Jen Wang^{1,2,3}

¹ Department of Mechanical Engineering, National Chung Hsing University, Taichung 40227, Taiwan

² Graduate Institute of Biomedical Engineering, National Chung Hsing University, Taichung 40227, Taiwan

³ Program in Tissue Engineering and Regenerative Medicine, National Chung Hsing University, 250 Kuo-Kuang Road, Taichung 40227, Taiwan

Correspondence should be addressed to Gou-Jen Wang; gjwang@dragon.nchu.edu.tw

Received 13 January 2014; Accepted 20 March 2014; Published 10 April 2014

Academic Editor: Tao Xu

Copyright © 2014 H.-C. Liu and G.-J. Wang. This is an open access article distributed under the Creative Commons Attribution License, which permits unrestricted use, distribution, and reproduction in any medium, provided the original work is properly cited.

The object of this paper is to develop a high antireflection silicon solar cell. A novel two-stage metal-assisted etching (MAE) method is proposed for the fabrication of an antireflective layer of a micronanohybrid structure array. The processing time for the etching on an N-type high-resistance (NH) silicon wafer can be controlled to around 5 min. The resulting micronanohybrid structure array can achieve an average reflectivity of 1.21% for a light spectrum of 200–1000 nm. A P-N junction on the fabricated micronanohybrid structure array is formed using a low-cost liquid diffusion source. A high antireflection silicon solar cell with an average efficiency of 13.1% can be achieved. Compared with a conventional pyramid structure solar cell, the shorted circuit current of the proposed solar cell is increased by 73%. The major advantage of the two-stage MAE process is that a high antireflective silicon substrate can be fabricated cost-effectively in a relatively short time. The proposed method is feasible for the mass production of low-cost solar cells.

1. Introduction

Solar cells are powered by the photoelectric conversion of solar light. Thus, it is desirable that the light reflectance of the cell surface be as low as possible to enable complete absorption of the solar energy. Current antireflection approaches can be categorized into two categories. The first approach is to coat an antireflection layer on the cell surface to reduce light reflection. Plasma enhanced chemical vapor deposition (PECVD) of a thin layer of hydrogenated silicon nitride (SiN_x:H) on the cell surface is a commonly adopted method [1]. Solar light within a specific wave range can thus be effectively absorbed. Wider spectrum absorption requires multiple antireflection coatings. Hence, the antireflection coating approach is relatively costly, complicated, and difficult to mass produce. The other approach is to texturize the cell surface so that different wavelengths of light can be efficiently absorbed through multiple reflections. This approach enables a wider spectrum of solar light to reach the

P-N junction of the solar cell, thus enhancing its short circuit current and photoelectric conversion efficiency.

In recent years, physical and chemical etching methods have been adopted for roughening the surface of the wafer substrate. Physical etching can be accomplished by reactive ion etching and creates a rough structure that possesses less than 20% reflectivity in the visible light spectrum [2]. The chemical approach uses potassium hydroxide (KOH) for alkaline etching or hydrogen fluoride acid (HF) for acid etching, and it can result in a rough surface with a reflectivity of around 17% under irradiation of visible light [3]. Wet chemical etching, using KOH to fabricate the pyramid structure, is a commonly used approach in the industry. Compared to physical etching, KOH-based wet etching is more cost effective, faster, and more feasible for mass production of large-area cells. However, the pyramid structure can reach a minimum reflectivity of 12% and can only absorb the solar energy of visible light. Moreover, a thin layer of silicon nitride (SiN) over the pyramid structure is required to assure the

TABLE 1: Materials, specifications, and vendors.

Material	Specification	Vendor
N-type silicon (100) wafers (monocrystalline)	1~3 Ω -cm	Wafer Works, Taiwan
AgNO ₃	99.8%	Union Chemical Works, Taiwan
HF	55%	Choneye, Taiwan
HNO ₃	69%	Union Chemical Works, Taiwan
Acetone	99.5%	Sigma-Aldrich
Polyethylene glycol	MW: 1000	Echo Chemical, Taiwan
Borosilicafilm	$C_o = 1 \times 10^{20}$	Emulsitone, USA
Phosphorosilicafilm	$C_o = 5 \times 10^{20}$	Emulsitone, USA

antireflective property. Therefore, silicon nanostructures have been adopted to enhance the antireflectivity [4–9]. Besides chemical wet etching, electrochemical etching, plasma etching, oxidation, and nanogold-catalyzed chemical etching can also be used to fabricate a rough structure with 5% less reflectivity.

Recent investigations observed that semiconductor silicon exhibits an electrochemical reaction in an HF solution. Accordingly, electroless metal deposition and electroless etching have been adopted for fabricating silicon nanowires for micronanoelectrical devices [10–18]. Further studies indicated that silicon nanowire structures possess the antireflective property in the ultraviolet (UV), visible light, and infrared (IR) spectra. Thus, silicon nanowiring is fast substituting chemical vapor deposition (CVD) as a way to reduce the reflectivity in the SiN layer [1]. Garnett and Yang [19] used silver nitrate (AgNO₃) as the etchant for electroless etching of silicon nanowire arrays, followed by the fabrication of the P-N junction through PECVD using boron trichloride (BCl₃) gas. The fabricated solar cell exhibited a short circuit current density (J_{sc}) of 4.28 mA/cm² and an open circuit voltage (V_{oc}) of 0.29 V. A photoelectric conversion efficiency (η) of 0.46% was achieved. Tang et al. [20] made use of the CVD approach to fabricate the P-N junction and then grew silicon nanowires using gold nanoparticles as the catalyst. Uncharged polymethyl methacrylate (PMMA) was employed to reduce the leakage current effect. A solar cell having a J_{sc} of 7.6 mA/cm² and an η of 2.73% was produced. In 2009, the National Renewable Energy Laboratory (NREL), USA [21], used chloroauric acid (HAuCl₄) as the etchant for electroless etching of nanoporous Si. The thermal oxidation process was then applied to deposit a silicon dioxide (SiO₂) passivation layer on the P-N junction surface to reduce the leakage current and indirectly enhance the short circuit current. The resulting solar cell had a high J_{sc} of 34.067 mA/cm², a V_{oc} of 0.6123 V, and an η of 16.8%. In 2011, the NREL etched nanostructures on the pyramid microstructure using HAuCl₄ to obtain an average reflectivity of 2.7% in the light spectrum of 350–1000 nm. The J_{sc} , V_{oc} , and η of the fabricated solar cell were 35.6 mA/cm², 0.615 V, and 17.1%, respectively [22]. Thereafter, tetramethylammonium hydroxide (TMAH)

was employed to smoothen the surface structure of the nanoporous silicon, so that the recombination of electron-hole pairs could be reduced. A solar cell having a J_{sc} of 36.45 mA/cm², a V_{oc} of 0.628 V, and an η of 18.2% was produced [23].

The above-mentioned studies indicate the development trends of solar cells, namely, the use of inexpensive processes to produce high photoelectric conversion efficiency devices. In this study, we propose a cost-effective solar cell production method comprising fabrications of a high antireflection micronanohybrid silicon substrate and the P-N junction using a liquid diffuser. The high antireflection micronanohybrid silicon substrate is fabricated by a two-stage metal-assisted (MAE) etching method using an AgNO₃ and HF mixing solution as the etchant to grow nanowires on a KOH wet-etched microstructure pyramid array.

2. Materials and Methods

2.1. Materials. The materials used in this study are listed in Table 1.

2.2. Methods

2.2.1. Fabrication of a High Antireflection Micronanohybrid Structure Array. An AgNO₃ and HF mixing solution is adopted as the etchant for the MAE. The silver ions in the etchant acquire electrons from the silicon substrate and are reduced to silver atoms, which are then deposited on the surface of the silicon substrate. Simultaneously, the silicon atoms donate electrons and are oxidized to SiO₂. The SiO₂ is then etched by the HF solution with zero applied potential. Silicon nanowire arrays can be fabricated through consecutive reduction and oxidation (redox) reactions [24–26]. In this study, the MAE method is used for fabricating a high antireflection micronanohybrid structure array. In the first stage, short-time etching using highly concentrated AgNO₃ is executed to deposit a coniferous-like silver layer on the wafer surface of the KOH-etched micropylramid array. Then, relatively long-time etching using a lower concentration of AgNO₃ is implemented for producing a bolt upright and uniform silicon nanowire array on each micropylramid. The fabrication procedures are described as follows.

- (1) Wafer cleaning: clean the wafer sequentially and ultrasonically in acetone, ethanol (EtOH), and distilled water for 30 min. Immerse the washed silicon wafer in diluted HF acid for 2-3 min to remove the oxide layer from the wafer surface. Then, rinse the wafer with distilled water.
- (2) Micropylramid array fabrication: prepare the wet-etching etchant with a weight ratio of DI: KOH (40 wt%): IPA = 70:2:5. Use it to wet-etch the micropylramid array on the cleaned wafer substrate. Then, remove the oxide layer from the wafer surface by immersing the wet-etched wafer into dilute HF acid for 2-3 min.

- (3) Two-stage MAE: conduct the first stage of the MAE using AgNO_3 (0.34 M) and HF (4.6 M) mixing etchant under various processing times. Then, process the second stage of the MAE using AgNO_3 (0.03 M) and HF (5.6 M) mixing etchant under various processing times. Both stages are conducted at 40°C . The optimal processing times for stages 1 and 2 were arrived at by exploring 30 designed processing time combinations between the stages, as tabulated in Table 2.
- (4) Removal of silver conifers: during the MAE process, the reduced silver nanoparticles dispersedly distribute on the wafer surface. After MAE, the reduced silver nanoparticles are removed by immersing the wafer into a solution of nitric acid (HNO_3) for 5 min.
- (5) SiO_2 layer removal: remove the bottom SiO_2 layer using an HF and distilled water mixing solution (ratio = 1 : 3).

2.2.2. Property Characterization of the Synthesized Micronanohybrid Silicon Substrate. The morphology of the micronanohybrid silicon substrates was characterized using a field emission scanning electron microscope (FESEM) (JSM-6700F, JEOL). The reflectivity for the light spectrum of 200–1000 nm was measured by a variable-angle UV, visible (VIS), and near IR (UV/VIS/NIR) spectrophotometer (Hitachi U-4100).

2.2.3. Growth of the P-N Junction. Instead of the commonly used CVD process, the less expensive silica film was adopted as the diffuser for the growth of the P-N junction. The growth procedures are described below.

- (1) Silica film spin coating: spin coat a 0.5 μm thick silica film on the micronanohybrid silicon substrate. Then, volatilize the contained organic solvent at 100°C for 60 min.
- (2) Thermal diffusion: place the silica-film-coated silicon substrates in a high temperature furnace to process the thermal diffusion. The processing time should be set to 60 min, and several diffusion temperatures (950, 1000, 1050, 1100, and 1150°C) should be selected to obtain optimal diffusion. Then, remove the glass oxide layer on the wafer surface by immersing the wet-etched wafer into diluted HF acid for 2–3 min. Wash the remaining HF solution using distilled water.
- (3) Sheet resistance measurement: use a four-point probe for the sheet resistance measurement.

2.2.4. Cell Fabrication and Photoelectric Conversion Efficiency Measurement. E-gun sputtering using metal masks was adopted for the fabrication of the front fishbone positive titanium electrode and the back negative silver electrode. The thicknesses of the front and back electrodes were 50 and 200 nm, respectively. The electrode sputtered silicon substrate was placed in a nitrogen-filled high temperature furnace at 400°C for 30 min to grow the ohmic contact. The photoelectric conversion efficiency was measured.

TABLE 2: Processing time combinations between stage 1 and stage 2.

Stage	Processing times					
1	20 s	25 s	30 s	35 s	40 s	45 s
2	2 min	5 min	7 min	10 min	15 min	

3. Results and Discussion

3.1. Fabrication Results of the Micronanohybrid Structure Array. The highly concentrated AgNO_3 (0.34 M) used in the first MAE stage helped in quickly obtaining the required amounts of reduced silver atoms needed to uniformly cover the entire surface of the pyramid array. However, the height of a wet-etched pyramid is about 3–5 μm . A relatively higher concentration of AgNO_3 results in a rapid redox reaction between the silver ions and the silicon substrate. As a result, the pyramid could be completely etched away in a long etching process. Therefore, the etching duration for the first etching stage was set to range from 20 to 45 sec. The second etching stage was employed to uniformly etch the silicon substrate downward under the silver-atom-covered area. Hence, a relatively low AgNO_3 concentration (0.03 M) was selected, and a longer etching time (1–5 min) was designed.

Figure 1 illustrates the SEM images of the fabricated micronanohybrid structures subjected to a 30 sec first-stage etching and various second-stage etching processing times. The straight etched nanowires cover the entire surface of the pyramid array, including the pyramid structure and the recesses between the pyramids. The length of the etched nanowires increases with increased etching time. The top view, illustrated by the inset in each image, indicates the hybrid structure of the pyramids and the nanopores.

It has been reported [27] that the antireflectivity of a nanosilicon substrate is closely proportional to nanowire length. Therefore, the second-stage processing time was set at 5 min to further investigate the antireflectivity of the micronanohybrid structure. Figure 2 shows the morphologies of various micronanohybrid structures fabricated by combinations of a fixed second-stage etching time (5 min) and various first-stage etching times. For these micronanohybrid structures subjected to the first-stage processing time of 20 and 25 sec (Figures 2(a) and 2(b)), the nanowires are more intensive, but shorter, when compared with the other samples. The possible reason is that the relatively shorter first-stage etching time may be insufficient to reduce silver nanoparticles to a suitable size for effective downward etching during the second-stage process. When the first-stage processing time was extended to 30, 35, and 40 sec (Figures 2(c), 2(d), and 2(e)), the fabricated nanowires possessed good uniformity and had microscale lengths. However, further increases in the processing time (45 sec) resulted in a looser nanowire array with a bent shape (Figure 2(f)). An excessively long first-stage processing time might result in overdense coverage of silver nanoparticles on the pyramid array, thus resulting in inhomogeneous second-stage etching.

3.2. Antireflectivity Property of the Micronanohybrid Structure Array. As discussed in Section 3.1, nanowire arrays with

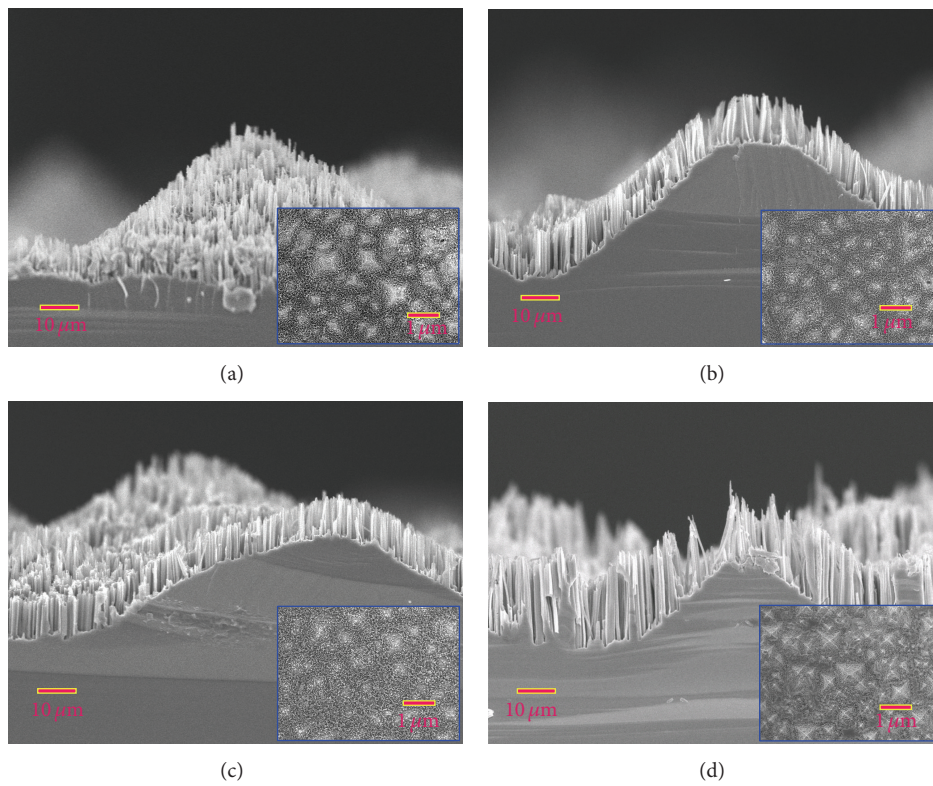


FIGURE 1: SEM images of micronanohybrid silicon substrates fabricated by combinations of a fixed first-stage processing time (30 sec) and various second-stage processing times: (a) 1 min, (b) 2 min, (c) 3 min, and (d) 4 min.

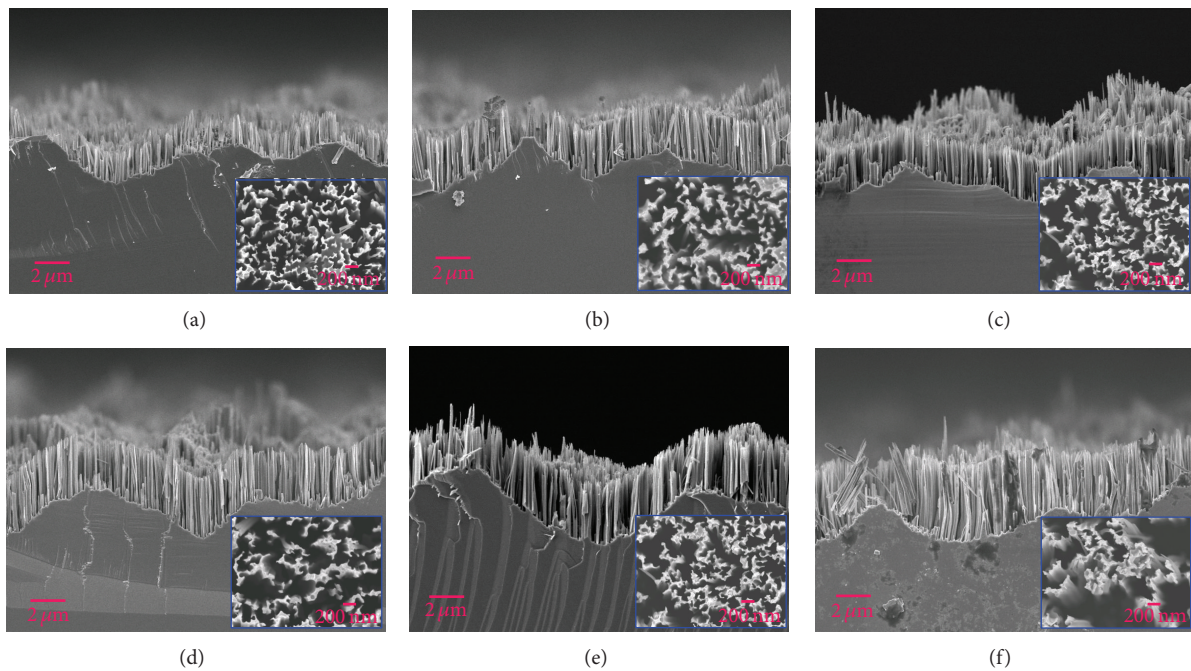


FIGURE 2: SEM images of micronanohybrid silicon substrates fabricated by combinations of a fixed second-stage processing time (5 min) and various first-stage processing times: (a) 20 sec, (b) 25 sec, (c) 30 sec, (d) 35 sec, (e) 40 sec, and (f) 45 sec.

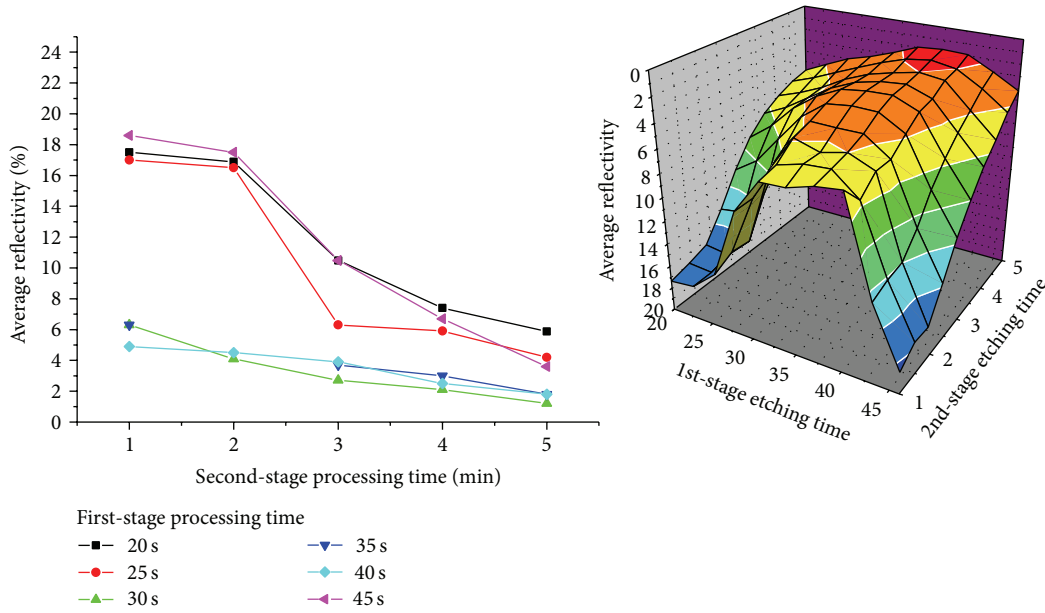


FIGURE 3: Relationship between the average reflectivity of a micronano hybrid structure fabricated by a certain two-stage MAE process and the corresponding etching time combination in the light spectrum of 200–1000 nm.

various heights could be fabricated by adjusting the processing time combinations of the first and second stages. The antireflectivity properties of the silicon substrates subjected to different processing time combinations were investigated. Figure 3 demonstrates the relationship between the average reflectivity of a silicon micronano hybrid structure fabricated by a certain two-stage MAE process and the corresponding etching time combination in the light spectrum of 200–1000 nm. For processes with a first-stage etching time of 20, 25, and 45 sec, the fabricated micronano hybrid structure arrays exhibited relatively higher reflectivity. For processes with a first-stage etching time of 30, 35, and 40 sec, the fabricated micronano hybrid structure arrays processed relatively lower reflectivity. Average reflectivity decreased with increasing second-stage processing times. When the second-stage processing time was 5 min, average reflectivity of less than 2% could be achieved. Up to a certain degree, the reflectivity measurement results agree with the morphologies of the fabricated hybrid structures shown in Figure 2, wherein processes with a first-stage etching time of 20, 25, and 45 sec could fabricate uniform and long hybrid microscale structures. The 3D graph shown in the inset represents average reflectivity as a function of processing time combination. The red area indicates the processing time combinations that resulted in average reflectivity of less than 2%, demonstrating that our two-stage fabrication method is capable of producing high antireflection micronano hybrid structures.

The above discussion reveals that the hybrid structure fabricated by the combinations of a first-stage processing time between 30 and 45 sec and a second-stage processing time of 5 min exhibits less than 2% reflectivity. Figure 4 further depicts the overall reflectivity for the light spectrum of 200–1000 nm for hybrid structures subjected to a 5 min second-stage processing time. It is evident that the reflectivity of

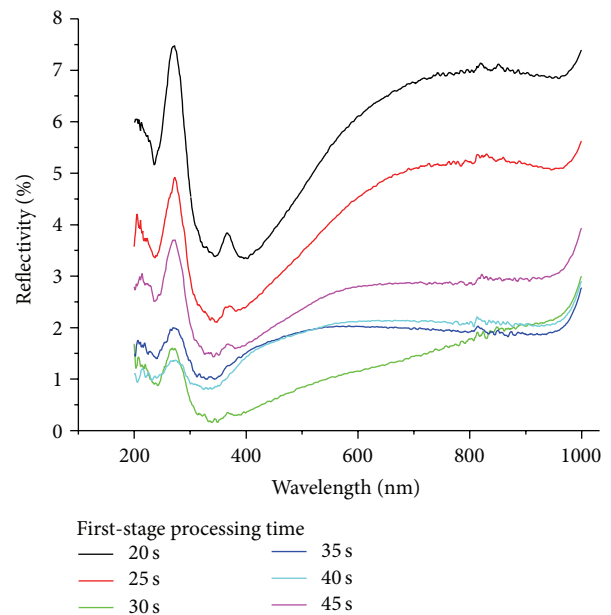


FIGURE 4: Reflectivity of the fabricated micronano hybrid structures subjected to the proposed two-stage MAE for the light spectrum of 200–1000 nm.

hybrid structures subjected to a first-stage processing time of 30 and 45 sec for the light spectrum of 200–1000 nm is less than 2%. The first-stage etching time of 30 sec could fabricate hybrid structures with relatively lower overall reflectivity. Table 3 tabulates the average reflectivity of the hybrid structures fabricated by combinations of a 30 sec first-stage processing time and various second-stage processing times. The 5 min second-stage processing time enabled the hybrid

TABLE 3: Average reflectivity of the two-stage MAE fabricated micronanohybrid structures subjected to a first-stage processing time of 30 sec for the light spectrum of 200–1000 nm.

Second-stage etching time (min)	Average reflectance (%)			
	200–400 nm	401–800 nm	801–1000 nm	200–1000 nm
1	4.26	5.49	8.16	5.85
2	5.26	3.45	4.41	4.16
3	3.16	3.34	3.51	3.54
4	1.96	2.19	2.57	2.32
5	0.74	1.12	1.97	1.21

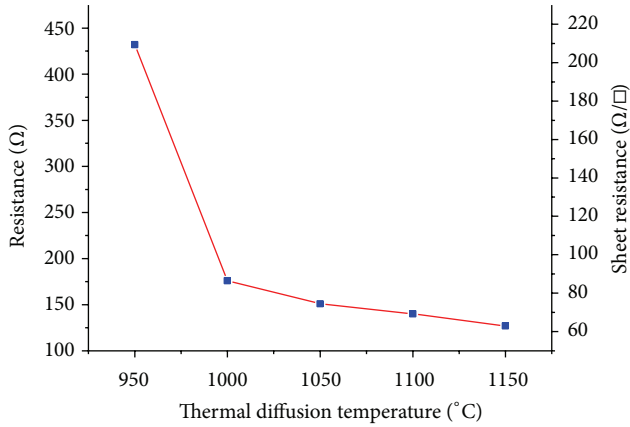


FIGURE 5: Sheet resistance measurements.

structures to have a low overall reflectivity of 1.21%, including 0.74% in UV, 1.12% in visible light, and 1.97% in IR.

3.3. Sheet Resistance Measurements. The hybrid structures with the best antireflectivity (first-stage processing time = 30 sec and second-stage processing time = 5 min) were then employed for the P-N junction synthesis using silica film.

Figure 5 shows the sheet resistance measurement results. The measured ranges of the resistance and sheet resistance are 100–450 Ω and 60–220 Ω/□, respectively. A diffusion temperature of 1000–1150 °C could grow a P-N junction with sheet resistance within the scope of the ideal P-N junction surface sheet resistance 60–200 Ω/□ [28–30]. Samples with P-N junction growth enabled by diffusion temperatures of 1000–1150 °C were used for further cell fabrication.

3.4. Photoelectric Conversion Efficiency Measurements. The cell with the micronanohybrid structure having the best antireflectivity (first-stage processing time = 30 sec and second-stage processing time = 5 min) and a P-N junction grown using the silica film (diffusion time = 60 min) was employed for further photoelectric conversion efficiency measurements. Figure 6 displays the current versus voltage (I-V) curves for the pure pyramid cells and the hybrid structured cells under various diffusion times for P-N junction growth. The major variations among the hybrid structured cells grown under different diffusion times are the open circuit voltage (V_{oc}) and the fill factor (FF). It can

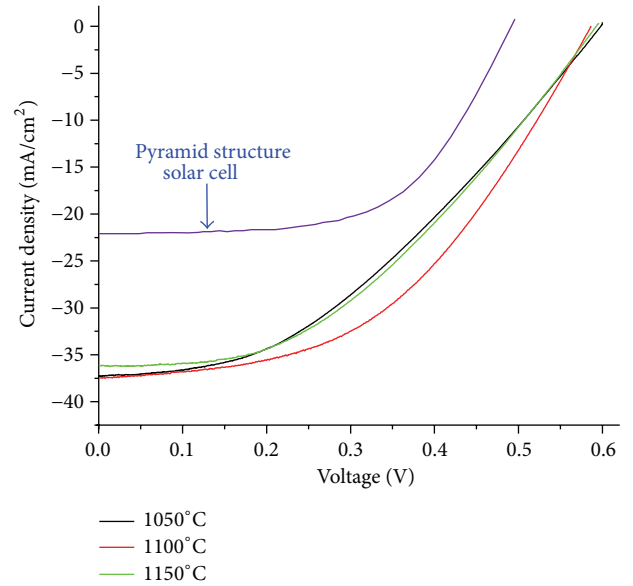


FIGURE 6: Photoelectric conversion efficiency of the fabricated solar cells subjected to various diffusion temperatures (diffusion time = 60 min).

also be observed that the hybrid structured cells exhibited much higher short circuit current density (J_{sc}). The detailed data appear in Table 4. Although the average V_{oc} and J_{sc} of the pure pyramid cells were measured as 0.52 V and 21.57 mA/cm², respectively, a conversion efficiency (η) of 6.729% was achieved due to a relatively higher FF (60%). The most efficient hybrid structured cells (diffusion temperature = 1100 °C) exhibited an efficiency of 12.319% (V_{oc} = 0.60 V, J_{sc} = 37 mA/cm², and FF = 56%). Compared with the pure pyramid cells, the large enhancement in J_{sc} can be attributed to the high antireflection property, while the relatively lower FF is due to the leakage current effects caused by the structural defects in the nanowires. Therefore, cells subjected to a diffusion temperature of 1100 °C were then immersed in an HNO₃ solution to reduce leakage current effects by growing passivation layers on their surfaces.

A 1-2 nm thick passivation layer of SiO₂ was grown by immersing the cells into a 55% HNO₃ solution for 15 min. Figure 7 displays the I-V curve and the photoelectric properties of the cell with the added passivation layer. It can be seen that the I-V curve for a cell with the added passivation

TABLE 4: Photoelectric properties of the fabricated solar cells subjected to various diffusion temperatures.

Thermal diffusion (°C)	J_{sc} (mA/cm ²)	V_{oc} (V)	FF (%)	η (%)	R_{sh} (Ω)
1050°C	37.31	0.60	45	10.10	35.1
1100°C	37.54	0.586	56	12.319	41.7
1150°C	36.12	0.595	53	11.31	50.5
Pyramid structure	21.57	0.52	60	6.729	115

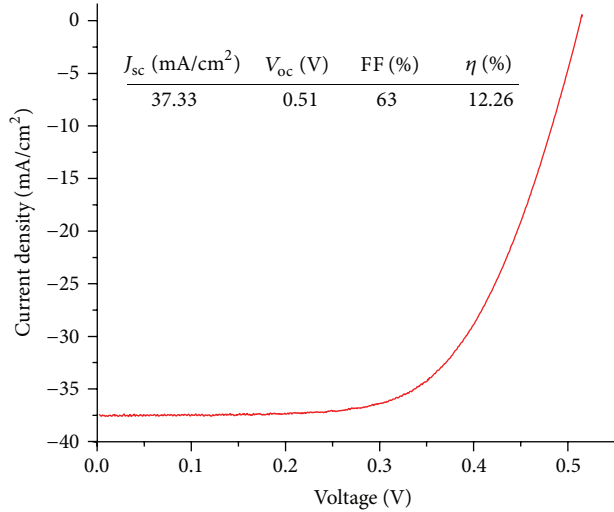


FIGURE 7: Photoelectric conversion efficiency measurement of the fabricated solar cells with a passivation layer.

layer begins to climb at 0.35 V, while that for a cell without this layer begins to climb at 0.1 V (Figure 6). Also, the FF increased from 56 to 63%, while the V_{oc} decreased from 0.586 to 0.51 V. These results imply that the passivation layer could effectively improve leakage current effects. The degradation in the V_{oc} can be attributed to the concentration variation of the diffusion source due to the redox reactions between HNO_3 and the substrate.

To further compensate for the concentration variation of the diffusion source, a longer diffusion time of 120 min was implemented to increase the diffusion depth. The photoelectric properties of the fabricated solar cells (i.e., those subjected to the diffusion process using a silica film for 120 min followed by passivation layer growth using HNO_3 solution for 15 min) are listed in Table 5. The J_{sc} and FF of the cells were about the same as those of the cells subjected to the 60 min diffusion process. However, the V_{oc} increased further to 0.56 V. Hence, the efficiency was enhanced to 13.01%.

4. Conclusion

This study developed a cost-effective method for the fabrication of high antireflection solar cells. A two-stage MAE process using an $AgNO_3$ and HF mixing solution as the etchant was adopted for the fabrication of a micronanohybrid silicon substrate. The process requires short-time etching using highly concentrated $AgNO_3$ in the first stage, followed by relatively long-time etching using less concentrated $AgNO_3$.

TABLE 5: Photoelectric properties of the fabricated solar cells subjected to a diffusion time of 120 min.

J_{sc} (mA/cm ²)	V_{oc} (V)	FF (%)	η (%)	R_{sh} (Ω)
37.401	0.56	63	13.01	58.9

The processing time for etching on an N-type high-resistance (NH) silicon wafer can be reduced to around 5 min. An inexpensive diffusion process using a liquid diffusion source was then employed to grow the P-N junction. To reduce leakage current effects, the HNO_3 solution was also used to generate a passivation layer on the cell surface. The fabricated hybrid structures exhibited a low average reflectivity of 1.21% in a wide light spectrum (200–1000 nm), including 0.74% in UV, 1.12% in visible light, and 1.97% in the IR spectra. A solar cell with the following photoelectric properties was obtained: $J_{sc} = 37.4$ mA/cm², $V_{oc} = 0.56$ V, FF = 63, and $\eta = 13.01$ %.

Conflict of Interests

The authors declare that there is no conflict of interests regarding the publication of this paper.

Acknowledgment

The authors would like to offer their thanks to the National Science Council of Taiwan under Grant no. NSC-101-2212-E-005-022-MY3 for their financial support to this research.

References

- [1] J. Schmidt, M. Kerr, and A. Cuevas, "Surface passivation of silicon solar cells using plasma-enhanced chemical-vapour-deposited SiN films and thin thermal SiO₂/plasma SiN stacks," *Semiconductor Science and Technology*, vol. 16, no. 3, pp. 164–170, 2001.
- [2] S. Winderbaum, O. Reinhold, and F. Yun, "Reactive ion etching (RIE) as a method for texturing polycrystalline silicon solar cells," *Solar Energy Materials and Solar Cells*, vol. 46, no. 3, pp. 239–248, 1997.
- [3] P. Panek, M. Lipiński, and J. Dutkiewicz, "Texturization of multicrystalline silicon by wet chemical etching for silicon solar cells," *Journal of Materials Science*, vol. 40, no. 6, pp. 1459–1463, 2005.
- [4] K. Tsujino and M. Matsumura, "Formation of a low reflective surface on crystalline silicon solar cells by chemical treatment using Ag electrodes as the catalyst," *Solar Energy Materials and Solar Cells*, vol. 90, no. 10, pp. 1527–1532, 2006.

- [5] J. S. Yoo, I. O. Parm, U. Gangopadhyay et al., "Black silicon layer formation for application in solar cells," *Solar Energy Materials and Solar Cells*, vol. 90, no. 18-19, pp. 3085–3093, 2006.
- [6] B. C. Chakravarty, J. Tripathi, A. K. Sharma et al., "The growth kinetics and optical confinement studies of porous Si for application in terrestrial Si solar cells as antireflection coating," *Solar Energy Materials and Solar Cells*, vol. 91, no. 8, pp. 701–706, 2007.
- [7] C.-H. Sun, W.-L. Min, N. C. Linn, P. Jiang, and B. Jiang, "Templated fabrication of large area subwavelength antireflection gratings on silicon," *Applied Physics Letters*, vol. 91, no. 23, Article ID 231105, 2007.
- [8] C. T. Wu, F. H. Ko, and C. H. Lin, "Self-organized tantalum oxide nanopyramidal arrays for antireflective structure," *Applied Physics Letters*, vol. 90, p. 171911, 2007.
- [9] C. H. Sun, P. Jiang, and B. Jiang, "Broadband moth-eye antireflection coatings on silicon," *Applied Physics Letters*, vol. 92, no. 6, Article ID 061112, 2008.
- [10] K. Nishioka, S. Horita, K. Ohdaira, and H. Matsumura, "Antireflection subwavelength structure of silicon surface formed by wet process using catalysis of single nano-sized gold particle," *Solar Energy Materials and Solar Cells*, vol. 92, no. 8, pp. 919–922, 2008.
- [11] P. Gorostiza, R. Diaz, J. Servat, F. Sanz, and J. R. Morante, "Atomic force microscopy study of the silicon doping influence on the first stages of platinum electroless deposition," *Journal of the Electrochemical Society*, vol. 144, no. 3, pp. 909–914, 1997.
- [12] P. Gorostiza, M. A. Kulandainathan, R. Díaz, F. Sanz, P. Allongue, and J. R. Morante, "Charge exchange processes during the open-circuit deposition of nickel on silicon from fluoride solutions," *Journal of the Electrochemical Society*, vol. 147, no. 3, pp. 1026–1030, 2000.
- [13] S. Ye, T. Ichihara, and K. Uosaki, "Spectroscopic studies on electroless deposition of copper on a hydrogen-terminated Si(111) surface in fluoride solutions," *Journal of the Electrochemical Society*, vol. 148, no. 6, pp. C421–C426, 2001.
- [14] G. J. Norga, M. Platero, K. A. Black, A. J. Reddy, J. Michel, and L. C. Kimerling, "Mechanism of copper deposition on silicon from dilute hydrofluoric acid solution," *Journal of the Electrochemical Society*, vol. 144, no. 8, pp. 2801–2810, 1997.
- [15] D. Aurbach and Y. Cohen, "The application of atomic force microscopy for the study of Li deposition processes," *Journal of the Electrochemical Society*, vol. 143, no. 11, pp. 3525–3532, 1996.
- [16] L. A. Porter Jr., H. C. Choi, J. M. Schmeltzer, A. E. Ribbe, L. C. C. Elliott, and J. M. Buriak, "Electroless nanoparticle film deposition compatible with photolithography, microcontact printing, and dip-pen nanolithography patterning technologies," *Nano Letters*, vol. 2, no. 12, pp. 1369–1372, 2002.
- [17] C. Carraro, L. Magagnin, and R. Maboudian, "Selective metallization of silicon micromechanical devices," *Electrochimica Acta*, vol. 47, no. 16, pp. 2583–2588, 2002.
- [18] F. C. Grozema, P. T. Van Duijnen, Y. A. Berlin, M. A. Ratner, and L. D. A. Siebbeles, "Intramolecular charge transport along isolated chains of conjugated polymers: effect of torsional disorder and polymerization defects," *Journal of Physical Chemistry B*, vol. 106, no. 32, pp. 7791–7795, 2002.
- [19] E. C. Garnett and P. Yang, "Silicon nanowire radial p-n junction solar cells," *Journal of the American Chemical Society*, vol. 130, no. 29, pp. 9224–9225, 2008.
- [20] Y. B. Tang, Z. H. Chen, H. S. Song et al., "Vertically aligned p-type single-crystalline GaN nanorod arrays on n-type Si for heterojunction photovoltaic cells," *Nano Letters*, vol. 8, no. 12, pp. 4191–4195, 2008.
- [21] H.-C. Yuan, V. E. Yost, M. R. Page et al., "Efficient black silicon solar cells with nanoporous anti-reflection made in a single-step liquid etch," in *Proceedings of the 34th IEEE Photovoltaic Specialists Conference (PVSC '09)*, pp. 141–145, June 2009.
- [22] F. Toor, M. R. Page, H. M. Branz, and H. C. Yuan, "17.1%-efficient multi-scale-textured black silicon solar cells without dielectric antireflection coating," in *Proceedings of the 37th IEEE Photovoltaic Specialists Conference (PVSC '11)*, pp. 20–24, 2011.
- [23] J. Oh, H.-C. Yuan, and H. M. Branz, "An 18.2%-efficient black-silicon solar cell achieved through control of carrier recombination in nanostructures," *Nature Nanotechnology*, vol. 7, pp. 743–748, 2012.
- [24] H. Morinaga, M. Suyama, and T. Ohmi, "Mechanism of metallic particle growth and metal-induced pitting on Si wafer surface in wet chemical processing," *Journal of the Electrochemical Society*, vol. 141, no. 10, pp. 2834–2841, 1994.
- [25] J. S. Kim, H. Morita, J. D. Joo, and T. Ohmi, "The role of metal induced oxidation for copper deposition on silicon surface," *Journal of the Electrochemical Society*, vol. 144, no. 9, pp. 3275–3283, 1997.
- [26] K. Peng and J. Zhu, "Morphological selection of electroless metal deposits on silicon in aqueous fluoride solution," *Electrochimica Acta*, vol. 49, no. 16, pp. 2563–2568, 2004.
- [27] H. C. Liu and G. J. Wang, "Fabrication of high anti-reflection nanowires on silicon using two-stage metal-assisted etching," *Journal of Renewable and Sustainable Energy*, vol. 5, Article ID 053115, 2013.
- [28] F. Granek, M. Hermle, D. M. Huljić, O. Schultz-Wittmann, and S. W. Glunz, "Enhanced lateral current transport via the front N⁺ diffused layer of N-type high-efficiency back-junction back-contact silicon solar cells," *Progress in Photovoltaics: Research and Applications*, vol. 17, no. 1, pp. 47–56, 2009.
- [29] D. S. Kim, M. M. Hilali, A. Rohatgi, K. Nakano, A. Hariharan, and K. Matthei, "Development of a phosphorus spray diffusion system for low-cost silicon solar cells," *Journal of the Electrochemical Society*, vol. 153, no. 7, pp. A1391–A1396, 2006.
- [30] B. Paviet-Salomon, S. Gall, R. Monna, S. Manuel, and A. Slaoui, "Experimental and analytical study of saturation current density of laser-doped phosphorus emitters for silicon solar cells," *Solar Energy Materials and Solar Cells*, vol. 95, no. 8, pp. 2536–2539, 2011.

Research Article

Design and Optimization of Fresnel Lens for High Concentration Photovoltaic System

Lei Jing, Hua Liu, Yao Wang, Wenbin Xu, Hongxin Zhang, and Zhenwu Lu

*Opto-Electronic Technology Center, Changchun Institute of Optics, Fine Mechanics and Physics,
Chinese Academy of Sciences, Changchun 130033, China*

Correspondence should be addressed to Hua Liu; 54153023@qq.com

Received 27 December 2013; Revised 22 February 2014; Accepted 24 February 2014; Published 30 March 2014

Academic Editor: Dimitrios Karamanis

Copyright © 2014 Lei Jing et al. This is an open access article distributed under the Creative Commons Attribution License, which permits unrestricted use, distribution, and reproduction in any medium, provided the original work is properly cited.

A practical optimization design is proposed, in which the solar direct light spectrum and multijunction cell response range are taken into account in combination, particularly for the Fresnel concentrators with a high concentration and a small aspect ratio. In addition, the change of refractive index due to temperature variation in outdoor operation conditions is also considered in the design stage. The calculation results show that this novel Fresnel lens achieves an enhancement of energy efficiency of about 10% compared with conventional Fresnel lens for a given solar spectrum, solar cell response, and corrected sunshine hours of different ambient temperature intervals.

1. Introduction

Because of the expensive cost and quality degradation, high reflectivity mirrors are not recommended for a concentration photovoltaic system (CPVs) [1], and optical refractive polymer components such as Fresnel lenses are most frequently used for commercial CPVs, which possess advantages of compactness, simplicity in manufacture, and relative cheapness [2–4]. However, the Fresnel lenses also have several inherent disadvantages.

The first is the dispersion of the solar spectrum, which leads to an essential decrease of the energy efficiency of the solar cells, especially for the Fresnel lens having a high concentration and a small aspect ratio (i.e., the ratio of focal length to the aperture of lens). The previous Fresnel lens design is mainly based on the concept that all the grooves are with the same design wavelength λ , which is popularly chosen to be either $0.54 \mu\text{m}$ [5] or the center wavelength of the solar spectrum limit [6], respectively, for the consideration of the relative peak irradiance of solar radiation and the balance of dispersion effect. Then each groove profile is obtained at this wavelength by means of simple trigonometry. These investigations were mostly devoted to analyzing the effect of dispersion of solar spectrum of the solar cell after designing,

rather than to considering the solar direct light spectrum in the design stage of Fresnel lens [6–10]. Although Watson and Jayroe Jr. [11] presented a method for the design of Fresnel lens with consideration of solar spectrum, the multijunction cell response and the influence of ambient temperature variation were not considered in design process.

The second is the variation of outdoor temperature conditions during operation, which directly affects the spectral decomposing of the Fresnel lens. Usually Fresnel lens concentrator modules are characterized under standard testing conditions by subjecting them to an irradiation of 1000 W/m^2 with an AM1.5D spectrum and a temperature of 20°C [12]. Nevertheless, the modules would not perform in accordance under actual conditions. Their efficiency is strongly affected by the environmental fluctuations. The previous studies paid more attention to the analysis of optical performances of CPVs affected by the variation of temperatures outdoors [13, 14]. The temperature dependence of refractive index caused thermal effects which had rarely been taken into account in the design stage of Fresnel lens.

With this background, in this paper, a more realistic optimization method is proposed to design a high concentration Fresnel lens with a small aspect ratio. Each groove is assumed with a specific design main wavelength related to

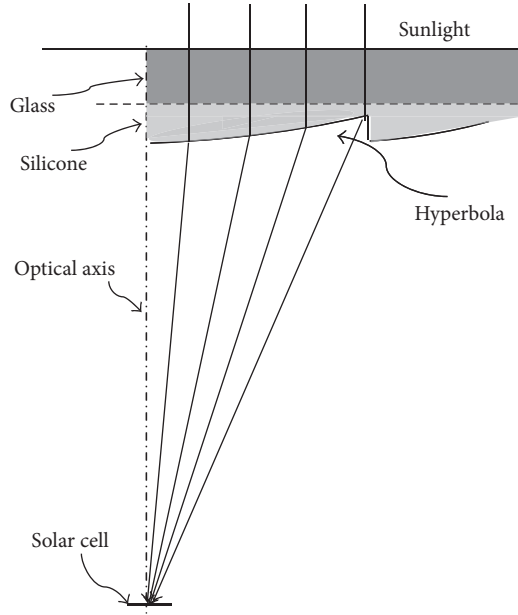


FIGURE 1: Determination of the profile for each groove with the main wavelength λ . Only one center groove of Fresnel lens is drawn for interpreting.

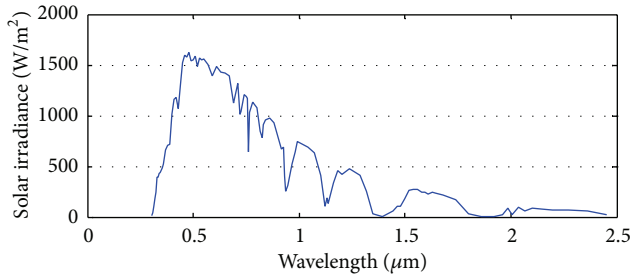


FIGURE 2: The irradiance distribution characteristic of AM1.5D solar spectrum.

the solar spectrum and the solar cell response. Then golden section search method is used to search the optimal design main wavelength to obtain the maximal energy efficiency of the solar cell. In addition, the influence of the change of refractive index caused by ambient temperature variation is also considered in the design process.

2. Optimization Design Method

For simplicity (in both designing and manufacturing), we restrict ourselves to the case as follows. The Fresnel lens array is replicated in one piece into a silicone rubber on glass; the exit surface of each groove is curvilinear and the depth of each groove is identical. As shown in Figure 1, the exit surface profile of each groove can be easily determined as a portion of a hyperbola in the condition that the parallel sunlight beam with a design wavelength λ is focused on the center of solar cell [15].

Considering the excellent performance of the solar cell at high concentration sunlight, one of the purposes of our work is to design a nonimaging Fresnel lens used in CPVs with a high concentration factor and an aspect ratio of a relatively small value.

For the most efficient design of Fresnel lens for CPVs, the lens should focus maximum amount of energy in a small spot size [1]. For this, an appropriate design method of the Fresnel lens which guarantees the CPVs with maximal energy collection efficiency is needed. In the next section we will describe the realistic optimization design method in detail, with the consideration of the solar spectrum, the multijunction cell response, and the variation of the ambient temperatures.

2.1. Consideration of the Solar Spectrum. For Fresnel lens concentrators, the solar radiation spectrum mostly used in the analysis is in the range of AM1.5D (at sea level) [16]. As can be seen in Figure 2, it has a quite wide wavelength range of 300–2500 nm. Considering the multijunction solar cell response, we are only interested in wavelength range of 350–1750 nm [17]. However, this spectrum range is still too wide for the Fresnel lens with serious dispersion effect. If we force all the wavelengths of sunlight to be collected by solar cell for a given relatively small aspect ratio, such as that often used in commercial CPVs of 1.2, the dimension of solar cell would be rather larger, corresponding to a small concentration factor of 175X (spectrum of 350–1750 nm). In other words, in order to achieve a high concentration, the dimension of solar cell should not be too large, and all the sunlight would be not captured by the relatively small solar cell (as shown in Figure 3).

Figure 3 illustrates schematically how the sunlight beam passes through an arbitrary groove of Fresnel lens and is intercepted by a small solar cell. It is noted that the dimensions of the solar cell and spectrum are locally exaggerated for the interpreting conveniently. The sunlight is dispersed at the focal plane of the Fresnel lens due to the wavelength dependence of refractive index of lens material $n = n(\lambda)$ and then is intercepted by the relatively small solar cell. The blue and red zones denote the loss of shorter and longer wavelength beam, respectively. Thus, the solar radiation spectrum interval effective for the solar cell changes from the entire spectrum (λ_s, λ_L) to the intercepted spectrum (λ_a, λ_b).

For each groove, any wavelength can be designated as the main wavelength of lens design. Since the incident flux of solar spectrum is wavelength dependent (on its way through the atmosphere, the sunlight suffers from Rayleigh scattering, aerosol extinction, and absorption of water vapor, ozone, and nitrogen dioxide), different design wavelength results in variety of the spectrum intervals corresponding to the change of captured energy. The energy can be expressed by integration:

$$E_{\text{groove}} = \int_{\lambda_a}^{\lambda_b} I_{\text{ns}} * T_{\text{ave}} d\lambda, \quad (1)$$

where E_{groove} denotes the collected energy of the solar cell for an arbitrary groove, T_{ave} denotes the average transmission

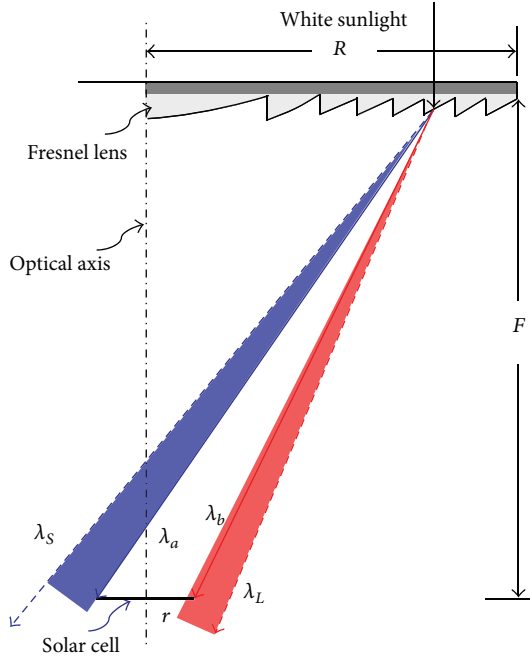


FIGURE 3: Plot of sunlight dispersion through an arbitrary groove of a Fresnel lens with aspect ratio 1.2, geometrical concentration 1200X, and design spectrum 350–1750 nm. It is noted that the dimensions of cell and spectrum are locally exaggerated.

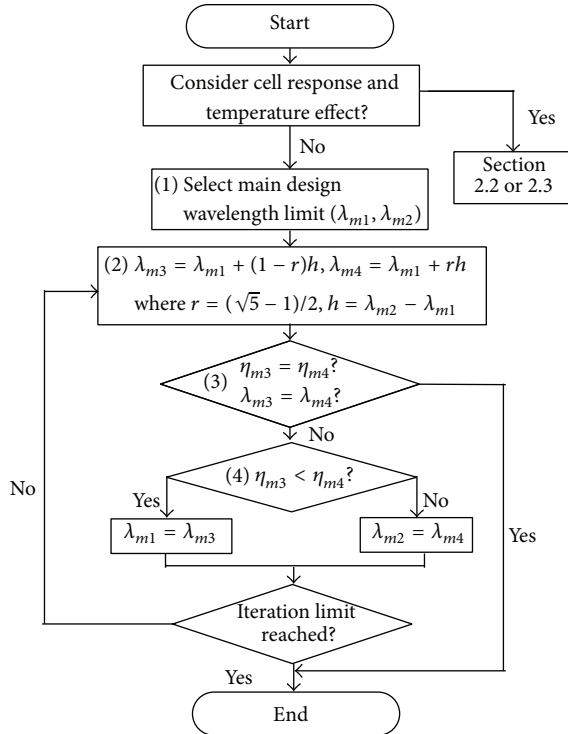


FIGURE 4: Flow chart of golden section search method for calculation of the main design wavelength.

factor, and I_{ns} denotes the normalized irradiance of solar radiation. For a given solar cell radius of r with Fresnel lens semidimension of R , focus of F , and depth of groove of d , both the intercepted spectrum interval and corresponding collected energy can be calculated using simple trigonometry for each groove [2, 11].

In view of the solar radiation spectrum normalization and its dependence on specified geographical location, it is more appropriate to use the collected energy efficiency η_n to evaluate the final performance of each groove, which is the ratio of energy collected by solar cell to solar radiation energy:

$$\eta_n = \frac{E_{\text{groove}}}{E_{\text{total}}} = \frac{\int_{\lambda_a}^{\lambda_b} I_{ns} \cdot T_{\text{ave}} d\lambda}{\int_{\lambda_S}^{\lambda_L} I_{ns} \cdot T_{\text{ave}} d\lambda}. \quad (2)$$

The total energy efficiency collected by the solar cell can be written as

$$\eta_{\text{total}} = \sum_n \frac{\eta_n \cdot S_n}{S}, \quad n = 1, 2, 3, \dots, N, \quad (3)$$

where S_n and S are the area of each groove and the total incident area of Fresnel lens, respectively, and N is the number of the grooves.

The objective of optimization design is to find the optimal main wavelength of design, corresponding to the maximal energy efficiency, which can be potentially realized via an iterative search, such as the well-known golden section search method. The flow chart of the basic procedure is shown in Figure 4 and the major steps of the algorithm are listed as follows. At first we determine whether we take into account the solar cell response and temperature effects. If yes, see Sections 2.2 or 2.3; otherwise, the following steps begin. (1) Select the main design wavelength limit $(\lambda_{m1}, \lambda_{m2})$. (2) Calculate the golden section points of λ_{m3} and λ_{m4} . (3) Determine whether the utilized energy efficiency η_{m3} equals η_{m4} and whether λ_{m3} equals λ_{m4} . If the condition is satisfied, the iteration finishes. (4) Compare the solar cell efficiency η_{m3} with η_{m4} . If η_{m3} is smaller than η_{m4} , make $\lambda_{m1} = \lambda_{m3}$. Otherwise, $\lambda_{m2} = \lambda_{m4}$. Then, judge whether the iteration limit reaches, if it reaches, the iteration finishes. If not, come back to step (2) and continue iteration. In general, the optical performance of the Fresnel lens is automatically improved by the iteration, and the iteration converges to a good solution at final.

2.2. Consideration of the Solar Cell Response. III–V based multijunction cells can operate easily at very high concentration levels and so they are excellent for high concentration system. For example, metamorphic monolithic dual-junction cells of GaInP/GaInAs achieved an efficiency of 30% at 1000 suns. A monolithic triple-junction cell of GaInP/GaInAs/Ge achieved efficiency of 39% at a concentration of 236 suns [18]. Multijunction solar cells consist of a monolithic stack of semiconductor structures of different materials. Each material has a different band-gap, and the junction is with a certain conversion range of the solar spectrum [19, 20] (Figure 5). Therefore, the combination of solar direct light

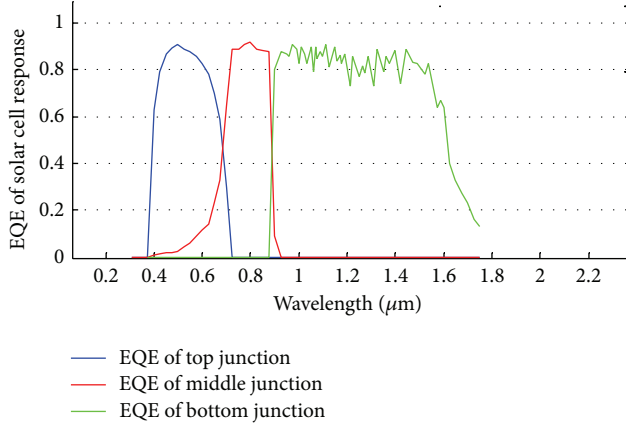


FIGURE 5: The different external quantum efficiency of triple-junction solar cell.

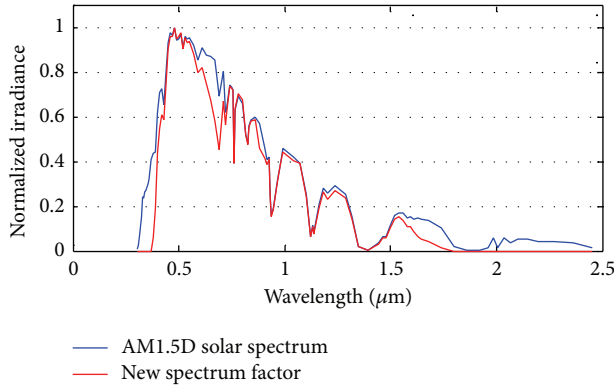


FIGURE 6: The introduced spectrum factor for consideration of the solar cell response.

spectrum and cell response range should be taken into account in the design stage of Fresnel lens.

In order to make the design more convenient, a spectrum factor of I_{sc} is introduced in this paper, which is defined as the product of the normalized irradiance of solar radiation I_{ns} (it is dependent on geographical location where the CPVs is actually installed) and the external quantum efficiency of solar cell η_{EQE} (Figure 6):

$$I_{sc} = I_{ns} \cdot \eta_{EQE}. \quad (4)$$

The characteristic of the normalized irradiance distribution of the spectrum factor that describes the compound relationship of the solar spectrum and the solar cell response will be specified as the design spectrum. In further design, the spectrum factor will substitute the solar spectrum in the optimization process mentioned above.

2.3. Consideration of the Outdoor Ambient Temperature. CPVs technology is particularly effective in areas of high direct normal incident (DNI) radiation (sunny locations), such as desert or high mountain plateaus. However, the climate there is often much harsher than the standard indoor

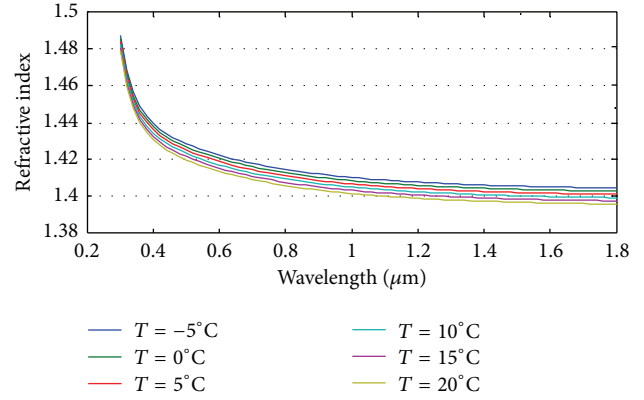


FIGURE 7: The dependence of refractive index of silicone on temperature: $K = -3.4e - 4^{\circ}C^{-1}$.

conditions. For example, the ambient temperatures of CPV may go below freezing point in winter and up to more than $40^{\circ}C$ in summer in desert. It deviates significantly from the conventional designing and testing standard temperature of $20^{\circ}C$, which leads to serious power degradation. The temperature dependence of refractive index of concentrator material may account for the degradation, especially for the polymer material of Fresnel lens [21]. The variation of the refractive index causes a shift of the focal plane away from or close to the Fresnel lens as temperature rises or falls. Thus, the temperature dependence of the refractive index of Fresnel lens material is also considered in the design of the research. Further analysis of other effects of temperature variation will be investigated in next research. A number of studies have been devoted to direct measurement of specific volume variations with respect to temperature for polymers [22]. For instance, the temperature dependence of the refractive index of silicone lens material is almost independent of wavelength and can be approximated by a linear relationship [23] very well in the interest range (Figure 7):

$$n = n_0 + k \cdot \Delta T, \quad (5)$$

where n_0 is the original refractive index, k is the temperature coefficient, and ΔT is the difference of temperature.

In this paper, for simplicity, we only consider the outdoor temperature variation during one day to optimize the Fresnel lens to achieve maximal energy efficiency. Having the monthly or annual solar radiation and temperature data adequately, the optimal design main wavelength for each groove and the maximal total energy efficiency could be obtained in the same way. Since the CPVs is usually exposed in outdoor environments for a long time, the operative temperature of Fresnel lens is assumed to be consistent with the ambient temperature. As shown in Figure 7, the temperature directly affects the refractive index of Fresnel lens material and finally affects the energy efficiency of Fresnel lens. Therefore, the optimization procedure may consider sunshine hours of

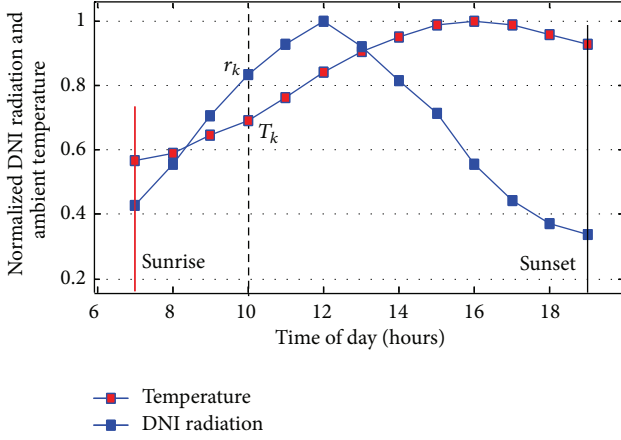


FIGURE 8: The normalized diurnal solar DNI radiation and ambient temperature.

different temperature intervals, and then the evaluation index η of the optimization can be rewritten as

$$\eta_T = \frac{\sum_{m=1}^M \eta_{T_m} \cdot H_{T_m}}{\sum_{m=1}^M H_{T_m}}, \quad (6)$$

where η_{T_m} represents the energy efficiency for solar cell with ambient temperature T_m , H_{T_m} represents the corresponding normalized diurnal amount of sunshine hours, and M represents the number of temperature intervals.

Generally speaking, the change of ambient temperature is primarily determined by the variation of solar radiation. Different ambient temperature always relates with different solar DNI radiation. Consequently, in the optimization process, the solar DNI radiation factor with different ambient temperature needs to be also included. As shown in Figure 8, in a clear and sunny location, though the normal diurnal variation of ambient temperatures is not simply dependent on solar DNI radiation and there is a slight delay in the response of temperature to changes in the solar DNI radiation, we do not pay too much attention to the specific formula of the solar DNI radiation and the ambient temperature. We only need to obtain the solar DNI radiation value of r_k at the ambient temperature value of T_k (Figure 8) to enhance the effect of the temperature. Thus, the normalized diurnal sunshine hours should be further corrected by the solar DNI radiation as

$$H_{T_m} = \frac{\sum_{k=1}^L r_k}{\sum_{k=1}^K r_k}, \quad 1 < L < K, \quad (7)$$

where r_k is the relevant solar DNI radiation at the temperature T_k , K is the total diurnal sunshine hours in one day, and L is the sunshine hours at the identical temperature intervals.

With the same optimization method as the optimization of solar spectrum mentioned above, as well as (6) and (7), the optimal design main wavelength for each groove and total maximal energy efficiency could be finally calculated under the consideration of ambient varying temperatures in one day.

3. Example and Discussion

A simple high concentration circular Fresnel lens is designed and simulated to validate this novel design method. The specifications of the design parameters are as follows. The diameter and the focal length of Fresnel lens are, respectively, 270 mm and 320 mm, the diameter of solar cell is 7.78 mm, and the solar half angle is 0.27° [24, 25]. The geometrical concentration is 1200X and the aspect ratio is 1.2. For this study we choose polymeric plastic silicone as the base material of Fresnel lens. This is a very good option with high transmission factor, susceptible of molding manufacture and low cost. Its temperature coefficient is $k = -3.4e - 4^\circ\text{C}^{-1}$. The depth of each groove has an identical value of 0.5 mm, which can be freely adjusted under manufacturing condition. The characteristic of multijunction cell response is shown in Figure 5. The geographical location of CPVs installed practically is selected at west of China, Qinghai-Tibet Plateau. It is a good location for constructing the solar power plant due to its greatly abundant solar resource with the annual radiation reaching the ground mostly more than $6700 \text{ MJm}^{-2} \text{ year}^{-1}$ (the data stems from China Meteorological Administration). More importantly, building power plant at this place will solve the problem of power shortage there and improve the living standard and the life quality of the western people.

Figure 9 shows the variation of solar DNI radiation as the ambient temperature in mid-June of Waliguan in Qinghai, which lies more than 3800 meters and has less cloud in sky. After sunrise solar DNI radiation reaches the ground, and the ambient temperature gradually increases. The solar DNI radiation reaches its maximum around noon time, but the maximum of temperature occurs at 4 p.m. The difference between the diurnal highest and lowest temperature is up to 15°C (Figure 9(a)). The maximal daily sunshine hours corrected by DNI radiation occur at temperature of 10°C – 15°C , which is considerably deviated from the conventional designing and testing standard temperature of 20°C for Fresnel lens (Figure 9(b)). It is clear that the change of the ambient temperature may badly impact the efficiency utilized by the solar cell.

According to the optimization method described above, the optimal design main wavelength and maximal energy efficiency of solar cell for each groove are finally obtained (Figures 10 and 11).

As shown in Figure 10, the design main wavelength is different for each groove, so that the energy collected by solar cell or the collection efficiency of each groove is bigger than that with the conventional design (Figure 11). It is more distinct particularly for the marginal grooves of the Fresnel lens. This could be attributed to the fact that the closer to the edge of Fresnel lens the grooves are, the more serious the dispersion of spectrum is.

As shown in Table 1, for the conventional designs with main wavelength of $\lambda_m = 0.54 \mu\text{m}$ and $\lambda_m = 1.05 \mu\text{m}$, they both have energy efficiency more than 92%. Due to the effect of dispersion of solar spectrum, the energy efficiency reduces to less than 65%. Moreover, due to the effect of the ambient temperature, it further reduces to about 62% further. But the novel design with the consideration of the solar spectrum

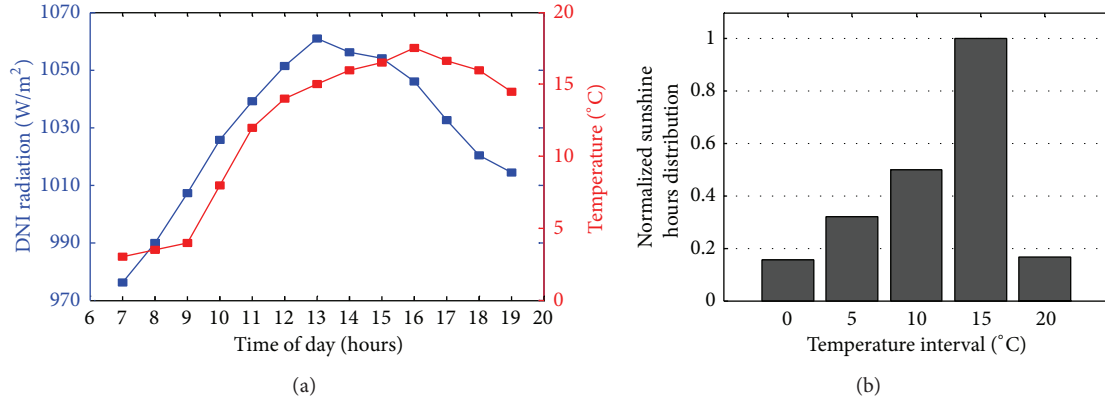


FIGURE 9: (a) The variation of solar DNI radiation as ambient temperature. (b) The corrected sunshine hours distribution of temperature interval 13th of June in 2006 (Waliguan in Qinghai).

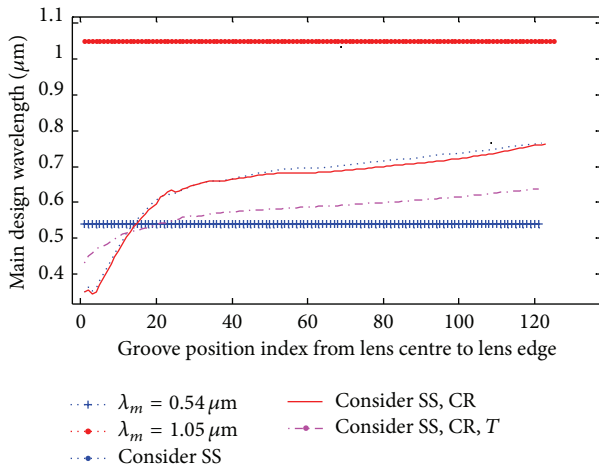


FIGURE 10: The different design main wavelength of each groove for the conventional design and the novel design (SS: solar spectrum; CR: cell response; T: temperature).

can obtain energy efficiency about 73%, which is, respectively, 9.1% and 9.7% higher than the conventional design with a constant design main wavelength of $\lambda_m = 0.54 \mu\text{m}$ and $\lambda_m = 1.05 \mu\text{m}$, respectively. Once the multijunction cell response and the temperature effects are also in consideration in design, the total efficiency would further increase more than 1.5%.

4. Conclusions

A novel optimization design of Fresnel lens used in CPVs was proposed in this paper, in which the solar direct light spectrum, the cell response range, and the change of refractive index resulting from ambient temperature are all taken into account. We assume that each groove of the Fresnel lens has a different design main wavelength and use the golden section method to search the optimal design main wavelength. In this way the intercepted wavelength interval corresponds to the maximal energy efficiency utilized by the solar cell. It is

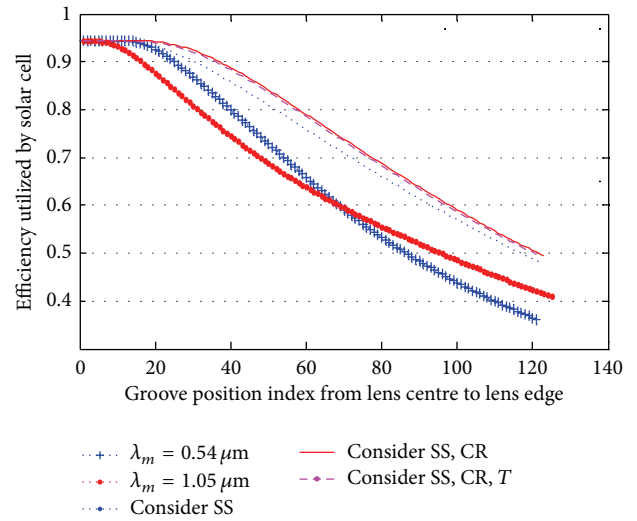


FIGURE 11: The energy efficiency of each groove for the conventional design and the novel design (SS: solar spectrum; CR: cell response; T: temperature).

TABLE 1: The calculated energy efficiency of the conventional design and the novel design for entire Fresnel lens.

Design method	Efficiency	Effect of temperature
Conventional method		
$\lambda_m = 0.54 \mu\text{m}$	SWS ^d	92.4%
	MWS ^c	64.73% (↓)
$\lambda_m = 1.05 \mu\text{m}$	SWS	92.7%
	MWS	64.08% (↓)
New method		
Consider SS ^a	73.84% (↑)	—
Consider SS, CR ^b	75.76% (↑)	—
Consider SS, CR, T ^c	75.32%	—

^aSolar spectrum; ^bcell response; ^ctemperature; ^dsingle wavelength; ^emultiple wavelengths.

indicated in a comparison of the novel with the conventional design of the Fresnel lens that an increase of energy efficiency more than 9% can be achieved. These will be helpful to substantially improve the performance of CPVs and reduce its related cost in mass installation. The concentration module based on this novel Fresnel lens is a promising option for the development of a cost-effective photovoltaic solar energy generation.

Conflict of Interests

The authors declare that there is no conflict of interests regarding the publication of this paper.

Acknowledgments

The authors sincerely thank Professor Wang ZhaoQi for his help with English language. And the authors gratefully acknowledge the financial support from National Basic Research Program of China under Grant no. 2013AA03A116 and Projects of Science and Technology Development Plan of Jilin Province under Grant no. 20130206018GX.

References

- [1] J. L. Alvarez, V. Díaz, and J. Alonso, "Optics design key points for high gain photovoltaic solar energy concentrators," in *Optical Design and Engineering II*, vol. 5962 of *Proceedings of SPIE*, September 2005.
- [2] R. Leutz and A. Suzuki, *Nonimaging Fresnel Lenses: Design and Performance of Solar Concentrators*, Springer Series in Optical Sciences, Springer, 2001.
- [3] G. Zubi, J. L. Bernal-Agustín, and G. V. Fracastoro, "High concentration photovoltaic systems applying III-V cells," *Renewable and Sustainable Energy Reviews*, vol. 13, no. 9, pp. 2645–2652, 2009.
- [4] D. Vázquez-Moliní, A. Á. Fernández-Balbuena, E. Bernabeu et al., "New concentrator multifocal Fresnel lens for improved uniformity design and characterization," in *High and Low Concentrator Systems for Solar Electric Applications IV*, vol. 7407 of *Proceedings of SPIE*, 2009.
- [5] J. H. Song, J. H. Yu, J. H. Lee et al., "Design of linear Fresnel lens for concentrated photovoltaic system," *Advanced Materials Research*, vol. 860–863, pp. 32–36, 2014.
- [6] E. Lorenzo, "Chromatic aberration effect on solar energy systems using Fresnel lenses," *Applied Optics*, vol. 20, no. 21, pp. 3729–3732, 1981.
- [7] E. Lorenzo and A. Luque, "Fresnel lens analysis for solar energy applications," *Applied Optics*, vol. 20, no. 17, pp. 2941–2945, 1981.
- [8] E. V. Bobkova, V. A. Grilikhes, A. A. Soluyanov, and M. Z. Shvarts, "Effect of chromatic aberration on the concentration of solar radiation by Fresnel lenses," *Technical Physics Letters*, vol. 32, no. 12, pp. 1039–1042, 2006.
- [9] D. Chemisana, A. Vossier, L. Pujol, A. Perona, and A. Dollet, "Characterization of Fresnel lens optical performances using an opal diffuser," *Energy Conversion and Management*, vol. 52, no. 1, pp. 658–663, 2011.
- [10] D. C. Miller, M. D. Kempe, C. E. Kennedy, and S. R. Kurtz, "Analysis of transmitted optical spectrum enabling accelerated testing of multijunction concentrating photovoltaic designs," *Optical Engineering*, vol. 50, no. 1, Article ID 013003, 2011.
- [11] M. D. Watson and R. R. Jayroe Jr., "Fresnel lens solar concentrator design based on geometric optics and blackbody radiation equation," in *Nonimaging Optics: Maximum Efficiency Light Transfer V*, vol. 3781 of *Proceedings of SPIE*, pp. 85–93, July 1999.
- [12] M. Z. Shvarts, V. M. Andreev, V. S. Gorohov et al., "Flat-plate Fresnel lenses with improved concentrating capabilities: designing, manufacturing and testing," in *Proceeding of IEEE Photovoltaic Specialists Conference*, 2008.
- [13] T. Hornung, A. Bachmaier, P. Nitz, and A. Gombert, "Temperature and wavelength dependent measurement and simulation of Fresnel lenses for concentrating photovoltaics," in *Photonics for Solar Energy Systems III*, vol. 7725 of *Proceedings of SPIE*, April 2010.
- [14] Y.-C. Chen and C.-H. Su, "Integrated opto-mechanical analysis of a PMMA Fresnel lens for a concentrated photovoltaic system," *Microsystem Technologies*, vol. 19, no. 11, pp. 1725–1729, 2013.
- [15] R. Winston, J. C. Miñano, and P. Benítez, *Nonimaging Optics*, Elsevier-Academic Press, New York, NY, USA, 2005.
- [16] ASTM, "Standard tables for reference solar spectral irradiances: direct normal and hemi-spherical on 0.37° tilted surface," ASTM G173-03e1, Book of standards, 2003.
- [17] "CIMJ-CDO-100-IC product data sheet," <http://www.spectro-lab.com>.
- [18] A. W. Bett, B. Burger, F. Dimroth, G. Siefert, and H. Lerchenmüller, "High-concentration PV using III-V solar cells," in *Proceedings of the 4th IEEE World Conference on Photovoltaic Energy Conversion (WCPEC '04)*, pp. 615–620, May 2006.
- [19] N. H. Karam, R. R. King, C. Fetzer et al., "Development and characterization of high-efficiency GaInPGe dual- and triple-junction solar cells," *Proceeding of IEEE Transactions on Electron Devices*, vol. 46, no. 10, 1999.
- [20] A. L. Luque and V. M. Andreev, *Concentrator Photovoltaics*, Springer, 2007.
- [21] T. Schult, M. Neubauer, Y. Bessler et al., "Temperature dependence of Fresnel lenses for concentrating photovoltaics," in *Proceedings of the International CPV Workshop*, Darmstadt, Germany, 2009.
- [22] P. Michel, J. Dugas, J. M. Cariou, and L. Martin, "Refractive-index variations with temperature of PMMA and polycarbonate," *Journal of Macromolecular Science—Physics*, vol. 25, no. 4, pp. 379–394, 1986.
- [23] A. Norris, J. DeGroot Jr., F. Nishida, U. Pernisz, N. Kushibiki, and T. Ogawa, "Silicone polymers for optical films and devices," in *Linear and Nonlinear Optics of Organic Materials II*, vol. 4798 of *Proceedings of SPIE*, pp. 79–86, July 2002.
- [24] L. Reed, R. Winston, and A. Ritschel, "Field results of a Kohler integrating photovoltaic system," in *Nonimaging Optics and Efficient Illumination Systems IV*, R. Winston and R. J. Koshel, Eds., vol. 6670 of *Proceedings of SPIE*, August 2007.
- [25] J. A. Duffie and W. A. Beckman, *Solar Engineering of Thermal Processes*, Wiley Interscience, New York, NY, USA, 1980.

Research Article

Effective Passivation of Large Area Black Silicon Solar Cells by $\text{SiO}_2/\text{SiN}_x\text{:H}$ Stacks

Zengchao Zhao, Bingye Zhang, Ping Li, Wan Guo, and Aimin Liu

School of Physics and Optoelectronic Technology, Dalian University of Technology, Dalian 116023, China

Correspondence should be addressed to Aimin Liu; aiminl@dlut.edu.cn

Received 30 December 2013; Accepted 3 February 2014; Published 6 March 2014

Academic Editor: Tao Xu

Copyright © 2014 Zengchao Zhao et al. This is an open access article distributed under the Creative Commons Attribution License, which permits unrestricted use, distribution, and reproduction in any medium, provided the original work is properly cited.

The performance of black silicon solar cells with various passivation films was characterized. Large area ($156 \times 156 \text{ mm}^2$) black silicon was prepared by silver-nanoparticle-assisted etching on pyramidal silicon wafer. The conversion efficiency of black silicon solar cell without passivation is 13.8%. For the SiO_2 and $\text{SiN}_x\text{:H}$ passivation, the conversion efficiency of black silicon solar cells increases to 16.1% and 16.5%, respectively. Compared to the single film of surface passivation of black silicon solar cells, the $\text{SiO}_2/\text{SiN}_x\text{:H}$ stacks exhibit the highest efficiency of 17.1%. The investigation of internal quantum efficiency (IQE) suggests that the $\text{SiO}_2/\text{SiN}_x\text{:H}$ stacks films decrease the Auger recombination through reducing the surface doping concentration and surface state density of the Si/ SiO_2 interface, and $\text{SiN}_x\text{:H}$ layer suppresses the Shockley-Read-Hall (SRH) recombination in the black silicon solar cell, which yields the best electrical performance of b-Si solar cells.

1. Introduction

For crystalline silicon solar cells, improving the conversation efficiency is one of the most important and challenging problems. It is well known that antireflection films on solar cells work effectively only at a limited range and for special angles of incidence light. In order to reduce the light loss, the texturing of front surfaces on crystalline silicon solar cells is mostly performed for improvement of the cell efficiency, by means of its antireflection properties and light trapping. Recently the black silicon (b-Si) has attracted much attention due to its excellent antireflection (AR) property [1, 2]. Several b-Si etching methods have been developed, including reactive ion etching [3], plasma immersion ion implantation etching [4, 5], metal nanoparticle assisted etching [6–8], and laser-induced etching [9]. Among these methods, the metal nanoparticle assisted etching is demonstrated to be a mainstream fabrication technique for texturing large area Si wafer due to the low cost and easy preparation for large area solar cells. Great efforts have been made to achieve more efficient b-Si solar cells, but despite the progress, the conversion efficiency is not significantly improved as expected. The dismal performance of b-Si solar cells is

mainly due to the enhanced surface recombination and Auger recombination in wafer-based nanostructured silicon solar cells [10]. Therefore, passivation plays an important role to depress the surface recombination in fabrication of high efficiency b-Si solar cells. Recently, the depressive passivation of b-Si becomes a bottleneck, which restricted the development of b-Si solar cells. Thus, choosing appropriate passivation thin films is proven to be very important to develop the performance of silicon solar cells. Great efforts have been made to obtain high efficient Si solar cells by using various passivation materials, such as silicon dioxide (SiO_2), silicon nitride ($\text{SiN}_x\text{:H}$), and aluminum oxide (Al_2O_3) [4, 11, 12]. Among these passivation materials, thermal SiO_2 is one of the obvious candidates to realize the above purpose due to simple technique and low cost, given the low density of interface states. In addition, hydrogenated silicon nitride is one of the most significant technological evolutions that have taken place in the solar cell industry, due to its ability to act simultaneously as antireflective film as well as a source of hydrogen for surface and bulk defect passivation. Although several investigations have been carried out to obtain high efficient b-Si solar cells, the results are also depressing, which requires more investigations to clarify the passivation

mechanism and break through the bottleneck of b-Si solar cells.

In our paper, the b-Si wafers with binary structure surface based on silver nanoparticle assisted etching are fabricated. The binary structure textured surface with silicon nanowires (SiNWs) on the pyramidal structure has lower area and better short wavelength response than the conventional b-Si surface with nanostructure on the planar silicon surface [11]. To depress the surface recombination of b-Si solar cells, three kinds of passivation film are prepared on the b-Si solar cells, SiO_2 , $\text{SiN}_x\text{:H}$, and a bi-layer passivation schemes of $\text{SiO}_2/\text{SiN}_x\text{:H}$ stacks film, which combines a thin thermal oxide with a low density of interface traps and a thick SiN_x film, acting as a source of hydrogen during further solar cell processing. The structural, optical, and electrical properties with various passivation films were investigated.

2. Materials and Methods

We perform alkaline etch and then the two-step black etch to create binary structure textured surface. Four P-type $\langle 100 \rangle$ unpolished monocrystalline silicon wafers with resistivity of $1\text{--}3\ \Omega\text{-cm}$, area of $156\ \text{mm} \times 156\ \text{mm}$, and thickness of $250 \pm 20\ \mu\text{m}$ were used in the experiment. Before etching silicon, the wafers were immersed in 10% HF for 1 min to remove any native oxide and rinsed in deionized water. The cleaned wafers were textured in KOH (2 wt%) solution and IPA at 80°C for 30 min to form pyramidal structures. The black etch can be summarized in the following two steps. Firstly, a thin silver nanoparticle layer was deposited on the textured silicon surface from solution I. Subsequently, the Ag nanoparticle covered Si wafers were immersed into mixture solution II at room temperature to fabricate nanowires on the pyramidal structure. To remove the Ag layer completely, the as-prepared samples were treated in a conventional Ag etchant solution consisting of $\text{NH}_4\text{OH}:\text{H}_2\text{O}_2:\text{DI}$ in the ratio of 1:1:5 by volume. Subsequently, the samples were rinsed with DI water and dried with pure N_2 .

Solution I and Solution II are the following solutions, respectively:

Solution I (for metallizing): 0.01 mol/L AgNO_3 and 4% HF,

Solution II (for etching): 4% HF and 1.2% H_2O_2 .

For the solar cell fabrication, n-type emitter was generated by doping the p-type silicon with phosphorus oxychloride (POCl_3) diffusion at the temperature 845°C forming a p-n junction underlying the nanowires. The emitter sheet resistance is around $55\ \Omega/\square$. A diluted HF solution was used to remove the phosphor silicate glass (PSG) layer and rinsed in deionized water. Three of b-Si wafers were passivated with SiO_2 , silicon nitride $\text{SiN}_x\text{:H}$, and $\text{SiO}_2/\text{SiN}_x\text{:H}$ stacks, respectively. One keeps unpassivated surface. SiO_2 was thermally grown on the samples surface at 850°C for 15 min. After edge isolation, the $\text{SiN}_x\text{:H}$ was deposited by plasma enhanced chemical vapor deposition (PECVD). Then the back and front sides were screen printed with silver-aluminum, aluminum, and silver pastes, followed by baking

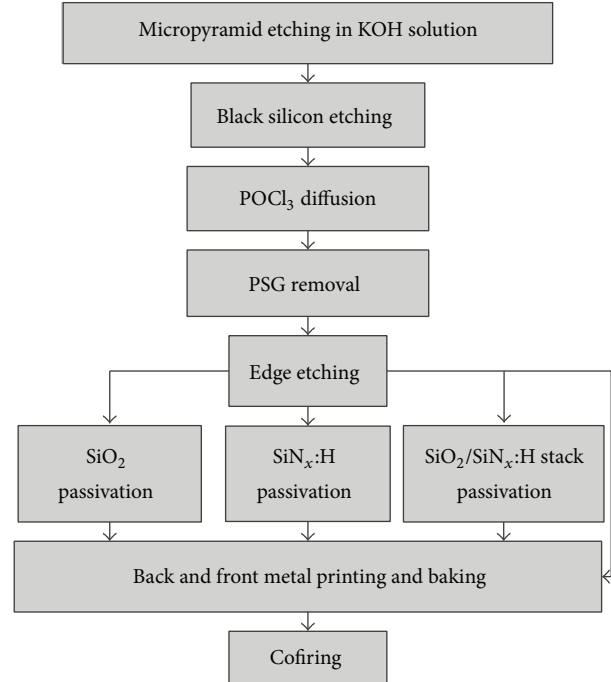


FIGURE 1: Fabrication process flow chart of the b-Si solar cells.

the pastes on the printed wafers. Finally, dried wafers were cofired in furnace to achieve ohmic contact at both of the front and rear side. The complete process flow chart was shown in Figure 1.

The morphology of the silicon nanowire structure was observed by field effect scanning electron microscope (FESEM) on Hitachi S-4800. Optical reflectance of the b-Si wafers was detected using a spectrophotometer with an integrating sphere. The internal quantum efficiency (IQE) of b-Si solar cells was measured by quantum efficiency measuring system. The doping concentration of diffused b-Si wafers was measured by electrochemical capacitance voltage (ECV) measurement on CVP 21. The electrical performances of b-Si solar cells were characterized using illuminated current-voltage under one sun global spectrum of AM1.5.

3. Results and Discussion

Figure 2 exhibits the images of top view and cross-sectional view on the surfaces of pyramidal textured silicon wafer and typical binary structure textured b-Si wafer. From Figure 2, it is shown that the SiNWs structures have been formed on the pyramidal structure surface. The nanowires which form along the $[001]$ crystal axis are not vertical on the pyramid facets ($[111]$ orientation), as shown in Figure 2(b). The average length and diameter of the nanowires are about 250 nm and 50 nm, respectively. The formation mechanism of SiNWs arrays can be well understood as being a self-assembled Ag-induced selective etching process; catalyst Ag takes an important role in the experiment. The whole reaction was divided into two parts:

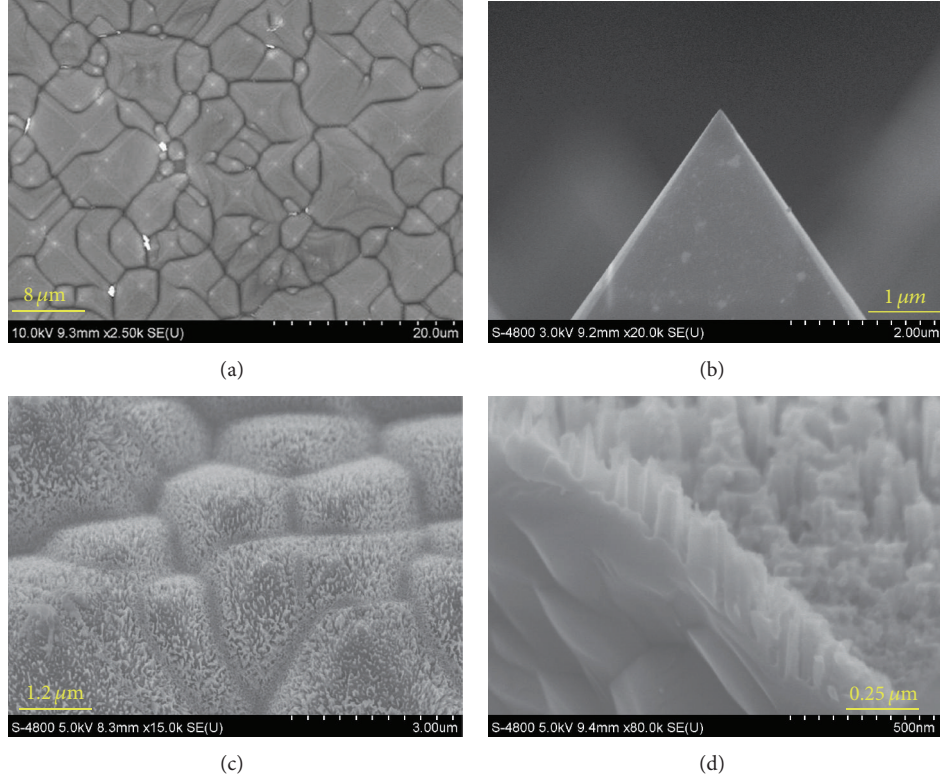
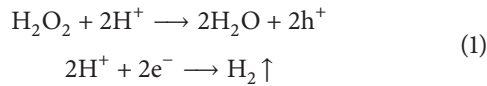


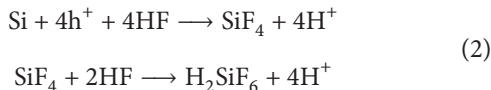
FIGURE 2: SEM images of top view (a) and cross-sectional view (b) of pyramidal textured Si. SEM images of top view (c) and cross-sectional view (d) of as-etched binary structure textured b-Si.

cathode and anode reactions, which are described as follows [13]:

cathode reaction (at silver):



anode reaction:



over reaction:

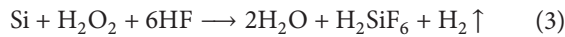


Figure 3 presents the reflectance of b-Si wafers and pyramidal structure wafer measured over the wavelength from 350 to 1000 nm. A remarkable decrease of reflectance in b-Si wafer was observed. The spectrum-weighted average reflectance (R_{ave}) can be defined as [14]

$$R_{\text{ave}} = \frac{\int_{350}^{1000} R(\lambda) N(\lambda) d\lambda}{\int_{350}^{1000} N(\lambda) d\lambda}, \quad (4)$$

where $R(\lambda)$ is the total reflectance and $N(\lambda)$ is the solar flux under AM 1.5 standard conditions. By calculation, the R_{ave} of the pyramidal structure wafer is 11.24%, while that of the

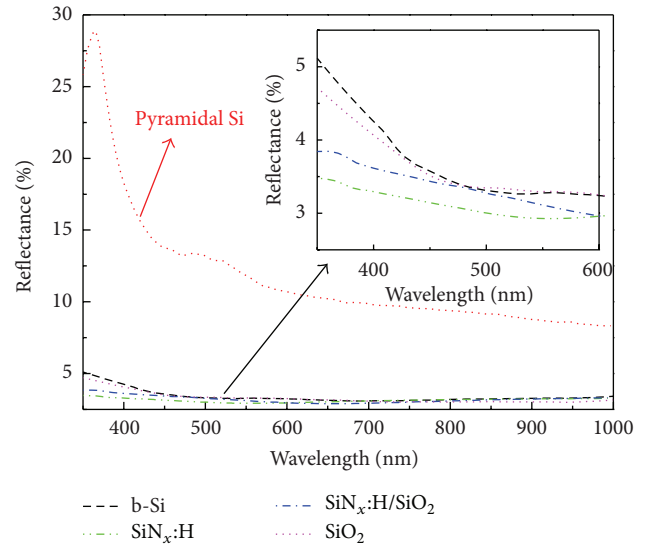
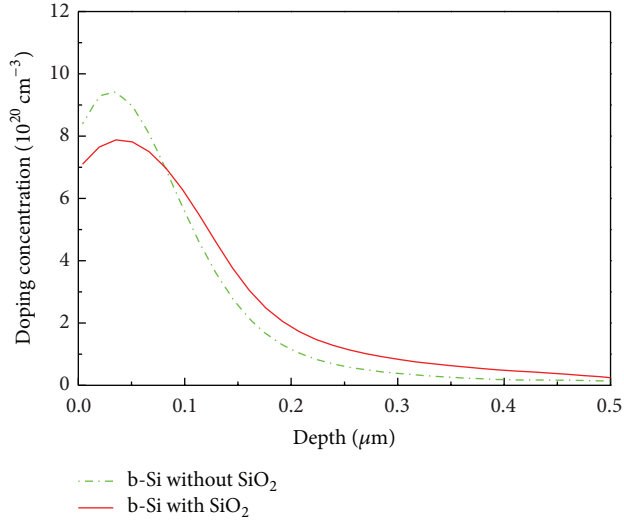


FIGURE 3: Reflectance as function of wavelength of b-Si and pyramidal Si. Insert shows the reflectance of b-Si and b-Si with different passivation films including SiO_2 , $\text{SiN}_x\text{:H}$, and $\text{SiO}_2/\text{SiN}_x\text{:H}$, respectively.

b-Si, b-Si with SiO_2 , $\text{SiN}_x\text{:H}$, and $\text{SiO}_2/\text{SiN}_x\text{:H}$ films is 3.42%, 3.29%, 3.08%, and 3.20%, respectively. A remarkable decrease of reflectance is observed for the SiNWs surface. The antireflection property of SiNWs array surface can be attributed to the morphology of SiNWs which is resembled with subwavelength-structure surface (SWS) [15]. In addition,

TABLE 1: The electrical properties of the black silicon solar cells with different passivation films.

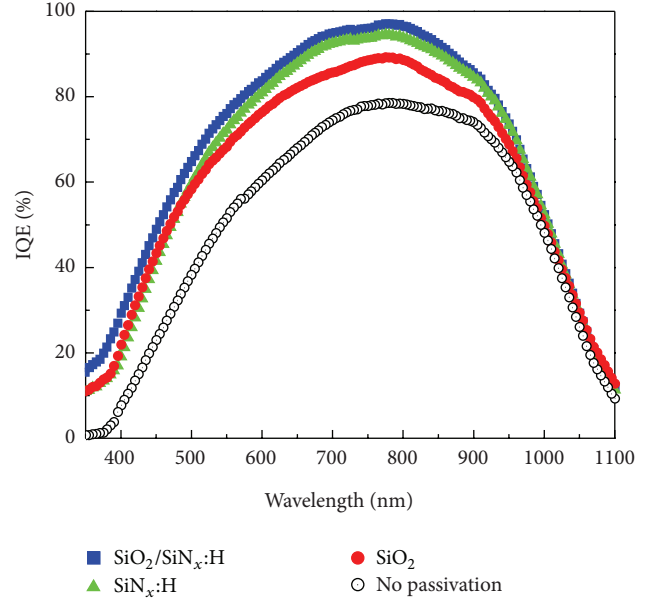
#	Passivation films	V_{oc} (V)	I_{sc} (A)	FF (%)	η (%)
S1	No passivation	0.598	7.470	73.71	13.8
S2	SiO_2	0.616	8.027	77.31	16.1
S3	$\text{SiN}_x\text{:H}$	0.615	8.409	76.04	16.5
S4	$\text{SiO}_2/\text{SiN}_x\text{:H}$	0.623	8.412	77.81	17.1

FIGURE 4: Doping profile for the diffused emitter of b-Si solar cells with and without SiO_2 passivation film by ECV.

because of unique morphology, there is porosity variation from top to bottom in the nanowire arrays which may cause a gradient in the refractive index with depth and, therefore, SiNWs arrays may give effectively the same antireflection properties as obtained in multilayer antireflection film.

The illuminated current-voltage (I - V) characteristics of the b-Si solar cells with passivation of SiO_2 , $\text{SiN}_x\text{:H}$, $\text{SiO}_2/\text{SiN}_x\text{:H}$ stacks were measured and the electrical properties were listed in Table 1. It can be found that the conversion efficiency (η) of the solar cell without surface passivation (denoted as S1) is 13.8%, with open circuit voltage (V_{oc}) of 0.598 V, short circuit current (I_{sc}) of 7.470 A, and fill factor (FF) of 73.1%, as shown in Table 1. The low V_{oc} and I_{sc} result from the excess carrier recombination at the nanostructured surface of b-Si solar cell due to the surface recombination. The efficiency of the b-Si solar cell with SiO_2 film (denoted as S2) increases to 16.1%, with the V_{oc} of 0.616 V, I_{sc} of 8.027 A, and FF of 77.31%. For the b-Si solar cell with $\text{SiN}_x\text{:H}$ film (denoted as S3) of 70 nm thickness, it can be found that the electrical performance increases to $\eta = 16.5\%$. To further improve the quality of passivation, the $\text{SiO}_2/\text{SiN}_x\text{:H}$ stacks passivation film (denoted as S4) was fabricated on b-Si solar cells. The best electrical performance of b-Si cells appears with η of 17.1%, I_{sc} of 8.412 A, V_{oc} of 0.623 V, and FF of 77.81%.

In order to investigate the passivation effects of SiO_2 layer, doping profile of diffused emitter was measured by ECV, as

FIGURE 5: Internal quantum efficiency (IQE) spectra of the b-Si solar cell and b-Si solar cells with SiO_2 , $\text{SiN}_x\text{:H}$, and $\text{SiO}_2/\text{SiN}_x\text{:H}$ stacks passivation films.

shown in Figure 4. The surface doping concentration of b-Si solar cells was $9.6 \times 10^{20} \text{ cm}^{-3}$, which means the Auger recombination associated with heavily doped emitter shows a significant influence on the electrical performance of b-Si solar cells [10]. As shown in Figure 4, the surface doping concentration of b-Si wafer was reduced from $9.6 \times 10^{20} \text{ cm}^{-3}$ to $7.8 \times 10^{20} \text{ cm}^{-3}$ via thermal oxidation process, which was due to the further diffusion of the n dopant at temperature of 850°C . When the surface doping concentration at the surface of b-Si wafer was reduced via fabricating SiO_2 , the Auger recombination and surface recombination were suppressed, leading to the better electrical performance of S2 cell.

To verify the above presumed further diffusion mechanism, the IQE properties of b-Si with various passivation films were measured, as shown in Figure 5. The IQE of S2 cell is higher than the S1 cell. Compared with the S2 cell, the IQE of S3 cell is higher at 500–900 nm regions, which leads to higher conversion efficiency and I_{sc} . As is well known, in heavily doped silicon, dislocation and dangling bonds are generated due to the mismatch between the covalent radius of an impurity atom occupying substitutional site and the silicon atom, which leads to serving SRH recombination in diffused emitter [16]. The improvement of the IQE and electrical

performances is attributed to the excellent hydrogen passivation, which suppress the SRH recombination near the surface of diffused emitter. In the process of $\text{SiN}_x\text{:H}$ deposition by PECVD, a large number of hydrogen atoms were generated in $\text{SiN}_x\text{:H}$ film, which can migrate into silicon to form the Si-H bonds after a thermal treatment, decrease the surface defect state density, and suppress the SRH recombination effectively [17–20]. In the process of metal electrode alloying the silicon wafer temperature is close to 800°C ; this process performs the role of thermal treatment [18]. Nevertheless, the IQE between 350–500 nm of the S3 cell is slightly lower than that of S2 cell, which can be explained as follows: (1) the surface state density at Si-SiO₂ interfaces is much lower than that of Si-SiN_x interfaces [17], which leads to the lower surface recombination velocity of S2 cell; (2) the surface doping concentration of S2 is reduced by thermal oxidation process which leads to the suppressing Auger recombination. The S4 cell exhibits the highest IQE at broad band of wavelength which may be assigned to the more effective passivation of SiO₂/SiN_x:H stacks film. Therefore, the short (350–500 nm) and long (500–1100 nm) wave responses were improved by the SiO₂ and SiN_x:H in SiO₂/SiN_x:H stacks film, respectively.

4. Conclusions

In summary, we demonstrated that the conversion efficiency of the large area b-Si solar cells is significantly enhanced by inducing various surface passivation films. The b-Si with binary structure textured surface was produced by silver-nanoparticle-assisted etching, and the length of nanowire is about 250 nm with the R_{ave} of 3.42%. The efficiency of b-Si solar cell without passivation is 13.8%, and the b-Si solar cells with SiO₂, SiN_x:H, and SiO₂/SiN_x:H stacks films increase to 16.1%, 16.5%, and 17.1%, respectively. The b-Si solar cells with SiO₂/SiN_x:H stacks films yield the best electrical performance, and the passivation mechanism can be given as follows: (1) the SiO₂ film not only has low surface state density at Si-SiO₂ interfaces but also reduces the surface doping concentration via thermal oxidation processing leading to the lower Auger recombination; (2) the SiN_x:H can effectively suppress the SRH recombination in the b-Si solar cell, especially in the emitter, which leads to the higher performance of b-Si solar cells.

Conflict of Interests

The authors declare that there is no conflict of interests regarding the publication of this paper.

Acknowledgment

This work is supported by the National High-tech R&D Program of China (863 Program) under Grant no. 2011AA050516.

References

- [1] S. K. Srivastava, D. Kumar, P. K. Singh, M. Kar, V. Kumar, and M. Husain, "Excellent antireflection properties of vertical silicon nanowire arrays," *Solar Energy Materials and Solar Cells*, vol. 94, no. 9, pp. 1506–1511, 2010.
- [2] K. Peng, Y. Xu, Y. Wu, Y. Yan, S.-T. Lee, and J. Zhu, "Aligned single-crystalline Si nanowire arrays for photovoltaic applications," *Small*, vol. 1, no. 11, pp. 1062–1067, 2005.
- [3] M. Moreno, D. Daineka, and P. Roca i Cabarrocas, "Plasma texturing for silicon solar cells: from pyramids to inverted pyramids-like structures," *Solar Energy Materials and Solar Cells*, vol. 94, no. 5, pp. 733–737, 2010.
- [4] Y. Xia, B. Liu, J. Liu, Z. Shen, and C. Li, "A novel method to produce black silicon for solar cells," *Solar Energy*, vol. 85, no. 7, pp. 1574–1578, 2011.
- [5] Y. Xia, B. Liu, S. Zhong, and C. Li, "X-ray photoelectron spectroscopic studies of black silicon for solar cell," *Journal of Electron Spectroscopy and Related Phenomena*, vol. 184, no. 11–12, pp. 589–592, 2012.
- [6] Y. Cao, A. Liu, H. Li et al., "Fabrication of silicon wafer with ultra low reflectance by chemical etching method," *Applied Surface Science*, vol. 257, no. 17, pp. 7411–7414, 2011.
- [7] D. Kumar, S. K. Srivastava, P. K. Singh, M. Husain, and V. Kumar, "Fabrication of silicon nanowire arrays based solar cell with improved performance," *Solar Energy Materials and Solar Cells*, vol. 95, no. 1, pp. 215–218, 2011.
- [8] H.-C. Yuan, V. E. Yost, M. R. Page, P. Stradins, D. L. Meier, and H. M. Branz, "Efficient black silicon solar cell with a density-graded nanoporous surface: optical properties, performance limitations, and design rules," *Applied Physics Letters*, vol. 95, no. 12, Article ID 123501, 2009.
- [9] M. Y. Shen, C. H. Crouch, J. E. Carey, and E. Mazur, "Femtosecond laser-induced formation of submicrometer spikes on silicon in water," *Applied Physics Letters*, vol. 85, no. 23, pp. 5694–5696, 2004.
- [10] J. H. Oh, H. C. Yuan, and H. M. Branz, "An 18.2%-efficient black-silicon solar cell achieved through control of carrier recombination in nanostructures," *Nature Nanotechnology*, vol. 7, no. 11, pp. 743–748, 2012.
- [11] F. Toor, H. M. Branz, M. R. Page, K. M. Jones, and H.-C. Yuan, "Multi-scale surface texture to improve blue response of nanoporous black silicon solar cells," *Applied Physics Letters*, vol. 99, no. 10, Article ID 103501, 2011.
- [12] W. C. Wang, C. W. Lin, H. J. Chen et al., "Surface passivation of efficient nanotextured black Silicon solar cells using thermal atomic layer deposition," *ACS Applied Materials and Interfaces*, vol. 5, no. 19, pp. 9752–9759, 2013.
- [13] X. Li and P. W. Bonn, "Metal-assisted chemical etching in HF/H₂O₂ produces porous silicon," *Applied Physics Letters*, vol. 77, no. 16, pp. 2572–2574, 2000.
- [14] P. Menna, G. Di Francia, and V. La Ferrara, "Porous silicon in solar cells: a review and a description of its application as an AR coating," *Solar Energy Materials and Solar Cells*, vol. 37, no. 1, pp. 13–24, 1995.
- [15] S. Wang, X. Z. Yu, and H. T. Fan, "Simple lithographic approach for subwavelength structure antireflection," *Applied Physics Letters*, vol. 91, no. 6, Article ID 061105, 2007.
- [16] X. X. Lin, X. Hua, Z. G. Huang et al., "Realization of high performance silicon nanowire based solar cells with large size," *Nanotechnology*, vol. 24, no. 23, Article ID 235402, 2013.

- [17] A. G. Aberle, "Surface passivation of crystalline silicon solar cells: a review," *Progress in Photovoltaics Research and Applications*, vol. 8, no. 5, pp. 473–487, 2000.
- [18] F. Duerinckx and J. Szlufcik, "Defect passivation of industrial multicrystalline solar cells based on PECVD silicon nitride," *Solar Energy Materials and Solar Cells*, vol. 72, no. 1–4, pp. 231–246, 2002.
- [19] M. Stavola, S. Kleekajai, L. Wen et al., "IR characterization of hydrogen in crystalline silicon solar cells," *Physica B*, vol. 404, no. 23–24, pp. 5066–5070, 2009.
- [20] F. Jiang, M. Stavola, A. Rohatgi et al., "Hydrogenation of Si from $\text{SiN}_x(\text{H})$ films: characterization of H introduced into the Si," *Applied Physics Letters*, vol. 83, no. 5, pp. 931–933, 2003.

Research Article

Investigating the Impact of Shading Effect on the Characteristics of a Large-Scale Grid-Connected PV Power Plant in Northwest China

Yunlin Sun,^{1,2} Siming Chen,² Liying Xie,¹ Ruijiang Hong,^{1,2} and Hui Shen^{1,2}

¹ Institute for Solar Energy Systems, School of Physics and Engineering, Sun Yat-sen University, Guangzhou Higher Education Mega Center, Guangzhou, Guangdong Province 510006, China

² Shunde SYSU Institute for Solar Energy, No. 1, Desheng Dong Road, Daliang, Shunde, Foshan, Guangdong Province 528300, China

Correspondence should be addressed to Ruijiang Hong; hongruij@mail.sysu.edu.cn and Hui Shen; shenhui1956@163.com

Received 3 January 2014; Accepted 18 January 2014; Published 5 March 2014

Academic Editor: Hongxing Yang

Copyright © 2014 Yunlin Sun et al. This is an open access article distributed under the Creative Commons Attribution License, which permits unrestricted use, distribution, and reproduction in any medium, provided the original work is properly cited.

Northwest China is an ideal region for large-scale grid-connected PV system installation due to its abundant solar radiation and vast areas. For grid-connected PV systems in this region, one of the key issues is how to reduce the shading effect as much as possible to maximize their power generation. In this paper, a shading simulation model for PV modules is established and its reliability is verified under the standard testing condition (STC) in laboratory. Based on the investigation result of a 20 MWp grid-connected PV plant in northwest China, the typical shading phenomena are classified and analyzed individually, such as power distribution buildings shading and wire poles shading, plants and birds droppings shading, and front-row PV arrays shading. A series of experiments is also conducted on-site to evaluate and compare the impacts of different typical shading forms. Finally, some feasible solutions are proposed to avoid or reduce the shading effect of PV system during operation in such region.

1. Introduction

Most of the large-scale PV power systems are usually installed in the areas with adequate solar resources and vast land. For example, northwest China, where gobies, desert, and shoals are widely distributed, is an ideal region for large-scale application of PV systems. Meanwhile, the annual average solar irradiation in most of northwest China is in a range from 5400 MJ/m²·yr. to 6700 MJ/m²·yr. Comparing to that in Germany, about 3600 MJ/m²·yr. [1], northwest China has greater potential for developing PV power plants.

However, in practical application, certain blocks, such as leafs and bird droppings from the natural environment, the shadows of wire poles, power distribution buildings, or even the shadows of front row PV arrays on the modules due to the improper design or the limitations of natural condition, will greatly impact the performance of PV arrays. It is reported that the causes of hot-spots on PV modules can be attributed to partial shading or uneven distribution of light intensity [2–5]. Hot-spot is defined as a localized region in a solar cell/PV

module whose operating temperature is obviously higher than its surrounding area, which will cause less current and become a reverse diode to the rest of parts of solar cells/PV modules connected in series. As a result, hot-spots would seriously reduce the performance of the partial shaded solar cells and PV modules, or even cause a potential irreversible damage to the PV modules, such as tedlar delamination and fire disaster [6, 7].

Generally, in PV modules level, the most common method to avoid hot-spots effect is to connect a bypass diode in parallel with reverse polarity for a group of solar cells, typically 18 or 20 pieces of solar cells in a group. Thus, the partial shaded cell is reverse biased while the bypass diode is forward conducted, which bypasses the excessive current and almost short circuits the group of cells in some degree which depends on the proportion of shadow area in one solar cell. The protection by using bypass diodes is simple and general method used in commercial PV products. However, less field research about the performance of PV modules with bypass diodes under partial shading is conducted. In this paper, a

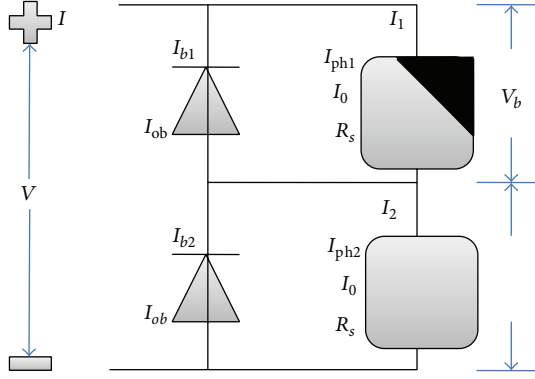


FIGURE 1: Equivalent circuit of a PV module with partial shading.

shading simulation model for PV modules is established and its reliability is verified under the standard testing condition (STC) in laboratory. The I - V and P - V characteristics of a 20-MWp grid-connected PV plant were also measured on-site to analyze the impacts of different types of partial shading. Finally some feasible solutions are proposed to avoid or reduce the shading effect during PV system operation in such region.

2. Shading Model

2.1. Shading Model for PV Modules. As shown in Figure 1, an equivalent circuit of a PV module is simplified into two cells in series with two bypass diodes. The parameters of these two cells and diodes are assumed to be constant, and the bypass diodes will shut down if the two cells receiving equal irradiation. Based on the commonly used single diode solar cell model, the output current I through the load is given by (1), where the effect of the very large shunt resistance R_{SH} is ignored [8, 9]:

$$I = I_{ph} - I_0 \left\{ \exp \left[\frac{q \cdot (V + IR_s)}{AkT} \right] - 1 \right\}, \quad (1)$$

where I_{ph} and I_0 are the photocurrent and the inverse saturation current, respectively. R_s is the series resistance. A and T are the ideality factor of the diode and temperature in Kelvin, respectively; q is electron charge (1.6×10^{-19} C) and k is Boltzmann's constant (1.38×10^{-23} J/K).

The current I_b through the bypass diode is given by

$$I_b = I_{ob} \left\{ \exp \left[\frac{-qV}{A_b k T_b} \right] - 1 \right\}. \quad (2)$$

As shown in Figure 1, a shadow falling on cell 1 reduced the energy input to the cell and consequently increased the energy loss in this partial shaded cell, while cell 2 is connected with cell 1 in series and under full illumination. Hence, the photocurrent, I_{ph2} , is higher than that of the shaded cell, I_{ph1} . The states of the bypass diode connecting in parallel with cell 1 are in two cases depending on the different level of output voltage V .

- (1) In the case of $I_{ph1} < I \leq I_{ph2}$, the output current I is almost equal to short circuit current I_{SC} when the output voltage V is relatively low. If there were no bypass diodes, the partial shaded cell 1 would be reverse biased and offer high resistance in the circuit, which results in consuming power and reducing the output current I . In this case, the bypass diode 1 connected with cell 1 in parallel is forward biased; then the redundant current $I - I_{ph1}$ flows through the bypass diode to protect the shaded cell 1 against the shading effect and hot-spots. The output power is mainly contributed by the solar cell 2 that is under full illumination.
- (2) As the output voltage V increases, the output current I turns out to be in the case of $0 \leq I \leq I_{ph1}$ and the shaded cell 1 is forward biased while the bypass diode 1 is in the state of shutting down as it is reverse biased. There is no risk for the shaded cell.

It is demonstrated that the output characteristics of the partial shaded PV module are different from those of the module fully illuminated because of the reduced luminous energy input. Besides, due to the existence of a bypass diode, as shown in Figure 1, the shaded cell is protected from damage of hot-spots. The I - V curve of the partial shaded PV module is described by a piecewise function (3), which breaks at the point of the state switching of the bypass diode:

$$V = \frac{AkT}{q} \ln \left(\frac{I_{ph2} - I}{I_0} + 1 \right) - \frac{A_b k T_b}{q} \ln \left(\frac{I - I_{ph1}}{I_{ob}} + 1 \right) - IR_s, \quad I_{ph1} < I \leq I_{ph2}, \quad (3)$$

$$V = \frac{AkT}{q} \ln \left(\frac{I_{ph1} - I}{I_0} + 1 \right) - \frac{AkT}{q} \ln \left(\frac{I_{ph2} - I}{I_0} + 1 \right) - 2IR_s, \quad 0 \leq I \leq I_{ph1}.$$

All above-mentioned the shading model analysis of PV module theoretically infers that a PV module containing N pieces of solar cells is divided into K groups by connecting K bypass diodes in parallel ($N \geq K$, not overlapping). If shadows fell on the solar cells in different proportion for every group, the I - V curve of the PV module would show K steps and there are corresponding K peaks in P - V curve [10, 11].

2.2. Experimental Verification. In order to verify the presented model, some experimental measurements have been carried out by using a commercial PV module (54 Wp, KC50T-1 produced by KYOCERA in Japan). The module includes two bypass diodes and 36 solar cells connected in series. The main parameters of the PV module at standard testing condition (AM 1.5, 1000 W/m², 25°C) are shown in

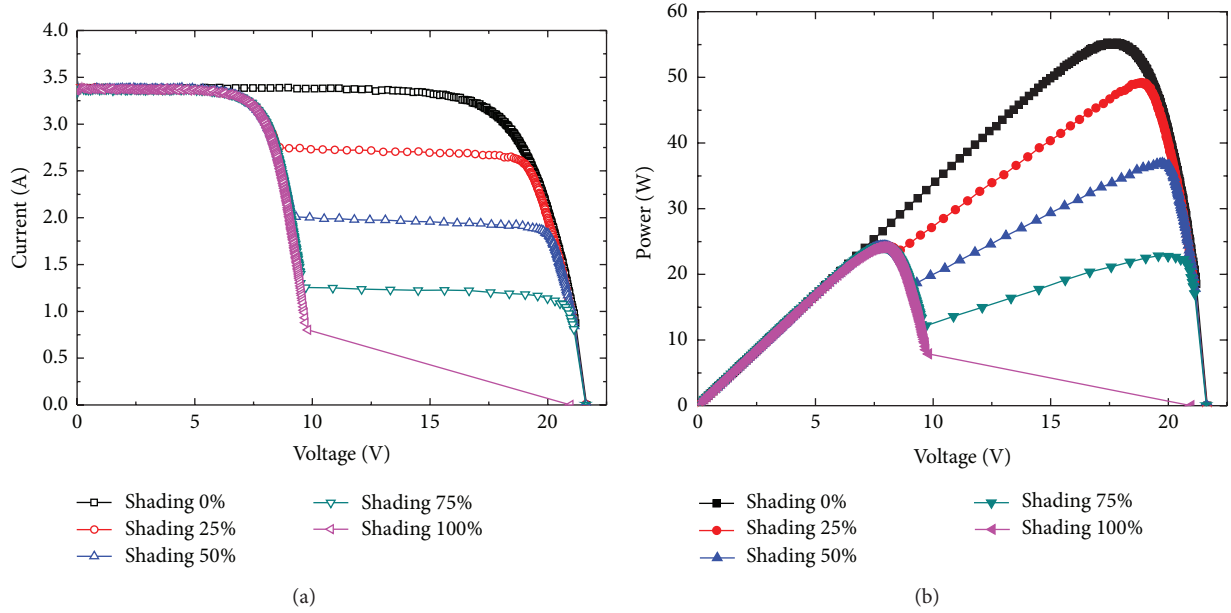


FIGURE 2: The output characteristics of KC50T-1 PV Module under 0%, 25%, 50%, 75%, and 100% shading on a single solar cell in one of the two groups which are parallel connected with two bypass diodes. (a) I - V curves and (b) P - V curves.

TABLE 1: Main parameters of the PV module used in shading model verification experiments (STC).

Sample	KC50T-1
$V_{oc}V_{oc}$ (V)	21.7
I_{sc} (A)	3.31
V_{mpp} (V)	17.4
I_{mpp} (A)	3.11
P_{mpp} (W)	54

Table 1. The I - V and P - V characteristics of the PV module under shading rates of 0%, 25%, 50%, 75%, and 100% on a single solar cell, as shown in Figure 2, were measured, respectively, by an OPTOSOLAR Module Tester made in Germany. Table 2 lists the main measurement parameters comparing with the nominal ones corresponding to Figure 2.

From Figure 2 and Table 2, it is seen that the open circuit voltages (V_{oc}) and short circuit currents (I_{sc}) are almost not varied with the variation of shading proportion. Considering that the PV module is divided into two groups by parallel connecting two bypass diodes without overlapping [8], all the shading I - V curves in Figure 2 show two steps while two peaks in P - V curves. The photocurrent I_{ph} is proportional to the solar cell active area, so it is found that the currents of latter half of the I - V curves, where the bypass diodes are not at conducting state, were reduced relatively to the shading rate. At low voltage values, a new local maximum power point appears in the P - V curves, which may be the new maximum power point depending on the shading proportion and the value of the breakdown voltage of the shaded cell. However, the straight lines appearing in the I - V and P - V curves of 100% shadow over the solar cell is attributed to the device's low

precision in this range. The output characteristics, obtained from the experiments results mentioned above, agree well with the developed shading model.

3. Results and Discussion

3.1. Shading Types Classification. Some different types of shading falling on the PV modules were observed in a 20-MWp grid-connected PV plant in northwest China [12–14]. And they can be classified into three types, namely, (1) power distribution buildings and wire poles shading, (2) plants and bird droppings shading, and (3) shading caused by front rows of PV array.

3.1.1. Power Distribution Buildings and Wire Poles Shading. Setting up electricity poles and wires is to collect and transport the electricity power produced by PV arrays. Some power distribution buildings are also necessary for PV plant to place inverters, transformers, and other equipment. However, some shadings and shadows would be formed and fall on the PV arrays, if the positions of power distribution buildings and wire poles were laid out inappropriately and too close to the PV modules, as shown in Figures 3(a) and 3(b). It is found that the shadows of the power distribution building and wire pole spread over several PV modules or even the whole PV array.

3.1.2. Plants and Bird Droppings Shading. As we know, developing PV power generation is eco-friendly to the ecology and environment of northwest China. Since desertification is so serious in there, both economic and environmental benefits can be obtained by desertification control and ecological environment protection. It was found that plants around PV



FIGURE 3: Different types of shading in a large scale grid-connected PV plant in northwest China. (a) Power distribution buildings shading; (b) wire poles shading; (c) plants shading; (d) bird droppings shading; (e) tracking PV system shading; (f) fixed PV system shading.

TABLE 2: The measurement results in shading effect experiments.

Shading proportion	0%	25%	50%	75%	100%	Nominal
$V_{oc} V_{oc}$ (V)	21.65	21.63	21.62	21.62	20.97	21.7
I_{sc} (A)	3.36	3.36	3.36	3.36	3.36	3.31
V_{mpp} (V)	17.64	18.67	19.62	7.40	7.84	17.4
I_{mpp} (A)	3.12	2.63	1.89	3.28	3.07	3.11
P_{mpp} (W)	55.19	49.21	37.15	24.31	24.14	54
FF (%)	76	68	51	33	34	75

arrays grow strong and a number of sparrows live in groups near the site of the PV power plant, which cause mass of plants and bird droppings shading on PV modules, as shown in Figures 3(c) and 3(d). The features of this kind of shadow are relatively of small area and of random shape and distribution.

Thus, it is needed to check and clean the modules in PV power plants one by one to completely rule out the shading.

3.1.3. Shading Caused by Front Rows of PV Arrays. According to on-site observation, the shading caused by front rows of

TABLE 3: Key parameters of the PV module under STC.

Sample	HH220(30)p
V_{oc} (V)	36
I_{sc} (A)	8.19
V_{mpp} (V)	29
I_{mpp} (A)	7.59
P_{mpp} (W)	220

PV arrays appears when the solar altitude angle is relatively small in early morning or late afternoon. Figures 3(e) and 3(f) show the shadows falling on the PV modules of tracking PV system and fixed PV system by front rows modules, respectively, which affected the rear rows arrays from 8:40 a.m. to 4:10 p.m. on the day when these two photographs were taken in November. This type of shading is due to the improper distance between the adjacent PV arrays. The differences of topography and surface structures between actual terrain and topographic contour map result in the construction processes of PV arrays being difficult to exactly match with the preliminary design, and the distance between the adjacent two arrays is too close, which causes the front row shading in the case of small solar height angle.

3.2. The Effect of Shading on the Characteristics of PV Modules.

A series of experiments were conducted on-site for these typical shading forms for evaluation and comparison. The studied HH220(30)p PV modules, produced by Huanghe Corporation, include three bypass diodes and 60 $156 \times 156 \text{ mm}^2$ polycrystalline silicon solar cells connected in series. The key PV module parameters under standard test conditions are listed in Table 3. The on-site experiments were conducted on September 12, 2012, from 10:00 a.m. to 11:00 a.m. with fine weather and clear sky. The solar irradiance is steady at about 850 W/m^2 . The I - V curves were measured by an I - V 400 PV Tester made by HT Italia, which can convert the I - V curves at arbitrary condition to the curve under STC.

3.2.1. Effect of Wire Pole Shading. To collect and transport the electricity generated by PV modules, a lot of wire poles were set up around the arrays. However, some of them, located at inappropriate position, would create shadows and spread on several modules surface to block solar irradiance for almost all the daytime. Figure 4 shows the shadow of a wire pole falling on 5 adjacent PV modules, where four of them were numbered as number 1 to number 4, as shown also in Figure 4. The shadow on the module left next to number 4 module faded away in less than 10 min before measurement, so the module does not analyze in this section. The number 5 PV module is considered to be a reference as the module with no shadow on it. The I - V and P - V curves of number 1 to number 5 modules were detected rapidly by HT Italia PV Tester I - V 400; the main parameters are listed in Table 4 and presented in Figures 6(a) and 6(b).

As the studied PV modules include 3 bypass diodes as shown in Figure 5, the I - V curves present 3 steps as shown in Figure 6(a) and there are 3 peaks in the P - V characteristics in



FIGURE 4: The numbers of the PV modules shaded by wire pole.

Figure 6(b). Detailed analysis was carried out for the number 1 module. There are 3 groups of 20 serially connected solar cells, and parallel connected with one bypass diode for each group, which are G_{1-1} , G_{1-2} , and G_{1-3} from right to left as shown in Figure 4. Because the maximum shading areas for one solar cell in each groups are 22.5%, 90%, and 96%, the photocurrents have relationship of $I_{ph1} > I_{ph2} > I_{ph3}$. As mentioned in Section 2.1, the characteristics of only Group G_{1-1} are displayed in the curve if the output current is obtained of $I_{ph1} \geq I > I_{ph2} > I_{ph3}$ and the bypass diodes parallel connected with G_{1-2} and G_{1-3} are conducted. While the output current is in the stated $I_{ph1} > I_{ph2} \geq I > I_{ph3}$, the combination characteristics of G_{1-1} and G_{1-2} are presented for the activation of the G_{1-3} bypass diode, and the characteristic of the complete module including G_{1-1} , G_{1-2} and G_{1-3} is plotted in the curve when the output current I is less than the photocurrents, that is, $I_{ph1} > I_{ph2} > I_{ph3} \geq I$, with the circuits of three bypass diodes open.

Since the maximum shading areas for one solar cell in each group of number 2 module from right to left were 96%, 90%, and 96% and of number 3 module 96%, 50%, and 0%, while 0%, 90%, and 96% for number 4 module, as the output currents of modules are negative correlated to the areas of shading, the shapes of the I - V curves consequently reveal as 3 steps, and 3 peaks to the P - V curves for they are the integrations of each I - V curves, the local minimum value points in the P - V curves are the state switching points of the bypass diodes. The solar irradiance to the shadow region is about 80 W/m^2 detected by I - V 400, the output characteristic can also be measured in the curves, even if the whole cell covered by shadow. As number 5 module was under the full illumination, the shape of output characteristic is consistent with the standard curves.

Although the wire pole that caused shadow area is not large, the narrow and long shape of shadow spreading on several groups of solar cells of some adjacent modules also severely reduced the power output of the modules or even the PV arrays. To avoid the influence of wire pole shading on PV arrays, the most effective solution is to carefully set up the poles and configuration of cables with detailed analysis in the design stage of PV power plant.

TABLE 4: Key parameters of the PV modules shaded by the wire pole under STC.

	1	2	3	4	5	Nominal
V_{oc} (V)	35.99	36.05	36.04	35.99	36.05	36
I_{sc} (A)	6.41	2.45	8.14	7.55	8.21	8.19
V_{mpp} (V)	31.99	32.52	19.13	7.12	27.16	29
I_{mpp} (A)	1.10	1.18	5.10	6.61	7.57	7.59
P_{mpp} (W)	35.26	38.32	97.61	47.01	205.53	220
FF (%)	15	43	33	17	69	75

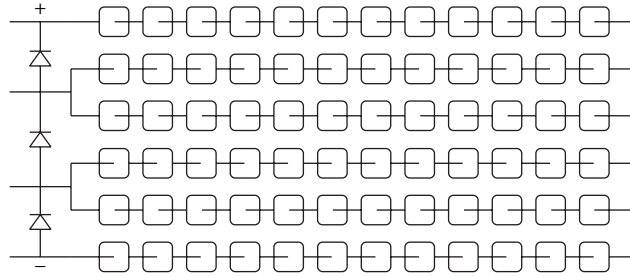


FIGURE 5: A schematic diagram of the PV module HH220(30)p.

3.2.2. Effect of Plants and Bird Droppings Shadings. Plants and bird droppings are very common to become shadings on PV modules. It was found that plants around PV arrays grow strong and a number of sparrows live in groups near the site of the studied PV plants, causing mass of plants and bird droppings shading on PV modules. The output characteristics of the PV module shaded by plants were measured before and after the removal of the plant by I - V 400 tester. The parameters are listed in Table 5; the I - V and P - V curves are presented in Figure 7.

The shadow caused by the plant as shown in Figure 3(c) is relatively small in area and random in shape, but its falling on all the three groups of cells by each group connected one bypass diode in parallel; the I - V curve displays 3 steps and P - V curves shows 3 peaks shape. Comparing with the maximum power of 215.34 W after the plant is removed, the output power under shading is just 107.93 W, which was reduced by 50.12%.

In addition, the bird dropping shading is also classified into the small area and random shape shading situation. The output characteristics of the PV module, as shown in Figure 3(d), were measured before and after the removal of the bird droppings by using I - V 400 tester. The parameters are presented in Table 6, and the I - V and P - V curves are illustrated in Figure 8.

As shown in Figure 8, the shadow area caused by bird droppings was small and only affected one of the three groups of the module, so its impact on the output characteristics of I - V and P - V is relatively low. Based on Table 6, Comparing with the output parameters of the module after the bird droppings removal, the maximum output power P_{mpp} was only reduced by 1 W and fill factor FF fell by 1%. The shape of the I - V curve of the shaded module reveals a one-step shape; though the step is tiny, it is demonstrated that the forward bias voltage applied on the bypass diode is larger than the voltage

TABLE 5: Key parameters of the PV modules shaded by plant under STC.

	Shading	Clear	Nominal
V_{oc} (V)	35.99	36.02	36
I_{sc} (A)	7.53	8.49	8.19
V_{mpp} (V)	21.25	27.27	29
I_{mpp} (A)	5.08	7.90	7.59
P_{mpp} (W)	107.93	215.34	220
FF (%)	40.00	70.00	75

TABLE 6: Key parameters of the PV modules shaded by bird litter under STC.

	Shading	Clear	Nominal
V_{oc} (V)	35.98	35.97	36
I_{sc} (A)	8.46	8.43	8.19
V_{mpp} (V)	27.36	27.82	29
I_{mpp} (A)	7.91	7.82	7.59
P_{mpp} (W)	216.51	217.57	220
FF (%)	71	72	75

threshold V_{th} which is 0.5 V for silicon diode, activating the bypass diode. If the shadow area was too small, the bypass diode would not conduct because of the applied forward bias voltage is lower than the voltage threshold, which results in the hot-spot effect at the position of the shading and finally causing damage to the solar cell and PV module.

Based on the effect of plants and bird droppings shading discussed above, it is illustrated that the smaller the area of the shadow is, the more dangerous is that to the solar cells and PV modules for that would induce hot-spot effect to damage the materials of the modules, and the more critical it is for us

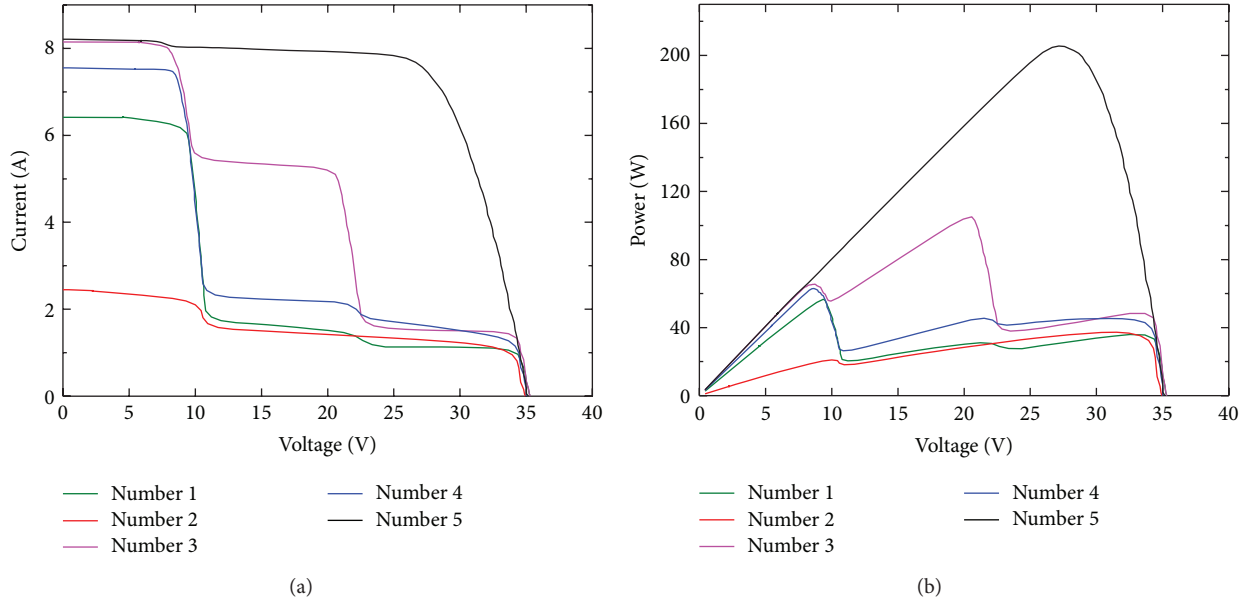


FIGURE 6: *I-V* curves and *P-V* curves of the five shaded PV modules. (a) *I-V* curves; (b) *P-V* curves.

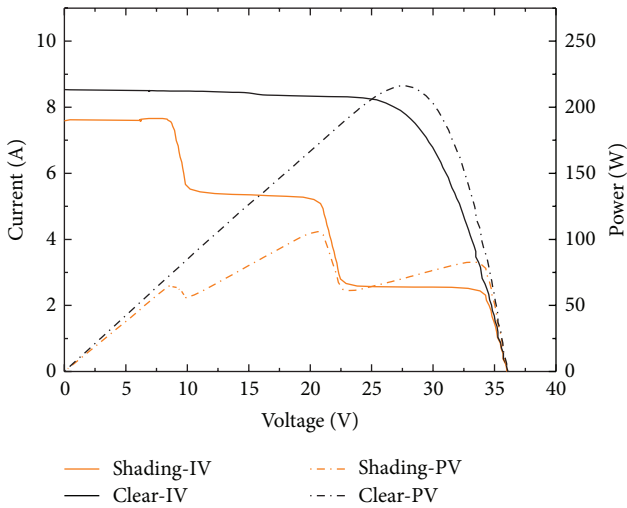


FIGURE 7: The *I-V* and *P-V* characteristics of the module before and after the plant removal.

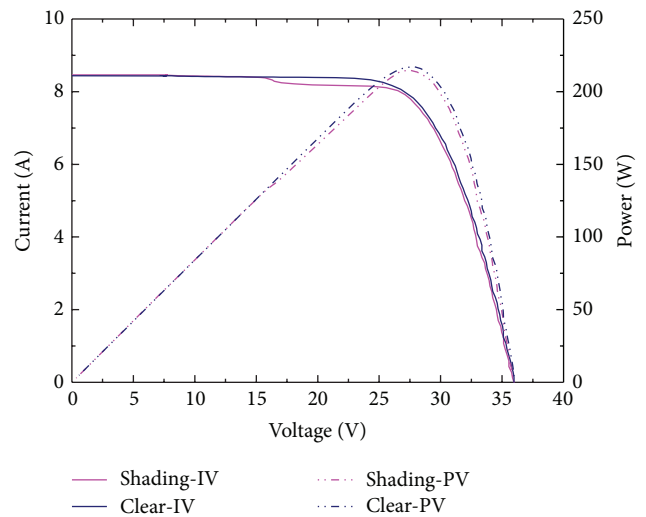


FIGURE 8: The *I-V* and *P-V* characteristics of the module before and after the bird droppings removal.

to remove the small area obstructions. Hence, plants around PV array getting trim and PV modules surface cleaning must proceed periodically during the PV plant operation and maintenance. Moreover, planting scrubs and setting up anti-bird devices can also be considered in this situation.

3.2.3. Effect of Shading Caused by Front Rows of PV Arrays. Distance setting between the two PV arrays is essential for the design stage of the PV system. The installation must follow the basis that at a site of certain latitude and longitude, from 9:00 a.m. to 3:00 p.m. on the winter solstice, the front PV arrays cause no shadow to the rear arrays at least by a distance between them, which is the minimum distance setting to

PV arrays configuration, whereas, because of the differences of the terrain and geological condition of the installation location, the PV arrays cannot be constructed in the distance consistent with the exact design setting, thus causing the shading to the PV modules by their front rows [15, 16]. This type of shadow is large in area and usually covering at the bottom side of the array for more than one complete solar cell in the groups; as can be seen in Figures 3(e) and 3(f), the very low output current of the groups will reduce the output power of the PV arrays and even the entire PV system.

As the solution, it is crucial for site selection of the PV plants, so adequate consideration to the terrain and geological condition of the installation location should be very helpful.

Besides, using the concept of bypass diodes in PV modules for reference, some bypass diodes are parallel connected with several serially connecting PV modules or arrays [17–20], insuring that the fully illuminated modules completely output their power generated, and reducing the power losses of PV arrays resulting with the so many modules shaded by shadows.

4. Conclusion

Shading effect is one of the influence factors resulting in power output reduction of PV modules and arrays. To protect against hot-spots emerging in the partial shaded PV modules, connecting a bypass diode with reverse polarity in parallel to a group of solar cells in serial connection of the module is one of the most common strategies applied in current commercial product. In this paper, a shading simulation model for PV modules was verified under the standard testing condition (STC) in laboratory; it was demonstrated that the total performance of the shaded module was the characteristics additive combination of the groups including some of the serially connecting cells which are connected with bypass diodes in parallel; the characteristics of the group are determined by the solar cell which is shaded by the maximum area of shadow, for the output current of the group, and even the PV module is forced to be equal to that of the maximum area shaded solar cell.

In addition, the modules characteristics of three types of shading that are wire pole shading, plants and bird litter shading, and front rows PV array shading observed in the large-scale grid-connected PV plant in northwest China were detected and analyzed depending on the laboratory experiments. The field investigation results illustrate that the area of shadows caused by wire pole and plants are not so large, but the shadows spread on several serial connecting groups of solar cell for some adjacent modules in many cases; it severely reduces the output power of the modules and even the PV arrays; the bird litter shading impacts on the output characteristics are relatively low for the small area; however, too small area of shadow could not activate the bypass diode because of the applied forward bias voltage lower than the voltage threshold of the diode, resulting in the formation of hot-spot. This paper also proposes some solutions to mitigate the shading effects of power distribution buildings and wire poles, plants and bird litters, and the shadow caused by front rows of PV arrays, offering some ideas for the design, operation, and maintenance of PV power generation.

Conflict of Interests

The authors declare that there is no conflict of interests regarding the publication of this paper.

Acknowledgments

This work was financially supported by Scientific and Technological Project in Guangzhou (2011Y1-0006) and

Guangdong Province Enterprise-University-Research Institute Cooperation Innovation Platform of Science and Technology (2012B090600041).

References

- [1] <http://solargis.info/doc/71>.
- [2] K. Morita et al., "Correlation between the change of the appearance and reduction in the output power of crystalline Si solar cell modules by outdoor exposure," in *Proceedings of the JSES/JWEA Joint Conference*, pp. 287–290, 2000.
- [3] D. Uchida, K. Otani, and K. Kurokawa, "Evaluation of effective shading factor by fitting a clear-day pattern obtained from hourly maximum irradiance data," *Solar Energy Materials and Solar Cells*, vol. 67, no. 1–4, pp. 519–528, 2001.
- [4] J. Appelbaum and J. Bany, "Shadow effect of adjacent solar collectors in large scale systems," *Solar Energy*, vol. 23, no. 6, pp. 497–507, 1979.
- [5] J. Munoz, E. Lorenzo, F. Martínez-Moreno, L. Marroyo, and M. García, "An investigation into hot-spots in two large grid-connected PV plants," *Progress in Photovoltaics*, vol. 16, no. 8, pp. 693–701, 2008.
- [6] A. Woyte, J. Nijs, and R. Belmans, "Partial shadowing of photovoltaic arrays with different system configurations: literature review and field test results," *Solar Energy*, vol. 74, no. 3, pp. 217–233, 2003.
- [7] J. C. Arnett and C. C. Gonzales, "Photovoltaic module hot spot durability design and test methods," in *Proceedings of the 15th IEEE Photovoltaic Specialists Conference*, pp. 1099–1105, 1981.
- [8] E. Karatepe, M. Boztepe, and M. Çolak, "Development of a suitable model for characterizing photovoltaic arrays with shaded solar cells," *Solar Energy*, vol. 81, no. 8, pp. 977–992, 2007.
- [9] S. Silvestre, A. Boronat, and A. Chouder, "Study of bypass diodes configuration on PV modules," *Applied Energy*, vol. 86, no. 9, pp. 1632–1640, 2009.
- [10] H. Kawamura, K. Naka, N. Yonekura et al., "Simulation of I-V characteristics of a PV module with shaded PV cells," *Solar Energy Materials and Solar Cells*, vol. 75, no. 3–4, pp. 613–621, 2003.
- [11] R. Ramaprabha, "Effect of shading on series and parallel connected solar PV modules," *Modern Applied Science*, vol. 3, no. 10, pp. 32–41, 2009.
- [12] M. Meinhardt G Cramer, "Multi-string-converter the next step in evolution of string-converter technology," in *Proceedings of Evolution of the European Power Electronics Conference*, 2001.
- [13] M. Drif, P. J. Pérez, J. Aguilera, and J. D. Aguilar, "A new estimation method of irradiance on a partially shaded PV generator in grid-connected photovoltaic systems," *Renewable Energy*, vol. 33, no. 9, pp. 2048–2056, 2008.
- [14] R. Ramaprabha and B. L. Mathur, "A comprehensive review and analysis of solar photovoltaic array configurations under partial shaded conditions," *International Journal of Photoenergy*, vol. 2012, Article ID 120214, 16 pages, 2012.
- [15] S. Silvestre and A. Chouder, "Effects of shadowing on photovoltaic module performance," *Progress in Photovoltaics*, vol. 16, no. 2, pp. 141–149, 2008.
- [16] P. Spirito V Albergamo, "Reverse bias power dissipation of shadowed or faulty cells in different array configurations," in *Proceeding of the 4th E.C. Photovoltaic Solar Energy Conference*, pp. 296–300, 1982.

- [17] M. C. Alonso-García, J. M. Ruiz, and F. Chenlo, "Experimental study of mismatch and shading effects in the I-V characteristic of a photovoltaic module," *Solar Energy Materials and Solar Cells*, vol. 90, no. 3, pp. 329–340, 2006.
- [18] A. K. Sharma, R. Dwivedi, and S. K. Srivastava, "Performance analysis of a solar array under shadow condition," *IEE Proceedings G*, vol. 138, no. 3, pp. 301–306, 1991.
- [19] H. Bo, N. Yuto, and Y. Ryuichi, "Influence of large-scale grid-connected photovoltaic system on distribution networks," *Automation of Electric Power Systems*, vol. 36, no. 3, pp. 34–96, 2012.
- [20] Y. Wang, H. Yang, Y. Liu et al., "The use of Ti meshes with self-organized TiO₂ nanotubes as photoanodes of all-Ti dye-sensitized solar cells," *Progress in Photovoltaics*, vol. 18, no. 4, pp. 285–290, 2010.

Research Article

Manipulation of MoSe₂ Films on CuIn(Ga)Se₂ Solar Cells during Rapid Thermal Process

Wei-Ting Lin,¹ Shih-Hao Chan,¹ Shao-Ze Tseng,¹ Jhih-Jian He,¹
Sheng-Hui Chen,¹ Ruei-Fu Shih,² Chien-Wei Tseng,² Tomi T. Li,² Sung-Cheng Hu,³
Wan-Xuan Peng,³ and Yung-Tien Lu³

¹ Department of Optics and Photonics, National Central University, 300 Chung-da Road, Chung-Li, Taoyuan 32001, Taiwan

² Department of Mechanical Engineering, National Central University, 300 Chung-da Road, Chung-Li, Taoyuan 32001, Taiwan

³ Chemical System Research Division, Chung-Shan Institute of Science & Technology, Lung-Tan, Taoyuan 32599, Taiwan

Correspondence should be addressed to Sheng-Hui Chen; ericchen@dop.ncu.edu.tw

Received 18 November 2013; Accepted 7 January 2014; Published 19 February 2014

Academic Editor: Tao Xu

Copyright © 2014 Wei-Ting Lin et al. This is an open access article distributed under the Creative Commons Attribution License, which permits unrestricted use, distribution, and reproduction in any medium, provided the original work is properly cited.

In this study, the CuIn(Ga)Se₂ (CIGS) crystalline quality and MoSe₂ thickness of films produced by the rapid thermal selenization process under various selenization pressures were investigated. When the selenization pressure increased from 48 Pa to 1.45×10^4 Pa, the CIGS films were smooth and uniform with large crystals of varying sizes. However, the MoSe₂ thicknesses increased from 50 nm to 2,109 nm, which created increased contact resistivity for the CIGS/MoSe₂/Mo structures. The efficiency of CIGS solar cells could be increased from 1.43% to 4.62% due to improvement in the CIGS crystalline quality with increasing selenization pressure from 48 Pa to 1.02×10^3 Pa. In addition, the CIGS crystalline quality and MoSe₂ thickness were modified by the pressure released valve (PRV) selenization process method. The crystalline qualities of the CIGS films were similarly affected by the selenization pressure at 1.02×10^3 Pa in the PRV selenization method and the MoSe₂ thicknesses were reduced from 1,219 nm to 703 nm. A higher efficiency of 5.2% was achieved with the thinner MoSe₂ obtained by using the PRV selenization method.

1. Introduction

There have been reports of the fabrication of 20.4% efficient CuIn(Ga)Se₂ (CIGS) thin film solar cells using the coevaporation method [1]. However, with this process it is still very difficult to scale up the useful area so as to achieve good solar cells. A better fabrication technique for CIGS to be used in industrial applications is sputtering using an ideally mixed Cu-In-Ga (CIG) alloy precursor followed by selenization in a rapid thermal process (RTP) system [2]. The problem is the ease with which an MoSe₂ layer forms at the interface between the CIGS and the Mo [3–5]. This occurs because of the high vapor pressure and the low melting point of Se at 221°C which is generated at the moment of rapid heating. Volobujeva et al. reported that high quality CIGS crystals could be formed with high Se pressure during the selenization process [6]. The MoSe₂ compound forms at the CIGS/Mo interface due to the diffusion of Se into the CIGS film and

the reaction with Mo above 440°C [7]. Many studies have reported that Mo has good electrical properties to serve as an ohmic contact, commensurate thermal expansion coefficient, and chemical stability during the CIGS film growth on a glass substrate [8]. The band gap of MoSe₂ is about 1.41 eV, which is higher than that of the CIGS material. A thin MoSe₂ compound forms between the CIGS/Mo interface which leads to a quasiohmic contact property [9] and an increase in the open-circuit voltaic (V_{oc}) device characteristics [10] due to the back surface field effect (BSF) [11]. The efficiency of a solar cell with a 140 nm thick MoSe₂ layer shows an enhancement of about 2.7% compared to a cell without the MoSe₂ layer [12]. However, it is found that the thicker MoSe₂ (10^1 – 10^4 Ω-cm) [13] forms high resistivity due to excessive selenization pressure. The related photovoltaic performance due to the short-circuit current density (J_{sc}) and series resistance (R_s) is affected which leads to a low efficiency in the solar cell. Some research studies have shown a decrease in the MoSe₂

thickness with increasing Mo sputtering pressure [14]. The MoSe_2 thickness can also be controlled by the Na content from the substrate [14]. However, there is a decrease in the efficiency of solar cells due to a high resistivity of Mo films produced with a high Mo sputtering pressure and the small grain size of CIGS films with excessive Na content. Palm et al. reported that CIGS films which formed on oxygen-rich Mo film had much thinner MoSe_2 layers [15]. Furthermore, Duchatelet et al. noted the formation of a thinner MoO_2 layer on the Mo surface when using the thermal oxidation method, which leads to an effective reduction of the MoSe_2 film thickness [16]. The conductivity characteristics decrease as the oxygen content in the Mo film increases [17], which leads to a reduction in the J_{sc} of the solar cell. The stability of the solar cell decreases due to the high water solubility of the MoO_2 layer. Therefore, it is more important to focus on how to control the relationship between the quality of the CIGS crystal and the thickness of the MoSe_2 . In this study, we adjusted the RTP selenization pressure to modify the quality of the CIGS crystal and the thickness of the MoSe_2 and then investigated the corresponding photovoltaic performance of CIGS solar Cells.

2. Experimental

The reaction kinetics of the CIGS/ MoSe_2 films was investigated using the Se/CIG/Mo structure. The CIG precursor was sputtered using Cu-In-Ga alloy targets (40 : 44 : 16 wt%) onto a Mo/glass substrate in a DC magnetron sputtering system. After deposition, the precursors were coated with a selenium layer using the thermal evaporation technique. The samples were then placed in a graphite box and loaded into the RTP system. The thickness of the Se and CIG precursor was controlled at $3.7 \mu\text{m}$ and $1.3 \mu\text{m}$, respectively. The samples were then selenized at 250°C for 180 sec and 550°C for 180 sec [18] under various selenization pressures (P_{Se} : 48 Pa, 1.02×10^3 Pa, and 1.45×10^4 Pa). In order to reduce the MoSe_2 thickness, the Se/CIG sample was selenized in a quartz lid with a pressure release valve (PRV), as shown in Figure 1. The crystalline structure and morphology of the CIGS films were analyzed by X-ray diffraction (XRD) and field emission scanning electron microscopy (FESEM). The elemental compositions were analyzed using energy dispersive X-ray spectrometry (EDS). The contact resistivity (ρ) of the CIGS/ MoSe_2 /Mo was determined using the three-point method [19]. Finally, CIGS solar cells were fabricated by the deposition of Al grid ($1 \mu\text{m}$)/AZO (800 nm)/i-ZnO (50 nm)/CdS (50 nm) using the standard process. The photovoltaic performance of the CIGS solar cells was measured under standard AM 1.5, $100 \text{ mW}/\text{cm}^2$ illumination. The effective area of the solar cell without electrode was about 1.25 cm^2 .

3. Results and Discussion

Figure 2 shows the EDS analysis of CIGS films fabricated under various selenization pressures. The ratios for the Se/CIG composition of the surface and bulk material were

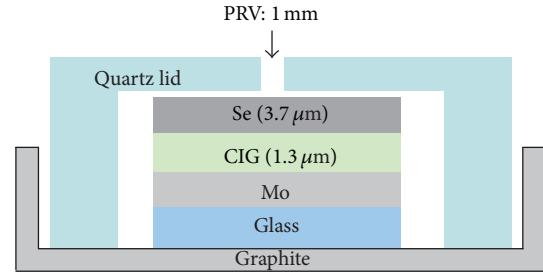


FIGURE 1: Schematic diagram of the selenization equipment with the pressure release valve design.

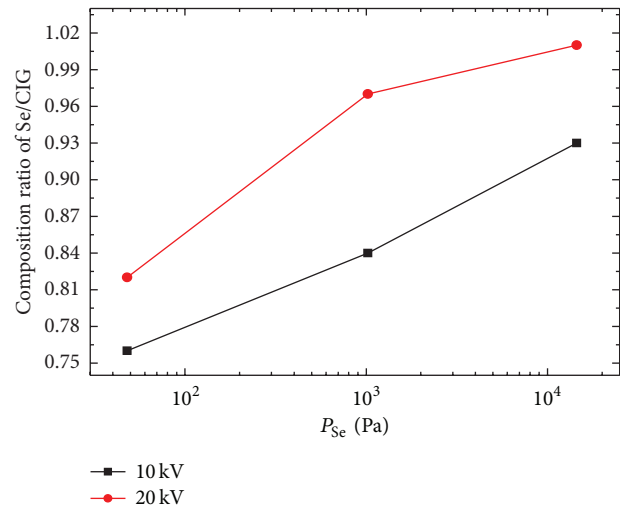


FIGURE 2: Composition ratio of Se/CIG with various selenization pressures.

calculated by EDS measurement applying acceleration voltages of 10 kV and 20 kV, respectively. Obviously, there was an increase in the Se concentration of the CIGS films due to an increase of the selenization pressure. The bulk CIGS appeared to be a Se-poor type with a selenization pressure below 10^3 Pa. The CIGS surface also appeared to be Se-poor due to a substantial amount of Se loss during the selenization process without the supply of Se. The reason is that the melt and vapor points of a Se thin film are lower than the melt and vapor points of a Se bulk. The Se layer is easy to be vaporized immediately during the rapid thermal process which affects the Se vapor to be kept in the unsealed box with difficulty. Figure 3(a) shows the XRD analysis from the Joint Committee on Powder Diffraction Standards (JCPDS) database, where each CIGS film appears to have a chalcopyrite structure (JCPDS number 35-1102). The crystalline intensity of the CIGS phases increased when the selenization pressures were increased as shown in Figure 3(b). There was a reduction in the metallic-Mo phases (JCPDS number 42-1120) due to an increase in the MoSe_2 compounds (JCPDS number 29-0914) with the high selenization pressure. A lower intensity of the MoSe_2 phase was also obtained in the PRV selenization system. Figure 4 shows the FESEM pictures of CIGS films produced with various selenization

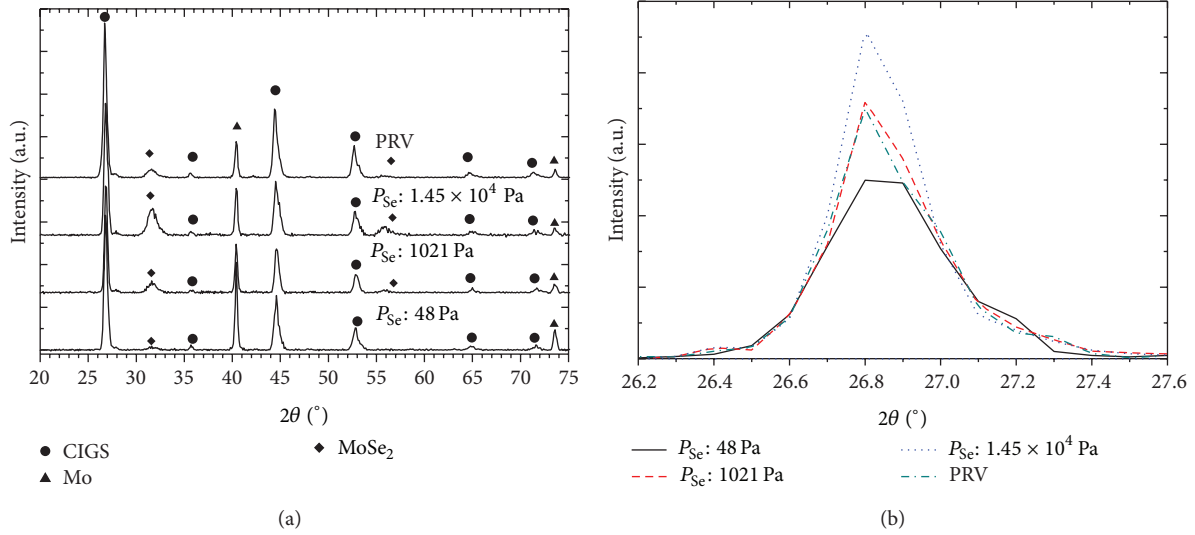


FIGURE 3: XRD patterns with various selenization pressures: (a) CIGS/MoSe₂/Mo films and (b) (112) peak of CIGS films.

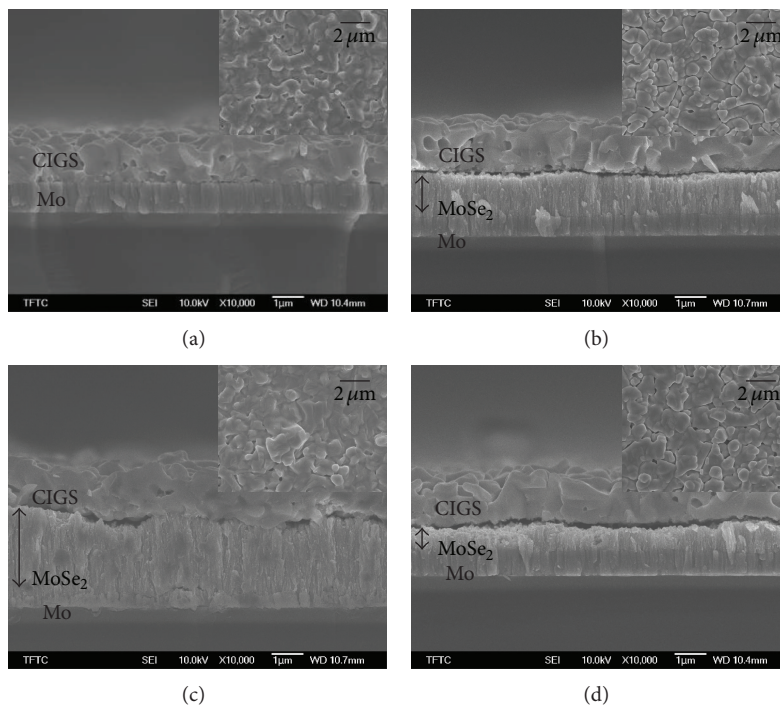


FIGURE 4: FESEM patterns of CIGS films with various selenization pressures: (a) 48 Pa, (b) 1.02×10^3 Pa, (c) 1.45×10^4 Pa, and (d) PRV.

pressures. The CIGS films were about $1.5 \mu\text{m}$ thick. Films shown in Figures 4(a), 4(b), and 4(d) were observed to have a rough surface and nonuniform grains when the selenization pressures were below 10^3 Pa or when using PRV selenization method. In this case, the pressure release valve caused a Se vapor turbulence flux phenomenon in the quartz lid during the selenization process. As can be seen in Figure 4(c), the CIGS film exhibited smooth, uniform, large crystals with sizes of about $2\text{-}3 \mu\text{m}$ at high selenization pressures of 1.45×10^4 Pa. Before the selenization process, the thickness of

the metallic-Mo film was about $1 \mu\text{m}$. During the selenization process, the Se vapor permeated into the bottom of the CIGS film and reacted with the metallic-Mo. With the increase of the selenization pressure, the thickness of the grown MoSe₂ film was between 50 nm to 2,109 nm which is similar to the previous reports [3, 4]. However, a peeling-off phenomenon at the CIGS/MoSe₂ interface was observed which was caused by excessive stress and expansion of the overly thick MoSe₂ layer that occurred at high selenization pressures, as shown in Figure 4(c). The MoSe₂ thickness could be reduced to 703 nm

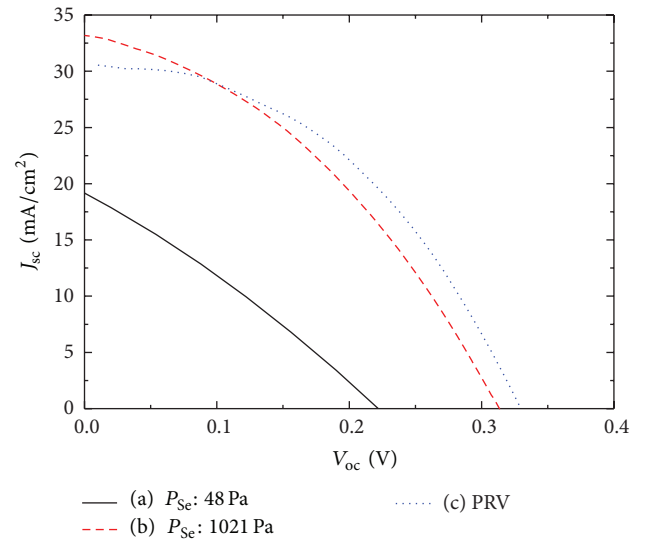
TABLE 1: Crystalline and electrical properties of CIGS/MoSe₂ films with various selenization pressures.

No.	Selenization		CIGS		CIGS/MoSe ₂ /Mo	
	P_{Se} (Pa)	FWHM (112) ori.	Grain size (112) ori.	MoSe ₂ (nm)	ρ ($\Omega\text{-cm}^2$)	
a	48	0.40	20.41	50	0.013	
b	1.02×10^3	0.35	23.32	1,219	0.032	
c	1.45×10^4	0.31	26.33	2,109	0.046	
d	PRV	0.36	22.67	703	0.022	

TABLE 2: Photovoltaic performance of CIGS solar cells with various selenization pressures.

No.	Selenization press. (Pa)	V_{oc} (V)	J_{sc} (mA/cm ²)	FF (%)	η (%)	R_s ($\Omega\text{-cm}^2$)
a	48	0.22	19.2	28.5	1.43	9.01
b	1.02×10^3	0.31	33.2	37.8	4.62	3.82
c	PRV	0.33	30.6	43.8	5.20	3.54

by using the PRV selenization method. The results showed that the diffusion rate of Se was much faster than the reaction kinetics rate of CIGS under a high selenization pressure. The diffusion rate of Se can be controlled by the selenization pressure. The MoSe₂ thicknesses, CIGS crystalline qualities, and contact resistivity of CIGS/MoSe₂/Mo films produced under various selenization pressures are summarized in Table 1. The CIGS crystalline quality and grain size with the (112) orientation were calculated using Scherrer equation from the XRD measurement. The results showed that the grain size of (112) orientation was increased with the increase of the selenization pressure. The results showed that high crystalline quality CIGS films could be achieved under high selenization pressures. The crystalline qualities of CIGS films were similar by selenization pressure at 1.02×10^3 Pa and by the PRV selenization method because the Se vapor was lost from the PRV during the selenization process. There was a decrease in the CIGS/MoSe₂/Mo contact resistivity from $0.046 \Omega\text{-cm}^2$ to $0.013 \Omega\text{-cm}^2$ which was due to the decrease in the MoSe₂ thickness from 2,109 nm to 50 nm. The photovoltaic performance of CIGS solar cells produced under various selenization pressures is shown in Figure 5 and Table 2. The CIGS films produced under a high selenization pressure at 1.45×10^4 Pa could not be fabricated into a solar cell due to the peeling-off phenomenon at the CIGS/MoSe₂ interface. When the selenization pressure increased from 48 Pa to 1.02×10^3 Pa, the J_{sc} improved from 19.2 mA/cm^2 to 33.2 mA/cm^2 and the R_s decreased from $9.01 \Omega\text{-cm}^2$ to $3.82 \Omega\text{-cm}^2$. This was due to the improvement in the CIGS crystalline quality, even the MoSe₂ thickness increased from 50 nm to 1,219 nm. When the selenization pressure was 1.02×10^3 Pa or the process was using the PRV selenization method, the CIGS films produced cells with a V_{oc} performance of 0.31 V and 0.33 V, respectively. This is related to the BSF effect where the voltage drops with the resistance characteristics due to the MoSe₂ thickness. The J_{sc} was reduced from 33.2 mA/cm^2 to 30.6 mA/cm^2 , which caused the nonuniform grains on the CIGS surface during the PRV selenization process shown in Figure 4. Making a comparison to Table 1, the results show that J_{sc} and R_s are related to the crystalline quality of CIGS films and have more influence than the MoSe₂

FIGURE 5: Photovoltaic performance of CIGS solar cells with various selenization pressures: (a) 48 Pa, (b) 1.02×10^3 Pa, and (c) PRV.

thickness in the solar cells. The efficiency of CIGS solar cells was increased from 1.43% to 4.62% with increasing only the selenization pressure. There are many factors like defect density, surface roughness, element concentration distribution, stoichiometry, and electrical properties that could also affect the cell efficiency. However, one of the important reasons is the properties of the MoSe₂. A higher efficiency of 5.2% was obtained with higher CIGS crystalline quality and thinner MoSe₂ layer by using the PRV selenization method.

4. Conclusions

The formation of CIGS/MoSe₂/Mo structures under various selenization pressures in the rapid thermal annealing selenization process was investigated. When the selenization pressures increased from 48 Pa to 1.45×10^4 Pa, the CIGS crystalline qualities were also improved and the thickness of the metallic-Mo was reduced due to an increase in the MoSe₂

thickness. The CIGS/MoSe₂/Mo contact resistivity decreased from 0.046 Ω-cm² to 0.013 Ω-cm² due to a decrease of the MoSe₂ film thickness from 2,109 nm to 50 nm. However, the excess selenization pressure at 1.45 × 10⁴ Pa led to the peeling-off phenomenon at the CIGS/MoSe₂ interface due to the excessive stress and expansion with a too thick MoSe₂. There was an increase in the efficiency of CIGS solar cells from 1.43% to 4.62% and the J_{sc} was improved from 19.2 mA/cm² to 33.2 mA/cm² due to an increase of the CIGS crystalline quality when the selenization pressure was increased from 48 Pa to 1.02 × 10³ Pa. The thickness of the MoSe₂ also increased from 50 nm to 1,219 nm. The results showed that the J_{sc} is related to the crystalline quality of CIGS films with a more significant influence than the MoSe₂ thickness on these solar cells. In addition, the crystalline qualities of CIGS films were similarly affected by the selenization pressure at 1.02 × 10³ Pa and by using the PRV selenization method. There was a reduction in the MoSe₂ thicknesses from 1,219 nm to 703 nm. A higher efficiency of 5.2% was achieved with a thinner MoSe₂ film by using the PRV selenization method.

Conflict of Interests

The authors declare that there is no conflict of interests regarding the publication of this paper.

Acknowledgments

The authors thank the Chung-Shan Institute of Science & Technology and the National Science Council of Taiwan for the financial support of this research under Contract no. NSC 102-2221-E-008-068 and 101-3113-P-008-009.

References

- [1] M. A. Green, K. Emery, Y. Hishihiro, W. Warta, and D. Dunlop, "Solar cell efficiency tables (version 42)," *Progress in Photovoltaics: Research and Applications*, vol. 21, no. 1, pp. 1–11, 2013.
- [2] V. Probst, W. Stetter, W. Riedl et al., "Rapid CIS-process for high efficiency PV-modules: development towards large area processing," *Thin Solid Films*, vol. 387, no. 1-2, pp. 262–267, 2001.
- [3] J. Koo, S. C. Kim, H. Park, and W. K. Kim, "Cu(InGa)Se₂ thin film photovoltaic absorber formation by rapid thermal annealing of binary stacked precursors," *Thin Solid Films*, vol. 520, no. 5, pp. 1484–1488, 2011.
- [4] H. Park, S. C. Kim, S.-H. Lee et al., "Effect of precursor structure on Cu(InGa)Se₂ formation by reactive annealing," *Thin Solid Films*, vol. 519, no. 21, pp. 7245–7249, 2011.
- [5] J. Koo, S. Jeon, M. Oh, C. Son, and W. K. Kim, "Optimization of Se layer thickness in Mo/CuGa/In/Se precursor for the formation of Cu(InGa)Se₂ by rapid thermal annealing," *Thin Solid Films*, vol. 535, pp. 148–153, 2013.
- [6] O. Volobujeva, M. Altosaar, J. Raudoja, and E. Mellikov, "SEM analysis and selenization of Cu-In alloy films produced by co-sputtering of metals," *Solar Energy Materials and Solar Cells*, vol. 93, no. 1, pp. 11–14, 2009.
- [7] W. K. Kim, E. A. Payzant, S. Yoon, and T. J. Anderson, "In situ investigation on selenization kinetics of Cu-In precursor using time-resolved, high temperature X-ray diffraction," *Journal of Crystal Growth*, vol. 294, no. 2, pp. 231–235, 2006.
- [8] J. H. Scofield, A. Duda, D. Albin, B. L. Ballard, and P. K. Predecki, "Sputtered molybdenum bilayer back contact for copper indium diselenide-based polycrystalline thin-film solar cells," *Thin Solid Films*, vol. 260, no. 1, pp. 26–31, 1995.
- [9] N. Kohara, S. Nishiwaki, Y. Hashimoto, T. Negami, and T. Wada, "Electrical properties of the Cu(In,Ga)Se₂/MoSe₂/Mo structure," *Solar Energy Materials and Solar Cells*, vol. 67, no. 1–4, pp. 209–215, 2001.
- [10] T. Nakada, D. Iga, H. Ohbo, and A. Kunioka, "Effects of sodium on Cu(In, Ga)Se₂-based thin films and solar cells," *Japanese Journal of Applied Physics*, vol. 36, no. 2, pp. 732–737, 1997.
- [11] T. Wada, N. Kohara, S. Nishiwaki, and T. Negami, "Characterization of the Cu(In,Ga)Se₂/Mo interface in CIGS solar cells," *Thin Solid Films*, vol. 387, no. 1-2, pp. 118–122, 2001.
- [12] X. L. Zhu, Y. Wang, A. Li, L. Zhang, and F. Huang, "The effect of N₂ gas pressure during the rapid thermal process on the structural and morphological properties of cigs films," *Advanced Materials Research*, vol. 463, pp. 614–617, 2012.
- [13] J. Pouzet and J. C. Bernede, "MoSe₂ thin films synthesized by solid state reactions between Mo and Se thin films," *Revue de Physique Appliquée*, vol. 25, pp. 807–815, 1990.
- [14] X. L. Zhu, Z. Zhou, Y. Wang, L. Zhang, A. Li, and F. Huang, "Determining factor of MoSe₂ formation in Cu(In,Ga)Se₂ solar Cells," *Solar Energy Materials and Solar Cells*, vol. 101, pp. 57–61, 2012.
- [15] J. Palm, V. Probst, A. Brummer et al., "CIS module pilot processing applying concurrent rapid selenization and sulfurization of large area thin film precursors," *Thin Solid Films*, vol. 431-432, pp. 514–522, 2003.
- [16] A. Duchatelet, G. Savidand, R. N. Vannier, and D. Lincot, "Effect of a thermal oxydation pre-treatment on Mo to control the growth and formation of MoSe₂ layers for CIGS solar cells," in *Proceedings of the 25th European Photovoltaic Solar Energy Conference and Exhibition and 5th Word Conference on Photovoltaic Energy Conversion*, pp. 3379–3381, Valencia, Spain, September 2010.
- [17] S.-Y. Kuo, M.-J. Jeng, L.-B. Chang et al., "Optimization of growth parameters for improved adhesion and electricity of molybdenum films deposited by RF magnetron sputtering," in *Proceedings of the 34th IEEE Photovoltaic Specialists Conference (PVSC '09)*, pp. 594–596, 2009.
- [18] W.-T. Lin, S.-H. Chan, S.-Z. Tseng et al., "Effect of selenization pressure during rapid thermal process on CIGS/MoSe₂ films and solar cells," in *Photovoltaic Technical Conference*, Aix-En-Provence, France, May 2013.
- [19] L. Assmann, J. C. Bernède, A. Drici, C. Amory, E. Halgand, and M. Morsli, "Study of the Mo thin films and Mo/CIGS interface properties," *Applied Surface Science*, vol. 246, no. 1–3, pp. 159–166, 2005.

Research Article

Chaos Synchronization Based Novel Real-Time Intelligent Fault Diagnosis for Photovoltaic Systems

Chin-Tsung Hsieh, Her-Terng Yau, and Jen Shiu

Department of Electrical Engineering, National Chin-Yi University of Technology, Taichung 41170, Taiwan

Correspondence should be addressed to Her-Terng Yau; pan1012@ms52.hinet.net

Received 7 December 2013; Accepted 3 January 2014; Published 18 February 2014

Academic Editor: Hongxing Yang

Copyright © 2014 Chin-Tsung Hsieh et al. This is an open access article distributed under the Creative Commons Attribution License, which permits unrestricted use, distribution, and reproduction in any medium, provided the original work is properly cited.

The traditional solar photovoltaic fault diagnosis system needs two to three sets of sensing elements to capture fault signals as fault features and many fault diagnosis methods cannot be applied with real time. The fault diagnosis method proposed in this study needs only one set of sensing elements to intercept the fault features of the system, which can be real-time-diagnosed by creating the fault data of only one set of sensors. The aforesaid two points reduce the cost and fault diagnosis time. It can improve the construction of the huge database. This study used Matlab to simulate the faults in the solar photovoltaic system. The maximum power point tracker (MPPT) is used to keep a stable power supply to the system when the system has faults. The characteristic signal of system fault voltage is captured and recorded, and the dynamic error of the fault voltage signal is extracted by chaos synchronization. Then, the extension engineering is used to implement the fault diagnosis. Finally, the overall fault diagnosis system only needs to capture the voltage signal of the solar photovoltaic system, and the fault type can be diagnosed instantly.

1. Introduction

In 2013, Hsieh and Shiu proposed a new method of the photovoltaic system fault diagnosis based on chaotic signal synchronization [1]. That method had many advantages. However, it is an offline fault diagnostic scheme. In order to improve the defect, this paper proposes the intelligent solar photovoltaic system real-time fault diagnostic device. Manual detection is replaced by the intelligent solar photovoltaic system real time fault diagnostic device. Its advantage is that, in the spacious solar photovoltaic array, as long as the output end of the array is measured and compared with previously created diagnostic data, the type of fault can be real time quickly diagnosed without manual inspection. Thus, the manual diagnosis time is shortened, while the manpower and cost losses are reduced. Therefore, this paper aims to research and develop an intelligent solar photovoltaic system real-time fault diagnostic device.

The traditional fault diagnostic device uses a neural network [1–4], Fourier analysis [5–7], or wavelet analysis [8–13] for fault diagnosis. The solar photovoltaic system fault diagnoses of different diagnostic methods are introduced

below. In 2011, Shimakage et al. proposed the artificial neural network control for solar photovoltaic array fault diagnosis [14]. The diagnostic effect of the artificial neural diagnostic method proposed in that study was better than the effect of the traditional neural network. Because the authors increased the number of training layers in the neural network to three, the diagnostic effect was very good. However, an additional sensor must be mounted on each series branch solar cell to measure the voltage signal, so the cost increases with the number of solar photovoltaic arrays. In 2011, Syafaruddin et al. discussed solar photovoltaic system fault diagnosis [15]. The assumed state of the solar fault in that study is similar to that in the present study, and the diagnostic methods used in that study were measurement and observation. That study recorded the power generated by the faulted solar photovoltaic system and then compared it with the presently measured power. Although the fault diagnosis based on measurement and observation is simple, there are merely four fault types proposed by the authors. If the number of faults increases, there may be different types of faults. However, the fault category cannot be recognized in the case of identical power. In 2011, Zhao et al. proposed the fault

analysis of inverse connection of the solar photovoltaic array at low light level [16]. That study proposed the I-V curve analysis for fault diagnosis, where the condition configuration is a serial array inverse connection in the array. This condition is equivalent to a major hardware configuration error in a solar photovoltaic array that burns the line. Although the I-V curve analysis is simple and easy to implement, the observation of variance in the current costs both manpower and time. In 2012, Gokmen et al. proposed decision tree-based diagnosis of solar photovoltaic array fault types [17]. That study divided the I-V characteristic curve into four regions, whereby the regions represented four fault categories. The measured voltage and current and the voltage and current of the maximum power point were recorded, and the decision tree method was used to compare the values of the four regions. Finally, the fault category was diagnosed. The experimental results showed that, although the diagnostic rate was as high as 99.8%, the decision-making condition needed 1,637 comparisons, and the best decision-making condition was found by multiple simulations and experiments; thus, the process was very complex. In 2012, Zhao et al. proposed a simple method to diagnose solar photovoltaic systems [18]. That study used three parameter values, including the temperature coefficient of the solar cell, the illumination, and the temperature when there was a fault, to work out the variance in power, so as to diagnose the fault condition. The method only needs two simple equations to diagnose the fault condition, but the data volume of the parameters is huge, and the establishment of parameter data of various temperature and illumination changes takes considerable time. In 2013, Zhao et al. [19] proposed a new image recognition method (ICA) to identify defects in the solar cell surface. In 2013, Zhang et al. proposed the fault analysis and overcurrent protection of the solar photovoltaic array line [20].

This study used a 10-series 2-parallel solar photovoltaic array as the model of fault diagnosis. The fault condition is the short circuit set in the solar cell, and then it is diagnosed by using the chaotic synchronization signal-based fault diagnosis method, proposed in this study, and the intelligent classification of the extension theory. The chaotic system is very sensitive to change in the system, and the system parameters must change if the solar photovoltaic system has a fault. Therefore, this method only needs to import the initial value signal of the photovoltaic system with faults into the chaotic synchronization system according to the variance in initial value, to capture the variance in dynamic error, and then it is imported into the extension theory to effectively distinguish the fault state. Moreover, the extension theory does not need learning time, so the diagnosis is very rapid.

2. Solar Photovoltaic System MPPT Control

The major function of a solar photovoltaic system is to convert solar irradiation into electrical energy using a solar photovoltaic cell and an electric power converter. The equipped electric power converter can stabilize, increase, and reduce

the output voltage or convert the frequency according to the requirements of the output load, and the output power depends on the area of solar photovoltaic cell, conversion efficiency, solar illumination, ambient temperature, and effect of the load. The solar photovoltaic array used in this study is a 10-series 2-parallel array, equipped with a boost converter and MPPT algorithm. This algorithm guarantees the maximum power output when the solar photovoltaic array has faults. The voltage variation is measured in the system operation to distinguish the fault.

The power characteristic generated by the solar photovoltaic cell is not linear, as the power varies with the current sunshine intensity and ambient temperature. In order to keep the output power at the maximum value of the characteristic curve, the solar photovoltaic system must be equipped with MPPT control to guarantee the maximum output power, so as to maximize the system output efficiency. At present, the common MPPT control methods are [21–25] (1) the voltage feedback method, (2) the power feedback method, (3) the straight-line approximation method, (4) the perturbation and observation method, and (5) the incremental conductance method. This paper further discusses the incremental conductance method. The extension theory is combined with this method to control the step output, which is compared with the general fixed step and the variable step.

3. Chaos Synchronization Theory and Extension Theory

3.1. Chaos Synchronization Theory. The behavior of the slave chaotic system tracking master chaotic system is chaos synchronization [26–29]. The master-slave chaotic system is described below:

$$\begin{aligned} \text{master system: } \dot{x}(t) &= f(t, x), \\ \text{slave system: } \dot{y}(t) &= f(t, y) + u(t). \end{aligned} \quad (1)$$

Among which, $x(t) = [x_1, x_2, \dots, x_n] \in R^n$ and $y(t) = [y_1, y_2, \dots, y_n] \in R^n$ are the status values of master system and slave system, $f: R \times R^n \rightarrow R^n$ is the nonlinear function, $B \in R^{n \times 1}$ and $C \in R^{1 \times n}$, u is the controller in the slave system, and the control objective is

$$\lim_{t \rightarrow \infty} \|x(t) - y(t)\| \rightarrow 0. \quad (2)$$

The primary fault characteristic signal in the research on solar power system fault diagnosis may be transient and fast, but the analysis of long-term signal characteristics takes much time, and too many data diagnoses are likely to cause misrecognition. Therefore, this study proposes the chaos synchronization whereby the instantaneous fault signal of the voltage is captured as the diagnostic basis of the chaotic system. Moreover, it defines the master chaotic system as the reference system and the slave chaotic system as the tracking reference system. The slave system is designed to track the reference system in a cycle length. Its tracking dynamic error convergence characteristic is used to extract dynamic error signals, and the fault feature is recorded.

3.1.1. Lorenz Chaos Synchronization System. Since the chaotic system is very sensitive to the change in system parameters, this paper specifically uses this characteristic of chaos. The solar photovoltaic system fault voltage signal is captured for chaos synchronization transformation, the trajectories of dynamic errors are extracted, and these dynamic trajectories are the fault features, so the extension theory is used to recognize fault conditions. From [1], the Lorenz chaos synchronization system is expressed as (3)

$$\begin{aligned} \text{master : } & \begin{cases} \dot{x}_1 = \alpha(x_2 - x_1), \\ \dot{x}_2 = \beta x_1 - x_1 x_3 - x_2, \\ \dot{x}_3 = x_1 x_2 - \gamma x_3, \end{cases} \\ \text{slave : } & \begin{cases} \dot{y}_1 = \alpha(y_2 - y_1) + u_1, \\ \dot{y}_2 = \beta y_1 - y_1 y_3 - y_2 + u_2, \\ \dot{y}_3 = y_1 y_2 - \gamma y_3 + u_3. \end{cases} \end{aligned} \quad (3)$$

The master-slave system error state can be expressed as $e_1 = x_1 - y_1$, $e_2 = x_2 - y_2$, and $e_3 = x_3 - y_3$; the dynamic error system is (4). The slave system tracking master system is observed, so that the control signal is chosen as $u_1 = u_2 = u_3 = 0$.

$$\begin{bmatrix} \dot{e}_1 \\ \dot{e}_2 \\ \dot{e}_3 \end{bmatrix} = \begin{bmatrix} -\alpha & \alpha & 0 \\ \beta & -1 & 0 \\ 0 & 0 & -\gamma \end{bmatrix} \begin{bmatrix} e_1 \\ e_2 \\ e_3 \end{bmatrix} + \begin{bmatrix} 0 \\ y_1 y_3 - x_1 x_3 \\ -y_1 y_2 + x_1 x_2 \end{bmatrix}. \quad (4)$$

According to [1], if the eigenvalue of the system is negative, the error system state is steady, so the chaotic attractor can be generated, and the dynamic trajectory of the chaotic attractor is used for various studies. This paper observes the dynamic trajectory of the chaotic attractor to distinguish the fault types of the solar photovoltaic system.

3.2. Extension Theory. The extension theory can solve the compatibility and contradictory problems, it describes the quality of things quantitatively without learning, and it has high accuracy. Based on the aforesaid characteristics, it is very suitable for classification recognition. This paper therefore uses extension theory as the solar photovoltaic system fault diagnosis method.

3.2.1. Definition of Extension Matter Element. In order to distinguish the differences among things, names are assigned. The extension can use the matter-element concept to present the differences among things in the matter-element model, expressed as [30]

$$R = (N, C, V) = \begin{bmatrix} N & c_1 & v_1 \\ & c_2 & v_2 \\ & \vdots & \vdots \\ & c_n & v_n \end{bmatrix}, \quad (5)$$

where N is the matter, c_j is the characteristic of the matter, and v_j is the value of the characteristic c_j .

3.2.2. Definition of the Extension Set. In classical mathematics, the classical set uses 0 and 1 to describe the characteristics of things, whereas, in fuzzy mathematics, the fuzzy set uses 0 to 1 to describe the fuzzy degree of characteristics of things. The extension set extends the range of the set to $-\infty$ to ∞ to represent the extension degree of the characteristics of things. The extension correlation function is of two intervals in the real number field $\langle -\infty, \infty \rangle$, which are the classical domain $S_o = \langle a, b \rangle$ and the joint domain $S_p = \langle c, d \rangle$, and interval $S_o \in S_p$. If there is a random point s in the real number field, the correlation function can be described as (6), and the overall extension set correlation grade can be expressed as in Figure 1:

$$D = (s, S_o, S_p) = \begin{cases} \rho(s, S_p) - \rho(s, S_o), & s \notin S_o, \\ -1, & s \in S_o, \end{cases} \quad (6)$$

$$K(s) = \frac{\rho(s, S_o)}{D(s, S_o, S_p)},$$

where

$$\begin{aligned} \rho(s, S_o) &= \left| s - \frac{a+b}{2} \right| - \frac{b-a}{2} \\ \rho(s, S_p) &= \left| s - \frac{c+d}{2} \right| - \frac{d-c}{2}, \end{aligned} \quad (7)$$

where $K(s)$ is the grade of correlation between s and S_o . When $K(s) \geq 0$, it is the degree of s belonging to S_o ; when $K(s) < 0$, it is the degree of s not belonging to S_o .

3.3. Diagnostic Process Architecture of the Chaos Synchronization System and Extension Diagnosis. Figure 2 is the chaotic signal synchronization and extension diagnostic system flow chart. First, the measured voltage of the solar photovoltaic system is recorded, and then the recorded voltage signal to be measured is imported into the slave system of the chaotic signal synchronization system. The chaotic synchronization system then generates the chaotic dynamic error signal after subtraction between the master and slave systems, and the dynamic trajectory formed of the chaotic dynamic error signal is the main basis of extension diagnosis, that is, the fault feature of the solar photovoltaic system. Finally, as long as the chaotic dynamic error signal is imported into the finished extension matter-element model, the fault category can be identified rapidly and accurately by extension diagnosis of the fault conditions.

4. Experimental Results

4.1. Extension Incremental Conductance Method. In terms of the solar photovoltaic system MPPT, this paper proposes the extension incremental conductance method (EICM) and compares it with the general fixed step incremental conductance method (FICM) and the variable step incremental conductance method (VICM). As the fixed step incremental conductance method has only one set of steps (step = 0.001), the tracking speed is always the same whatever the dP/dV is.

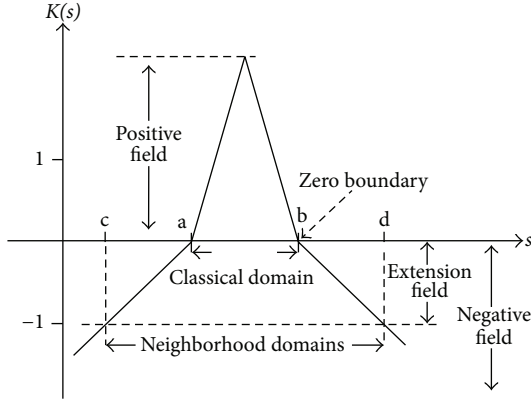


FIGURE 1: Schematic diagram of the correlation function.

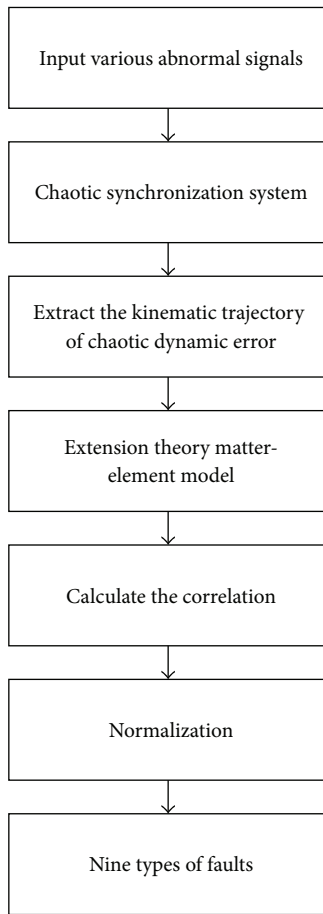


FIGURE 2: Chaotic signal synchronization and extension diagnostic system flow chart.

Neither the speed nor the step can be adjusted, which becomes the main defect in the most fundamental incremental conductance method. The variable step incremental conductance method has large steps (step = 0.005) and small steps (step = 0.001), and its tracking speed is much higher than that of the general fixed step incremental conductance method, but the dP/dV identification mode is not intelligent

TABLE 1: Matter-element model of the extension incremental conductance method for dP/dV .

[Joint domain, c_1 , $\langle 0, 10000 \rangle$]
[Large step, c_1 , $\langle 5.0001, 10000 \rangle$]
[Small step, c_1 , $\langle 0, 5 \rangle$]

TABLE 2: Solar panel model and specifications.

Solar panel model	SM 1611
Open circuit voltage	3.0 V
Short circuit current	0.8 A
Maximum power point voltage	2.36 V
Maximum power point current	0.7 A
Maximum power	1.65 W

TABLE 3: Solar photovoltaic system fault category.

Fault type	Fault condition (short circuit set in faulted solar cell)
SCF ₁	There is no fault in the two-series branch solar photovoltaic system.
SCF ₂	One solar cell fault occurs in any series branch of the two-series branch solar photovoltaic system.
SCF ₃	Two solar cell faults occur in any series branch of the two-series branch solar photovoltaic system.
SCF ₄	Three solar cell faults occur in any series branch of the two-series branch solar photovoltaic system.
SCF ₅	One solar cell fault occurs in each series branch of the two-series branch solar photovoltaic system.
SCF ₆	Two solar cell faults occur in each series branch of the two-series branch solar photovoltaic system.
SCF ₇	One solar cell fault occurs in one series branch and two solar cell faults occur in the other branch of the two-series branch solar photovoltaic system.
SCF ₈	One solar cell fault occurs in one series branch and four solar cell faults occur in the other branch of the two-series branch solar photovoltaic system.
SCF ₉	Two solar cell faults occur in one series branch and three solar cell faults occur in the other branch of the two-series branch solar photovoltaic system.

enough. The extension incremental conductance method proposed in this paper can extend the matter-element model according to the dP/dV value and reach intelligent identification and rapid tracking under the same condition (step = 0.005 and 0.001). The result is shown in Figure 3. The classical domain and joint domain of the extension incremental conductance method are shown in Table 1.

4.2. Implementation of the Solar Photovoltaic System Real-Time Fault Diagnosis. The solar cell in this paper is SM 1611; its specifications are shown in Table 2. The solar illumination is $1,000 \text{ W/m}^2$, and the ambient temperature is 25°C . The system architecture is shown in Figure 4. The connection mode is 10-series 2-parallel, as shown in Figure 5. The fault state should be simulated before the fault condition is diagnosed. The fault types are shown in Table 3 [31, 32]. The V-P

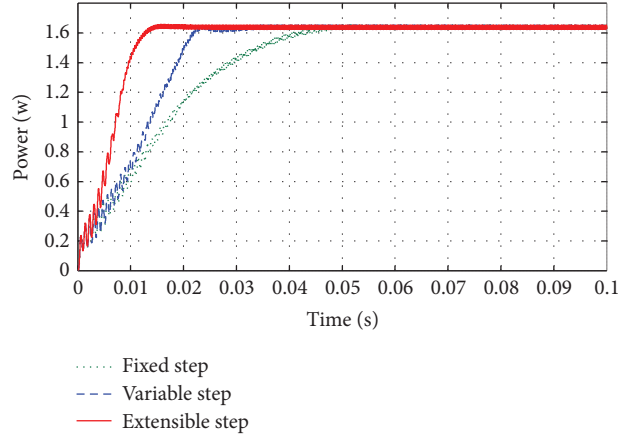


FIGURE 3: Comparison result of FICM, VICM, and EICM.

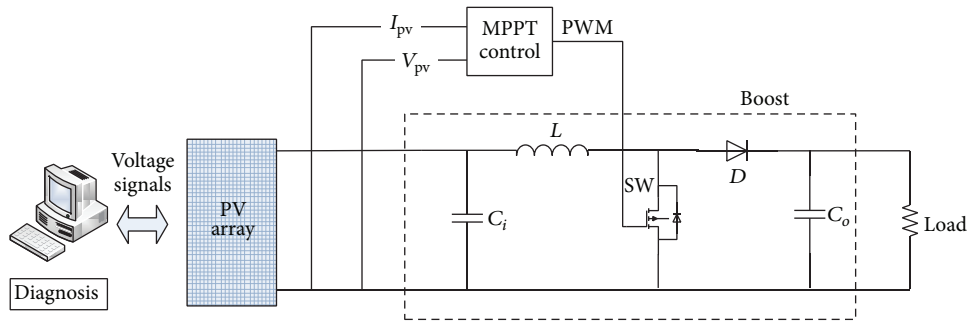


FIGURE 4: System architecture of the solar photovoltaic system.

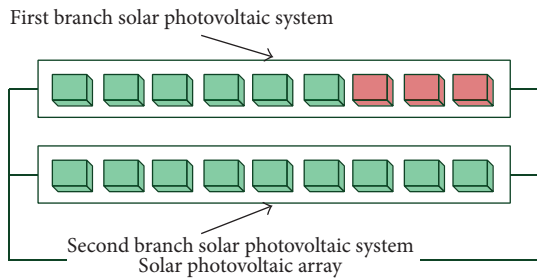


FIGURE 5: Schematic diagram of faults in the solar photovoltaic array (SCF₇).

and V-I characteristic curves of the solar photovoltaic array vary with the sunshine and ambient temperature. The fault condition in this paper is the short circuit set in the solar panel, and nine kinds of solar cell fault (SCF) are simulated. Therefore, there are nine kinds of V-P and V-I characteristic curves, as shown in Figures 6(a) and 6(b). The fault voltage signal is mixed with a minute quantity of Gaussian noise, as shown in Figure 7. The maximum power point voltage when a fault occurs is measured and recorded, as shown in Figure 8. The addition of Gaussian noise is helpful in enlarging the dynamic trajectory of chaotic dynamic error, so

as to highlight the fault feature; meanwhile the tolerance of the system for noise can be written in the extension matter-element model, so that the system can resist noise. Finally, as long as the nine kinds of fault voltage signal are imported into the chaos synchronization system, the fault features can be extracted as the base of extension matter-element modeling. The environment noise of a physical system is usually a high frequency signal. Therefore, a low-pass filter could be used to pretreat the system signal.

The solar photovoltaic array for this experiment is the Agilent Technologies E4360A modular solar array platform. When the nine fault characteristic curves of solar energy in Figures 6(a) and 6(b) are imported into the E4360A modular solar array platform, nine fault voltages can be exported. The MPPT algorithm is implemented by dSPACE and is finally connected to the boost converter to record the voltages of various fault conditions for fault diagnosis. Figure 8 shows the measured voltage with Gaussian noise. The experimental sampling rate is 10 kHz. The master system of the chaos synchronization system bears the normal voltage signal of the solar photovoltaic system, and the slave system bears the faulted voltage signal of the solar photovoltaic system. The unmeasured voltage signal is imported into the chaos synchronization system of (1) the chaos synchronization error is converted into dynamic error to obtain the $\dot{e}_1\dot{e}_2\dot{e}_3$ three-dimensional motion trajectory, as shown in Figure 9.

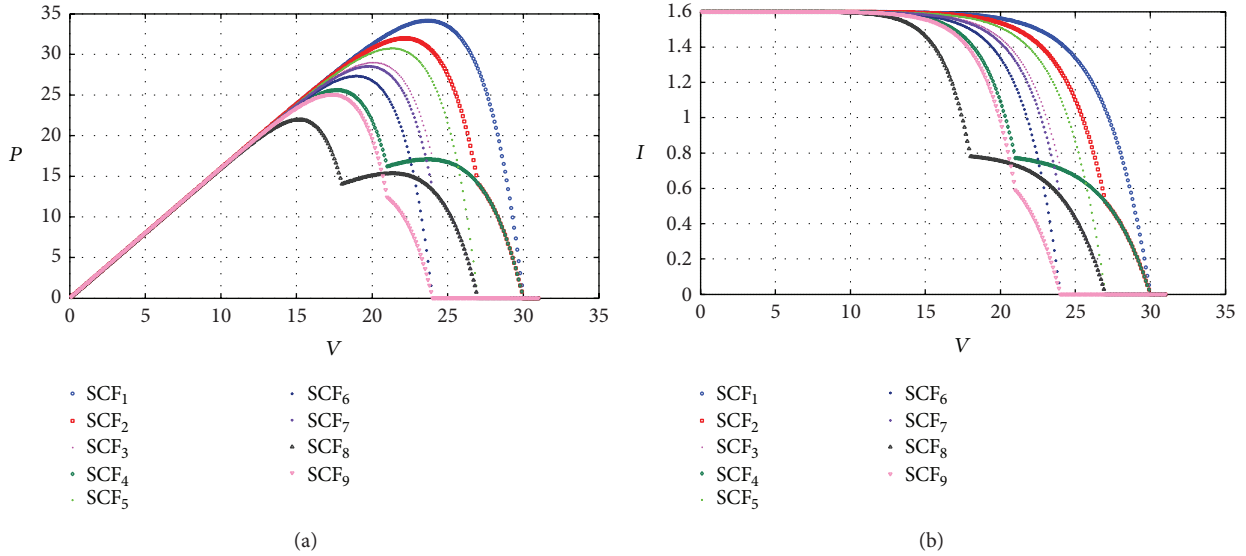


FIGURE 6: (a) V-P characteristic curves of nine faults. (b) V-I characteristic curves of nine faults.

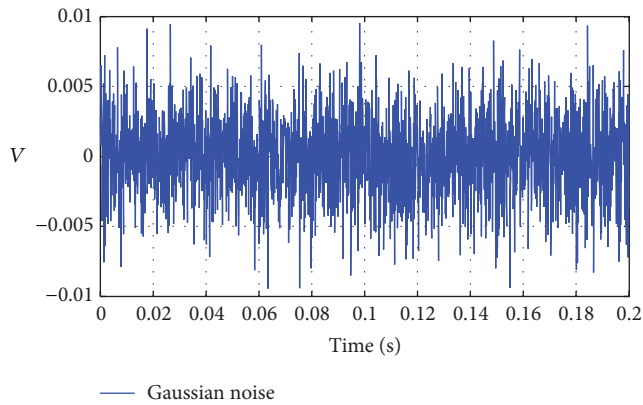


FIGURE 7: Gaussian noise (0.1%).

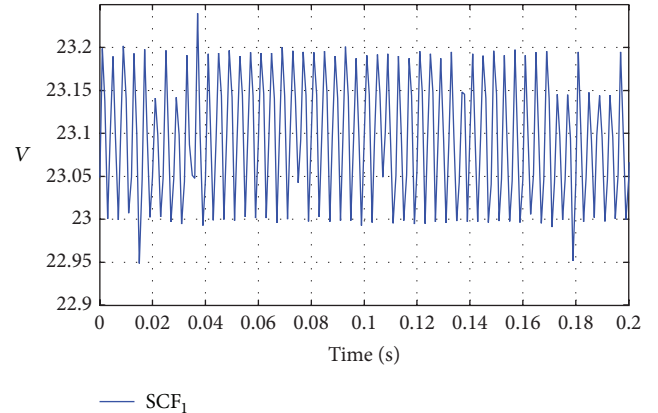


FIGURE 8: Voltage signal of SCF₁ with Gaussian noise.

The plan view of the dynamic error of the nine faults is shown in Figure 9.

The nine patterns are put on the same plane. The dynamic trajectory of each fault is shown in Figure 10. The chaotic dynamic trajectory is used to build the extension matter-element model. Figure 10 shows the chaotic waveform circle 0 of \dot{e}_1 , which tends to be symmetrical. As the chaotic dynamic trajectory of \dot{e}_1 in $\langle -2, -0 \rangle$ and $\langle 0, 2 \rangle$ intervals is very apparent, \dot{e}_1 in $\langle -2, 0 \rangle$ and $\langle 0, 2 \rangle$ intervals is used as the basis of the extension matter. The \dot{e}_3 corresponding to \dot{e}_1 interval landing point is calculated, and the average of \dot{e}_3 landing point is extracted as the eigenvalue extracted in this paper. The matter-element model is shown in Table 4. The weight in this paper is set as 0.5. The solar photovoltaic system can be diagnosed after the extension matter-element model is built.

If the fault diagnosis cannot implement real-time measurement and diagnosis, it wastes both time and money. Therefore, this study implemented real-time fault diagnosis of

the solar photovoltaic system, saving a considerable amount of time. The fault state displayed by the diagnostic system needs to be considered. The real-time fault diagnosis system is implemented using the dSPACE hardware system, the system sampling rate is 10 kHz, and the diagnosis is renewed when the number of data is 10,000; that is, the diagnostic values are updated per second. Therefore, the fault diagnosis system needs only one second to diagnose the faults in the solar photovoltaic system, so as to implement real-time diagnosis. Figure 11 shows the system hardware facilities. Figure 12 shows the real-time diagnosis interface of dSPACE. In the experiment of real-time diagnosis, this paper measured the nine faults 20 times, respectively. Meanwhile five percentages of Gaussian noise (0.1%, 0.3%, 0.5%, 1%, and 5%) were added in to test the real-time diagnosis rate of the system and to test the tolerance of the diagnostic system with the noise. Table 5 shows the real-time diagnosis rate.

In the traditional fault diagnosis system, once there is a little noise interference, the diagnosis will be inaccurate.

TABLE 4: Chaotic dynamic trajectory matter-element model.

Neighborhood domains =	Normal	c_1	$\langle 200, 500 \rangle$		c_2	$\langle 200, 500 \rangle$	$SCF_1 =$	Fault	c_1	$\langle 460, 480 \rangle$
									c_2	$\langle 460, 480 \rangle$
$SCF_2 =$	Fault	c_1	$\langle 430, 450 \rangle$		c_2	$\langle 430, 450 \rangle$	$SCF_3 =$	Fault	c_1	$\langle 380, 390 \rangle$
									c_2	$\langle 380, 390 \rangle$
$SCF_4 =$	Fault	c_1	$\langle 310, 320 \rangle$		c_2	$\langle 310, 320 \rangle$	$SCF_5 =$	Fault	c_1	$\langle 410, 420 \rangle$
									c_2	$\langle 410, 420 \rangle$
$SCF_6 =$	Fault	c_1	$\langle 340, 360 \rangle$		c_2	$\langle 340, 360 \rangle$	$SCF_7 =$	Fault	c_1	$\langle 370, 375 \rangle$
									c_2	$\langle 370, 375 \rangle$
$SCF_8 =$	Fault	c_1	$\langle 230, 250 \rangle$		c_2	$\langle 230, 250 \rangle$	$SCF_9 =$	Fault	c_1	$\langle 295, 307 \rangle$
									c_2	$\langle 295, 307 \rangle$

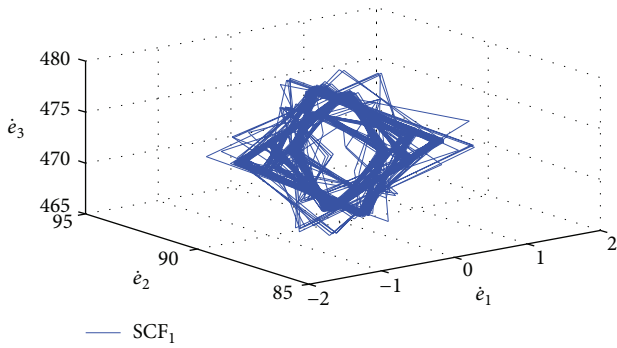


FIGURE 9: Three-dimensional diagram of $\dot{e}_1\dot{e}_2\dot{e}_3$ dynamic error of SCF_1 .

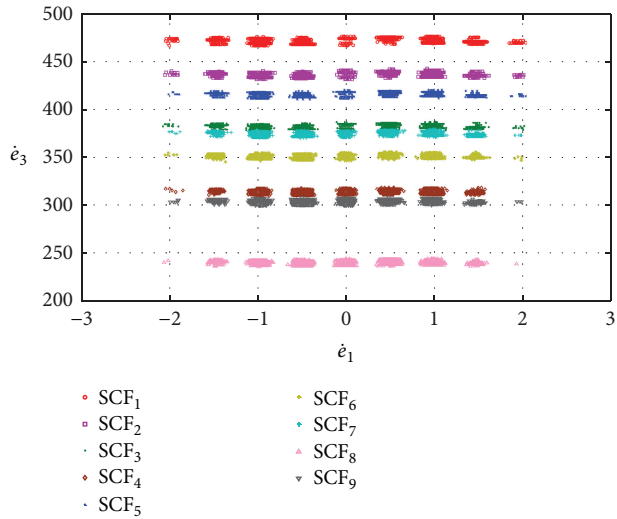


FIGURE 10: Plan view of $\dot{e}_1-\dot{e}_3$ dynamic errors of SCF_1-SCF_9 .

However, in the chaotic system, not only does a little noise make the dynamic error trajectory more apparent, but also the system can tolerate the noise interference. Therefore, the diagnostic system in this paper resists noise, and its diagnostic rate is still high when the noise changes drastically.

TABLE 5: Real-time diagnosis rate.

Percentage of additional Gaussian noise (%)	Number of intercepted real-time diagnostic signals (signals)	Diagnostic rate (%)
0.1	180	100
0.3	180	100
0.5	180	100
1	180	100
5	180	98.89

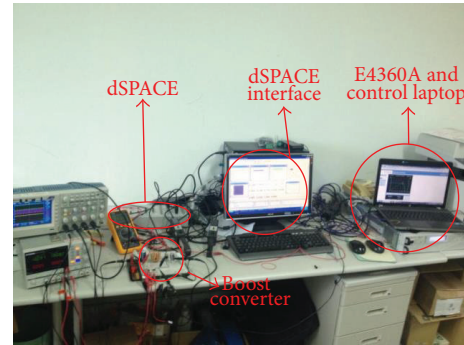


FIGURE 11: System hardware facilities.

5. Conclusions

The paper derived a real-time system to diagnose the faults in a solar photovoltaic system. The chaos synchronization and extension theory were used to distinguish the fault types. The extension theory does not need to create too much data, and neither does it require training or learning. Its diagnosis is very fast in comparison with general neural diagnosis. This method proposed in this paper only needs one set of sensors to capture a voltage signal, which is then imported into the chaos synchronization system. In the dynamic error graph of the chaos synchronization system converted from voltage signals, accurate, rapid, timesaving, and cost saving fault recognition can be implemented only by capturing two fault features. In comparison with other traditional fault diagnosis methods which need at least three sensor modules to capture the physical quantities before system diagnosis,

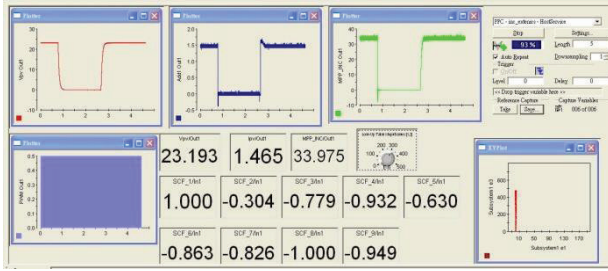


FIGURE 12: dSPACE real-time diagnosis interface.

the fault diagnostic device of this paper can save the cost of sensors while implementing real-time diagnosis. As an intelligent fault diagnostic device, its diagnosis is very rapid and accurate.

Conflict of Interests

The authors declare no conflict of interests regarding the publication of this paper.

References

- C. T. Hsieh and J. Shiu, "Study of intelligent photovoltaic system fault diagnostic scheme based on chaotic signal synchronization," *Mathematical Problems in Engineering*, vol. 2013, Article ID 816296, 6 pages, 2013.
- H. Guolian, J. Pan, W. Zhentao, and Z. Jianhua, "Research on fault diagnosis of wind turbine control system based on Artificial Neural Network," in *Proceedings of the 8th World Congress on Intelligent Control and Automation (WCICA '10)*, pp. 4875–4879, Jinan, China, July 2010.
- H. Fang and C. Xia, "A fuzzy neural network based fault detection scheme for synchronous generator with internal fault," in *Proceedings of the 6th International Conference on Fuzzy Systems and Knowledge Discovery (FSKD '09)*, pp. 433–437, Tianjin, China, August 2009.
- G. Xiong, D. Shi, L. Zhu, and X. Duan, "A new approach to fault diagnosis of power systems using fuzzy reasoning spiking neural p systems," *Mathematical Problems in Engineering*, vol. 2013, Article ID 815352, 13 pages, 2013.
- M. Pineda-Sanchez, M. Riera-Guasp, J. A. Antonino-Daviu, J. Roger-Folch, J. Perez-Cruz, and R. Puche-Panadero, "Diagnosis of induction motor faults in the fractional fourier domain," *IEEE Transactions on Instrumentation and Measurement*, vol. 59, no. 8, pp. 2065–2075, 2010.
- J. H. Lee, Y. K. Seong, C. H. Chang et al., "Fourier-based shape feature extraction technique for computer-aided b-mode ultrasound diagnosis of breast tumor," in *Proceedings of the Annual International Conference of the IEEE Engineering in Medicine and Biology Society (EMBC'12)*, pp. 6551–6554, San Diego, Calif, USA, August 2012.
- E. Uslu and G. Bilgin, "Exploiting locality based Fourier transform for ECG signal diagnosis," in *Proceedings of the International Conference on Applied Electronics (AE'12)*, pp. 323–326, Pilsen, Czech Republic, September 2012.
- K. Li, P. Chen, and H. Wang, "Intelligent diagnosis method for rotating machinery using wavelet transform and ant colony optimization," *IEEE Sensors Journal*, vol. 12, no. 7, pp. 2474–2484, 2012.
- A. Bouzida, O. Touhami, R. Ibtouen, A. Belouchrani, M. Fadel, and A. Rezzoug, "Fault diagnosis in industrial induction machines through discrete wavelet transform," *IEEE Transactions on Industrial Electronics*, vol. 58, no. 9, pp. 4385–4395, 2011.
- J. Pons-Llinares, J. A. Antonino-Daviu, M. Riera-Guasp, M. Pineda-Sanchez, and V. Climente-Alarcon, "Induction motor diagnosis based on a transient current analytic wavelet transform via frequency B-Splines," *IEEE Transactions on Industrial Electronics*, vol. 58, no. 5, pp. 1530–1544, 2011.
- Q. Liu, F. Chen, Z. Zhou, and Q. Wei, "Fault diagnosis of rolling bearing based on wavelet package transform and ensemble empirical mode decomposition," *Advances in Mechanical Engineering*, vol. 2013, Article ID 792584, 6 pages, 2013.
- G. Campetelli, D. Zumoffen, and M. Basualdo, "Improvements on noninvasive blood glucose biosensors using wavelets for quick fault detection," *Journal of Sensors*, vol. 2011, Article ID 368015, 11 pages, 2011.
- W. Li, Z. Wang, Z. Zhu, G. Zhou, and G. Chen, "Design of online monitoring and fault diagnosis system for belt conveyors based on wavelet packet decomposition and support vector machine," *Advances in Mechanical Engineering*, vol. 2013, Article ID 797183, 10 pages, 2013.
- T. Shimakage, K. Nishioka, H. Yamane, M. Nagura, and M. Kudo, "Development of fault detection system in PV system," in *Proceedings of the 33rd International Telecommunications Energy Conference (INTELEC'11)*, Amsterdam, The Netherlands, October 2011.
- S. Syafaruddin, E. Karatepe, and T. Hiyama, "Controlling of artificial neural network for fault diagnosis of photovoltaic array," in *Proceedings of the IEEE 33rd International Telecommunications Energy Conference (INTELEC'11)*, pp. 1–5, Amsterdam, The Netherlands, September 2011.
- Y. Zhao, B. Lehman, J. F. De Palma, J. Mosesian, and R. Lyons, "Fault analysis in solar PV arrays under: low irradiance conditions and reverse connections," in *Proceedings of the 37th IEEE Photovoltaic Specialists Conference (PVSC'11)*, pp. 2000–2005, Seattle, Wash, USA, June 2011.
- N. Gokmen, E. Karatepe, B. Celik, and S. Silvestre, "Simple diagnostic approach for determining of faulted PV modules in string based PV arrays," *Solar Energy*, vol. 86, no. 11, pp. 3364–3377.
- Y. Zhao, L. Yang, B. Lehman, J.-F. De Palma, J. Mosesian, and R. Lyons, "Decision tree-based fault detection and classification in solar photovoltaic arrays," in *Proceedings of the 27th Annual IEEE Applied Power Electronics Conference and Exposition (APEC'12)*, pp. 93–99, Orlando, Fla, USA, February 2012.
- Y. Zhao, J. F. De Palma, J. Mosesian, R. Lyons, and B. Lehman, "Line-line fault analysis and protection challenges in solar photovoltaic arrays," *IEEE Transactions on Industrial Electronics*, vol. 60, no. 9, pp. 3784–3795, 2013.
- X. Zhang, H. Sun, Y. Zhou, J. xi, and M. Li, "A novel method for surface defect detection of photovoltaic module based on independent component analysis," *Mathematical Problems in Engineering*, vol. 2013, Article ID 520568, 8 pages, 2013.
- H. Wu and X. Tao, "Three phase photovoltaic grid-connected generation technology with MPPT function and voltage control," in *Proceedings of the International Conference on Power Electronics and Drive Systems (PEDS'09)*, pp. 1295–1300, Taipei, Taiwan, January 2009.

- [22] M. A. Elgendy, B. Zahawi, and D. J. Atkinson, "Assessment of perturb and observe MPPT algorithm implementation techniques for PV pumping applications," *IEEE Transactions on Sustainable Energy*, vol. 3, no. 1, pp. 21–33, 2012.
- [23] F. Liu, S. Duan, F. Liu, B. Liu, and Y. Kang, "A variable step size INC MPPT method for PV systems," *IEEE Transactions on Industrial Electronics*, vol. 55, no. 7, pp. 2622–2628, 2008.
- [24] Q. Mei, M. Shan, L. Liu, and J. M. Guerrero, "A novel improved variable step-size incremental-resistance MPPT method for PV systems," *IEEE Transactions on Industrial Electronics*, vol. 58, no. 6, pp. 2427–2434, 2011.
- [25] H. T. Yau, C. J. Lin, and C. H. Wu, "Sliding mode extremum seeking control scheme based on PSO for maximum power point tracking in photovoltaic systems," *International Journal of Photoenergy*, vol. 2013, Article ID 527948, 10 pages, 2013.
- [26] C. Bianca and L. Rondoni, "The nonequilibrium ehrenfest gas: a chaotic model with flat obstacles?" *Chaos*, vol. 19, no. 1, Article ID 013121, 2009.
- [27] C. Bianca, "Weyl-flow and the conformally symplectic structure of thermostatted billiards: the problem of the hyperbolicity," *Nonlinear Analysis: Hybrid Systems*, vol. 5, no. 1, pp. 32–51, 2011.
- [28] H.-T. Yau, "Generalized projective chaos synchronization of gyroscope systems subjected to dead-zone nonlinear inputs," *Physics Letters A*, vol. 372, no. 14, pp. 2380–2385, 2008.
- [29] H.-T. Yau, C.-C. Wang, C.-T. Hsieh, and C.-C. Cho, "Nonlinear analysis and control of the uncertain micro-electro-mechanical system by using a fuzzy sliding mode control design," *Computers and Mathematics with Applications*, vol. 61, no. 8, pp. 1912–1916, 2011.
- [30] M. H. Wang, "Application of extension theory to vibration fault diagnosis of generator sets," *IEE Proceedings Generation Transmission and Distribution*, vol. 151, no. 4, pp. 503–508, 2004.
- [31] K.-H. Chao, S.-H. Ho, and M.-H. Wang, "Modeling and fault diagnosis of a photovoltaic system," *Electric Power Systems Research*, vol. 78, no. 1, pp. 97–105, 2008.
- [32] K.-H. Chao, C.-T. Chen, M.-H. Wang, and C.-F. Wu, "A novel fault diagnosis method based-on modified neural networks for photovoltaic systems," in *Advances in Swarm Intelligence*, vol. 6146 of *Lecture Notes in Computer Science*, pp. 531–539, Springer, Berlin, Germany, 2010.